A compact mode-locked diode laser system for high precision frequency comparison experiments

D I S S E R T A T I O N

zur Erlangung des akademischen Grades
doctor rerum naturalium
(Dr. rer. nat.)
im Fach Physik

eingereicht an der
Mathematisch-Naturwissenschaftlichen Fakultät
Humboldt-Universität zu Berlin

von
Dipl.-Phys. Heike Christopher

Präsidentin der Humboldt-Universität zu Berlin:
Prof. Dr.-Ing. Dr. Sabine Kunst

Dekan der Mathematisch-Naturwissenschaftlichen Fakultät:
Prof. Dr. Elmar Kulke

Gutachter:
1. Prof. Achim Peters, Ph.D.
2. Prof. Dr. Günther Tränkle
3. Prof. Dr. Gaetano Mileti

Tag der mündlichen Prüfung: 08.02.2021

Abstract

Optical frequency combs (OFCs) have revolutionized various applications in applied and fundamental sciences that rely on the determination of absolute optical frequencies and frequency differences. For absolute frequency measurements, the optical frequency comb generator (OFCG) requires a highly complex system typically comprising a mode-locked laser, optical amplifiers, spectral broadening systems, typically to more than one octave, as well as an absolute stabilization of the OFC. In contrast, measurements of frequency differences require only stabilization of the spectral distance between the individual comb lines of the OFC. In this case, the OFCG can be tailored to the application and the system complexity can be reduced. One such application is the quantum test of the universality of free fall (UFF) within the QUANTUS (*Quantengase unter Schwerelosigkeit*; quantum gases under weightlessness) experimental series that aims to push the accuracy of UFF tests. This test intends to compare the rate of free fall of two atomic species, rubidium (Rb) and potassium (K), in micro-gravity. Such an experiment would greatly benefit from an opportunity to directly compare optical frequencies in the vicinity of the D2 transition of Rb (∼780 nm) with those in the vicinity of the D2 transition of K (∼767 nm). The aim of this thesis was the development of a highly compact, robust, and space-suitable diode laser-based OFCG providing a mode-locked optical spectrum in this wavelength range.

The diode laser-based OFC was required to feature a spectral bandwidth of at least 13.5 nm at 20 dBc. To provide the means for generation of beat note signals with the Rb and K reference lasers, the optical power of the comb lines at 20 dBc needed to exceed 100 nW. For use of electronics similar to those used for the interferometry part of the QUANTUS experiments, a pulse repetition rate of 6.8 GHz or its subharmonics was desired. To take advantage of the frequency comparison by means of the diode laser-based OFC, the RF linewidth of the stabilized pulse repetition rate was required to be smaller 40 Hz (for a pulse repetition rate of 6.8 GHz). It was estimated that this RF linewidth can be reached with active stabilization as long as the free-running RF linewidth does not exceed 10 kHz. In the frame of this thesis, a diode laser-based OFC with a pulse repetition rate of 3.4 GHz was realized that provided a spectral bandwidth exceeding 16 nm (at 20 dBc). The comb lines at 20 dBc of that OFC featured an optical power of more than 650 nW. Furthermore, a free-running pulse repetition rate with an RF linewidth of less than 10 kHz was demonstrated.

An important aspect for the realization of a space-suitable diode laser-based OFCG was the hybrid integration of that OFCG into a compact and robust technology platform that was developed for implementation in future QUANTUS experiments. By means of setting up a proof-of-concept demonstrator module, critical integration technology aspects were identified and an integration strategy was developed. Based on this, the hybrid integration of a large spectral bandwidth diode laser-based OFCG into a technology platform featuring a footprint of only 25×80 mm^2 was successfully demonstrated.

Proof of a sufficient RF stability of the OFCG in terms of the RF linewidth of the pulse

repetition rate was required within the scope of this thesis. To that end, an experimental test bed was developed that allowed for the stabilization of the pulse repetition rate to an external RF reference. Use of a feedback loop with a servo bandwidth of around 72 kHz allowed for demonstration of a stabilized pulse repetition rate featuring an RF linewidth of less than about 1.4 Hz (resolution limited). This result exceeds the requirement by more than one order of magnitude.

The development of the diode laser-based OFCG carried out within the scope of this thesis paves the way towards an improved comparison of the rate of free fall of Rb and K quantum gases within the QUANTUS experiments in micro-gravity. Thus, this thesis represents an important step towards a quantum test of the UFF within future space-borne experiments.

Zusammenfassung

Optische Frequenzkämme (OFCs) haben eine Vielzahl von Anwendungen in den angewandten Wissenschaften und der Grundlagenforschung, die auf der Bestimmung von absoluten Frequenzen und Frequenzdifferenzen beruhen, revolutioniert. Für absolute Frequenzmessungen benötigt der optische Frequenzkammgenerator (OFCG) ein hochkomplexes System, das üblicherweise aus einem modengekoppelten Laser, optischen Verstärkern, Systemen zur spektralen Verbreiterung, typisch zu mehr als einer Oktave, sowie einer absoluten Stabilisierung des OFCs besteht. Im Gegensatz dazu wird für Messungen von Frequenzdifferenzen nur die Stabilisierung des spektralen Abstandes zwischen den individuellen Kammlinien des OFCs benötigt. In diesem Fall kann der OFCG auf die Anwendung zugeschnitten und die Systemkomplexität reduziert werden. Eine solche Anwendung ist der Quantentest der Universalität des Freien Falls (UFF) im Rahmen der Experimentserie QUANTUS (Quantengase unter Schwerelosigkeit), die die Genauigkeit von UFF-Tests verbessern will. Mit diesem Test soll der Freie Fall zweier atomarer Spezies, Rubidium (Rb) und Kalium (K), in Mikrogravitation vergleichen werden. Ein solches Experiment würde sehr von der Möglichkeit profitieren, optische Frequenzen in der Nähe des D2-Übergangs von Rb (∼780 nm) direkt mit denen in der Nähe des D2-Übergangs von K (∼760 nm) vergleichen zu können. Das Ziel dieser Doktorarbeit war die Entwicklung eines hochkompakten, robusten, und weltraum-tauglichen diodenlaser-basierten OFCGs, der ein modengekoppeltes optisches Spektrum in diesem Wellenlängenbereich emittiert.

Der diodenlaser-basierte OFC musste eine spektrale Bandbreite von wenigstens 13,5 nm bei 20 dBc aufweisen. Um Schwebungssignale mit den Rb- und K-Referenzlasern erzeugen zu können, sollte die optische Leistung der Kammlinien bei 20 dBc mindestens 100 nW erreichen. Zur Nutzung ähnlicher Steuerungs- und Stabilisierungselektronik wie im Interferometrieteil des QUANTUS-Experiments war eine Pulswiederholrate bei 6,8 GHz oder Subharmonischen davon gewünscht. Um die Vorteile des Frequenzvergleichs mit Hilfe des diodelaser-basierten OFCs nutzen zu können, war eine RF-Linienbreite der stabilisierten Pulswiederholrate von weniger als 40 Hz (bei einer Pulswiederholrate von 6,8 GHz) erforderlich. Abschätzungen haben ergeben, dass diese RF-Linienbreite mittels aktiver Stabilisierung erreicht werden kann, solange die frei-laufende RF-Linienbreite 10 kHz nicht übersteigt. Im Rahmen dieser Arbeit wurde ein diodenlaser-basierter OFC mit einer Pulswiederholrate von 3,4 GHz entwickelt, der eine spektrale Bandbreite von mehr als 16 nm (bei 20 dBc) bietet. Die Kammlinien dieses OFCs bei 20 dBc wiesen eine optische Leistung von mehr als 650 nW auf. Zudem wurde eine frei-laufende Pulswiederholrate mit einer RF-Linienbreite von weniger als 10 kHz demonstriert.

Ein wichtiger Aspekt für die Realisierung eines weltraum-tauglichen diodenlaser-basierten OFCGs war die hybride Integration dieses OFCGs in eine kompakte und robuste Technologieplattform, die für die Anwendung in zukünftigen QUANTUS-Experimenten entwickelt wurde. Durch den Aufbau eines Demonstratormoduls im Rahmen einer Machbarkeitsstudie konnten kritische Aspekte der Integrationstechnologie identifiziert und eine Integrationsstrategie entwickelt

werden. Darauf aufbauend wurde ein diodenlaser-basierter OFCG, der eine große spektrale Bandbreite aufweist, erfolgreich in eine Technologieplattform mit einer Grundfläche von nur 25×80 mm^2 integriert.

Der Nachweis einer ausreichend hohen RF-Stabilität des OFCGs in Form der RF-Linienbreite der Pulswiederholrate war im Rahmen dieser Arbeit erforderlich. Zu diesem Zweck wurde eine experimentelle Testumgebung entwickelt, die die Stabilisierung der Pulswiederholrate auf eine externe RF-Referenz erlaubt. Durch Anwendung einer Regelschleife mit einer Bandbreite von ungefähr 72 kHz konnte eine stabilisierte Pulswiederholrate mit einer RF-Linienbreite von weniger als 1,4 Hz (auflösungsbegrenzt) nachgewiesen werden. Dieses Ergebnis übertrifft die Anforderung um mehr als eine Größenordnung.

Die Entwicklung des diodenlaser-basierten OFCGs, die im Rahmen dieser Arbeit durchgeführt wurde, ist ein Wegbereiter für einen verbesserten Vergleich des Freien Falls von Rb- und K-Quantengasen innerhalb der QUANTUS-Experimente in Mikrogravitation. Daher stellt diese Arbeit einen wichtigen Schritt in Richtung eines Quantentests der Universalität des Freien Falls in zukünftigen weltraum-basierten Experimenten dar.

Contents

1. Introduction **1**
- 1.1. The optical frequency comb . . . 2
  - 1.1.1. Theoretical description of mode-locked operation . . . 4
  - 1.1.2. Phenomenological description of mode-locked operation . . . 5
  - 1.1.3. Measurement of optical frequencies and frequency differences . . . 6
- 1.2. A tailored optical frequency comb for a spaceborne experiment . . . 7
  - 1.2.1. The QUANTUS experiments: a test of the universality of free fall . . . 8
  - 1.2.2. An advanced frequency stabilization scheme for future QUANTUS experiments . . . 9
  - 1.2.3. The LASUS projects: development of diode laser technology for use in the QUANTUS experiments . . . 13
  - 1.2.4. Requirements on an optical frequency comb for spaceborne tests of the universality of free fall in the QUANTUS experiments . . . 16
- 1.3. State of the art optical frequency combs operating in the wavelength region around 780 nm . . . 20
- 1.4. Thesis organization . . . 23
  - 1.4.1. Goals of this thesis . . . 23
  - 1.4.2. Outline of this thesis . . . 23

2. Mode-locking of semiconductor lasers **25**
- 2.1. Introduction to mode-locked diode lasers . . . 25
- 2.2. Diode laser chips . . . 25
- 2.3. Mode-locking techniques . . . 29
  - 2.3.1. Active mode-locking . . . 29
  - 2.3.2. Passive mode-locking . . . 30
  - 2.3.3. Hybrid mode-locking . . . 32
- 2.4. Optical absorption and gain in passively mode-locked diode lasers . . . 33
- 2.5. Resonator concepts for passively mode-locked diode lasers . . . 36
- 2.6. Optical components of an ML-ECDL . . . 38
  - 2.6.1. Coating of the diode laser chip's facets . . . 39
  - 2.6.2. Beam shaping optics . . . 39
  - 2.6.3. External mirror . . . 40

3. Measurement methods and setup **41**
- 3.1. Introduction to measurement and analysis feedback loop . . . 41
- 3.2. Requirements on the experimental setup and techniques . . . 41

3.3. Experimental setup . . . 43
3.3.1. Laser test mount . . . 43
3.3.2. Measurement setup . . . 45
3.4. Experimental techniques . . . 47
3.4.1. Optical frequency domain . . . 47
3.4.2. RF frequency domain . . . 48
3.4.3. Time domain-based investigation of RF characteristics . . . 51
3.4.4. Time domain . . . 54
3.4.5. Optical power . . . 56
3.4.6. Measurement procedure and control . . . 57
3.5. Performance analysis . . . 59
3.6. Summary . . . 60

4. Development of a diode laser-based optical frequency comb 61
4.1. Introduction to the evaluation . . . 61
4.2. Influence of the laser design parameters on the mode-locking performance . . . 62
4.2.1. Optical design . . . 62
4.2.2. External mirror . . . 63
4.2.3. Laser resonator length . . . 64
4.2.4. Epitaxial layer design of the diode laser chip . . . 67
4.2.5. Longitudinal design of the diode laser chip . . . 75
4.2.6. Facet reflectivity of the diode laser chip . . . 82
4.2.7. Conclusion for optimization of the laser design . . . 87
4.3. Influence of the laser operating parameters on the performance of the best suited device . . . 88
4.3.1. Optical frequency domain characteristics . . . 88
4.3.2. RF frequency domain characteristics . . . 93
4.3.3. Time domain-based RF characteristics . . . 94
4.3.4. Time domain characteristics . . . 96
4.3.5. Optical power characteristics . . . 97
4.4. Conclusion of the development of the diode laser-based optical frequency comb . 98

5. Micro-integration of the diode laser-based optical frequency comb generator 101
5.1. Introduction to the micro-integration concept . . . 101
5.2. First generation ML-ECDL module . . . 101
5.2.1. The micro-integration technology platform . . . 101
5.2.2. Integration strategy . . . 103
5.2.3. Mode-locking performance . . . 106
5.2.4. Conclusions from the first generation micro-integrated ML-ECDL . . . 109
5.3. Advanced ML-ECDL module . . . 110
5.3.1. The micro-integration technology platform . . . 110
5.3.2. Integration strategy . . . 112
5.3.3. Mode-locking performance . . . 116
5.3.4. Conclusion from the advanced ML-ECDL module . . . 125

5.4. Conclusion from micro-integration of a diode laser-based optical frequency comb generator . . . 126

6. Pulse repetition rate stabilization **127**
6.1. Introduction to stabilization of the pulse repetition rate . . . 127
6.2. Experimental setup . . . 127
6.3. Results . . . 131
6.3.1. RF characteristics . . . 131
6.3.2. Optical characteristics . . . 133
6.3.3. Temporal and optical power characteristics . . . 134
6.4. Conclusion from the stabilization of the pulse repetition rate . . . 134

7. Conclusion and outlook **137**
7.1. Conclusion . . . 137
7.2. Outlook on future advancements . . . 139

A. Derivation of equations **143**
A.1. Influence of the spectroscopy stabilization in the advanced stabilization scheme . 143
A.2. Optical gain and absorption . . . 143

Lists of figures **145**

Lists of tables **149**

List of abbreviations **151**

List of symbols **155**

Bibliography **161**

List of publications **179**

Acknowledgments **183**

Selbständigkeitserklärung **185**

1. Introduction

In the past two decades, optical frequency combs (OFCs) have become an invaluable tool in a multitude of applied science and fundamental physics applications. These range from, e.g., time keeping [1], to ranging [2], and sensing [3]. An emerging technology within the field of sensing are quantum optical sensors for, e.g., testing fundamental physics models [4–7]. The vast potential of OFCs was acknowledged in the awarding of the Nobel Prize in Physics to J. Hall and T. Hänsch in 2005 [8, 9].

Typical optical frequency comb generators (OFCGs) provide an optical spectrum spanning at least one octave or more [10]. This ultra-broadband optical spectrum allows for absolute stabilization of the OFC [11] providing the means to measure optical frequencies absolutely [12] and for comparing optical frequencies hundreds of THz apart [13]. The laser systems required to enable this are based on mode-locked solid-state [14] or fiber [4] lasers, or nonlinear processes in, e.g., micro-resonators [15]. Additionally, these highly complex laser systems typically comprise an optically pumped laser medium, high power pump diode lasers, elements for spectral broadening, beam shaping and distribution optics, as well as dispersion control elements. Though efforts are made to miniaturize the OFC generators, see, e.g., Refs. [4, 16], their complexity, power consumption, and footprint are still significant. Thus, the implementation of absolute stabilized OFCs in highly compact out-of-the-lab systems for field applications remains a formidable challenge.

Considerable reduction of OFC system complexity can be achieved for those applications that base on frequency comparison rather than absolute frequency determination [17]. Here, only control of the spectral distance between the individual comb lines is required and absolute stabilization of the OFC is not necessary. Further alleviation of system complexity is possible for those applications that compare frequencies spaced only few or tens of THz. The OFCs employed within such applications only need to cover the specific frequency interval between the frequencies of interest. This can allow for the omission of additional spectral broadening elements and can enable use of the OFC directly emitted from the mode-locked laser. However, the need for optical pumping still makes mode-locked solid-state or fiber lasers cumbersome devices. Additionally, control of the comb line spacing is not easily achieved for those lasers.

In contrast, mode-locked diode lasers offer not only control of their emission characteristics through electrical bias, diode lasers can also be integrated into miniaturized laser modules. These feature the level of compactness, robustness, and integrability that makes them ideal candidates for applications in the field and even in space [6, 18–20]. Moreover, compound semiconductors provide emission in most of the optical spectrum from the ultraviolet (UV) to the mid-infrared (IR) spectral range [21]. Since its first documentation in the 1970s, mode-locking of diode lasers has become a well established technology across the accessible spectral range [22–25]. For these lasers direct control of the comb line spacing is achieved via manipulation of the electrical bias [24].

One application that would greatly benefit from a diode laser-based OFC in the wavelength range around 780 nm are the QUANTUS (*Quantengase unter Schwerelosigkeit*; quantum gases under weightlessness) experiments. These aspire to implement a quantum test of the universality of free fall (UFF) in space by means of comparing the rate of free fall of different atomic species, rubidium (Rb) and potassium (K) [6, 26–31]. Employing the respective D2 transitions, an OFC spanning about 13 nm (approx. 7 THz) from 767 nm (approx. 391 THz) to 780 nm (approx. 384 THz) is required to facilitate frequency comparison and control experiments.

A similar spectral bandwidth of about 9 THz has already been reported for mode-locked diode lasers in the wavelength range around 830 nm [32]. Further, a diode laser-based OFC has been reported to be used as a means to control very closely spaced optical frequencies around the D2 transition of Rb [33]. Another, more recent diode laser-based approach utilized to generate an OFC is to inject the emission of a diode laser into a whispering gallery mode (WGM) microresonator [34–36]. When the diode laser's emission frequency is appropriately detuned relative to the resonance frequencies of the WGM microresonator, an OFC is generated that can span more than one octave. These OFCs are typically centered in the wavelength range of 1550 nm. However, some of those OFC even extend down to around 780 nm when the diode laser's power is strongly amplified by a fiber amplifier before injection into the WGM microresonator [34]. However, at the beginning of this work, to the best of my knowledge, no diode laser-based OFCs existed in the wavelength range around 780 nm that provided the spectral bandwidth required for the QUANTUS experiments, and no diode laser-based OFCG[1] was available that provided the compactness and robustness required for experiments carried out at a drop tower or in space.

The scope of this thesis, thus, is the development of a diode laser-based OFC which provides a spectral bandwidth of more than 13 nm in the wavelength range around 780 nm for use in future spaceborne QUANTUS experiments.

To introduce this thesis' scope in more detail, the OFC as a tool for determination and control of optical frequency differences is first discussed in the subsequent section. Then, the idea of the QUANTUS experiments is presented and an advanced frequency stabilization scheme for future QUANTUS experiments is sketched. Further, the status of the laser technology development for the QUANTUS experiments at the beginning of this thesis work is described. Requirements on a diode laser-based OFC for future QUANTUS experiments are identified. An overview of the state of the art of OFCs in the wavelength range around 780 nm is given. This chapter closes by highlighting the goals and outline of this thesis.

1.1. The optical frequency comb

Soon after the dawn of the laser [38, 39], generation of ultra-short (optical) pulses has been observed, see e.g. Refs. [40–46]. Shortly afterwards in the early sixties, phase locking of the longitudinal modes of a laser, also called mode-locking, was identified to be the underlying mechanism producing those ultra-short pulses [47–50]. A prerequisite for successful mode-locking

[1] Parallel to the beginning of this thesis work, first tests of a drop-tower suitable fiber-based OFCG were carried out [37]. However, this OFCG occupied the whole catapult capsule and was, thus, by far not compact enough for implementation within the QUANTUS experiments.

is an equidistant frequency separation between the longitudinal modes making up the optical spectrum of the laser [51, 52]. That comb-like optical spectrum produced by an ultra-short pulse mode-locked laser, see schematic in Fig. 1.1, is known as an OFC.

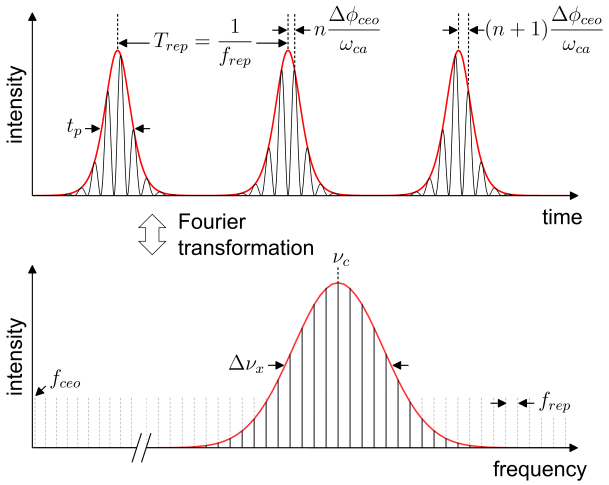

Figure 1.1.: Schematic of an optical frequency comb (solid black lines in bottom graph). In the time domain (top) the OFC is determined by a train of n pulses featuring a composition of a carrier frequency ω_{ca} (black) and an envelope function (red) with a width of t_p, a periodicity T_{rep}, and a carrier-envelope-offset (carrier-envelope-offset (CEO)) phase slip $\Delta\phi_{ceo}$. In the optical frequency domain (bottom) the OFC is determined by an envelope function (red line) with a center frequency ν_c, an inter-mode spacing equal to the pulse repetition rate f_{rep}, a spectral bandwidth $\Delta\nu_x$ at x dBc, and a CEO frequency f_{ceo}.

Measurement of optical frequency differences by means of an OFC generated by a mode-locked laser was first conducted in the late seventies [17]. Then, only a frequency interval of 1 GHz was bridged. Twenty years later, the frequency comb technique matured to allow for measurements of frequency intervals of tens of THz, and also of absolute frequencies [12, 53, 54]. Absolute frequency measurement can be facilitated by means of stabilizing the pulse repetition rate of the OFC, and stabilizing one of its comb lines to an atomic reference. The development of OFCs spanning more than one octave [55, 56] then provided the means for phase-coherent measurements of optical frequencies [57]. Since the first demonstration of an absolute stabilized OFC spanning more than one octave, employment of such an OFC as an optical ruler for precise measurements of absolute optical frequencies and frequency differences has become well-established [58–62].

For the future QUANTUS experiments in which the OFC developed within this thesis is to be employed, however, phase-coherent frequency measurement and comparison is not required. For these experiments, an OFC suitably spanning the wavelength range of interest (approx. 13 nm, and covering the K and Rb D2 transitions), and featuring suitable spectral and mechanical characteristics is envisioned.

In the following, the tool OFC is presented. To that end, a theoretical description of an OFC and a phenomenological description of its build-up is discussed. Further, measurement of optical

frequencies and frequency differences by means of an OFC is introduced.

1.1.1. Theoretical description of mode-locked operation

The subsequent description follows Ref. [63].

The time-dependent electrical field of a single optical pulse is a composition of a carrier of frequency ω_{ca} and an envelope function $\hat{E}(t)$ written in complex notation as

$$E_p(t) = \hat{E}(t) \cdot \exp\left[\, i \cdot (\omega_{ca} t + \phi_{ceo})\right] \tag{1.1}$$

where ϕ_{ceo} is the carrier-envelope-offset (CEO) phase. For a pulse train consisting of identical pulses with a periodicity T_{rep} traveling through a non-dispersive medium, so that ϕ_{ceo} can be considered constant, the electrical field is given as

$$E(t) = \sum_n E_p(t - nT_{rep}). \tag{1.2}$$

In case of a pulse train traveling through a dispersive medium, however, the CEO phase evolves from pulse to pulse by an amount $\Delta\phi_{ceo}$ due to the difference in phase and group velocity. Thus, the n-th pulse experiences $\phi_{ceo,n} = n\Delta\phi_{ceo} + \phi_0$, where ϕ_0 is the CEO phase at time zero, see schematic in Fig. 1.1. The electric field of the pulse train is then given in the time domain as

$$E(t) = \sum_n \hat{E}(t - nT_{rep}) \cdot \exp\left[\, i\,(\omega_{ca} t + n(\Delta\phi_{ceo} - \omega_{ca} T_{rep}) + \phi_0)\right]. \tag{1.3}$$

This corresponds to

$$E(\omega) = \mathrm{e}^{i\phi_0} \mathfrak{F}(\hat{E})(\omega - \omega_{ca}) \sum_m \delta(\Delta\phi_{ceo} - \omega T_{rep} - 2\pi m) \tag{1.4}$$

in the frequency domain where $\mathfrak{F}(\hat{E})(\omega)$ is the Fourier-transform of $\hat{E}(t)$.

If ϕ_0 is equal for all pulses, as assumed in Eq. 1.3, the optical spectrum of the mode-locked pulse train consists of equally spaced spectral lines of frequency

$$\nu_m = m f_{rep} + f_{ceo} \tag{1.5}$$

where

$$f_{ceo} = \Delta\phi_{ceo} f_{rep}/(2\pi) \tag{1.6}$$

is the CEO frequency and

$$f_{rep} = \frac{1}{T_{rep}} = \frac{c_0}{2 n_g L_{res}}, \tag{1.7}$$

is the pulse repetition rate. The pulse repetition rate is given by the inverse of the round trip time T_{rep} (periodicity) of the pulses in the laser resonator. It is calculated using the vacuum speed of light c_0, the group refractive index n_g, and the length of the laser resonator L_{res}. The identity of the inter-mode spacing in the frequency domain and the pulse repetition rate in the time domain has been verified experimentally [53].

The laser intensity $I(t) \propto |E(t)|^2$ features the same periodicity as well. Using the intensity distribution in the optical frequency domain, typical characteristics of the frequency comb such as center frequency (center of gravity) ν_c and the spectral bandwidth $\Delta\nu_x$ at x dBc are determined, see Fig. 1.1. Including the time domain, characteristics such as the pulse width t_p, typically determined at full width at half maximum (FWHM) intensity, can be quantified, see Fig. 1.1.

1.1.2. Phenomenological description of mode-locked operation

Build-up of an OFC can phenomenologically be described as follows.

A free-running laser without any frequency-selective element features a multitude of longitudinal optical modes with random phases. This case is illustrated in Fig. 1.2(left). Mode competition leads to large fluctuations in the instantaneous frequency and the emitted intensity, see Fig. 1.2(bottom left).

Spontaneous locking of (some) modes occurs when the modes have a constant (locked) phase relationship [64, 65]. A spontaneously mode-locked wave packet forms. Maintaining the constant phase relationship between the spontaneously locked modes allows this spontaneously formed wave packet to travel back and forth in the laser resonator. In this case, a mode-locked optical pulse is emitted from the laser at time intervals T_{rep} corresponding to the resonator length, see Fig. 1.2(right). Further modes can lock to the wave packet during its travel in the laser resonator. This results in an increase of peak intensity of the wave packet compared to the case of only spontaneously locked modes, see Fig. 1.2(bottom).

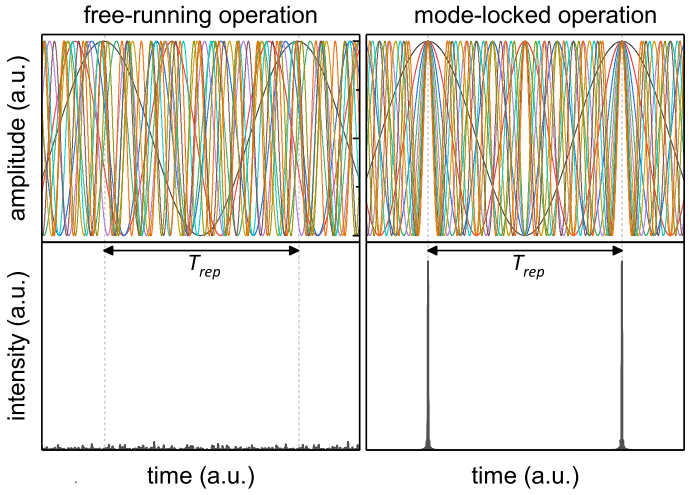

Figure 1.2.: Schematic of the temporal distribution of multiple emitted longitudinal modes at a fixed point outside the laser resonator: individual electric fields of (top, 10 modes for better visibility of the individual modes) and their intensity (bottom, 100 modes for better comparison of free-running and mode-locked operation) in a free-running (left) and (right) mode-locked laser. Free-running operation features random phases between the modes where spontaneous locking of some modes can occur. In mode-locked operation, in contrast, a phase-locked relationship between the modes exists and leads to build-up of a wave packet in the laser resonator.

The wave packet can be maintained in the laser resonator if it experiences more optical net-gain than the non-phase locked modes. This can be facilitated either by an element internal or external to the laser resonator.

An external element is realized by, e.g., modulating the optical gain or losses of the laser at a frequency corresponding to the inverse of the round trip time T_{rep} of the wave packet in the laser resonator. Here, a signal generator providing the modulation signal is required.

In contrast, an internal element is realized by, e.g., inserting a nonlinear element into the laser resonator that provides less optical losses for higher optical powers. Thus, the power-dependency of that internal element results in an overall net-gain for the appropriately mode-locked wave packet and net-loss for the other, still free-running optical modes of the laser resonator. Such an element is called a saturable absorber. Depending on the position of the saturable absorber in the laser resonator, the wave packet is emitted from the laser resonator with a rate that corresponds to the inverse round trip time or its harmonics [24, 66, 67]. In the former case, a single wave packet travels inside the laser resonator. This is called fundamental mode-locking. In the latter case, multiple wave packets are generated in the laser resonator. This case is called harmonic mode-locking.

1.1.3. Measurement of optical frequencies and frequency differences

Determination of an unknown optical frequency ν_1 (Fig. 1.3) by means of an OFC can be realized in a two-step measurement, see, e.g., Ref. [68]. In the first step, the comb line number m_{c1} of the closest comb line ν_{c1}, see Eq. 1.5, is ascertained using, e.g., a wavelength meter that provides sufficient measurement resolution ($\Delta\nu_{res} \ll f_{rep}/2$). In the second step, a beat note measurement between this OFC and the unknown optical frequency is performed yielding a microwave (radio frequency (RF)) frequency $|f_{b1}| = |\nu_1 - \nu_{c1}|$ that can precisely be detected by a frequency counter. Assuming $\nu_{c1} < \nu_1$ as shown in Fig. 1.3, the optical frequency under investigation is then given as

$$\nu_1 = \nu_{c1} + f_{b1} = m_{c1} f_{rep} + f_{ceo} + f_{b1}. \tag{1.8}$$

The sign of f_{b1} can be determined from the frequency position of ν_1 relative to ν_{c1} in the first step by, e.g. controlled breathing of f_{rep}. A consequence of Eq. 1.8 is that absolute control of all parameters of the OFC, i.e. the pulse repetition rate f_{rep} and the CEO frequency f_{ceo} is essential for accurate determination of an unknown optical frequency.

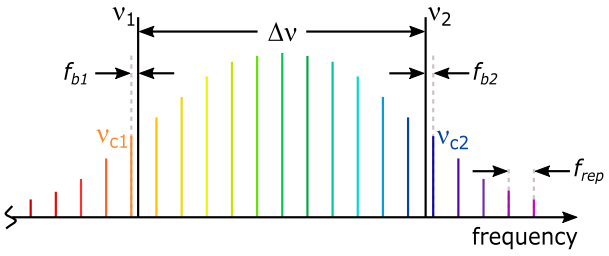

Figure 1.3.: Measurement of optical frequencies and frequency differences.

Frequency differences between two lasers can be determined in a similar way, yielding

$$\Delta\nu = \nu_1 - \nu_2 = (m_{c1} - m_{c2})f_{rep} + (f_{b1} + f_{b2}) \tag{1.9}$$

which only requires

(i) determination of the two comb line numbers m_{c1} and m_{c2},

(ii) determination of the repetition rate f_{rep}, and

(iii) counting of the RF beat note (in this case the sum frequency) between the two optical beat notes f_{b1} and f_{b2} derived from overlapping the two lasers with the OFC.

Thus, in contrast to absolute optical frequency measurements, comparison of two optical frequencies by measurement of their frequency difference eliminates the need to analyze and control the CEO frequency f_{ceo}, see Eq. 1.9. Further, if only variations in the frequency difference are of interest, then observing a microwave beat note of the two optically generated beat notes f_{b1} and f_{b2} is sufficient. While knowledge of the number of comb lines between the two frequencies under investigation is not necessary here, stabilization of the pulse repetition rate f_{rep} is essential to not produce frequency noise induced variations in the final beat note. An additional measurement of the pulse repetition rate, however, allows for determination of its (residual) frequency fluctuations which can then be observed in the determination of the frequency difference of interest.

Thus, the implementation of an OFC spanning only the spectral bandwidth of interest for measurement of frequency differences is possible. With this, the complexity of the required laser system can be minimized.

1.2. A tailored optical frequency comb for a spaceborne experiment

The development of a tailored OFC, which was conducted within this thesis work, was motivated by an application in the field of inertial sensing: a quantum sensor for testing the weak equivalence principle (WEP), also known as the universality of free fall (UFF). Such tests are of interest since quantum theories predict violations of the WEP [27, 69]. These violations could, to date, neither be confirmed nor rejected by experiment. For quantum sensor-based tests, the accuracy has been limited by, e.g., a too large thermally induced spread of the test masses, limited interrogations times, and residual accelerations in the experimental chamber [27]. One experimental series intending to push the accuracy for tests of the UFF are the QUANTUS (*Quantengase unter Schwerelosigkeit*; quantum gases under weightlessness) projects, see, e.g., Refs. [6, 28, 30, 31, 70].

The framework of the QUANTUS collaboration encompasses not only the test of the UFF itself, but also the development of the technology required to successfully conduct the experiments on micro-gravity platforms, first in the drop tower of the ZARM (*Zentrum für angewandte Raumfahrttechnologie und Mikrogravitation*; Center of Applied Space Technology and Microgravity) and later also onboard of sounding rockets. The development of the laser technology was facilitated within the LASUS (*Entwicklung von neuartigen Diodenlasersystemen für Präzisionsexperimente unter Schwerelosigkeit für zukünftige TEXUS-Missionen*; Development of novel

diode laser systems for precision experiments under weightlessness for future TEXUS missions) project series. This thesis work was also conducted within the framework of the LASUS projects for the QUANTUS experiments.

In this section, the objective of the QUANTUS experiments is introduced. An advanced frequency stabilization scheme for future QUANTUS experiments is presented. Here, the advantage of employing an OFC is highlighted. Then, the status of the diode laser technology that had been developed within LASUS specifically for the QUANTUS experiments until the beginning of this thesis work is described. This section closes with identifying the requirements on a diode laser-based OFC for spaceborne tests of the UFF in the QUANTUS experiments.

1.2.1. The QUANTUS experiments: a test of the universality of free fall

The QUANTUS collaboration has made it its objective to employ the enhanced sensitivity of quantum sensor technology, particularly of light pulse atom interferometry, in microgravity to push the limit of measurement sensitivity for gravitational acceleration [70]. A light pulse atom interferometer is an inertially sensitive Mach-Zehnder-type matter wave interferometer in which the wave character of matter (atoms) is exploited to measure the inertial acceleration caused by the gravitational force of the earth [71]. Manipulation of the atoms (beam splitting, redirection, and re-combining) and read-out of the atom interferometer is facilitated by well-defined light pulses from high power, narrow linewidth continuous wave (CW) diode lasers.

With a suitably oriented apparatus, the accumulated interferometer phase shift due to gravitational acceleration is given by

$$\Phi = k_{\mathit{eff}} a T^2, \tag{1.10}$$

with the effective wave vector of the counter-propagating light pulses of the atom interferometer

$$k_{\mathit{eff}} = |\vec{k}_1 - \vec{k}_2| \approx 2k = 4\pi/\lambda = 4\pi\nu/c_0 \tag{1.11}$$

with wavelength λ (frequency ν, vacuum speed of light c_0), the local acceleration a and the interrogation time T between the light pulses [27]. The relative amount of atoms in the two output states of the interferometer allows for determination of Φ.

It can be seen in Eq. 1.10 that the sensitivity for measuring a scales quadratically with the interrogation time T. Hence, large interrogation times are advantageous. One of the major benefits of conducting experiments in a micro-gravity environment is the accessibility of these large interrogation times due to the lack of gravitational pull on the test masses (the atoms) towards the experimental chamber's wall. Additionally, weightlessness offers benefits such as improved preparation of the test masses [31, 70]. Further, in a micro-gravity environment vibrational (acceleration) noise due to, e.g., seismic activity of the earth can be minimized or even eliminated.

A test of the UFF can be performed with a light pulse atom interferometer by comparing the gravitational acceleration a_1 and a_2 of two different atomic species in simultaneously conducted experiments. The difference in acceleration is expressed by the Eötvös ratio [27]

$$\eta = 2\frac{a_1 - a_2}{a_1 + a_2} \tag{1.12}$$

which is non-zero in case of the violation of the UFF. Using K and Rb atoms as test masses in the same experiment simultaneously, as planned in future QUANTUS experiments [27], offers several advantages [27, 30, 70, 72, 73]. First, the cooling mechanisms and the interactions of Rb and K vapor mixtures are well-known [27]. Both atomic species feature a large difference in mass, and a large variety of isotopes. Second, similar wavelengths of respective D2 transitions of K and Rb, approx. 767 nm and 780 nm, respectively, allow for simplification of the laser system design by use of the same optics, e.g., mirrors and retardation plates, as well as shared optical fibers and a shared interferometry setup. Further, diode laser technology can be applied as frequency comparison with an OFC requires only modest optical bandwidth (BW) of the OFC.

Systematical errors, however, limit the measurement accuracy. A differential measurement approach minimizes some noise sources by common mode rejection. Nevertheless, precise control of the optical frequencies (via $k_{eff,i} \approx 2k_i$ of each atomic species) is a fundamental requirement for the experiment's success. In existing setups of the QUANTUS collaboration, individual frequency stabilization of two lasers emitting at around 767 nm and 780 nm to a K and Rb atomic reference, respectively, is performed. Hence, the determination of the respective k_{eff} is limited by the accuracy of the respective spectroscopy-based frequency stabilization. Further, knowledge of the frequency difference between the K and the Rb interrogation lasers is also limited by the spectroscopy-based frequency stabilization. However, referencing both lasers to a common atomic reference (e.g. Rb) would allow to omit the other atomic reference (e.g. K) and the associated uncertainty. A stabilization scheme implemented with an OFC that can bridge the required frequency region spanning the approx. 13 nm (6.8 THz) from the Rb to the K D2 transition frequency, about 384.23 THz ($\approx$ 780.24 nm) and 391.02 THz ($\approx$ 766.70 nm), respectively, would be of advantage for successful implementation of future experiments.

1.2.2. An advanced frequency stabilization scheme for future QUANTUS experiments

In essence, an advanced stabilization scheme can be understood as a determination of the frequency difference of the K and Rb interrogation lasers, see Fig. 1.4(a). This scheme can be facilitated by an OFC of which the pulse repetition rate has been stabilized to a microwave reference f_{ref}. A schematic for a potential frequency control in future QUANTUS experiments is sketched in Fig. 1.4(b). The electronics are shown in blue and the optical components are sketched in black. The reference signals (f_1, f_2, f_{ref}) feature a common frequency reference.

Firstly, the pulse repetition rate of the OFC is stabilized to a reference providing a reference frequency of, e.g., $f_{ref} = 6.8$ GHz. This allows for use of similar electronics as for the preparation of the interferometry beams, simplifying the electronics system. The optical frequency of the reference laser for the Rb experimental part (CW 780 nm) is frequency-stabilized by means of a Rb vapor cell. Then, one comb line of the OFC is frequency-stabilized to the Rb reference laser. To precisely control the CEO frequency of the OFC, the phase of the RF beat note signal between the Rb reference laser and the above-mentioned comb line of the OFC is compared to the frequency of a RF frequency reference with an appropriately selected frequency f_1, and the resulting phase error is fed back to the CEO frequency of the OFC.

Secondly, frequency comparison of the reference lasers for K and Rb is conducted with the

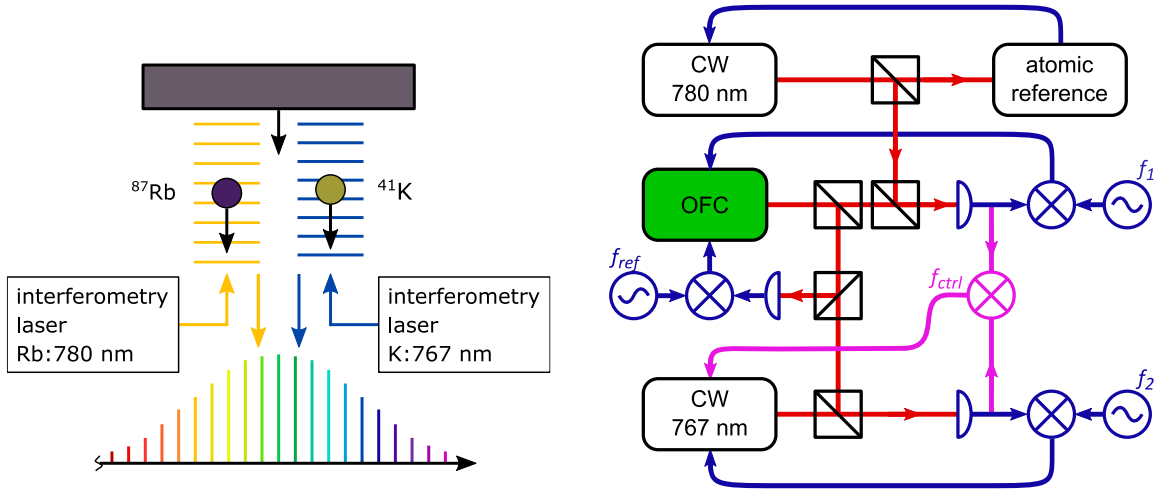

(a) (b)

Figure 1.4.: Schematic of an advanced (a) frequency comparison and (b) frequency control for future QUANTUS experiments. The reference signals (f_1, f_2, f_{ref}) feature a common frequency reference.

OFC in order to offset stabilize the reference laser of the K part relative to that of the Rb part. To this end, the optical frequency of the K reference laser (CW 767 nm) is compared to that of the closest comb line of the OFC. A control signal for the K reference laser is then generated by comparison of the phase of the RF beat note signal between the OFC and the K reference laser and a second RF frequency reference f_2, the frequency of which is set appropriately. Alternatively, the beat note signals of the reference lasers for the K and Rb experiment parts and the respective closest comb lines of the OFC can be directly compared to generate a control signal f_{ctrl} for the K reference laser (sketched in pink). In this alternative scenario, a stabilization of the OFC to the Rb atomic reference, which would imply an absolute stabilization of the OFC, is not necessary, see Eq. 1.9.

The stabilization scheme, however, depends directly on the RF linewidth Δf_{rep} of the pulse repetition rate as can be illustrated as follows. Employing the stabilization scheme sketched in pink in Fig. 1.4(b), the frequency stability of the Rb laser is transferred to the K reference laser via the OFC. Thus, the K frequency ν_K can be described by

$$\nu_K = \nu_{Rb} + \Delta\nu = \nu_{Rb} + \nu_{trans} + f_{b-Rb} + f_{b-K} \tag{1.13}$$

where ν_{Rb} is the Rb laser's frequency, and f_{b-Rb} and f_{b-K} are the RF beat note frequencies of the comb lines closest to the Rb and K D2 transition frequencies with the K and Rb lasers, respectively. The frequency ν_{trans} is the part of the frequency difference between the frequencies of the K and Rb lasers that is directly bridged by the OFC.

With this stabilization scheme, the frequency uncertainty of the K reference laser frequency

ν_K is given by

$$(\delta\nu_K)^2 \approx (\delta\nu_{Rb})^2 + (\delta\nu_{trans})^2 , \tag{1.14}$$

where $\delta\nu_{Rb}$ is the frequency uncertainty of the spectroscopy stabilization of the Rb reference laser at ν_{Rb} and $\delta\nu_{trans}$ is the frequency uncertainty introduced by the frequency stability transfer with the OFC. The uncertainty introduced by the measurement of the beat notes of the comb lines with the respective reference lasers for K and Rb is negligible as those frequencies can be measured with sufficient accuracy in the RF domain. The uncertainty of the frequency transfer is given by

$$\delta\nu_{trans} = \Delta f_{rep} \cdot \frac{\nu_{trans}}{f_{rep}}, \tag{1.15}$$

where the uncertainty of the pulse repetition rate is called the RF linewidth of the pulse repetition rate Δf_{rep}. In order for the uncertainty of ν_K not to be limited by the uncertainty of the transfer,

$$\delta\nu_{trans} \ll \delta\nu_{Rb} \tag{1.16}$$

is required. Hence, the requirement on the RF linewidth of the pulse repetition rate of the OFC is given by

$$\Delta f_{rep} \ll \frac{\delta\nu_{Rb}}{\nu_{trans}/f_{rep}}. \tag{1.17}$$

The natural linewidth of the Rb D2 frequency, which is in the range of megahertz [74], is used as an upper limit for estimation of $\delta\nu_{Rb}$. Thus, when employing an OFC with a pulse repetition rate f_{rep} of, e.g., 6.8 GHz, to transfer the frequency stability from the Rb to the K D2 frequency ($\nu_{trans} \approx \nu_K - \nu_{Rb} \approx 6.8$ THz), the RF linewidth of the pulse repetition rate is required to be much smaller than 1 kHz.

Above, an upper limit for the RF linewidth of the pulse repetition rate has been estimated purely based on the comparison with a frequency determination by means of spectroscopy. Now, the actual goal of the QUANTUS experiments shall be taken into account. In the QUANTUS experiments, the Eötvös ratio η (Eq. 1.12) of the local accelerations due to gravity in the K (1) and Rb (2) atom interferometers is to be determined. It would be advantageous to connect the intended measurement uncertainty $\delta\eta$ of this ratio to the uncertainty $\delta(\Delta\nu)$ of the frequency transfer by the OFC and thus the RF linewidth of the OFC's pulse repetition rate (Eq. 1.15). This can be done as follows.

A differential measurement in the atom interferometers for K and Rb allows for determination of the difference of the local accelerations

$$\Delta a = a_1 - a_2 \tag{1.18}$$

of both quantum gases [75]. Any deviation of this difference from zero would then directly imply a violation of the UFF. Typically, the denominator of the Eötvös ratio is determined independently and given as an average [27, 75]

$$\bar{a} = \frac{a_1 + a_2}{2}. \tag{1.19}$$

The Eötvös ratio can thus be written as

$$\eta = 2 \cdot \frac{a_1 - a_2}{a_1 + a_2} = \frac{\Delta a}{\bar{a}}. \tag{1.20}$$

Hence, the relationship between the uncertainty $\delta(\Delta a)$ of the determination of the difference in local accelerations and the uncertainty $\delta(\Delta\nu)$ of the frequency transfer by the OFC needs to be investigated.

With the accumulated phase shift Φ due to gravitational acceleration in the atom interferometer (Eq. 1.10) and the effective wave vector k_{eff} (Eq. 1.11), the local acceleration a_i of the test mass i ($i = 1$ (K), 2 (Rb)) is described by

$$a_i \approx \frac{\Phi_i}{T_i^2} \cdot \frac{c}{4\pi} \cdot \frac{1}{\nu_i}. \tag{1.21}$$

Using the frequency transfer scheme described above[2], the frequency of the K laser can be determined relative to the Rb laser as

$$\nu_1 = \nu_2 + \Delta\nu \tag{1.22}$$

where $\Delta\nu \approx \Delta\nu_{trans}$ is the frequency difference of the comb lines closest to the Rb and K laser's frequencies of interest. For the estimation of the measurement uncertainty $\delta(\Delta a)$, the microwave frequencies of the beat notes of the comb lines closest to the K and Rb lasers' frequencies with the K and Rb lasers' frequencies can be neglected. With this assumption and Eq. 1.21, Δa is given as

$$\Delta a = a_1 - a_2 \approx \frac{c}{4\pi} \cdot \left[\frac{\Phi_1}{T_1^2} \cdot \frac{1}{\nu_1} - \frac{\Phi_2}{T_2^2} \cdot \frac{1}{\nu_2}\right] = \frac{c}{4\pi} \cdot \left[\frac{\Phi_1}{T_1^2} \cdot \frac{1}{\nu_2 + \Delta\nu} - \frac{\Phi_2}{T_2^2} \cdot \frac{1}{\nu_2}\right] \tag{1.23}$$

with

$$\frac{\partial(\Delta a)}{\partial(\Delta\nu)} \approx \frac{c \cdot \Phi_1}{4\pi T_1^2} \cdot \frac{(-1)}{(\nu_2 + \Delta\nu)^2} = -\frac{a_1}{\nu_1}. \tag{1.24}$$

The contribution of the uncertainty of the frequency transfer to the single shot measurement uncertainty $\delta\eta$ of the Eötvös ratio is described by

$$(\delta\eta)^2 = \left(\left|\frac{\partial\eta}{\partial(\Delta\nu)}\right|^2 \cdot (\delta(\Delta\nu))^2\right) + \dots \ . \tag{1.25}$$

Thus, a lower limit for $\delta\eta$ can be estimated by

$$\delta\eta > \left|\frac{\partial\eta}{\partial(\Delta\nu)}\right| \cdot \delta(\Delta\nu). \tag{1.26}$$

[2]The emission frequency of Rb laser is stabilized to an atomic reference and the emission frequency of the K laser is determined via transfer with the OFC, see Fig. 1.4(b).

With Eq. 1.20 and Eq. 1.24, it follows that

$$\left|\frac{\partial\eta}{\partial(\Delta\nu)}\right| = \left|\frac{\partial\eta}{\partial(\Delta a)}\cdot\frac{\partial(\Delta a)}{\partial(\Delta\nu)}\right| \approx \left|\frac{1}{\bar{a}}\cdot\left(-\frac{a_1}{\nu_1}\right)\right| = \frac{a_1}{\bar{a}}\cdot\frac{1}{\nu_1}. \tag{1.27}$$

Consequently, $\delta\eta$ is described by

$$\delta\eta > \frac{a_1}{\bar{a}}\cdot\frac{1}{\nu_1}\cdot\delta(\Delta\nu). \tag{1.28}$$

With this estimation, the local acceleration a_1 of the K test mass can be approximated by $\bar{a}$. Thus, the upper limit of the uncertainty $\delta(\Delta\nu)$ can be estimated by

$$\delta(\Delta\nu) < \nu_1\cdot\delta\eta \approx 4\cdot 10^{14}\ \text{Hz}\cdot\delta\eta \tag{1.29}$$

where ν_1 is the emission frequency of the K laser. It can be seen that the requirement on the uncertainty of the frequency transfer with the OFC decreases with decreasing the intended measurement uncertainty $\delta\eta$ of the Eötvös ratio. A realistic target measurement uncertainty for the Eötvös ratio in a single shot measurement is $\delta\eta|_{\text{single shot}} = 10^{-10}$ [27]. This target results in a required uncertainty of the frequency transfer with the OFC of

$$\delta(\Delta\nu) < 40\ \text{kHz}. \tag{1.30}$$

Please note that a requirement equivalent to the one given in Eq. 1.30 would also apply to each of the two spectroscopy stabilized lasers in a scheme without an OFC. However, utilizing the scheme depicted in Fig. 1.4(b) relaxes the requirement on the uncertainty of the remaining spectroscopy stabilization by about a factor of 60 (see App. A.1).

Using Eq. 1.15 and 1.30, the requirement on the RF linewidth of the pulse repetition rate of the OFC is given by

$$\Delta f_{rep} < \frac{\delta(\Delta\nu)}{\Delta\nu/f_{rep}} \approx \frac{40\ \text{kHz}}{1000/n_H} \approx n_H\cdot 40\ \text{Hz}, \tag{1.31}$$

with $\Delta\nu \approx 6.8$ THz, and $f_{rep} = n_H\cdot 6.8$ GHz with the harmonic number n_H.

To enable the experimental scheme described above for future QUANTUS experiments in a micro-gravity environment, a suitable OFC is needed. At the beginning of this thesis' work, no OFCG was available that provided the required electro-optical performance as well as featured the compactness and robustness needed for experiments conducted in micro-gravity at the drop tower and in space. Therefore, a suitable technology platform for the integration of the OFCG needed to be developed.

1.2.3. The LASUS projects: development of diode laser technology for use in the QUANTUS experiments

Within the LASUS project series, the laser technology for the QUANTUS experiments is developed, realized, and readied for use in micro-gravity environments. These environments are provided by, e.g., the ZARM drop tower facilities in Bremen and sounding rockets launched in Kiruna, Schweden [6, 28]. Operation of the experimental apparatus at the drop tower facility or onboard sounding rockets puts stringent requirements on the robustness, compactness, and

energy efficiency of the experimental setups, specifically to a key element of the experimental apparatuses, i.e. to the lasers for manipulation and detection of the atoms in the atom interferometer. Diode lasers are ideally suited for employment in harsh and demanding environments. Their ability to operate in CW and mode-locked operation offers a significant advantage for the development of an OFC tailored for the stabilization scheme sketched above.

To ready diode lasers for implementation in weightlessness, a multi-purpose micro-integration technology platform for semiconductor diode lasers and amplifiers was developed at the Ferdinand-Braun-Institut, Leibniz-Institut für Höchstfrequenztechnik (FBH) within the LASUS project series. That technology platform has shown to successfully operate under the harsh conditions of micro-gravity experiments [19, 20, 70, 76–78]. This thesis' work, the development of a diode laser-based OFC for a spaceborne test of the UFF, is part of the LASUS-I and -II projects within the Joint Lab Lasermetrology of the FBH and Humboldt-Universität zu Berlin (HUB).

Fig. 1.5 shows photos of micro-integrated continuous wave extended-cavity diode laser (CW-ECDL) (left) and (continuous wave) master oscillator power amplifier (MOPA) (right) laser modules available at the beginning of this thesis' work. The technology platform features a heatsink with a footprint of only 5×2.5 cm^2. This heatsink carries a micro-optial bench (MIOB) made of aluminum nitride (AlN) ceramics with a footprint of 5×1 cm^2. Diode laser chips, micro-optics and micro-electronics are directly integrated into the MIOB in a linear optical layout. Electronic contact is realized via wire-bonding to contact pads carrying pin jacks. It should be noted that numerous lasers of the MOPA-type have been operated for years in the drop tower experimental apparatus of the QUANTUS experiments [79, 80].

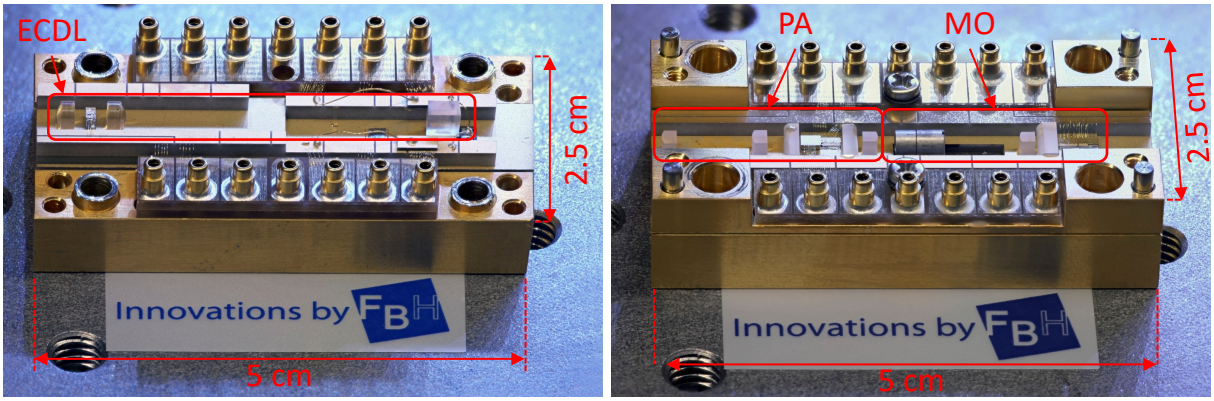

Figure 1.5.: Photos of (left) a micro-integrated CW-ECDL and (right) a micro-integrated CW-MOPA laser module designed for use in the QUANTUS laser system. Both modules' laser output is to the left-hand side of the modules. © FBH/schurian.

These laser modules constitute the (mechanical) baseline for this thesis' work, the development of a diode laser-based OFC. For mode-locked operation, however, the laser modules need to be modified, e.g. to allow for appropriate biasing. Further limitations regarding the optical layout of the OFCG are posed by the physical dimensions of the laser modules. Nevertheless, the use of the same laser module body for CW and mode-locked diode lasers for the implementation of the tailored OFC minimizes the complexity of the laser system for the QUANTUS experiments.

Parallel to this thesis' work, an advanced micro-integration technology platform with a higher degree of integration was developed at FBH for those CW lasers to be implemented in sounding rocket laser systems [20, 77]. An extended-cavity diode laser (ECDL)-type module is shown in Fig. 1.6. The MIOB features multi-layer AlN ceramics with an overall footprint of 8×2.5 cm^2. It provides an RF-suitable electrical interface for the diode laser chip. The heatsink onto which the module is clamped and the electronic boards attached to it provide a housing for the module. Additionally, thermal control of the volume holographic Bragg grating (VHBG) is achieved by means of an integrated micro-thermo-electric cooler (TEC).

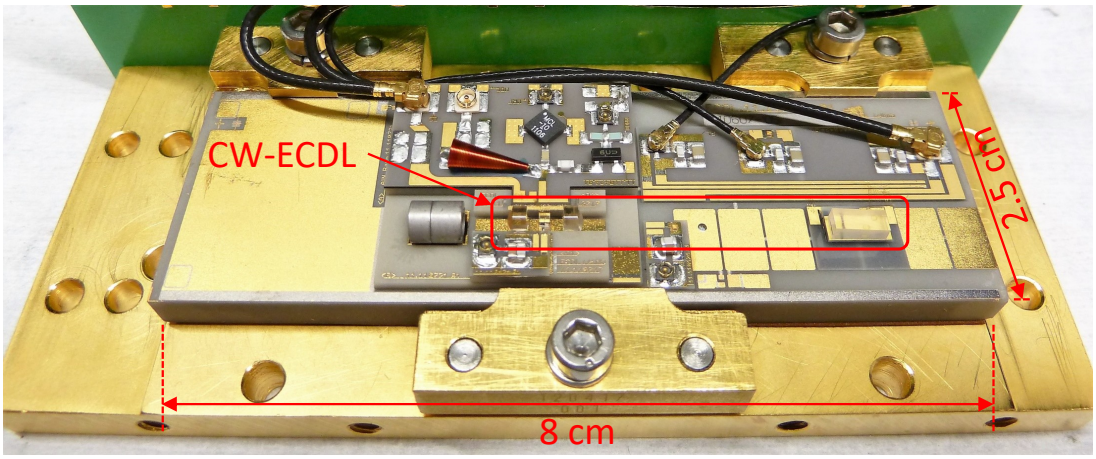

Figure 1.6.: Photo of an advanced ECDL-type laser module designed for use in sounding rocket laser systems. The module's laser output is to the left-hand side. © FBH/schurian.

As with the laser modules presented before (Fig. 1.5), this advanced ECDL-type laser module requires modification for micro-integration of a diode laser-based OFC. Due to the higher complexity of the OFC module, the modifications are necessary not only in terms of electrical bias but also regarding the physical design of the modules.

At the beginning of this thesis' work and parallel to the diode laser system developments, the suitability of a fiber-based frequency comb for use in drop tower experiments was evaluated within the project series LASUS, the project series PRIMUS (*Präzisions-Interferometrie mit Materiewellen unter Schwerelosigkeit*; Precision interferometry with matter waves in zero gravity), which is another project series in the scientific environment of the QUANTUS collaboration [27, 37]. Although operation in drop mode was successfully demonstrated, it turned out that the size of this fiber-based frequency comb did not allow for installing the actual experimental setup into the same capsule. Hence, a more compact OFCG was required. This underlines the need for employing the above introduced LASUS micro-integration technology to set up a compact diode laser-based OFC spanning the wavelength range from the K to the Rb D2 transition wavelengths.

The development of such a tailored diode laser-based, micro-gravity compatible OFC in the wavelength range around 780 nm is the main topic of this thesis.

1.2.4. Requirements on an optical frequency comb for spaceborne tests of the universality of free fall in the QUANTUS experiments

The requirements on an OFC which can be implemented into the experiment sketched above are twofold: on the one hand, spectral characteristics have to be fulfilled and, on the other hand, platform-related technical demands have to be met.

Requirements on spectral characteristics

To implement frequency comparison with the emission frequency of the CW lasers in the advanced frequency control scheme for future QUANTUS experiments (Sec. 1.2.2), the comb lines closest to the D2 transition wavelengths of K and Rb, respectively, must have sufficient optical power, discussed in more detail below, to allow for an analysis of the respective beat notes. Experiments conducted by the Optical Metrology group at HUB have shown that a beat note between a comb line and an unknown optical frequency can be detected with a sufficient (coherent) signal-to-noise-ratio (SNR) when the comb line features at least 100 nW of optical power [81]. In the following, the mode-locking characteristics of a suitable OFC will be derived.

For experiments using both the K and Rb D2 transitions, the OFC must cover the wavelength region from about 766.70 nm (λ_K) to about 780.24 nm (λ_{Rb}) with comb lines of sufficient optical power. Thus, the OFC is required to feature a spectral bandwidth $\Delta\lambda$ in excess of 13.5 nm ($\Delta\nu > 6.8$ THz). If a symmetrical OFC with center wavelength λ_c of around 773.5 nm would be realized, similar optical power at the comb lines closest to each optical frequency under investigation would be achieved.

A pulse repetition rate f_{rep} of 6.8 GHz or its subharmonics allows for employment of the microwave signal that serves as reference for the generation of the Raman laser beams applied to implement beam splitter and combiner for the Rb atom interferometer. Thus, the pulse repetition rate can be directly compared and stabilized to the hyperfine transition of the Rb D2 transition [27].

While the optical power of the comb lines closest to the K and Rb D2 transition frequencies is the limit for employment of the diode laser-based OFC, it cannot easily be directly measured. The average optical power of the OFC, in contrast, can be directly and easily measured during the development process of an OFC suitable for the presented experiment. The average optical power P_{avg} of the OFC required for providing a comb line power $P_i = 100$ nW at the K and Rb D2 transition can estimated as follows. The optical power P_i of the comb line i can then be estimated from the measured average optical power P_{avg} by calibration of the actual optical power spectral density (PSD) $S_T(f_i)$ of the comb line with the optical PSD $S_M(f_i)$ measured with a bandwidth Δf_{BW} using

$$P_{avg} = \int_0^\infty S(f)\,\mathrm{d}f = \sum_i \left[S_T(f_i)\cdot\Delta f_{BW}\right] = A\cdot\sum_i \left[S_M(f_i)\cdot\Delta f_{BW}\right] = \sum_i P_i. \tag{1.32}$$

A is a calibration factor that can be determined using

$$A = \frac{P_{avg}}{\sum_i [S_M(f_i) \cdot \Delta f_{BW}]} \tag{1.33}$$

where the denominator is the area given by the measured optical spectrum. The bandwidth is determined by the pulse repetition rate: $\Delta f_{BW} = f_{rep}$. Thus, the optical power P_i of comb line i is given by

$$P_i = A \cdot S_M(f_i) \cdot f_{rep} = \frac{P_{avg}}{\sum_j [S_M(f_j) \cdot \Delta f_{BW}]} \cdot S_M(f_i) \cdot f_{rep}. \tag{1.34}$$

The optical spectrum of an OFC is typically recorded in the wavelength domain. However, the individual comb lines of the OFC developed within this thesis' work cannot be resolved with the optical spectrum analyzer employed in this work[3], see Sec. 3.4.1. Thus, the measured optical spectrum can be assumed to be continuous.

For, e.g., a Gaussian shaped spectral profile the optical power of the individual comb lines can be described by

$$P_i = \frac{f_{rep} \cdot P_{avg}}{\sqrt{\pi} \cdot \sigma_{20}} \cdot \exp\left[-\left(\frac{\nu_i - \nu_c}{\sigma_{20}}\right)^2\right] \tag{1.35}$$

where $\sigma_{20} = \Delta\nu_{20}/(2\sqrt{\ln 100})$ is an auxiliary variable which allows for implementation of the spectral bandwidth $\Delta\nu_{20}$ at 20 dBc. Thus, with $P_i = P_{Rb,K} = 100$ nW at 20 dBc and $f_{rep} = 6.8$ GHz, a minimum average optical power of about 4 mW is estimated. Including a safety factor of 2, a minimum average optical power emitted by the diode laser-based OFC of 8 mW is required.

In future QUANTUS experiments, the stability of the Rb laser is intended to be transferred to the K laser via the OFC (Fig. 1.4(b)). To that end, the pulse repetition frequency of the OFC is to be stabilized to a (microwave) reference frequency, and a comb line close to the emission frequency of the Rb laser is to be stabilized to that frequency (Fig. 1.4(b)). By these means, the OFC can be employed for the proposed frequency stability transfer to the K laser. For the frequency transfer not to be limited by the phase stability of the pulse repetition rate of the OFC (Eq. 1.15), the phase noise PSD of the pulse repetition rate is required to be below an upper limit given by the (future) QUANTUS experiments. It will be shown later in this work, that the phase noise PSD can be translated into a limit for the RF linewidth of the pulse repetition rate. This limit could not yet be defined by the operators of the QUANTUS experiments at the beginning of this thesis' work. Thus, to allow for evaluation of the developed diode laser-based OFC, an upper limit of the required RF linewidth of the pulse repetition rate will be estimated in the following.

In Sec. 1.2.2, an upper limit for the RF linewidth of $\Delta f_{rep} < n_H \cdot 40$ Hz ($f_{rep} = n_H \cdot 6.8$ GHz with the harmonic number n_H, see Eq. 1.31) has already been estimated based on the proposed stabilization scheme depicted in Fig. 1.4(b). In this scheme, the pulse repetition rate of the OFC is required to be stabilized. During the development of the diode laser-based OFC, however, it

[3] The employed pulse repetition rates (equal to the inter-mode spacing) of 6.8 GHz and 3.4 GHz correspond to 13.5 nm and 6.8 nm, respectively.

is impractical to immediately implement a stabilization of the pulse repetition rate. Thus, the requirement for the RF linewidth of the free-running pulse repetition rate will be considered in the following. Due to the stabilization of the pulse repetition rate, the RF linewidth of the pulse repetition rate is typically reduced by several orders of magnitude. A reduction of the RF linewidth of at least three orders of magnitude can typically be assumed. Hence, with an RF linewidth of at most a few ten Hertz required in the experiment, an RF linewidth of at most 10 kHz is required for a free-running (non-stabilized) pulse repetition rate during the development of the OFC.

Tab. 1.1 summarizes the spectral requirements for the OFC.

Table 1.1.: Spectral requirements for diode laser-based OFC.

Wavelength region of interest		λ_K - λ_{Rb}	$\approx$ 766.70 nm - 780.24 nm
Spectral bandwidth		$\Delta\lambda$	$\geq$ 13.5 nm (20 dBc)
Pulse repetition rate		f_{rep}	= 6.8 GHz or subharmonics n_H
RF linewidth	stabilized	Δf_{rep}	$< n_H \cdot$ 40 Hz (3 dBc)
	free-running		< 10 kHz (3 dBc)
optical power per comb line		P_{cl}	$\geq$ 100 nW/comb line at λ_{Rb} and λ_K
Average optical power		P_{avg}	> 8 mW

Platform-related technical demands

In the following, the platform-related demands will be presented.

The implementation of the diode laser-based OFC in future spaceborne experiments of the QUANTUS collaboration poses stringent demands on the robustness of its technology platform. Micro-integration of the laser into the technology platform developed at FBH, see Figs. 1.5 and 1.6, allows for exploitation of the platform's already shown suitability for space deployment. To maximize the robustness and compactness of the diode laser-based OFCG, the diode laser is required to comprise as few components as possible. Following this, the platform-related technical demands are as follows.

Due to the mechanical layout of both the micro-integration technology platforms, a linear laser cavity of at most 50 mm length, including all laser components, can be micro-integrated into them. Further, use of components similar to those employed in the CW lasers (diode laser chip, beam shaping optics, and external components, e.g. external mirror) is required to allow for exploitation of the existing micro-integration concept for CW lasers. The diode laser chip must be mounted into a submount that can be micro-integrated into the platform. Thus, the submount must be similar in dimension to those used for the CW lasers. The height of the submount is required to be 1.1 mm. The width of the submount (perpendicular to the laser's optical axis) needs to measure less than 2.2 mm to allow for micro-integration into both technology platforms. The length of the submount (parallel to the laser's optical axis) needs to be chosen according to the length of the diode laser chip providing the required resonator length L_{res} (Eq. 1.7) if a solitary, monolithic diode laser is chosen. The length of a diode laser chip

providing a pulse repetition rate of, e.g., 6.8 GHz, is about 6.3 mm assuming a group refractive index of 3.5 which is in the typical range for diode laser chips emitting the wavelength range of interest. In case of an ECDL-type laser configuration, shorter diode laser chips can be employed. The length of the submount must be chosen appropriately to avoid beam clipping.

To allow for use of commercial external optical components in both, the development test bed for the OFC and the micro-integration technology platform, components are required to be mechanically machinable as custom-substrates and coatings can cost several thousands of euro. These components are, e.g., micro-lenses, and an external mirror in case of an ECDL-type laser configuration.

The micro-lenses employed for beam shaping need to provide a collimated output beam with a beam diameter of about 600 µm ($1/e^2$, intensity). The use of single micro-lenses is preferred to simplify the laser setup and reduce the number of components of the laser. For the development test bed, round micro-lenses with a diameter of about 3 mm are required. For micro-integration, rectangular micro-lenses with a width of about 2 mm are required that provide a beam height above the micro-optical bench of about 1 mm. Use of the same micro-lenses at the laser output and in the extended cavity is preferred to minimize the system complexity.

As the developed OFCG is be micro-integrated, an external mirror featuring the same characteristics, e.g. in particular regarding the coating, needs to be used in both, the test bed during the development of the OFC and in the micro-integrated technology platform. The requirements on the coating of the external mirror are as follows. To avoid distortion of the optical spectrum which might cause spectral narrowing, a spectral bandwidth of the coating of the external mirror of at least 40 nm is necessary. Further, timing (phase) distortions due to group velocity dispersion (GVD) across the spectral range of the pulses are to be avoided. Thus, nearly-zero GVD across the spectral bandwidth of the coating is required. The size requirements on the external mirror are as follows. For the development test bed an external mirror with a substrate diameter of ½" or 1" is required. In contrast, for micro-integration an external mirror with a surface area of about 2×4 mm^2 with and substrate thickness of about 1 to 2 mm is required. Further, an external mirror is required to avoid parasitic optical feedback into the diode laser chip. This can be realized by implementation of a wedged substrate for the external mirror.

The multi-purpose multi-port electrical interface of the technology platforms provides the basis for implementation of a mode-locked diode laser generating the OFC. Thus, on this end, no further requirements are posed.

Tab. 1.2 summarizes the platform-related requirements for the OFCG.

Table 1.2.: Platform-related requirements for diode laser-based OFCG.

laser layout	linear cavity	
length of laser cavity	$\leq$ 50 mm	
submount for diode laser chip	electrical compatibility	
	height = 1.1 mm	
	width $<$ 5 mm (1^{st} gen.), $<$ 2.2 mm (2^{nd} gen.)	
	length $\leq$ 6.3 mm for f_{rep} = 6.8 GHz	
external optical components	same for development test bed and for micro-integration	
	mechanically machinable	
- micro-lenses	collimated beam diameter ($1/e^2$, intensity) $\approx$ 600 µm	
	for test bed	round substrate
		diameter = 3 mm
		rectangular substrate
	for micro-integration	width $\approx$ 2 mm
		for beam height $\approx$ 1 mm
- external mirror	spectral bandwidth of coating $>$ 40 nm	
	nearly-zero GVD across spectral bandwidth	
	wedged substrate with dimensions:	
	for test bed	mirror diameter $\leq$ 1"
	for micro-integration	mirror area = 2×4 mm^2
		substrate thickness $<$ 2 mm
electrical interface	compatible with mode-locked diode lasers	

1.3. State of the art optical frequency combs operating in the wavelength region around 780 nm

Tab. 1.3 summarizes state of the art OFCGs operating in the wavelength region around 780 nm. Here, the wavelengths λ_1 and λ_2 denote the shortest and longest wavelength of the OFC, respectively, that feature an optical power of at least 20 dBc (without wavelength peak of the pump). Also listed, if available, are the spectral bandwidth $\Delta\lambda_{20}$ at 20 dBc, the pulse repetition rate f_{rep}, and the FWHM RF linewidth Δf_{rep} of the free-running[4] pulse repetition rate.

While solid-state, see, e.g., Refs. [83–85], and fiber-laser-based, see, e.g., Refs. [86, 87], OFCGs easily encompass the wavelength region of interest, they are highly complex systems comprising a pump laser, power amplifier elements, and spectral-broadening components.

In contrast, micro-resonator-based OFCGs show a high potential for realization in a compact and space-suitable set-up as they can be electrically pumped [36]. While generation of an OFC with micro-resonators is possible in the wavelength range around 780 nm, see, e.g., Ref. [82], the spectral bandwidth provided is well below the requirement of more than 13.5 nm (at 20 dBc).

[4] In case of micro-resonator-based OFC, the pulse repetition rate of the laser is self-locked to the light that is back-scattered from micro-resonator [82]. As no additional locking electronics were employed, the RF linewidth is considered free-running.

To cover the spectral bandwidth of interest for this thesis, this type of OFCG typically also requires power amplification and spectral broadening, see, e.g., Refs. [88–90]. Nevertheless, Yu *et al.* (Ref. [90]) demonstrated a micro-resonator-based OFC providing optical power at the comb line closest to the Rb D2 transition, approximately 0.3 µW, which is sufficient for beat note generation.

In contrast, directly generating an OFC of suitable spectral bandwidth from a diode laser, as stated above, allows for a very compact and robust OFCG. Both, quantum dot (QD)- and quantum well (QW)-based, devices have been employed for that purpose, see, e.g., Refs. [91–93]. Spectral bandwidths of about 25 nm at 20 dBc were reported for QD-based diode lasers [93]. Further, QD-based devices, typically, feature a high RF stability [91]. However, the center wavelength for QD-diode laser based OFCs is typically in the telecom wavelength range of 1300 nm [92] or 1550 nm [93]. Thus, in the wavelength range around 780 nm, QW-based diode lasers are typically employed. Spectral bandwidth at 20 dBc of about 20 nm and about 13 nm were reported for diode laser-based OFCs emitting at around 830 and 850 nm, respectively, see Refs. [32, 94]. The employed laser resonators, however, were very long extended cavities ($L_{res} > 23$ cm). For similar lasers emitting below 800 nm in or close to the wavelength region of interest, the reported spectral bandwidths at 20 dBc are smaller than 10 nm, see, e.g., Refs. [95–98]. In the vicinity of 780 nm, mode-locked semiconductor lasers providing a spectral bandwidth of up to 5 nm at 20 dBc were reported [95–97]. Further, passively mode-locked semiconductor lasers with a spectral bandwidth of about 4.5 nm at around 795 nm and a pulse repetition rate of around 6.85 GHz were demonstrated [97, 99].

For comparison, results achieved within this thesis' work are also shown in Tab. 1.3 for those laser designs that provided the maximum spectral bandwidth at 20 dBc (asymmetric double quantum well (aDQW) laser) and the minimum RF linewidth (symmetric double quantum well (sDQW) laser).

Table 1.3.: State of the art OFC generation in the wavelength range of 780 nm. λ_1 and λ_2 denote the shortest and longest wavelength of the OFC, respectively, that feature an optical power of at least 20 dBc (without wavelength peak of the pump). Also listed, if available, are the spectral bandwidth $\Delta\lambda_{20}$ at 20 dBc, the pulse repetition rate f_{rep}, and the FWHM RF linewidth Δf_{rep} of the free-running pulse repetition rate. The star (*) denotes parameters estimated from figures given in respective references. The plus ($^+$) denotes a spectral bandwidth at 40 dBc, as that OFCG (Ref. [90]) provided an optical power (denoted (0.3 µW)) sufficient for beat note generation. The mode-locking performance parameters achieved in this work are given for those laser designs that provided the maximum spectral bandwidth at 20 dBc (aDQW laser), and the minimum RF linewidth (sDQW laser).

λ_1/nm - λ_2/nm	$\Delta\lambda_{20}$/nm	f_{rep}/GHz	Δf_{rep}/kHz	P_{avg}/mW	[Ref.] (year)
solid-state OFCs					
400 - 1800	1400 *	0.08	–	–	[83] (2019)
675 - 1395*	750 *	1.05	–	–	[84] (2017)
510 - 1110*	590 *	0.22	–	–	[85] (2017)
fiber laser-based OFCs					
660 - 2100*	1440	0.25	–	–	[86] (2012)

Table 1.3.: (*continued*)

λ_1/nm - λ_2/nm	$\Delta\lambda_{20}$/nm	f_{rep}/GHz	Δf_{rep}/kHz	P_{avg}/mW	[Ref.] (year)
510 - 1370*	860 *	0.1	–	–	[87] (2017)
micro-resonator-based OFCs					
1508 - 1543*	35 *	149	–	–	[36] (2019)
700 - 2000	1300	15	–	–	[88] (2018)
780 - 1610*+	830 *+	1000	–	(0.3 µW)	[90] (2019)
773 - 783*	9 *	20	–	–	[89] (2017)
779.2 - 780.8	1.6*	10	$12 \cdot 10^{-3}$	–	[82] (2014)
950 - 2150*	1200 *	15	–	–	[88] (2018)
diode laser-based OFCs					
QD-based devices					
1281 - 1294*	13 *	39.5	–	–	[92] (2014)
1523 - 1548*	25 *	21.5	450	1	[93] (2017)
QW-based devices					
765 - 768*	3 *	20	–	–	[95] (2014)
782.3 - 783.8*	1.5*	0.5	–	–	[96] (2007)
791.5 - 796*	4.5*	6.8	–	–	[99] (2011)
793 - 798*	5 *	6.8	$95 \cdot 10^{0}$	–	[97] (2012)
824 - 830*	6 *	2.5	–	–	[98] (2006)
815 - 845*	30 *	0.65	–	–	[32] (1995)
844 - 857*	13 *	0.13	–	–	[94] (2015)
this work					
aDQW laser					
769 - 785	16.1	3.4	$5.7 \cdot 10^{0}$	25.4	[100] (2017)
sDQW laser					
786 - 792	6.3	3.4	$6 \cdot 10^{-4}$	91.3	

1.4. Thesis organization

This thesis' work was carried out within the framework of the LASUS-I and -II projects. In the following, the goals of this thesis are summarized and the outline of this thesis is presented.

1.4.1. Goals of this thesis

The main goal of this thesis is to develop a diode laser-based OFC for future spaceborne tests of the UFF within the QUANTUS experiments. The requirements on the OFC performance and the OFCG were discussed in detail in Sec. 1.2.4.

The spectral constraints demand for a mode-locked optical spectrum spanning from about 766.7 nm to 780.2 nm. The pulse repetition rate is required to be 6.8 GHz or its first subharmonic (n_H =1/2) for implementation in future QUANTUS experiments. The first subharmonic is the minimum pulse repetition rate due to the maximum resonator length ($\approx$ 50 mm) that can be realized on the intended micro-integration technology platform. The RF linewidth of the free-running pulse repetition rate shall not exceed 10 kHz. The comb lines closest to the K and Rb D2 transition wavelengths are required to feature an optical power of at least 100 nW for implementation of this OFC in the advanced stabilization scheme for future QUANTUS experiments. Thus, a minimum average output power of 8 mW was estimated. To enable the development of the diode laser-based OFC, an experimental setup and a measurement setup to investigate the mode-locking performance of the lasers under test is to be designed and realized.

The second objective of this thesis is to develop a concept for micro-integrating the diode laser-based OFC into the existing micro-integration technology platform developed at FBH for CW-ECDLs. Thus, within this thesis, a diode laser-based OFC is to be micro-integrated for the first time.

The third objective of this thesis is to demonstrate that the pulse repetition rate of the diode laser-based OFC can be actively stabilized to an RF frequency reference. The reduction of the RF linewidth by means of active stabilization is essential for accurate frequency comparison by means of the OFC.

1.4.2. Outline of this thesis

This thesis is organized as follows.

Chapter 2 introduces the mode-locked diode laser as an optical frequency comb generator. First, techniques to mode-lock a diode laser are presented. Then resonator concepts for edge-emitting mode-locked diode lasers are discussed. Further, the layout of the diode laser chips (epitaxial layer, lateral, and longitudinal structure) and the passive laser components (lenses and external mirror) are presented.

Chapter 3 presents the laser test mount and the experimental setup which are developed to characterize the mode-locking performance of the diode laser under test. The laser test mount comprises individual mounts for the components of the diode laser that provide the means for the exchange of individual components of the diode laser-based OFCG during the development

process. The laser test mount is integrated into the experimental setup which comprises an opto-mechanical setup for beam distribution to the measurement instruments that allow for recording of the mode-locking performance. Further, the experimental techniques are introduced that are utilized within this work to characterize the mode-locking performance in the optical frequency, RF frequency, and time domain as well as in terms of the emitted optical power.

Chapter 4 begins with detailing the strategy employed to evaluate the diode laser's mode-locking performance. Then the optical design of the ECDL is discussed in terms of the beam shaping optics, external mirror, and resonator length. It is found that single aspheric micro-lenses, a plane dielectric mirror, and a resonator length of about 44 mm offer the best mode-locking performance in terms of spectral bandwidth and RF stability. In a subsequent step, the influence of the epitaxial design is investigated. Diode laser chips with an epitaxial layer structure featuring a double quantum well (DQW) active region are employed. Symmetric and asymmetric DQW structures are compared. It is shown that the latter design can be used to generate an OFC spanning (more than) the required 13.5 nm at 20 dBc compared to the symmetric DQW approach which only provides a spectral bandwidth of at most 7.5 nm. Diode lasers implementing the asymmetric DQW design achieve an RF linewidth well below the required 10 kHz. Next, the longitudinal design of the available diode laser chips is investigated. Further, evaluation of the diode laser chips' facet reflectivities is conducted showing preference to lower reflectivities. At the end of chapter 4, the dependence of mode-locking performance of the best suited diode laser on the values of the operating parameters is presented in detail.

Chapter 5 presents the successful micro-integration of passively mode-locked extended-cavity diode lasers (ML-ECDLs) for the first time. To that end, a micro-integration concept is developed based on the already existing concept for the implementation of CW-ECDLs. The micro-integration concept comprises modifications of the existing micro-integration platform and modifications of the existing micro-integration procedure. A proof-of-concept demonstrator diode laser-based OFC laser module is realized. Lessons learned from this ML-ECDL module are applied to advance the micro-integration concept. An advanced ML-ECDL module is realized based on this concept. The mode-locking performance of each micro-integrated laser module is compared to that of a structurally identical diode laser-based OFCG mounted in the laser test mount. Lastly, possible future improvements of the micro-integration concept and technology are suggested.

Chapter 6 describes experiments to stabilize the pulse repetition rate of the diode laser-based OFC developed in this thesis. The injection current into the gain section of the diode laser chip is employed as an actuator for manipulation of the pulse repetition rate. A servo bandwidth of around 70 kHz is achieved.

Chapter 7 summarizes the results of this thesis and suggests future improvements of the diode laser-based OFCG and the micro-integration technology platform. This thesis is closed with an outlook towards future implementations of diode laser-based OFCs in field and space experiments.

2. Mode-locking of semiconductor lasers

2.1. Introduction to mode-locked diode lasers

Soon after the first experimental demonstration of the laser in 1960 [39], semiconductor lasers were realized in 1962 [101]. However, while mode-locking of solid-state or vapor based lasers was reported early on, only partial mode-locking of semiconductor lasers was reported up to the early 70s [102, 103]. Successful mode-locking of a semiconductor laser was first reported in the late 70s when efficient diode laser (double hetero-)structures became available [22, 104–106]. Since then, various approaches to mode-locking a diode laser have been realized by, e.g., external modulation, inhomogeneous current injection, and saturable absorber elements both external of or monolithically integrated into the diode laser chip [105, 107–109]. These lasers have been realized with different resonator concepts like ring and folded as well as linear cavities [110–112]. Further, different epitaxial concepts such as QW and QD concepts have been employed to realize mode-locked diode lasers [92, 93, 113] featuring a large spectral bandwidth.

In the wavelength range near 780 nm, diode lasers featuring QWs are well-established for narrow linewidth CW operation [114]. This thesis' work followed a two-step approach in order to develop an OFCG in the wavelength range near 780 nm based on diode laser featuring QWs. First, an initial design for the laser chips was selected and laser chips were manufactured accordingly by FBH. The performance of the OFCs based on these chips was analyzed. Second, the results were used to advance the laser chip design for mode-locked operation with a large spectral bandwidth.

In the sections of this chapter, the diode laser chips employed in this work is introduced. Techniques to mode-lock semiconductor lasers are presented and evaluated for the purpose of this work. Further, optical gain and absorption in mode-locked diode lasers are discussed. Then, two resonator concepts for mode-locked diode lasers are evaluated and compared. Finally, passive optical components (lenses, feedback mirror, facet coating) of an ML-ECDL and their influence on the mode-locking performance are described.

2.2. Diode laser chips

A diode laser chip is, in essence, a stack of epitaxial layers of semiconductor material featuring transverse and longitudinal optical mode and carrier confinement structures realized by a lithographic process. A schematic of an edge-emitting diode laser, as used in this work, is depicted in Fig. 2.1. The transverse structure herein combines vertical (direction perpendicular to epitaxial layers) and lateral (direction parallel to the epitaxial layers and parallel to the facets) structures of the diode laser chip. The longitudinal structure of the diode laser chip, in contrast, is given along the optical axis of the laser (direction perpendicular to the facets). This structure com-

prises the laser resonator that is formed by either the (partial reflection (PR) coated) facets of the diode laser chip or the mirrors external to the diode laser chip, see Fig. 2.8 and 2.9.

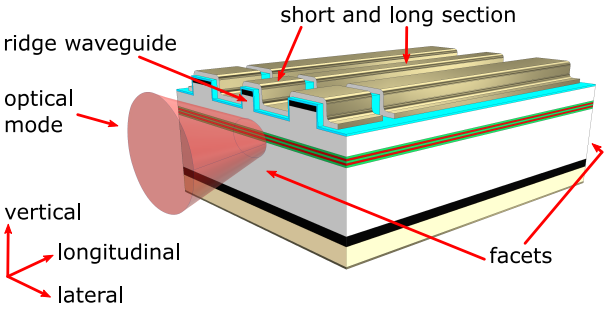

Figure 2.1.: Schematic of a sectioned diode laser chip. (not to scale)

This section gives an insight on general aspects of the type of diode laser chips which are used in this thesis' work. The vertical and lateral carrier and optical confinement methods are presented. To that end, the epitaxial (vertical) structure of the laser diode is described and optical gain and saturable absorption are discussed.

Epitaxial layer structure of the diode laser chip

The epitaxial layer structure of the diode laser chips provides, amongst others, the means for light emission as well as vertical confinement of the optical mode. To that end, a so-called separate confinement heterostructure (SCH) is employed. It combines an active double heterostructure (p-i-n structure) and a passive optical waveguide, see schematic in Fig. 2.2. The active structure enables efficient vertical carrier transport into and carrier confinement within the active region to provide optical gain. The passive structure provides vertical optical mode confinement for the generated optical fields. The epitaxial layer structure is grown by metal-organic vapor-phase epitaxy (MOVPE) on gallium arsenide (GaAs) substrates. This technique allows for precise control of stoichiometric composition and thickness of the layers to adjust the optical gain and optical mode [115]. Metal contact layers on the top and bottom of the epitaxial layers allow for electrical biasing of the diode laser chip.

A III-V compound semiconductor featuring a direct band-gap is employed for light generation in the spectral region of interest around 780 nm. The active region of these diode lasers is realized as a DQW structure for efficient light emission. In this work, the active region comprises a tensile-strained QW design based on gallium arsenide phosphide (GaAsP) QWs and undoped GaAs barrier layers. This design is used to allow for reliable and efficient devices [114]. The wavelength of maximum optical gain is defined by the thickness of the layers of the active region and the stoichiometric ratio of arsenic (As) and phosphorus (P) in the QWs. Customization of this ratio for each QW individually will be utilized in this work to facilitate a large spectral bandwidth, mode-locked operation.

The active structure is located between aluminum gallium arsenide (AlGaAs) epitaxial layers that form the vertical optical waveguide, see Fig. 2.2. Appropriate p- and n-doping of the AlGaAs optical waveguide material with carbon (C) and silicon (Si), respectively, allows for

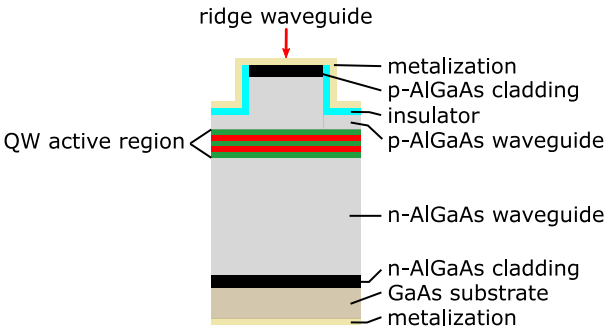

Figure 2.2.: Schematic of the epitaxial layer structure of a diode laser chip, corresponding to the diode laser chip depicted in Fig. 2.1. (not to scale)

efficient carrier transport to the active region and supports the establishment of an efficient optical waveguide structure. Careful design of the optical waveguide enables suppression of higher order vertical modes. To allow for the implementation of the diode laser chip in the experimental scheme sketched in Sec. 1.2.2, a high optical output power is required, see Sec. 1.2.4. However, the magnitude of optical intensity could cause diode laser chip failure due to catastrophic optical mirror damage (COMD). Thus, an asymmetric super-large optical cavity (ASLOC) design is implemented to realize a large vertical optical waveguide which, for a given optical power, reduces the optical intensity by widening the optical field [116]. Consequently, the confinement factor that is defined as the overlap fraction of the vertical distribution of the optical power $J(x)$ with the gain region of thickness d_{az} [115]

$$\Gamma = \frac{\int_{-d_{az}/2}^{d_{az}/2} J(x)\,\mathrm{d}x}{\int_{-\infty}^{\infty} J(x)\,\mathrm{d}x} \tag{2.1}$$

is small. Further, the resulting large vertical mode field diameter leads to a small vertical far field divergence angle of the radiation emitted out of the facets. This is beneficial for the micro-integration as nearly round mode fields can be realized so that round aspheric lenses with modest numerical aperture (NA) can be employed.

Ontop of the above described epitaxial layers of the p-side waveguide and cladding, an insulator layer is deposited after forming the lateral structure of the diode laser chip that is subsequently discussed. Typically, this insulation is a layer of silicon nitride (SiN_x) with a thickness of a few hundred nanometer. Finally, a metalization comprising layers of titanium, platinum, and gold, that is in sum a few hundred nanometer thick, is deposited on the p- and n-side of the wafer to provide the p- and n-side electrical contact, respectively.

Lateral structure of the diode laser chip

Lateral confinement of the carriers and the optical mode is either implemented via so-called gain-guided or index-guided stripe-geometry [117].

The gain-guided confinement is realized by implementation of an aperture for current injection. This current aperture is formed by omitting the insulator across a defined area ontop of the p-side of the vertical optical waveguide. This area is defined by lithographically structuring the diode laser chip after epitaxial growth. Light is emitted in the active region below the current aperture in an effective width much broader than the current aperture width due to current spreading. The optical mode is, thus, laterally confined to that area. The spreading, however, results in a low carrier density and consequently high threshold currents.

The index-guided confinement enables lateral confinement of the optical mode by means of an effective index step. This index step profile can be realized by etching a narrow ridge into the p-side of the diode laser chip before the deposition of the insulator and p-side metalization, see Fig. 2.1 and 2.2. The optical structure formed is, thus, called a ridge waveguide. Typically, the ridge waveguide does not need to be etched through the active region to allow for lateral single mode operation [115]. Additionally to providing the means for optical confinement, the ridge waveguide allows for reduction of current spreading from the current aperture on top of the ridge waveguide (Fig. 2.1) compared to the gain-guided confinement. Thus, a high carrier density and consequently low threshold currents are possible [115]. Typical effective index steps of about 10^{-3} are implemented for fundamental lateral optical mode operation [118]. Appropriate design of the lateral confinement in conjunction with the vertical confinement enables a (nearly) round fundamental transverse optical mode profile minimizing the number of beam shaping optics. In optimal cases a single round lens can provide a round collimated beam.

The diode laser chips employed in this work use lateral index-guided confinement. It is implemented by means of a 4.0 µm wide ridge waveguide which is not etched through the active region. The ridge waveguide is realized by etching 20 µm wide trenches into p-side epitaxial layers, see Fig. 2.1.

Longitudinal structure of the diode laser chip

The diode laser chips employed in this work are segmented into sections in the longitudinal direction, see Fig. 2.1. By this means a short and a long section are realized that, appropriately biased, will provide a saturable absorber and a gain section, as will be discussed in the next paragraph.

These sections are implemented as follows. During epitaxial growth of the wafer, the metalization on the p-side of the wafer is omitted at designated areas in longitudinal and lateral direction (Fig. 2.1) to provide electrical isolation between the longitudinal sections. Typically, these areas are additionally implanted with helium ions to further electrically isolate the sections. The electrical contact on the n-side of the diode laser chip is not sectioned which provides a common n-contact for the saturable absorber and gain section.

In addition to realizing these sections, electrically isolating areas are typically implemented close to the facets. By that means, an accumulation of carriers close to the facets can be avoided

as that could lead to COMD.

In this work, a typically 100 µm long section is, thus, electrically isolated from the rest of the diode laser chip. Additionally, an about 15 µm wide electrically isolating area is implemented at both facets of the diode laser chip.

2.3. Mode-locking techniques

This section gives an overview over mode-locking techniques for diode lasers. These techniques can be divided into three categories: active, passive, and a combination thereof called hybrid mode-locking.

2.3.1. Active mode-locking

Active mode-locking involves modulation of the round trip gain of the laser resonator at a frequency f_{rep} synchronized with the inverse round trip time T_{rep} or its harmonics or sub-harmonics [112, 119–121]. In the frequency domain, this gain modulation results in the locking of the longitudinal modes of the laser resonator that feature a frequency distance of f_{rep} [122]. In the time domain, a pulse train comprising (identical) pulses with a temporal distance of T_{rep} from each other is emitted from the laser resonator.

The physical implementation of gain modulation is based on the realization of a modulation of the carrier density. The carrier density and, thus, the gain is modulated with an appropriately chosen RF frequency signal superimposed onto the direct current (DC) injection current. Often, a sinusoidal signal is chosen to be superimposed onto an injection current close to the threshold current of the diode laser. The resulting gain modulation is sketched in Fig. 2.3(a). The corresponding electrical interface is shown in Fig. 2.3(b). It can be seen that modulation of the carrier density around the value corresponding to the threshold current density results in a short increase of the gain above the loss. Thus, a short net-gain window is created during the time when the carrier density exceeds the value corresponding to the current threshold for lasing. In this short time interval, the actively mode-locked optical pulse is formed.

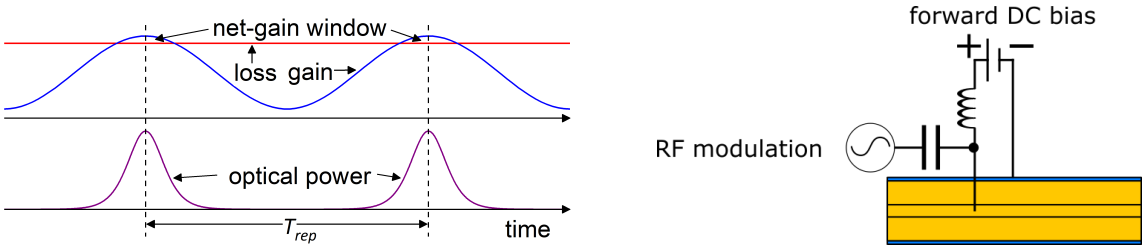

(a) Gain modulation (b) Electrical interface

Figure 2.3.: Active mode-locking of a diode laser: Schematic for (a) modulation of the gain and (b) corresponding electrical interface for the edge-emitting diode laser chip for superposition of a DC injection current and an RF modulation signal. The optical pulse produced by the RF modulation of the optical gain is sketched in (a).

The achievable minimum pulse width and, hence, the maximum spectral bandwidth depend, amongst others, on the temporal width of the net-gain window as well as the steepness of the modulation signal [112, 123]. To avoid failure of the diode laser chip due to a too high amplitude of the modulation signal, only a modulation signal with a limited amplitude can be implemented for a given modulation frequency. For the typically sinusoidal modulation signal, this, however, limits the steepness.

Further, a high frequency RF signal generator is typically required for actively mode-locking a diode laser. For, e.g., a monolithic diode laser with a 1 mm long optical resonator, a modulation frequency of around 40 GHz is required for fundamental mode-locking. The frequency of the RF signal can be reduced significantly if a long laser resonator is used, see Eq. 1.7. For an optical resonator length of 10 cm, a modulation frequency of only 1.5 GHz is required.

Nevertheless, subpicosecond pulses have been obtained from an active mode-locked semiconductor laser, see, e.g., Ref. [112]. The need for a low noise signal generator, however, makes this approach unappealing for realizing a very compact mode-locked diode laser. Thus, this technique is not employed in this work.

2.3.2. Passive mode-locking

Passive mode-locking, in contrast to active mode-locking, requires the implementation of a nonlinear absorbing element into the laser resonator which will cause self-modulation of the optical field propagating in the optical resonator [123, 124]. For a diode laser, this is typically implemented by means of a saturable absorber. In a diode laser a saturable absorber can be realized by electrically separating a short section of the diode laser chip or by adding an additional, separate semiconductor segment to the laser resonator. The main requirement for pulse generation is that the loss in the saturable absorber section saturates at a lower energy than the gain in the (DC current injected) other section. This requirement can be expressed in terms of the saturation energy E_s^a and E_s^g of saturable absorber and gain section, respectively [122]:

$$E_s^a = \frac{\hbar\omega A_a}{\partial a/\partial N_a} < \frac{\hbar\omega A_g}{\partial g/\partial N_g} = E_s^g \tag{2.2}$$

where ω is the angular optical frequency, and $\partial a/\partial N$ and $\partial g/\partial N$ are differential absorption and differential gain with respect to the carrier density, respectively. A_a and A_g are the effective cross-section areas of the optical mode in the saturable absorber (a) and gain (g) section, respectively. These effective areas are given by $A_{a,g} = A_{az_{a,g}}/\Gamma_{a,g}$ where $A_{az_{a,g}}$ is the area of the active region and $\Gamma_{a,g}$ the confinement factor in the respective sections.

For a sectioned diode laser chip, as employed in this work, the epitaxial layers of and the optical waveguide in the saturable absorber and the gain section, respectively, are identical. Therefore, the areas of the active region as well as the confinement factors in both sections are identical. Thus, it follows that $A_a = A_g = A_{az}/\Gamma$. Consequently, the requirement of $E_s^a < E_s^g$ reduces to $\partial g/\partial N_g < \partial a/\partial N_a$. Further, the optical gain/absorption of QW-based diode lasers can be approximated by a logarithmic model [117], see Fig. 2.4. At the transparency carrier density N_{tr} the optical field remains unchanged. The (electrically unpumped or reverse biased) absorber section features a carrier density below the transparency carrier density N_{tr}. In contrast, the

(carrier injected) gain section has a carrier density in excess of the transparency carrier density N_{tr}. Thus, an appropriately sectioned diode laser chip satisfies the requirement stated in Eq. 2.2.

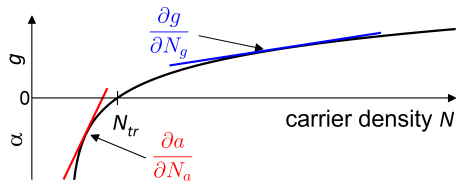

Figure 2.4.: Schematic of a logarithmic model of QW-based diode laser chips for optical gain g and absorption α. The differential gain and differential absorption are exemplary highlighted by blue and red lines, respectively.

The interaction of the optical pulse with the saturable absorption and the gain in the respective sections of the diode laser chip is sketched in Fig. 2.5(a). For better visualization of the interaction, the states of the maximum saturation of saturable absorption and gain are plotted at the same point in time.

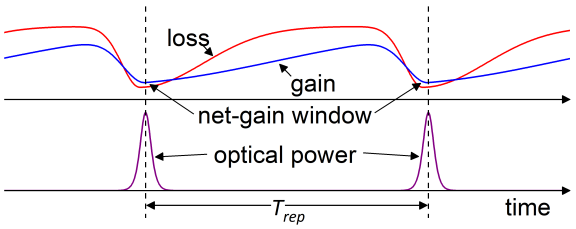

(a) Loss modulation

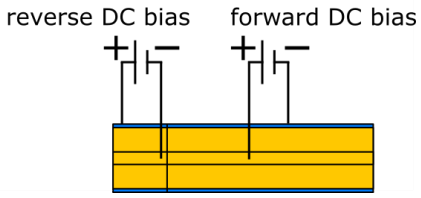

(b) Electrical interface

Figure 2.5.: Passive mode-locking of a diode laser: Schematic for (a) a modulation of loss in the laser resonator and (b) an exemplary electrical interface of an edge-emitting diode laser. The net-gain window results from the accumulated action of saturable absorption and optical gain that the pulse experiences in the respective sections of the laser during its round trip in the laser resonator.

First, the interaction of the optical pulse with the saturable absorber is discussed. An optical pulse generated by spontaneously mode-locked modes starts to saturate the saturable absorber. The generated photocarriers cause a reduction of absorption (loss). Due to the non-linear nature of the saturable absorption, the pulse's peak experiences less absorption than its rising and falling edge. The rising edge of the optical pulse sharpens. If the recovery time of the saturable absorption is shorter than the pulse width, the falling edge of the pulse can be shaped by the saturable absorption, too. Due to the saturable absorption, the center of gravity of the pulse shifts towards the pulse's falling edge. Further, in the time interval between the pulses, the saturable absorber ensures suppression of spontaneous emission.

Second, the interaction of the optical pulse with saturable optical gain is described. The gain depletes due to the increasing optical power on the rising edge of the pulse. Thus, the

rising edge and the center of the pulse experience optical gain. Due to gain depletion and non-instantaneous gain recovery the falling edge of the pulse experiences less gain than the rising edge. The interaction of the optical pulse with the saturable gain, thus, leads to a sharp steepening of the rising edge of the optical pulse. As a consequence, the center of gravity of the pulse shifts towards the pulse's rising edge.

The combined action of saturable absorption and gain leads to the creation of a so-called net-gain window [122], see Fig. 2.5. Due to this net-gain window, an optical pulse is formed, shortened, and can travel in the laser resonator. The shape of the pulses is a result of the combined action of saturable absorption and gain. Typically, the pulse shape of a passively mode-locked diode laser features a squared hyperbolic secant (sech^2) form [122], as sketched in Fig. 2.5. As the facets of the diode laser provide optical feedback, the, thus, generated optical pulse is partially emitted from the diode laser chip. The remaining optical power of the pulse is then used to recreate the pulse during its round trip in the laser resonator.

The gain bandwidth, absorption recovery time, and self-phase modulation (SPM) limit the pulse shortening and create a balanced steady state operation [65]. Hence, passive mode-locking of a diode laser is a self-starting and self-balancing process. Typically, the timing noise of the pulse train emitted by passively mode-locked lasers exceeds the timing noise of actively mode-locked lasers due to the absence of an external reference signal [125]. Passive mode-locking allows for fundamental as well as harmonic mode-locking depending on the recovery time of the saturable absorption.

Saturable absorption can be enhanced by, e.g., aging [126], proton bombardment [108], ion implantation [126], and application of a reverse voltage [127] to that specific section. The latter method allows for fine-tuning of the absorber characteristics during operation by adjusting the reverse bias [128, 129]. This method is therefore selected for this thesis' work. A schematic of the electrical interface for the edge-emitting diode laser featuring a reverse bias applied to the saturable absorber is shown in Fig. 2.5(b).

In this work, passive mode-locking is employed for self-starting, large spectral bandwidth OFC generation.

2.3.3. Hybrid mode-locking

Hybrid mode-locking is a combination of both, active and passive mode-locking [130]. Here, either the absorber or the gain section are modulated with an RF signal at a frequency that corresponds to the pulse repetition rate [131, 132]. Thus, hybrid mode-locked lasers utilize the self-starting and self-balancing passive-mode-locking mechanisms. If the driving RF signal is close enough to the „native“ repetition rate of the passively mode-locked laser, then the pulse repetition rate of the laser locks to the signal provided by the RF signal generator, minimizing temporal fluctuations of the pulse repetition rate. A schematic of an electrical interface is depicted in Fig. 2.6. Here, an implementation is shown where the RF signal is injected into the absorber section.

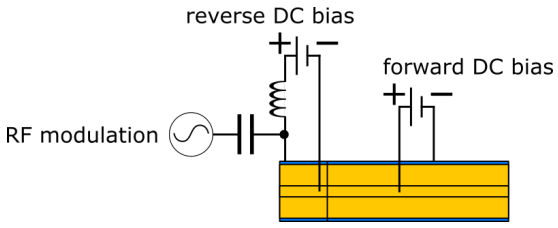

Figure 2.6.: Schematic of an electrical interface for hybrid mode-locking.

2.4. Optical absorption and gain in passively mode-locked diode lasers

A detailed analysis of optical gain and absorption in passively mode-locked diode lasers can be found in, e.g., Refs. [117, 133–135]. The subsequent description follows those given in these references.

The population inversion required for stimulated photon emission and light amplification (optical gain) is realized by forward biasing the laser diode chip (or a section of it) for injection of current I_{DCI}. Under forward bias, the quasi-Fermi-levels in the intrinsic layer (in the QW active region) are located inside the conduction and valence band, see Fig. 2.7(a), [117]. The band structure eases carrier transport into the QWs in the active region. Optical gain is then allowed for $E_g \leq \hbar\omega < \Delta E_F$ where E_g is the band gap energy, ω the optical angular frequency of the photon, and ΔE_F the difference in quasi-Fermi levels of the conduction (E_{FC}) and valence (E_{FV}) band [117, 136]. Thus, only photons with optical angular frequencies ω meeting this requirement can experience optical gain [137]. Due to the spread of the energy levels into energy bands, however, optical gain for photons in a frequency band is provided [136, 138, 139].

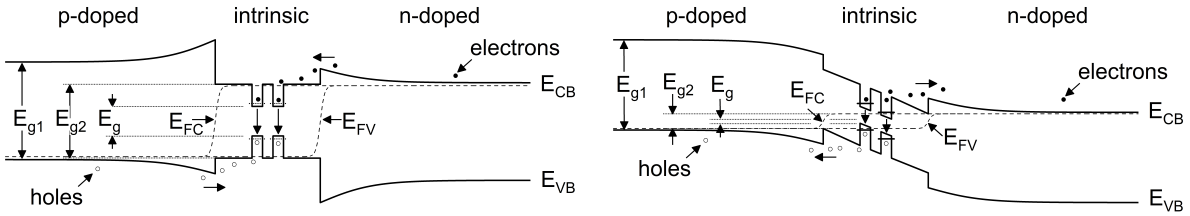

(a) forward bias (b) reverse bias

Figure 2.7.: Schematic of the energy-band diagram of a DQW double heterostructure resulting from (a) a forward bias for optical gain and (b) a reverse voltage for saturable absorption. E_{CB}, E_{VB} - conduction (C) and valence (V) band; E_{FC}, E_{FV} - quasi Fermi levels; E_{g1}, E_{g2} - band gap energies of heterostructure; E_g - band gap energy of QWs [117, 135].

The temporal change of the carrier concentration N in the active region is described by the rate equation. At a fixed spatial point in the diode laser chip the rate equation is given by

$$\frac{\mathrm{d}N(t)}{\mathrm{d}t} = J_{az}(t) - \frac{N}{\tau_g} - v_g g(N) S(t). \tag{2.3}$$

Here, a similar carrier concentration for electrons (N) and holes (P) is assumed.

The first term on the right-hand side of Eq. 2.3 describes the current injection into the active region with

$$J_{az}(t) = \eta_i \cdot \frac{I_{DCI}}{qV_{az}}. \tag{2.4}$$

Here, q is the unit charge and $V_{az} = A_{az}L_{az}$ the volume of the active region with the cross section A_{az} and the length L_{az} of the active region. I_{DCI} describes the injection current which is then transferred into the active region with efficiency η_i.

The middle term on the right-hand side of Eq. 2.3 considers the carrier recombination which depends on the carrier lifetime τ_g. Using $N/\tau_g = R(N) = A_rN + B_rN^2 + C_rN^3$, this term describes non-radiative (A_r), spontaneous (B_r), and Auger (C_r) recombination processes.

The last term on the right-hand side of Eq. 2.3 denotes the carrier loss due to stimulated emission. Here, reduction of the carrier concentration due to stimulated emission is taken into account via the optical gain $g(N)$ and the density $S(t)$ of the photons already present in the laser resonator stimulating the emission of further photons. The photons are transported through the active region at the the group velocity v_g.

The optical gain determines the basic emission properties of the diode laser. The relation between optical gain and carrier density described above can be linearly approximated close to the threshold by

$$g(N) = g' \cdot (N - N_{tr}) \tag{2.5}$$

where N_{tr} ($N > N_{tr}$) is the carrier density at transparency and $g' = \partial g/\partial N$ is the differential gain close to the threshold. The optical gain at transparency is zero ($g(N_{tr}) = 0$). The change of optical gain with time can be expressed as

$$\frac{\mathrm{d}g(N)}{\mathrm{d}t} = g'\frac{\mathrm{d}N}{\mathrm{d}t} = g'J_{az} - \frac{g(N) + g'N_{tr}}{\tau_g} - g'v_g g(N)S(t), \tag{2.6}$$

using $g'N = g(N) + g'N_{tr}$.

Depending on the optical pulse length t_p the gain can be classified as slow ($\tau_g \gg t_p$) and fast ($t_p \gg \tau_g$). This distinction describes whether the gain can saturate instantaneously but recovers slowly or fully instantaneously reacts to the incident optical pulse.

In the analysis of the slow gain, the second term on the right-hand side in Eq. 2.6 can hence be neglected. Neglecting carrier injection as well, the slow optical gain can be expressed as

$$g_{slow}(t_p) \approx g_0 \exp\left[-g'v_g \int_0^{t_p} S(t')\,\mathrm{d}t'\right] \tag{2.7}$$

where $g(t_p = 0) = g_0$. Assuming no optical power aside from that concentrated in the optical pulse and observing the relationship between the photon density and optical power $P(t)$, the integral in the exponent of Eq. 2.7 can be written as

$$\int_0^{t_p} S(t')\,\mathrm{d}t' = \frac{\int_0^{t_p} P(t')\,\mathrm{d}t'}{v_g\hbar\omega A_g} = \frac{E_p}{v_g\hbar\omega A_g} \tag{2.8}$$

where E_p is the pulse energy and A_g the overlap area of the active region with the optical mode (see Eq. 2.2). With the saturation energy E_s^g of the optical gain (Eq. 2.2), the slow optical gain is given by

$$g_{slow}(t_p) = g_0 \exp\left[-E_p/E_s^g\right]. \tag{2.9}$$

Thus, while the slow optical gain is time-independent ($g_{slow}(t_p) = g_{slow}$), it depends on the pulse energy.

In contrast, the fast optical gain allows for an instantaneous recovery of the optical gain and, thus, instantaneous reaction of the optical gain to incident photons. Here, $\mathrm{d}g/\mathrm{d}t = 0$ applies. Using Eq. 2.6 and, again, neglecting carrier injection, the fast optical gain is expressed by

$$g_{fast}(t_p) = \frac{g(N=0)}{1 + \frac{P(t_p)}{P_s^g}} \tag{2.10}$$

where the saturation optical power is $P_s^g = E_s^g/\tau_g$. A more detailed derivation can be found in App. A.2.

The approximations describing the optical gain (and absorption) need to be modified when including other effects. High optical powers, e.g., induce nonlinearities, e.g. intra-band processes which reduce the material gain (and absorption) [122, 135, 140, 141]. Employing a phenomenological nonlinear coefficient ϵ_g for the gain includes these effects and modifies the linear models: $g = g_{lin}\, N/(1 + \epsilon_g S)$. For QW edge-emitting lasers at steady state, an empirically validated logarithmic model describes the optical gain the best: $g(N) \propto g' \ln(N/N_{tr})$ [117].

For edge-emitting diode laser chips featuring a QW active region, not just the local dielectric function ϵ^{QW} of the QW, but modal quantities, specifically the modal gain g_m, have to be considered to account for the mediation of the QW operation by the guided transverse optical mode [142]. The dielectric function can be determined from a microscopic model which is based on the band structure and oscillator strengths. These can be obtained from an eight-band k·p model taking into account all possible transitions. Phenomenological corrections for gain broadening (hyperbolic secant shape) and band-gap renormalization include many-body effects into the model [142]. The modal gain for the transverse magnetic (TM)-polarized optical mode, which is preferred by the epitaxial layer design [114], can then be calculated from the imaginary part of the dielectric function $\Im(\epsilon)$ using the confinement factor Γ and the effective index n_{eff} for a given vertical waveguide [142]

$$g_m = 2 \cdot \Im(\beta) \approx \Gamma \frac{\Im(\epsilon)}{n_{eff}} \frac{2\pi}{\lambda} \tag{2.11}$$

where β is the propagation constant and λ the wavelength.

In the following, the effect of the reverse voltage applied to the saturable absorber is considered. For the saturable absorber under reverse voltage, the energy-band structure is strongly modified compared to the forward biased state. The band-edges incline which reduces the band-gap energy [129, 143, 144], see Fig. 2.7(b). With that, the reverse voltage causes on the one hand, a red-shift due to the effectively reduced band gap energy. On the other hand, saturation leads to a blue-shift due to filled carrier states in the energy bands close to the band gap. This saturation

effect is strongest for the lowest photon energies where absorption occurs [145, 146], and occurs highly pronounced in asymmetric quantum wells [147].

The reverse voltage provides the means for carrier sweep-out from the active region for fast absorption recovery, as sketched in Fig. 2.7(b). Effects occur in the absorption and sweep-out process that prolong or shorten the absorption recovery time. Effects enhancing absorption recovery by reducing the absorber recovery time are as follows [129, 143, 145, 146]. The reverse voltage field enhances sweep-out of photoexcited carriers from the active region by tunneling, thermionic emission, and inter-valley scattering. Also, band-gap renormalization causes shrinkage of the band-gap increasing absorption. Thus, it effectively reduces the carrier lifetime. Effects weakening absorption recovery are, e.g., the barrier thickness, and the effective barrier height that can hinder carrier sweep-out [143]. Despite or because of these partially counteracting processes, carrier lifetimes of a few picoseconds and lower can be achieved [145, 146].

The rate equation for saturable absorption at a fixed spatial point in the diode laser chip can be derived from that given in Eq. 2.3 for the optical gain. Without current injection and with generation of photoexcited carriers, the rate equation at a fixed spatial point in a saturable absorber can be described by

$$\frac{\mathrm{d}N}{\mathrm{d}t} = -\frac{N}{\tau_a} + v_g \alpha(N) S(t) \tag{2.12}$$

with the carrier lifetime in the absorber τ_a and the carrier density dependent absorption $\alpha(N)$.

Similar to the optical gain, the saturable absorption can be classified into slow and fast absorption. Here, too, a linear approximation of the relation between absorption and carrier density can be assumed as $\alpha(N) = \alpha'(N_{tr} - N)$ where $\alpha' = \partial\alpha/\partial N$ is the differential absorption close to the threshold. The time dependent slow and fast saturable absorption are derived analogously to the slow and fast optical gain, Eq. 2.9 and 2.10,

$$\alpha_{slow}(t_p) = \alpha_0 \exp\left[-E_p/E_s^a\right] \qquad \text{and} \tag{2.13}$$

$$\alpha_{fast}(t_p) = \frac{\alpha_0}{1 + P(t_p)/P_s^a}, \tag{2.14}$$

respectively. Similar to the optical gain, effects induced by, e.g., high optical powers can be implemented via a phenomenological nonlinear coefficient ϵ_a [122, 135, 140, 141]. Thus, the linear approximation for the saturable absorption is modified to $\alpha = \alpha_{lin}\, N/(1 + \epsilon_a S)$. Further, similar to the optical gain, an empirically validated logarithmic model $\alpha(N) \propto \alpha' \ln(N/N_{tr})$ describes the saturable absorption of QW edge-emitting lasers operating in steady state the best [117].

2.5. Resonator concepts for passively mode-locked diode lasers

Resonator configurations, such as, e.g., ring, folded, and linear cavities provide interesting approaches to realize compact mode-locked diode lasers. However, the micro-integration platform that is intended to be employed within this thesis work requires a restriction to linear cavities [76, 77]. In the following, an overview of the basic linear resonator concepts will be given.

Monolithic (cavity) diode laser

A mode-locked diode laser featuring a monolithic laser cavity offers the utmost compactness and robustness. The laser comprises only a diode laser chip, see Fig. 2.8. Collimation optics are used to collect the light emitted through the facets. The diode laser chip is sectioned by electrically

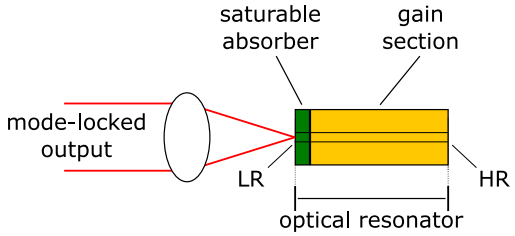

Figure 2.8.: Schematic of a mode-locked diode laser in a monolithic cavity. HR: high reflection coating, LR: low reflection coating.

isolating a section of the laser diode chip to provide a short saturable absorber and, typically, one long gain section. To allow for stable fundamental mode-locking with a pulse repetition rate corresponding to the round trip time in the optical resonator, the saturable absorber is located at a facet with a low-reflection (LR) coating which typically acts as laser output [24], as shown in Fig. 2.8. The other, high-reflection (HR) coated (rear) facet of the diode laser chip then acts as back reflector. This configuration is called anti-colliding pulse mode-locking (ACPM) and has shown to enhance the mode-locking stability compared to the case where the saturable absorber is placed at the HR coated (rear) facet of the diode laser chip (self-colliding pulse mode-locking (SCPM) configuration) [148]. For ACPM, the part of the pulse, that is reflected at the LR coated (front) facet of the diode laser chip and that moves back through the optical resonator, features a reduced optical power compared to the part of the pulse moving towards the LR coated (front) facet. In contrast, for SCPM, the pulses incident at and reflected by the HR coated (rear) facet (and moving in opposite direction) are essentially identical in optical power. The cause for the difference in the mode-locking stability in ACPM and SCPM configuration is the decreased gain saturation, but increased absorber saturation [148] in the ACPM compared to the SCPM. Therefore, an ACPM configuration is employed in this work.

To provide a pulse repetition rate of 6.8 GHz or subharmonics thereof as intended within this work, see Tab. 1.1, diode laser chips providing an optical resonator featuring a physical length of about 6 mm or multiples thereof are required. However, the amount of active semiconductor material of such a diode laser typically leads to high levels of phase noise from spontaneous emission and injection current noise [121, 149, 150]. As such, a monolithic diode laser is not chosen to realize an OFC. Therefore, an alternative configuration of the optical resonator employing shorter diode laser chips is required for the purpose of this thesis.

Extended-cavity diode laser

An alternative to using a long monolithic diode laser is provided by integrating a short laser diode chip into an extended cavity, see Fig. 2.9. To that end, the rear facet of the laser diode

chip located at the gain section is anti-reflection (AR) coated. The rear mirror then is realized by an external mirror in an appropriate distance to allow for the required pulse repetition rate. Thus, the laser resonator is formed between the LR coated (front) facet of the laser diode chip

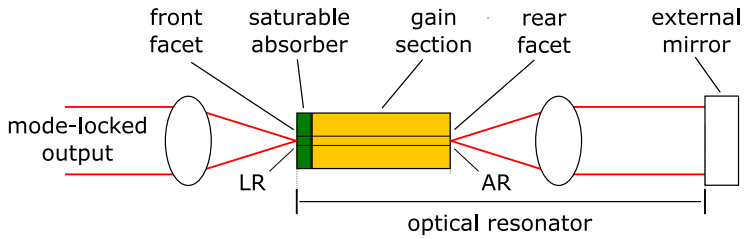

Figure 2.9.: Schematic of an ML-ECDL in an ACPM configuration. AR: anti-reflection coating, LR: low reflection coating.

and the external mirror. This minimizes the amount of active semiconductor material in the laser resonator and, thus, minimizes phase noise. Thus, this so-called ECDL-type resonator concept is used in this work. In the following, a passively mode-locked ECDL-type laser is called ML-ECDL.

The implementation of an ML-ECDL poses several challenges. The quality of the anti-reflection coating of the rear facet of the laser diode chip is vital for providing stable mode-locking and avoiding parasitic feedback [24]. When using a plane external mirror, as shown in the schematic, intra-cavity beam shaping, i.e. collimation or focusing onto the external mirror, is required. Further, precise alignment and high mechanical stability of the laser resonator are essential. All these challenges have been overcome within this thesis work, as will be discussed.

2.6. Optical components of an ML-ECDL

An ML-ECDL with a minimum amount of components can be realized by using a curved mirror to back-reflect the divergent optical mode into the diode laser chip. However, the size of the corresponding mirror would be rather large, as can be seen from the following estimation employing Eq. 1.7. For fundamental mode-locking at 6.8 GHz or harmonics thereof, as intended in this thesis, an optical laser resonator length L_{res} of at least 22 mm is required. Assuming a 1 mm long diode laser chip featuring a group refractive index of about 3.7, the out-of-chip portion of the laser resonator measures about 18 mm. In combination with a beam divergence angle of about 20 deg (FWHM), a usable external mirror surface with a diameter of more than 10.7 mm[1] would be required. This not only limits the achievable compactness of the ML-ECDL. Also, the implementation of the ML-ECDL in the presented micro-integration technology platform (Sec. 1.2.3) would not be possible, as the emitter point of the diode laser chip is about 1 mm above the surface of the module's optical bench. A way around that is to employ appropriate

[1]This number corresponds to the $1/e^2$ beam diameter of a Gaussian beam at the given distance from the beam waist. A mirror with this size is required in order to ensure reflection of a reasonable amount of power. Achieving a reasonable beam quality would require an even larger mirror to avoid, e.g., beam clipping at the mirror.

beam shaping optics, i.e. lenses, to reduce the beam diameter to, e.g., less than a millimeter in the appropriate distance and to employ a plane external mirror.

This section briefly expands on the passive optical components of an ML-ECDL, the reflection coating of the diode laser chip, the beam shaping optics and the external mirror. Details of the implementation in this work are also discussed.

2.6.1. Coating of the diode laser chip's facets

The facets of a diode laser chip as cleaved out of a wafer require further processing before implementation into an ECDL. Oxygen contamination of the facets leads to an increased thermal load due to light absorption and non-radiative recombinations close to the facet [151, 152]. Potential consequences are a reduced lifetime and failure of the device due to COMD. To that end, both facets, typically, are first cleaned after cleaving in air and then passivated. For aluminum (Al)-free active regions, a single, 40 nm thick layer of ZnSe is employed to inhibit oxidation and, thus, passivate the facets [152].

Afterwards, a coating is applied to achieve the required reflectivity. Typical coating materials are Al_2O_3, TiO_2, or ZnSe [151, 152].

The rear facet needs to be anti-reflection coated to avoid parasitic back reflections within the intended resonator and to avoid build-up of parasitic, coupled cavities (between the facets of the diode laser chip and between the rear-facet of the diode laser chip and the external mirror). Such an AR coating can be realized by a $\lambda/4$ thick single layer coating. Alternatively, a stack of multiple layers with appropriate thickness can employed to achieve, e.g., a broadband coating.

The front facet reflectivity is adjusted to optimize the optical output power and the optical power within the laser resonator, reducing frequency and amplitude noise arising from, e.g., increased amounts of amplified spontaneous emission (ASE) [153]. To that end, an LR coating providing between 1 % and 20 % reflectivity is implemented. The methods employed for such an LR coating are comparable to the ones of an AR coating. In case a high reflectivity is required, a coating consisting of pairs of $\lambda/4$ thick layers with high and low refractive index is applied.

In this work, typical LR coatings of 5 % and 10 % are realized by means of single Al_2O_3 layers of appropriate thickness. For HR (30 %) and AR coatings, stacks of Al_2O_3 and TiO_2 layers of appropriate thickness are used. The respective layer thickness corresponds to a few tens of nanometers.

2.6.2. Beam shaping optics

The principal design of the diode laser chip provides a fundamental transverse spatial mode. Beam shaping optics are required either for collimation or focusing of the emitted optical mode onto the external mirror. The divergence angle of the beam emitted from the diode laser chip is defined by the optical confinement in the diode laser chip. Typically, vertical and lateral confinement vary in such a way that different divergence angles are realized for both directions requiring individual shaping. That can be achieved by employing cylindrical lenses which provide one-dimensional beam shaping. Special care has to be taken with respect to the focal lengths to ensure re-injection. Careful design of the optical confinement in the diode laser chip allows for (near) identical divergence angles in the vertical and lateral direction. Thus, employment of

a single round lens for intra-cavity and output beam shaping, respectively, is possible, which is advantageous for reduction of laser module complexity. The focal lengths of these single lenses can be selected to tailor the intra-cavity and output beam diameter. In addition, the use of aspheric lenses eliminates spherical aberrations.

In this work, single aspheric micro-lenses are employed to shape the beam emitted by the diode laser chip inside and outside the laser resonator.

2.6.3. External mirror

As described above, a plane external mirror in combination with appropriate beam shaping optics allows for a compact resonator design. An external mirror, specifically designed with respect to its group velocity dispersion, can assist the pulse shaping within the optical resonator of the laser. Compressing the pulses could increase their peak power to introduce stronger SPM in the gain medium which induces spectral broadening [154]. Lengthening the pulses could increase the maximum average output power [155–158]. However, a specific design of the external mirror demands detailed knowledge of the pulse substructure (chirp).

The main focus of this thesis is to develop a compact and robust ECDL providing the required spectral bandwidth. Optimization of the intra-cavity dispersion by means of an appropriate external mirror is a promising option for future developments. Thus, a commercially available mirror, that, by itself, does not or only minimally influence the pulse shape is employed.

3. Measurement methods and setup

3.1. Introduction to measurement and analysis feedback loop

The development of a passively ML-ECDL emitting an OFC in the spectral range around 780 nm requires a suitable test bed to analyze the mode-locking performance. Fig. 3.1 illustrates the very basics of such a test bed. On the one hand, a laser test mount is required wherein all components of the ECDL are individually exchangeable to find the best combination of diode laser chip and optical components. On the other hand, the laser emission needs to be distributed to various analysis instruments to characterize the mode-locking performance.

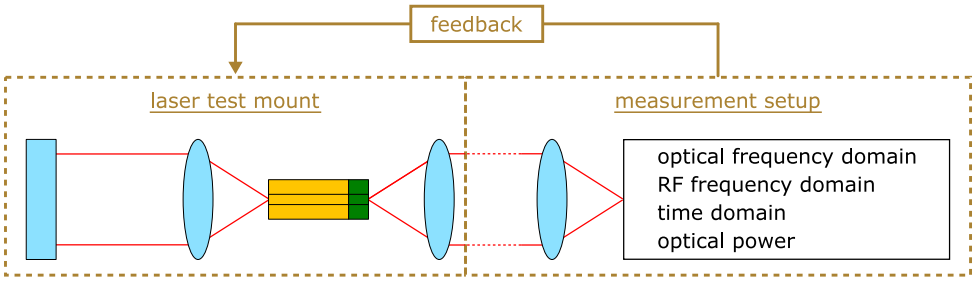

Figure 3.1.: Schematic of feedback loop for development of passively mode-locked ECDL consisting of a laser test mount and a measurement setup.

Thus, an experimental setup was realized for the implementation of the ML-ECDL and the investigation of the mode-locking behavior to facilitate advancement of the development of the ML-ECDL.

This chapter first provides an overview of the requirements on the experimental setup and experimental techniques. Then, a detailed description of the realized experimental setup is given. Finally, the experimental techniques employed will be presented.

3.2. Requirements on the experimental setup and techniques

The requirements on the experimental setup and techniques are determined by the design, and by the expected (required) mode-locking performance of the OFCG that is developed within this work.

Requirements on the experimental setup

The requirements on the experimental setup are as follows.

- The setup, in particular the test mount for the laser, is required to provide high mechanical stability due to the intended ECDL-type configuration of the laser. This requirement includes mechanical isolation of the laser test mount from the optical table to avoid mechanical shocks.
- The laser test mount has to allow for each component of the ML-ECDL to be individually exchangeable for optimizing the mode-locking performance.
- The ML-ECDL's resonator length is required to be adjustable to allow for manipulation and precise setting of the pulse repetition rate during laser operation. Taking into account the required value for the pulse repetition rate of 6.8 GHz (or its subharmonics), see Tab. 1.1, results in a requirement on the length of the laser test mount which needs to be at least about 40 mm.
- Thermal control of the diode laser is required as the mode-locking performance of the ML-ECDL strongly depends on the temperature of the diode laser chip, and thermal expansion of the setup would modify, e.g., the pulse repetition rate.
- The setup needs to provide the means for separate biasing of the two sections of the diode laser chip, the saturable absorber and the gain section.
- The experimental, electro-optical setup into which the laser test mount is integrated is required to provide the means for verification of the spectral requirements stated in Tab. 1.1.

Requirements on the experimental techniques

The experimental techniques that are employed in this work are required to allow for the investigation of the mode-locking performance of the ML-ECDL for the development of a diode laser-based OFC matching the spectral requirements stated in Tab. 1.1. In the following, the mode-locking characteristics which are to be analyzed are listed together with the associated measurements:

- the wavelength region and spectral bandwidth of the OFC by means of the optical spectrum,
- the pulse repetition rate and the SNR by means of the RF spectrum,
- the RF stability of the mode-locked pulse train by means of the RF frequency noise PSD and the RF linewidth, and
- the optical power of the comb lines of particular interest (i.e. those closest to the Rb and K D2 transitions) utilizing the (average) optical power.

While not essential for the intended future implementation of the OFC developed in this work (Sec. 1.2.2), but for the sake of getting a more complete analysis of the mode-locking performance of the ML-ECDL, the pulse width and shape as well as the pulse peak power will be investigated.

In the following, the realized experimental setup and employed experimental techniques fulfilling the requirements stated above are introduced.

3.3. Experimental setup

The experimental setup used to analyze the mode-locking performance of the ML-ECDLs can be divided into two parts, the laser test mount and the measurement setup (Fig. 3.1). Both parts will be described in the following.

3.3.1. Laser test mount

Prior to micro-integration into a laser module body, each component of the ML-ECDL (diode laser chip, collimation optics, external mirror) has to be selected carefully and tested to ensure compliance with the OFC requirements and the limits set by the MIOB (see Sec. 1.2.3). Observing the requirements presented in the previous section, a suitable laser test mount has been developed. The design, computer-aided design (CAD) models by C. Pyrlik (FBH), is based on one designed by and employed at FBH for single-section, CW-ECDLs.

A photo of the fully assembled laser test mount is shown in Fig. 3.2. It consists of a temperature controlled base plate with a heatsink and mounts for the laser components. The base plate is a 1 cm thick, nickel (Ni) plated phosphorous bronze (CuSn8) breadboard with a footprint of 15×28 cm^2 providing high mechanical stability. It features M6 threaded bore holes for the mirror mount adapter. Grooves are implemented to countersink a temperature sensor (Analog Devices AD590KF). Fitting pins allow for precision mounting of the diode laser chip mount and the lens mount. Temperature control is realized via eight TECs (Dr. Neumann TAL) that are evenly placed to minimize the temperature gradient across the base plate. A 3 cm thick Ni plated copper (Cu) block with similar footprint as the base plate is employed as heatsink. An additional water-cooled heatsink made of the same material as the main one is attached to the heatsink to ensure sufficient heat dissipation. To isolate the setup from mechanical vibrations of the optical table, the whole laser test mount is placed on damping pads (Sunnex 10710-SP-710).

The diode laser chip mount and the lens mount are made from a single block of solid phosphorous bronze (CuSn8) by means of electric discharge machining (EDM) to allow for precise alignment of the lenses relative to the diode laser chip. Fitting pins assure independent reproducibility of the placement of both, the chip and the lens mount, onto the base plate.

The gold (Au) plated diode laser chip mount, see Fig. 3.2 (bottom right), is designed to hold a diode laser chip mounted onto a c-mount by means of a flexure bearing. Per design the target height of the diode laser chip is determined by the optical axis of the micro-lenses to about 22 mm. The diode laser chip is precisely mounted to that height as follows. First, the diode laser chip on c-mount is "blindly" mounted and roughly collimated on the resonator side. Then, the beam height is determined at two distances from the diode laser chip, 4 cm and 20 cm, and the momentary chip height calculated. Lastly, the diode laser chip mount is removed from the setup, the height of the diode laser chip on the mount is adjusted, and the diode laser chip mount is repositioned into the setup. For the height adjustment, an auxiliary setup with an actuator (Newport BM17.51) featuring a resolution of 10 µm is employed.

The Ni plated lens mount requires lenses that are rotational symmetric, e.g. round lenses, see Fig. 3.2(right). To coarsely align the lenses, the lenses are mounted in threaded adapters with a resolution of 1.25 mm per turn. After alignment, the threaded lens adapters are fixed in position by means of nylon-tipped set screws. Fine adjustment of the lens alignment is realized

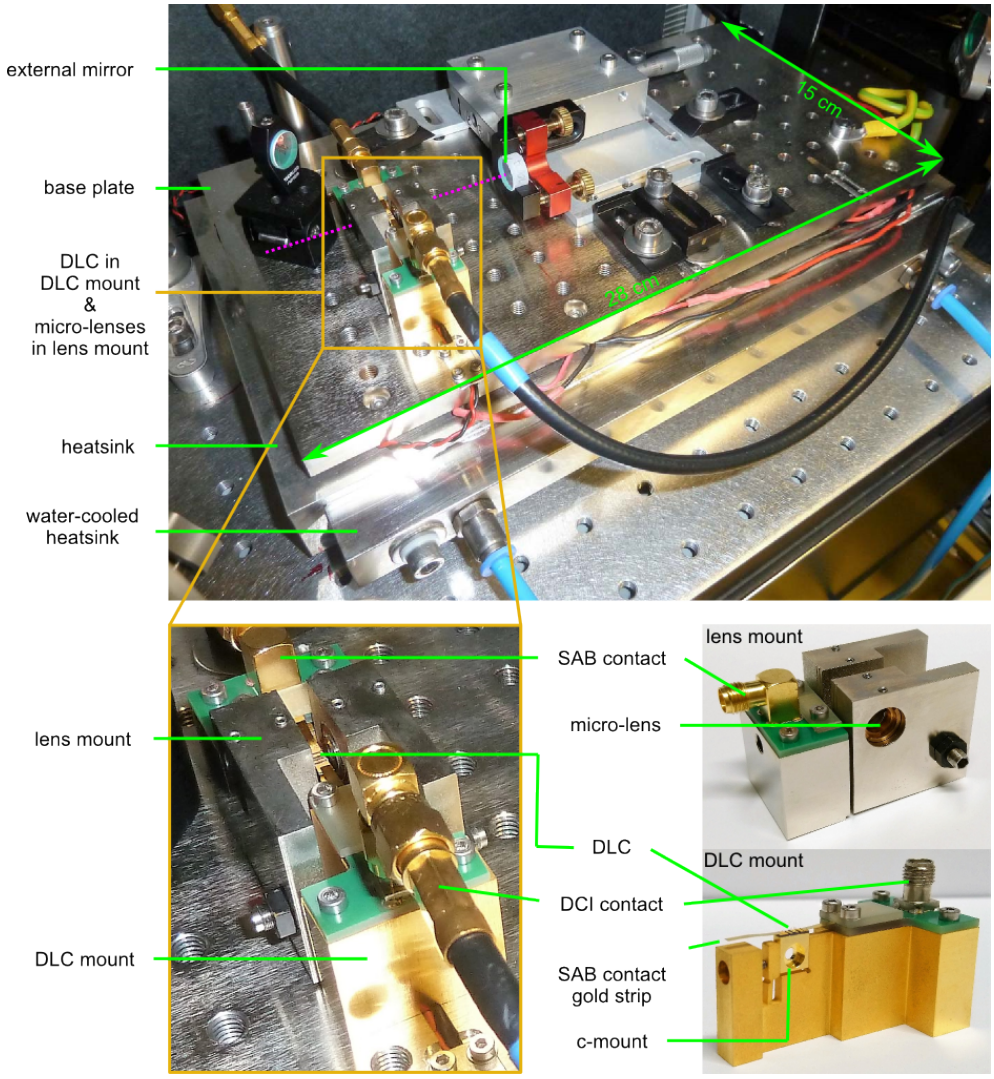

Figure 3.2.: Photo (top) of the fully assembled laser test mount consisting of a diode laser chip (DLC) mounted on the DLC mount, aspheric micro-lenses mounted in the lens mount, external mirror in adapter mount, base plate, heatsink, and a water-cooled heatsink. The dotted pink line highlights the optical axis of the ML-ECDL. The DLC and lens mount assembly is highlighted by the orange box and for better visibility shown assembled and separated in the bottom photos. The main (front) output of the ML-ECDL is on the left-hand side.

by means of flexure bearings that are implemented into the lens mount with a geometrical gear of 3:1. An estimated resolution of better than 10 µm is achieved by means of precision set screws featuring a pitch of 0.25 mm per turn and the flexure bearings of the lens mount.

For the mounting of the external mirror, a combination of commercially available and specifically designed parts is used, see Fig. 3.2(top). The external mirror is mounted into a precision, highly stable commercial mirror mount (Radiant Dyes MNI-2-3030 with 0.15 mm fine thread rise actuators). This mirror mount in turn is attached to a precision linear translation stage (Newport M-UMR5.25). This linear translation stage is mounted on a base adapter for coarse manual alignment of the mirror to the optical axis of the diode laser chip/lens ensemble. The base adapter is clamped on three points to the base breadboard for maximum stability. The fine adjustment of the resonator length is then realized by means of a micro-meter actuator (Newport BM11.25, 20 µm fine thread resolution) attached to the linear translation stage which allows for a setting resolution of the pulse repetition rate better than 1.5 MHz.

The diode laser chip itself is center-symmetrically mounted p-side up onto a 400 µm high Au plated unstructured AlN submount. This assembly is then center-symmetrically soldered onto a c-mount, see Fig. 3.2(bottom right). The c-mount is 2.3 mm wide (along the optical axis) to avoid beam clipping. For the investigation of the electro-optical performance, the c-mount is clamped into the diode laser chip mount as described above.

As the n-side of the laser diode chip features a single galvanic contact, a common n-contact for the saturable absorber and the gain section is implemented. It is in electrical contact with the whole setup. The p-side of the laser diode chips features two sections, as described in Sec. 2.3.2. Individual p-contacts for the saturable absorber and the gain section are realized via wire bonding to gold strips (Fig. 3.2(bottom right)) that are integrated into the c-mount.

The electrical interface for the gain section and the absorber section of the diode laser chip, respectively, is realized by means of two printed circuit boards (PCBs). These PCBs are mounted on the diode laser chip mount and on the lens mount, see Fig. 3.2 (bottom right, lens and DLC mount). Both PCBs feature galvanically realized contact layers on the bottom and the top and also carry a SubMiniature version A (SMA) socket. The inner contact of the SMA sockets are electrically connected to the top layers of the PCBs while the outer contacts are electrically connected to the bottom layers. Thus, the n-contact and p-contact of the diode laser chip are electrically interfaced with the inner and outer conductor of the SMA socket.

3.3.2. Measurement setup

The laser test mount described above is embedded into an opto-mechanical setup (measurement setup), see in Fig. 3.3. This setup distributes the laser emission to the appropriate measurement instruments to analyze the mode-locking performance of the ML-ECDL (red box in Fig. 3.3). It is presented in detail in this section.

The main (front) output of the ML-ECDL (red box in Fig. 3.3) is oriented towards the left-hand side. The ML-ECDL, the beam guiding part of setup part 2, and the entire setup part 3 are mounted on a honeycomb breadboard (Newport M-SG-23-2) for mechanical isolation from the optical table. To that end, the breadboard is also placed on damping pads (Sunnex 10710-SP-710). Iris apertures (IA) in appropriate positions of the measurement setup allow for

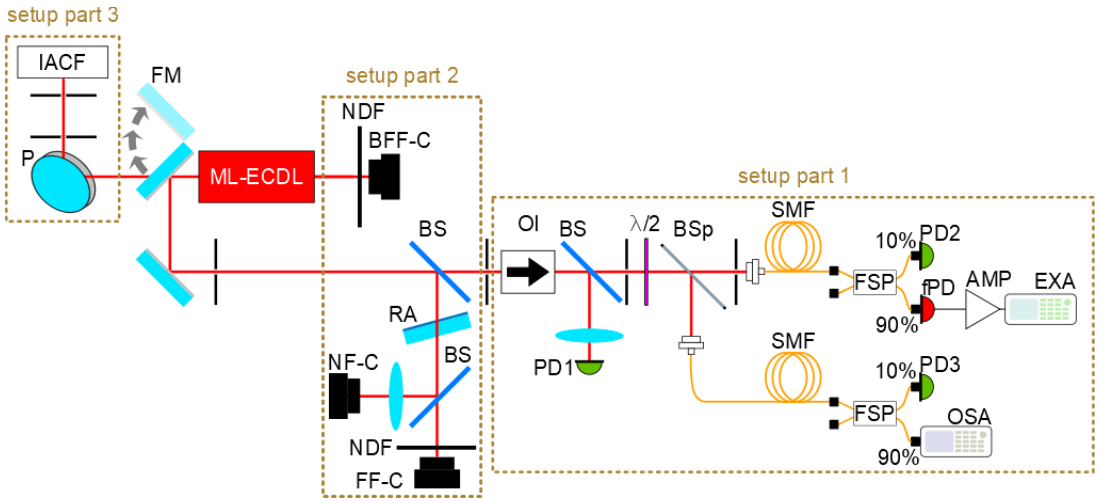

Figure 3.3.: Functional schematic of measurement setup. The red box denoted ML-ECDL represents the laser on its test mount. The golden boxes highlight the parts of the setup used for different analysis purposes. BFF-C: back-side far field camera, BS: beam sampler, BSp: beam splitter, EXA: electrical spectrum analyzer, FF-C: far field camera, FM: mirror on flip-mount, FSP: fiber splitter (10:90), fPD: fast photodetector, IACF: intensity autocorrelator, $\lambda/2$: half-wave plate, NF-C: near field camera, NDF: neutral density filter, OI: optical Faraday isolator, OSA: optical spectrum analyzer, P: periscope, PD1,2,3: photodetector 1,2,3, RA: reflective attenuator, SMF: single-mode optical fiber.

reproducible beam alignment. All mirrors employed in this measurement setup are silver (Ag)-coated metal mirrors (Layertec 1" or 1/2" fused silica substrate with coating no. 113976).

The measurement setup can be divided into three parts, indicated by the golden boxes in Fig. 3.3. In the following the three parts of the measurement setup are described.

In setup part 1 (right-hand side of Fig. 3.3), the collimated (front) output of the ML-ECDL is distributed to be analyzed in the optical frequency domain (optical spectrum analysis), in the RF domain (RF spectrum analysis), in the time domain (frequency noise analysis), and for its optical power. For that purpose, the laser light is first guided through an optical isolator (OI, Qioptic DLI-1) to avoid optical feedback into the diode laser chip. Behind the optical isolator, about 10 % of the optical power is split off by means of a beam sampler for measurement of the average optical power using a calibrated photodetector (PD1) and an oscilloscope (Agilent DSO6014A). The remaining light is split using a combination of a half-wave plate (HWP, Döhrer Elektrooptik GmbH WPA2410-650-1100) and a polarization-dependent beam splitter (BSp, Newport 20RQ00UB.2) for appropriate power division and coupled into two single-mode optical fibers (SMF). The fiber-coupled laser light in each SMF is further split using a 90:10 optical fiber splitter (FSP, FOC custom specifications) to allow for simultaneous recording of the mode-locking performance by the analysis instruments (90 %-path) and monitoring of the average optical power (10 %-path) by means of calibrated photodetectors (PD2 and PD3) and an oscilloscope (Agilent DSO6014A, same instrument as mentioned above). The signal analysis in the optical frequency domain is carried out by an optical spectrum analyzer (Yokogawa

AQ6373, minimum 3 dB-resolution bandwidth 20 pm). For signal analysis in the RF frequency domain, the optical pulse train is converted into an electrical signal using a fast photodetector (fPD, Newport 1004, bandwidth DC - 40 GHz), amplified by 30 dB by means of a broadband RF amplifier (AMP, Centellax TA0L50VA, bandwidth 100 kHz - 50 GHz), and fed to an electrical spectrum analyzer (EXA, Rohde & Schwarz FSV-30, bandwidth 10 Hz - 30 GHz). The analysis of the frequency noise characteristics of the pulse repetition rate of the ML-ECDL is conducted via a time domain-based in-phase and quadrature (IQ) measurement tool provided by the electrical spectrum analyzer.

The setup part 2 allows for examination of the near-field (NF) and the far-field (FF) beam intensity profiles as well as the (back-side) far-field (BFF) beam profile of the front and rear output of the laser, respectively. For the front output beam profiles, about 10 % of the laser light directed to setup section 1 is split off, attenuated appropriately (RA), split again with a beam sampler, and directed onto IR cameras (IDS UI-1545LE-M). For the near-field analysis, the laser light is focused onto the camera using an spherical lens (L1, Thorlabs LA1978-B, focal length 750.0 mm). The rear output of the laser is appropriately attenuated and also directed onto a similar IR camera. All cameras are employed to collimate the laser output and to monitor the beam profiles during laser operation.

In setup part 3, the temporal behavior of the laser pulses is analyzed by means of an intensity autocorrelator. As the mechanical setup of the autocorrelator requires a beam height of about 15 cm, a periscope (P) is employed. This periscope also allows to omit a half-wave plate by rotating the polarization of the laser light by 90° to p-polarization which is required by the autocorrelator (based on Newport M-LSA-MT-KT).

3.4. Experimental techniques

The experimental investigation of mode-locked laser can be divided into techniques determining the laser's characteristics in the optical frequency, the RF frequency, and the time domain, techniques combining the RF and time domains, and techniques to investigate the laser's optical power. In the following, the experimental techniques are described.

3.4.1. Optical frequency domain

Analysis of the mode-locked pulse train includes the analysis of the optical spectrum of the laser emission with regard to its center wavelength λ_c, its spectral bandwidth $\Delta\lambda_x$ at x dBc as well as the spectral shape of its spectrum, see schematic in Fig. 3.4. For this purpose an optical spectrum analyzer (OSA, Yokogawa AQ6373, bandwidth 350 nm - 1200 nm, minimum 3 dB-resolution of 20 pm ($\approx$ 10 GHz at 780 nm), see Fig. 3.3 setup part 1) is employed.

Using the relationship between the spectral bandwidth at 3 dBc of the OFC in units of wavelength ($\Delta\lambda_3$) and in units of frequency ($\Delta\nu_3$)

$$\Delta\nu_3 = \frac{c_0 \cdot \Delta\lambda_3}{\lambda_c^2}, \tag{3.1}$$

the modulation of the optical spectrum ($\lambda_c = 773.5$ nm) resulting from the mode-locking of the

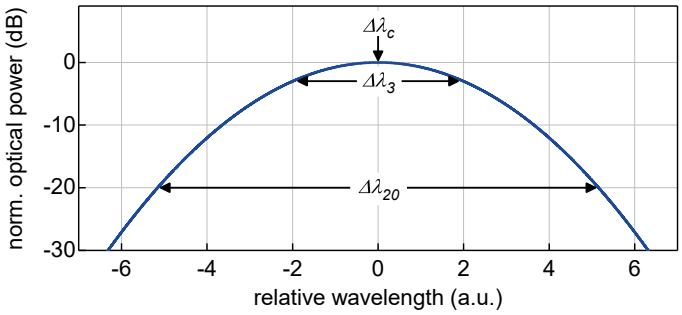

Figure 3.4.: Schematic of the envelope of a mode-locked optical spectrum with the center wavelength λ_c, the spectral bandwidth $\Delta\lambda_3$ and $\Delta\lambda_{20}$ at 3 dBc and 20 dBc, respectively.

diode laser at a pulse repetition rate of 6.8 GHz ($f_{rep} = \Delta\nu_3$) amounts to $\Delta\lambda_3 \approx 14$ pm. This cannot be resolved with the optical spectrum analyzer (OSA). In contrast, modulation arising from parasitic coupled cavities resulting from imperfect AR coating of the resonator-side facet of the diode laser chip, e.g. $L_{chip} = 2$ mm ($\Delta\nu_3 \approx 20$ GHz (Eq. 1.7) and thus $\Delta\lambda_3 \approx$ 40 pm), can be detected.

3.4.2. RF frequency domain

One way to gain information on the "low frequency" modulation of the optical spectrum, that cannot be detected by means of an OSA, is to analyze the mode-locked pulse train in the RF frequency domain by means of an electrical spectrum analyzer (see Fig. 3.3 setup part 1). The subsequent description follows Ref. [159].

The RF spectrum of a mode-locked pulse train

The temporal intensity profile of a mode-locked pulse train can be described by the sum of a noise-less, perfectly mode-locked part $I_0(t)$ and a smaller noisy part $\delta I(t)$

$$I(t) = I_0(t) + \delta I(t). \tag{3.2}$$

The PSD of this signal, conventionally referred to as the RF spectrum, can then be calculated as

$$S_I(\omega) = \frac{1}{2\pi} \int_{-\infty}^{+\infty} G_I(t) \cdot \mathrm{e}^{i\omega t}\, \mathrm{d}t, \tag{3.3}$$

where $G_I(t) = \langle I(t+\tau)I(t)\rangle$ is the intensity autocorrelation function. Assuming amplitude $A(t)$ and timing $J_t(t)$ fluctuations that vary slowly compared to the temporal intensity profile $I_p(t)$ of each pulse, the intensity of the pulse train can be expressed as

$$I(t) = I_0(t) + I_0(t)A(t) + \dot{I}_0(t)T_{rep}J_t(t), \tag{3.4}$$

where $\dot{I}_0(t)$ is the time derivative of the noise-less laser intensity. With these random fluctuations the intensity autocorrelation function of $I(t)$ factorizes and the RF spectrum of the noisy mode-locked pulse train can be written as

$$S_I(\omega) = 2\pi f_{rep} \cdot \left|\tilde{I}_p(\omega)\right|^2 \cdot \sum_{n_H} \left\{\delta(\omega_{n_H}) + S_A(\omega_{n_H}) + (2\pi n_H)^2 S_J(\omega_{n_H})\right\}, \tag{3.5}$$

with the harmonic number $-\infty < n_H < +\infty$, $\omega_{n_H} = \omega - 2\pi n_H f_{rep}$, and the Fourier transform $\tilde{I}_p(\omega)$ of the intensity profile $I_p(t)$. $S_A(\omega_{n_H})$ and $S_J(\omega_{n_H})$ are the PSDs arising from amplitude and timing noise of the pulse train. Thus, the RF spectrum corresponding to a noisy mode-locked pulse train is composed of noise-less δ-shaped RF peaks at frequencies corresponding to the pulse repetition rate and its harmonics n_H, and noise sidebands around those δ-shaped peaks that correspond to amplitude noise $S_A(\omega_{n_H})$ and phase noise (timing jitter) $(2\pi n_H)^2 S_J(\omega_{n_H})$, see schematic in Fig. 3.5.

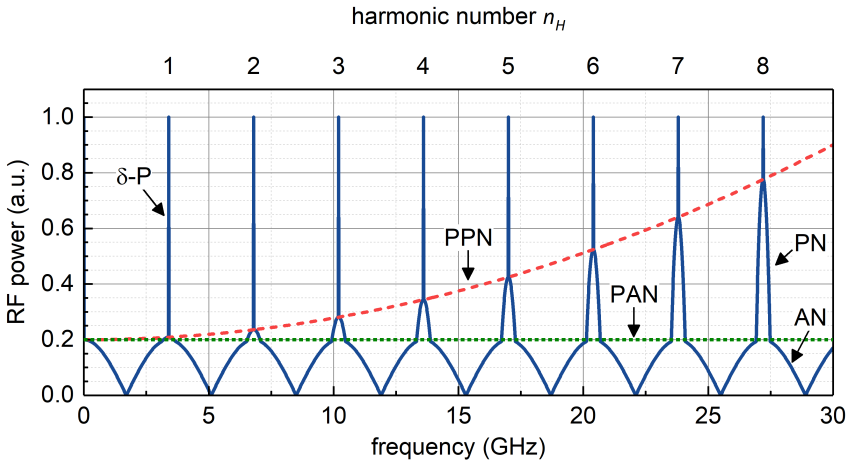

Figure 3.5.: Schematic of an RF spectrum (solid blue line) generated by a mode-locked pulse train comprising δ-functions at $n_H f_{rep}$, and sidebands at $n_H f_{rep}$ resulting from amplitude (AN) and phase (PN) noise. The peak RF power of the amplitude (dotted green line, PAN) and phase (dashed red line, PPN) noise sidebands are highlighted.

Mode-locking is typically identified in the RF spectrum by the ratio of the RF power of the coherent RF signal ($n_H = 1$) corresponding to the mode-locked pulse train and the RF power in the noise sidebands (within a given integration bandwidth). In this work, a power ratio of at least 30 dB in an RF spectrum recorded with an resolution bandwidth (RBW) of 3 MHz[1] is employed to identify mode-locking.

Another important parameter for characterizing the mode-locking performance can be extracted from the RF spectrum. Phase (timing) noise results in a Lorentzian-shaped pedestal of the δ-shaped peak of the mode-locked RF signal [160]. The FWHM of the phase noise pedestal

[1]Here, the RBW effectively acts as the integration bandwidth used for the determination of the RF power in the noise sidebands.

centered at the Fourier frequency corresponding to the pulse repetition rate ($n_H = 1$), is the so-called RF linewidth which is an additional measure of the mode-locking stability. However, frequency drifts during a single spectrum measurement due to, e.g., temperature fluctuations of the laser, limit the measurement accuracy of the center frequency and the RF linewidth. The reason for that lies with the swept RF spectrum measurement method that is employed by the electrical spectrum analyzer (Rohde & Schwarz FSV-30, 10 kHz - 30 GHz) to record the RF spectrum in a broad frequency span. This measurement method can distort the actual signal and deliver false results for the RF spectrum. This problem is described in more detail and an alternative method for the determination of the phase noise, the amplitude noise, and the RF linewidth is therefore introduced in Sec. 3.4.3.

Nevertheless, it can be seen that the ratio of the coherent RF signal corresponding to the mode-locked pulse train and the RF power in the noise sidebands at the fundamental RF signal (pulse repetition rate) as well as at the harmonics of the pulse repetition rate is an important measure of the stability of the pulse train.

The RMS integrated timing jitter

A typical characteristic derived from the phase noise of the RF signal of a mode-locked laser is the root-mean-square (RMS) integrated timing jitter of the pulses [159, 161, 162]. It is a measure of timing stability of the pulse train. The RMS integrated timing jitter is calculated as

$$j_t = \frac{1}{2\pi n_H f_{rep}} \sqrt{2 \cdot \int_{f_{min}}^{f_{max}} \mathfrak{L}(f)\,\mathrm{d}f}, \tag{3.6}$$

where $\mathfrak{L}(f)$ is defined by the IEEE Standards Coordination Committee 27 on Time and Frequency as *one half of the one-sided* [power] *spectral density of* [the] *phase* [(timing)] *fluctuations* [161]. For small mean squared phase deviations, i.e.

$$\int_{f_{min}}^{\infty} \mathfrak{L}(f) < 0.1\ \mathrm{rad}^2, \tag{3.7}$$

this definition is equivalent to the ratio of the RF power in a phase noise sideband of an RF carrier signal relative to the total RF power of that signal (here at a carrier frequency corresponding to the pulse repetition rate or its harmonics) [161]. Hence, $\mathfrak{L}(f)$ is given in units of dBc/Hz. This means that the RF spectrum (see Eq. 3.5) in the vicinity of a carrier can be utilized to derive the corresponding phase noise power spectral density (PN-PSD) of this carrier. Identification of the corresponding term in the RF spectrum given in Eq. 3.5 results in

$$\mathfrak{L}(f) = n_H^2 \cdot \frac{S_J(f + n_H f_{rep})}{2}. \tag{3.8}$$

The harmonic number n_H is implemented in Eq. 3.6 to allow for the determination of the RMS integrated timing jitter at higher harmonics of the fundamental RF signal corresponding to, e.g., the pulse repetition rate.

However, the determination of the PN-PSD from the RF spectrum is limited by the capability of the experimental setup to discern and separate phase noise and amplitude noise components of the RF spectrum. Further, the timing (frequency) jitter and frequency drift of the RF carrier signal can smear the corresponding RF spectrum and falsify the determination of the resulting RMS integrated timing jitter. Hence, a specific measurement tool is required that allows for tracking of the carrier's amplitude and frequency. One such tool is the phase noise measurement tool (Rohde & Schwarz K40) of the employed electrical spectrum analyzer (Rohde & Schwarz FSV-30). However, the speed of the tracking electronics allows for valid detection of the PN-PSD only far from the carrier signal. A way to circumvent that limitation and to allow for valid measurements close to the carrier will be presented in the next section.

3.4.3. Time domain-based investigation of RF characteristics

As described above, frequency drifts can distort the RF spectrum recorded with a swept electrical spectrum analyzer. This in turn limits the accuracy with which the RF linewidth can be determined from that RF spectrum. Determination of the PN-PSD is limited due to amplitude noise (see Fig. 3.5) in combination with the insufficient capability of a swept electrical spectrum analyzer to separate phase noise from amplitude noise. A time domain technique based on IQ demodulation of the RF signal allows to reduce frequency drift related smearing of the RF spectrum as well as to separate amplitude and phase noise [163]. This technique will be introduced in this section. The description follows Refs. [79] and [163].

Keeping in mind the spectral structure of the pulse train, the RF signal $V(t)$ recorded with the fast photodetector of setup part 1 in Fig. 3.3 can in general be written as

$$V(t) = \sum_{n_H} \left\{ V_{n_H}(t) \cdot \cos\left(2\pi n_H \bar{f}_{rep} t + \varphi_{n_H}(t)\right) \right\}, \tag{3.9}$$

with the harmonic number n_H, the corresponding voltage amplitudes $V_{n_H}(t)$ and time dependent phases $\varphi_{n_H}(t)$ as well as the averaged pulse repetition rate $\bar{f}_{rep}$ determined over the measurement period. To determine and record the time dependent IQ components, an IQ measurement tool of an electrical spectrum analyzer is employed. This tool converts the RF input signal band to an intermediate frequency (IF) band. Then the converted signal is digitized, and the in-phase (I) and quadrature (Q) components are digitally generated with a demodulation bandwidth (DBW) given by the spectrum analyzer. For the lasers developed within this work, the pulse repetition rate is significantly larger than the filter bandwidths used in the aforementioned processing steps. This allows for selection and subsequent analysis of the RF signal at a specific harmonic number by appropriate frequency setting of the RF analyzer. The resulting $\mathtt{I}$ and Q quadrature signals are given as

$$\mathtt{I}(t) \propto V_{n_H}(t) \cdot \cos\left(\Delta\tilde{\omega} t + \varphi_{n_H}(t)\right) \quad \text{and} \tag{3.10}$$

$$Q(t) \propto V_{n_H}(t) \cdot \sin\left(\Delta\tilde{\omega} t + \varphi_{n_H}(t)\right), \tag{3.11}$$

where $\Delta\tilde{\omega}$ is the difference between the average angular frequency of the selected baseband signal, i.e. $2\pi n_H \bar{f}_{rep}$, and the center frequency set for the measurement at the spectrum analyzer. A

common phase offset for both quadrature components has been neglected w.l.o.g.. Thus, the electrical spectrum analyzer allows to measure a time record.

Post processing of the IQ components provides, within the DBW, access to the instantaneous amplitude and to the instantaneous phase. Further, the RF spectrum of the input RF signal within a frequency span of ± DBW around the center frequency set for the measurement at the spectrum analyzer can be derived. The post processing of the IQ data is visualized in the schematic depicted in Fig. 3.6.

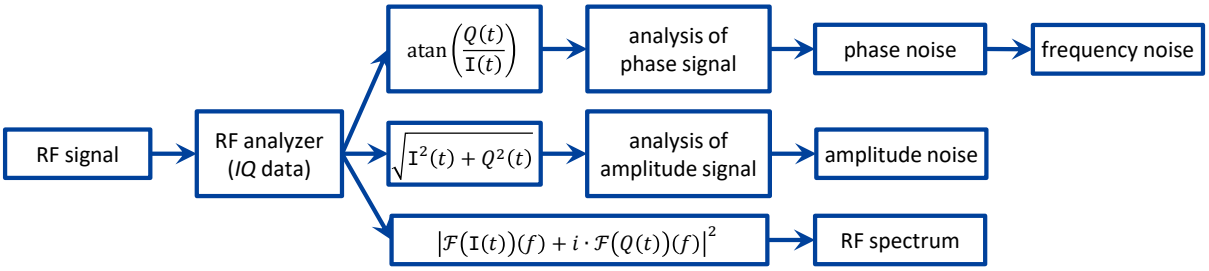

Figure 3.6.: Schematic of IQ data acquisition and analysis.

The instantaneous signal phase is given by

$$\arctan\left(Q/\mathtt{I}\right) = \Delta\tilde{\omega}t + \varphi(t). \tag{3.12}$$

After removal of the linear component $\Delta\tilde{\omega}t$ of the phase evolution the instantaneous phase noise $\varphi(t)$ can be determined. The frequency dependent one-sided PN-PSD $S_\varphi(f_k)$ [161] is estimated via (fast) Fourier transformation using the inverse sampling rate Δt and the measurement time $T_m = n_p \cdot \Delta t$:

$$S_\varphi(f_k) = \frac{T_m}{n_p^2} \cdot \left| \sum_{n=0}^{n_p-1} \varphi(n\Delta t) \cdot \mathrm{e}^{2\pi i f_k n \Delta t} \right|^2 , \tag{3.13}$$

where n_p is the number of measurement points. This measurement and determination process allows for the investigation of the PSD of the phase noise close to the carrier frequency, e.g. f_{rep}, even for Fourier frequencies at which a determination by means of the RF spectrum (see Sec. 3.4.2) would violate the requirement given in Eq. 3.7. Furthermore, this technique to determine the PN-PSD enables separation of effects resulting from timing and amplitude fluctuations. Hence, in order to quantify timing fluctuations by means of the RMS integrated timing jitter j_t, Eq. 3.6 and $\mathfrak{L}(f) \equiv \frac{1}{2} \cdot S_\varphi(f)$ are employed.

In the following, three methods will be introduced that allow for determination of the FWHM RF linewidth of the pulse repetition rate f_{rep} from recorded IQ data.

The power spectral density of the frequency fluctuations of the pulse repetition rate (FN-PSD) is related to the phase noise PN-PSD through $S_\nu(f) = f^2 \cdot S_\varphi(f)$ with $\nu = {}^1\!/_{2\pi} \cdot {}^{d\phi}\!/_{dt}$ [159]. Please note that the quantity $S_\nu(f)$ will be referred to as FN-PSD of the pulse repetion rate in the following. It is known that the FN-PSD of random phase noise is white and the typical lineshape of the corresponding RF spectrum is an RF signal with a Lorentzian spectrum [164]. A schematic of a typical measurement of an FN-PSD corresponding to a Lorentzian RF signal

is depicted in Fig. 3.7(a).

The RF linewidth Δf_{rep} of the fundamental frequency component (around f_{rep}) of an RF spectrum generated by a mode-locked laser can be investigated as follows. First, the FN-PSD $S_\nu(f)$ is determined. Then, the FWHM RF linewidth Δf_{rep}^L can be estimated from the white noise floor S_{f0} of $S_{\Delta f_{rep}}(f)$ using [164]

$$\Delta f_{rep}^L = \pi \cdot S_{f0}. \tag{3.14}$$

However, the detection of S_{f0} is limited by the instrument's detection noise floor, as indicated in Fig. 3.7(a).

Another approach to determine the RF linewidth is to employ the IQ quadrature components to reconstruct the RF power spectrum using

$$P_F(f) = S_{IQ}^{RF}(f) = \left|\mathfrak{F}(\mathtt{I}(t))(f) + i \cdot \mathfrak{F}(Q(t))(f)\right|^2, \tag{3.15}$$

where $\mathfrak{F}(\mathtt{I}(t))(f)$ and $\mathfrak{F}(Q(t))(f)$ are the Fourier transformed quadrature components that are shifted by the difference between the original RF frequency $\tilde{f}$ and the frequency the electrical spectrum analyzer was set to. Due to the splitting of the recorded IQ data into interleaving intervals [163], the recorded center (peak) frequency of each interval can be determined and used for shifting each spectrum accordingly prior to averaging. A Lorentzian fit of the averaged RF spectrum then reveals the resulting FWHM RF linewidth Δf_{rep}^L. This procedure also allows for the determination of the drift of the center frequency during the measurement time. A schematic of a reconstructed RF spectrum is shown in Fig. 3.7(b).

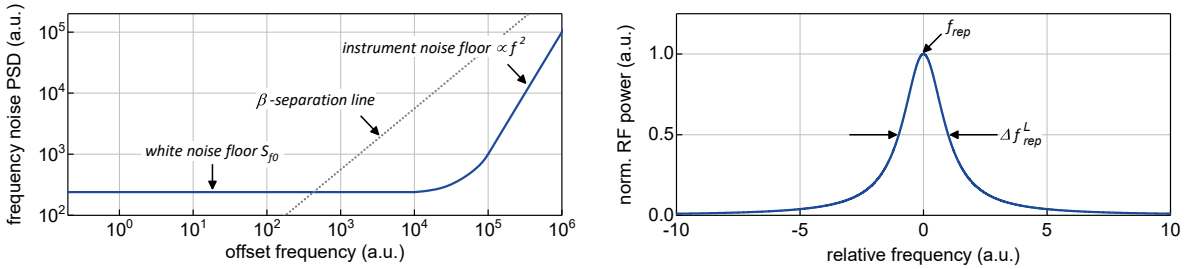

(a) (b)

Figure 3.7.: Schematic of (a) an FN-PSD and (b) a reconstructed RF spectrum.

DiDomenico *et al.* [164] have shown another way to estimate the RF linewidth by further analyzing the FN-PSD. They have shown that the FN-PSD can be divided into two sections: a low-offset frequency region which directly contributes to the RF linewidth and a large-offset frequency region above a certain cut-off frequency which contributes only to the wings of the RF line. The cut-off frequency f_{cut} that separates the two regimes is determined by the point (frequency) of intersection of the so-called β-separation line

$$L_\beta = \frac{8 \ln 2}{\pi^2} \cdot f \tag{3.16}$$

and the FN-PSD, see Fig. 3.7(a). The FWHM RF linewidth is then estimated by

$$\Delta f_{rep}^{L} \approx \Delta f_{rep}^{\beta} = \sqrt{8 \ln 2 \cdot \sum_{\Delta f}^{f_{cut}} (S_f(f) \cdot \Delta f)}. \tag{3.17}$$

This method can be employed when the FN-PSD does not feature noise peaks. If, however, the FN-PSD features noise peaks such as at the power line hum frequency, then the aforementioned IQ data based methods for the determination of the RF linewidth[2] are better suited so as to not overestimate the FWHM RF linewidth.

3.4.4. Time domain

In this section, the intensity autocorrelation measurement technique will be introduced. This technique is well-established to determine the shape and width of mode-locked pulses in the picosecond range and below. In the following, the employed intensity autocorrelator (based on Newport M-LSA-MT-KT) is described. It is integrated into the measurement setup of the ML-ECDL as measurement setup part 3, see Fig. 3.3.

An intensity autocorrelator is based on a Michelson interferometer, see Fig. 3.8. The incoming pulse is split into two copies of equal intensity using an ultrashort pulse beam splitter plate (Newport 20RQ00UB.2).

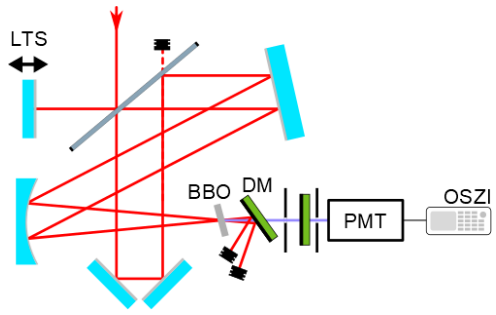

Figure 3.8.: Schematic of an experimental setup for measurement of the intensity autocorrelation function. Iris apertures and beam dumps are inserted into the setup to avoid increased background scattered light to be detected. BBO: beta-bariumborate crystal (nonlinear crystal), DM: dichroic mirror, LTS: mirror on a linear translation stage, OSZI: oscilloscope, PMT: photomultiplier tube.

The reflected pulse copy is sent into the interferometer arm with variable arm length to impose an adjustable relative delay τ. The actuator (Newport Corp. CMA-25CCCL) employed for this allows for minimum steps of 0.2 µm (corresponding to a step in τ of about 1 fs) with a bi-directional repeatability of better than 15 µm. With a maximum travel of 25 mm, a maximum delay of about 170 ps is possible [165].

[2]This means, on the one hand, determination from the white noise floor of the FN-PSD (Eq. 3.14), and, on the other hand, from a Lorentzian fit of the reconstructed RF spectrum (Eq. 3.15).

The transmitted copy is vertically (horizontally in the sketch in Fig. 3.8 for better visualization) translated and back-reflected to realize a non-collinear background-free autocorrelator.

Both copies are then directed to a concave mirror (CM) with an effective focal length (EFL) of 25 cm to be recombined in a nonlinear crystal (beta barium borate (BBO)) for sum frequency generation (SFG). The intensity of the generated light (autocorrelation function (ACF)) I_{AF} is given by the convolution of the identical intensity profiles of the pulse copies [166]. Conventionally, the intensity autocorrelation function is normalized to its maximum intensity and, thus, given as [166]:

$$I_{AF}(\tau) = \frac{\int_{-\infty}^{\infty} I(t) \cdot I(t-\tau)\,\mathrm{d}t}{\int_{-\infty}^{\infty} (I(t))^2\,\mathrm{d}t}. \tag{3.18}$$

Essentially, the incoming pulse scans a copy of itself to give information about its temporal shape and width. However, the intensity autocorrelation is not unambiguous for any given pulse shape due to its symmetrical nature. Hence, a possible pulse shape is estimated via fit of the autocorrelation of a plausible temporal pulse form function to I_{AF}. This way, a correlation between the recorded and the assumed autocorrelation functions is determined that allows for inference of the pulse shape and width. Hence, the pulse width t_p (FWHM) can be estimated from the width of the intensity autocorrelation function τ_p using

$$t_p = k_p \cdot \tau_p\,, \tag{3.19}$$

where k_p is a constant depending on the pulse shape [167]. In Tab. 3.1 the constant k_p is listed for typical pulse shapes.

Table 3.1.: Constant k for typical pulse shape.

function of pulse shape	k_p
Gaussian	$1/\sqrt{2}$
squared hyperbolic secant (sech^2)	≈ 0.6481
Lorentzian	0.5

In the experiment described in this work, the typical average optical power of the mode-locked pulses is below 100 mW, whereas typical peak optical powers are more than 1 W[3]. With a beam diameter of about 1 mm, average intensities of the mode-locked pulses at the entrance of the autocorrelator as low as a few tens of $\mathrm{mW/mm^2}$ result in a SFG signal with an average optical power of only a few picowatt. The intensity of the SFG signal is further limited by the effective interaction length of both pulse copies inside the nonlinear crystal (about 200 µm) and the walk-off angle between the fundamental signal and the SFG signal (around 9 mrad). To still get useful information about the pulses' shape and width, a photomultiplier tube (PMT) is employed for detection of the SFG signal.

[3]The broadest optical spectra are recorded for pulses featuring an average optical power of about 26 mW and a peak optical power of around 1.3 W.

The use of a PMT puts further requirements on the experimental apparatus due to its detection sensitivity and the amount of background noise from scattered light. To filter residual fundamental light that is transmitted through the nonlinear crystal both, two iris apertures and two dichroic mirrors, are employed, see Fig. 3.8. The first dichroic mirror after the nonlinear crystal is inserted at an angle to direct the fundamental light into a beam dump. To reduce background light even further, a ten centimeter long lens tube is attached to the PMT. The second dichroic mirror is mounted in the lens tube. After that second dichroic mirror, an almost closed iris aperture is inserted into the lens tube to enhance backlight reduction by further spatial filtering the SFG signal. For further isolation of the experimental apparatus, the complete autocorrelator setup is housed with only a narrow entrance aperture.

3.4.5. Optical power

An important parameter of mode-locked pulses is their optical power. In this work, the average optical power P_{avg} is directly measured using a calibrated photodetector in conjunction with an oscilloscope, see Sec. 3.3.2. By means of reflective neutral density filter, the incident optical power is adjusted to the power acceptance range of the photodetector.

However, the optical power P_i of the comb lines of interest (at 20 dBc) and the optical peak power P_p typically cannot be measured directly. As discussed before (Sec. 1.2.4), P_i can be determined using the average optical power, the pulse repetition rate, and the shape of the optical spectrum. The optical peak power of the pulses, which have a duration of a few picoseconds, cannot be measured directly due to the relatively slow response time of the photodetectors. It can, instead, be inferred from the average optical power, the pulse repetition rate, and the pulse width and shape as will be discussed in the following.

The average (optical) power of a pulse interval of duration T_{rep} is given as

$$P_{avg} = \frac{1}{T_{rep}} \int_0^{T_{rep}} P(t)\,\mathrm{d}t = f_{rep} \cdot E_p, \tag{3.20}$$

where $P(t)$ is the optical power of the pulse train, and E_p is the optical energy contained in one pulse interval. Taking into account the temporal pulse shape, the optical power of a single pulse can be written as

$$P_{pulse}(t) = \frac{p(t) \cdot E_p}{\int_{-\infty}^{\infty} p(t)\,\mathrm{d}t}, \tag{3.21}$$

where $p(t)$ is the function describing the temporal pulse shape that follows

$$\lim_{|t|\to\infty} p(t) = 0. \tag{3.22}$$

The corresponding peak optical power is calculated using

$$P_p = \frac{p_{max} \cdot E_p}{\int_{-\infty}^{\infty} p(t)\,\mathrm{d}t} = p_s \cdot \frac{E_p}{t_p} = p_s \cdot \frac{P_{avg}}{t_p f_{rep}} \tag{3.23}$$

where $p_{max} = \max(p(t))$ and

$$p_s = \frac{p_{max} \cdot t_p}{\int_{-\infty}^{\infty} p(t)\,\mathrm{d}t} \tag{3.24}$$

is a form factor depending on the shape of the pulses. For typical pulse shapes the pulse-shape dependent form factors p_s are collected in Tab. 3.2.

Table 3.2.: Pulse shape dependent form factor p_s for typical pulse shapes. The first two significant digits are shown.

pulse shape	p_s
Gaussian	0.94
sech^2	0.88
Lorentzian	0.66

Unless stated otherwise, the average optical power is measured using a calibrated photodetector and an oscilloscope (Agilent DSO6014A). For calibration a powermeter (Newport Corp. console 1918-C or 1918-R, photodetector 918D-SL-OD3) is used.

3.4.6. Measurement procedure and control

For the investigation of the mode-locking performance, a measurement procedure was developed. To efficiently analyze the mode-locking performance, which depends on the laser parameters and the bias parameters of the employed diode laser chip, an automated measurement control software was developed. Both, the measurement procedure and the measurement control, will be described in the following.

Measurement procedure

The measurement procedure includes on the one hand the configuration of the diode laser for large spectral bandwidth (at 20 dBc) mode-locked operation and on the other hand the measurement process itself.

The configuration of the diode laser was conducted as follows.

The diode laser chip is mounted into the laser test mount, see Fig. 3.2. The temperature T_{mount} of the laser test mount is set to 20.0 °C. Both the saturable absorber and the gain section are first connected in parallel to allow for investigation of the ASE and CW operation characteristics of the diode laser chip and the ECDL, respectively. The output emission of the diode laser chip is then collimated and aligned to the measurement setup. To investigate the

ASE performance, the intra-cavity lens is removed and the divergent emission of the diode laser chip blocked to avoid unwanted optical feedback. Then, prior to recording the ASE performance, a burn-in of the diode laser chip with a duration of about 3 h at an injection current of 100 mA is conducted. For investigation of the ASE regime, the voltage drop across the diode laser chip, the (average) optical power, and the optical spectrum are recorded and analyzed for a constant mount temperature T_{mount} and varying injection currents. An upper injection current limit of 250 mA[4] is set to avoid damage to the diode laser chip.

After analysis of the ASE operation regime, the ECDL is assembled. To that end, the intra-cavity output of the diode laser chip is collimated. The resonator length is set to a value that roughly corresponds to the intended pulse repetition rate. Then, the ECDL is aligned using the external mirror to minimum CW threshold current. Here, too, both sections of the diode laser chip are operated in parallel. The ECDL then undergoes another burn-in lasting about 3 h at 100 mA. Afterwards, the CW performance is recorded in terms of the same characteristics as the ASE performance of the diode laser chip described above.

Starting from the configuration for CW operation, the ECDL is prepared for mode-locked operation. To that end, the electrical interface for both sections is separated to allow for the operation of the saturable absorber section in reverse bias configuration. Thus, the values of the operating parameters (mount temperature T_{mount}, the saturable absorber reverse voltage U_{SAB}, and the gain section injection current I_{DCI}), and the feedback angle of the external mirror are used as actuators to align the ECDL for mode-locked operation. To maximize the spectral bandwidth, the following process is carried out iteratively while the optical and the RF spectrum are monitored. For each step, the respective other actuators are kept constant.

1. The saturable absorber reverse voltage and the gain section injection current are adjusted.
2. The mount temperature is adjusted.
3. The saturable absorber reverse voltage and the gain section injection current are adjusted.
4. The feedback angle is optimized.

These steps are repeated until no further broadening of the optical spectrum can be detected. Afterwards, the resonator length is precisely adjusted to the value corresponding to the intended pulse repetition rate while monitoring the RF spectrum and the optical spectrum. If changes in the optical spectrum are observed, the above mentioned adjustment steps 1 to 4 are repeated.

Following this optimization process, the ML-ECDL undergoes a 24 h burn-in. Afterwards, the optimization process is repeated as the burn-in typically slightly modifies the optimal values of the operating parameters.

Now, the mode-locked performance is analyzed by means of the techniques described in Sec. 3.4. In order to prioritize the associated measurements, the intended use of the mode-locked ECDL needs to be taken into account.

Implementation of the ML-ECDL in future QUANTUS experiments (Sec. 1.2.2) requires, on the one hand, stabilization of the pulse repetition rate and, on the other hand, stabilization of the

[4]This current limit is convention for the diode laser chips employed in the CW-ECDLs discussed before, see Sec. 1.2.3, and reasonable for implementation in the ML-ECDLs.

OFC to an atomic (Rb) reference. Thus, an actuator is required to establish the feedback loop of the stabilization process. As the ECDL is to be realized with no moving parts (Sec. 1.2.3), the feedback angle cannot be employed as actuator. The mount temperature can be used to suppress slow frequency drifts. The saturable absorber reverse voltage and the gain section injection current offer fast actuators to compensate for fast frequency jitter and frequency drifts, see, e.g., Sec. 2.3.3.

In this work, stabilization of the pulse repetition rate will be investigated in detail. To that end, the pulse repetition rate will be stabilized by means of the gain section injection current as actuator. Consequently, the tuning characteristics of the mode-locked performance of the ML-ECDL with the gain section injection current are analyzed in detail.

Measurement control

For the investigation of the electro-optical characteristics of the ML-ECDL a LabVIEW program was developed, that remotely controls

- the gain section injection current I_{DCI} via a laser controller driver (ILX LDC-3724C),
- the mount temperature T_{mount} via a temperature control unit of the laser controller (ILX LDC-3724C), and
- the measurement and analysis instruments employed (setup part 1 in Fig. 3.3).

The saturable absorber reverse voltage U_{SAB} is manually set with a single channel voltage source (Agilent E3611A). Therefore, while a sweep of the saturable absorber bias is possible with the EO-program, the program prompts for each voltage step to be manually set by the operator. Thus, all three bias parameters of the diode laser chip can be swept with the EO-program. For each step of a sweep, an appropriate time for achieving thermal equilibrium, approximately 1.5 min, is implemented to allow the setup to settle.

A second LabVIEW program (based on the program delivered with Newport M-LSA-MT-KT) remotely controls the intensity autocorrelator as well as an oscilloscope (Agilent DSO6014A) and records the autocorrelation function (setup part 3 in Fig. 3.3). This program allows for sweeps of the gain section injection current for mapping of the pulse width and shape. The values of the other operating parameters of the diode laser are kept constant during the sweep.

The RF noise characteristics are manually recorded using the electrical spectrum analyzer employed (setup part 1 in Fig. 3.3) to investigate the RF spectrum. For a first analysis step of the IQ data, a LabVIEW program for determination of the noise PSD and the frequency drift characteristics is employed [79].

For the evaluation of the mode-locking performance, an OriginC program (for software OriginLab Origin) was developed that automatizes the analysis process for each measurement described above.

3.5. Performance analysis

The analysis of the mode-locking performance of the diode lasers developed in this thesis includes the analysis of various performance characteristics:

- The optical power of the comb lines closest to the relative power level of 20 dBc can be determined from the optical spectrum, from the pulse repetition rate, and from the average optical power, see Sec. 3.4.1.
- The mode-locking order (fundamental or higher harmonic), and the modulation depth (SNR) of the RF spectrum at the pulse repetition rate and its harmonics can be determined from the RF spectrum, see Sec. 3.4.2.
- The RF noise characteristics, such as the frequency noise PSD and the RMS integrated timing jitter, can be determined from the IQ data, see Sec. 3.4.3.
- The peak optical power of the pulses can be determined from the average optical power, from the pulse shape and width, and from the RF characteristics (the pulse repetition rate), see Sec. 3.4.5.
- The frequency chirp of the mode-locked pulses can be inferred from the so-called time-bandwidth-product (TBP) $\Delta\nu \cdot t_p$ [122]. The minimum TBP for bandwidth-limited pulses equals the Fourier-limit, see Tab. 3.3. The stronger the pulses are chirped, the larger the TBP becomes, showing that the optical frequencies contained within the pulse are spread out in time.

Table 3.3.: Fourier-limited TBP for typical pulse shapes. The first three significant digits are shown.

pulse shape	Fourier-limited TBP
Gaussian	0.441
sech^2	0.315
Lorentzian	0.142

3.6. Summary

In this chapter the experimental setup consisting of the laser test mount and the beam distribution and analysis setup was presented. The laser test mount was specifically developed with respect to realizing a mechanically highly stable test bed for a multi-section ML-ECDL. Further, the beam distribution and analysis setup was designed and realized to analyze the mode-locking performance of the diode laser developed in this work.

The experimental techniques employed allow for detailed analysis and evaluation of the optical and RF frequency domain, the time domain, and optical power characteristics of the ML-ECDLs. This not only allows for the verification of the requirements on the OFCG to be developed within thesis (see Sec. 1.2.4), but also enables the corresponding development process.

The investigation of the influence of values of the laser operating parameters of the ML-ECDL developed within this work on the mode-locking performance of that ML-ECDL will be presented in the subsequent chapter.

4. Development of a diode laser-based optical frequency comb

The results presented in this chapter were already partially published in Refs. [100, 168–170].

4.1. Introduction to the evaluation

The main purpose of this thesis is to develop an OFC based on a passively mode-locked ECDL which fulfills the requirements stated in Sec. 1.2.4. In order to realize a diode laser-based OFCG comprising as few components as possible, the focus of this work lies on generating such an OFC with a large spectral bandwidth essentially based on the characteristics of the diode laser chip itself. Hence, any spectral shaping outside the diode laser chip shall be avoided. To that end, the evaluation of possible ML-ECDL components and parameters was conducted as follows.

The micro-lenses and the external mirror are evaluated and selected with focus on a minimum influence on the mode-locking performance. The diode laser chips are evaluated by means of their performance within an ML-ECDL according to the following criteria:

1. Primarily, the diode laser chips are evaluated by the achievable spectral bandwidth at 20 dBc. As such the mode-locking performance of the diode laser chips is investigated with the main focus on that characteristic.

2. For the metrology application, the pulse repetition rate and its RF stability are of high importance. Therefore, the second evaluation criterion for the diode laser chips' suitability is the RF stability.

3. The average output power of the ML-ECDL determines whether the laser provides sufficient optical power at the 20 dBc level.

4. The pulse shape and width determined by means of the autocorrelation function are used to verify single pulse fundamental mode-locked operation.

5. The pulse peak power is calculated by means of the characteristics determined before for comparison purpose.

In the following, the influence of the ML-ECDL components and design parameters on the mode-locked operation characteristics will be presented. Subsequently, the influence of the ML-ECDL's operating parameters will be discussed. In the end, the findings on component design and selection as well as on the choice of the values of the operating parameters are summarized and conclusions are drawn.

4.2. Influence of the laser design parameters on the mode-locking performance

To develop the ML-ECDL, the following steps were performed.

First, an optical design for the ML-ECDL was developed.

Second, the requirements on the external mirror are identified and compared to what is commercially available.

Third, the influence of the resonator length on the mode-locking characteristics is studied to find the configuration that allows for mode-locked operation with a large spectral bandwidth.

Fourth, the characteristics of the diode laser chip are investigated. This includes investigations of the influence of the design of the quantum wells, of the length of the diode laser chip and its sections, and of the facet coatings. For comparison of the characteristics, each ML-ECDL was operated with those values of operating parameters that allow for the largest spectral bandwidth.

In the end, the laser parameters found to be best suited to provide an OFC with a large spectral bandwidth are summarized.

Please note that not all comparison experiments were performed with diode laser chips from that wafer of which the epitaxial structure was identified to provide the largest spectral bandwidth. This is due to the fact that general tendencies of mode-locking characteristics had to be investigated prior to the identification of this epitaxial structure. However, wherever possible the investigations were performed with diode laser chips taken from a single wafer.

4.2.1. Optical design

In the lateral direction, the optical mode inside all diode laser chips used within this work is defined by a 4 µm wide ridge waveguide. In the vertical direction, the same 4.8 µm AlGaAs-based ASLOC-concept (Fig. 2.2) with the p- and n-side waveguide doped with carbon and silicon, respectively, is implemented for all diode laser chips used within this work. This design results in a sufficiently round beam profile emitted by the diode laser with a vertical and a horizontal divergence angle of about 19° and 12° (full width at $1/e^2$ intensity), respectively [171]. Thus, collimation or focusing can be achieved with a single aspheric lens reducing the laser complexity. In this work, single aspheric micro-lenses with an effective focal length of 2.0 mm (Thorlabs 350150) are employed inside the extended cavity and at the laser output to achieve a collimated beam.

An optical simulation tool (FBH WinABCD) using an ABCD matrix formalism allows for visualization of the intra- and extra-cavity beam profile, see Fig. 4.1. Here, a schematic of an ML-ECDL featuring the above described diode laser chip and a 37 mm long extended cavity is shown. The collimated ($1/e^2$, intensity) beam diameter w_0 corresponds to about 660 µm in the vertical direction and 420 µm in the horizontal direction. The corresponding Rayleigh range z_R measures about 440 mm and 180 mm, respectively.

As will be discussed later (Chap. 5), the implemented micro-lenses are also employed for micro-integration of the ML-ECDL into the micro-integration technology platform.

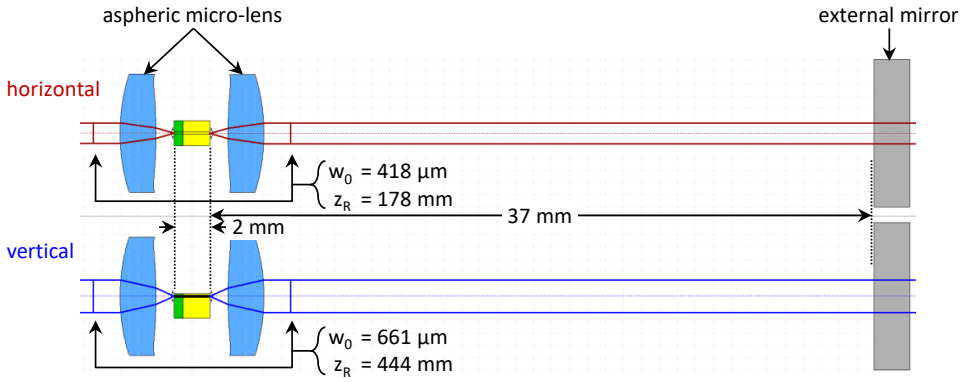

Figure 4.1.: Schematic of the optical design of the ML-ECDL with a 2 mm long diode laser chip and a resonator length of about 44 mm. w_0 - beam diameter ($1/e^2$, intensity), z_R - Rayleigh range.

4.2.2. External mirror

The spectral and size requirements on the external mirror were discussed in Sec. 1.2.4. Here, the consequences of these requirements for the choice of the mirror are described and the chosen mirror is presented.

Mirrors with the same coating properties but with different sizes are required for the laser test mount and for the micro-integration technology platform. One approach to handle this issue is the use of custom-substrates and custom-coatings. However, the associated costs (several thousand euros) render this approach unfavorable. Hence, a spectrally suitable commercial (off-the-shelf) mirror shall be selected that can be readily used in the laser test setup, and that can also be grinded to the dimensions required by the micro-integration technology platform. While metallic coatings can provide excellent surface and spectral characteristics, those mirrors are not easily mechanically machined as the coating might peel off of the substrate. Therefore, a mirror with a dielectric coating is preferable.

A commercial plane dielectric mirror (Layertec 101085) featuring near-zero group velocity dispersion fulfilling the above-mentioned requirements has been chosen for use in this work, see Tab. 4.1. The mirror coating is realized for employment in a wavelength range from 750-850 nm. The GVD slightly decreases with increasing wavelength across the spectral range of interest but is kept well within ± 20 fs^2 around zero-GVD. A reflectivity of 97 % allows for investigation of the beam profile within the extended cavity while still providing high optical feedback into the diode laser chip. A rear facet reflectivity of less than 0.2 % and a slight wedge of 5′ allow for avoiding parasitic feedback into the diode laser chip. The mirror substrate measures about 1/2" in diameter and is about 6.35 mm thick. It features a high surface quality (flatness of $\lambda/10$, scratch-dig 10-5).

Mirrors of the same type will be used throughout this thesis to allow for comparability for comparison reason. For later micro-integration, mirrors of the same type were grinded to the required size.

Table 4.1.: Surface and coating characteristics of external mirror (Layertec 101085).

quantity		value
surface and dimensional parameters		
surface	shape	plane
	flatness	$\lambda/10$
	quality (scratch-dig)	10-5
	area diameter	12.7 mm
substrate thickness		6.35 mm
wedge		$5'$
coating parameters		
wavelength range		750 - 850 nm
front facet	reflectivity	97 %
	GVD	< 20 fs^2
rear facet	reflectivity	< 0.2 % (AR)
angle of incidence		0 °

4.2.3. Laser resonator length

In this work, an ML-ECDL featuring a pulse repetition rate of 6.8 GHz or its n_H-th subharmonic is developed that is intended to be implemented in future QUANTUS experiments (Secs. 1.2.2 and 1.2.4). This pulse repetition rate corresponds to a resonator length L_{res} of about $N\cdot$ 22 mm. It is known that the resonator length strongly influences the RF stability of an ML-ECDL [160]. Therefore, the influence of the laser resonator length on the mode-locking performance is investigated in this section. To that end, the external mirror position is linearly translated, partially via the linear translation stage and partially by manually moving the whole translation stage with the help of position markers along the adapter mount of the translation stage, see Fig. 3.2. The resonator length was adjusted in mode-locked operation with those values of the operating parameters that allow for the largest spectral bandwidth. No major re-alignment of the mirror was necessary. Please note that for the investigation presented here, an sDQW(780) diode laser chip (see subsequent section) was employed.

Three resonator lengths L_{res} were investigated: 25 mm, 100 mm, and 150 mm. These L_{res} correspond to pulse repetition rates f_{rep} of 6.0 GHz, 1.5 GHz, and 1.0 GHz, respectively. While the average optical power and the pulse width remain nearly constant at about 25 mW and 5 ps, respectively, a strong influence of the resonator length on the optical spectrum and on the FN-PSD at the pulse repetition rate can be detected. For those values of operating parameters (mount temperature T_{mount}, saturable absorber reverse voltage U_{SAB}, gain section injection current I_{DCI}) that allow for the largest spectral bandwidth, see Tab. 4.2, the optical spectra and corresponding FN-PSDs are depicted in Fig. 4.2. For better comparison of the spectra derived for different resonator lengths, the spectra are normalized to their respective peak power P_{λ_p} and shifted in wavelength by the wavelength λ_0 at which 20 dBc is reached at the long-wavelength wing (red wing), see Tab. 4.2.

Table 4.2.: Operating parameters and normalization parameter for data shown in Fig. 4.2. L_{res} - resonator length, f_{rep} - pulse repetition rate, T_{mount} - mount temperature, U_{SAB} - saturable absorber reverse voltage, I_{DCI} - gain section injection current, λ_0 - wavelength at 20 dBc at long-wavelength wing of optical spectrum, P_{λ_p} - peak power of optical spectrum.

parameter	L_{res}	f_{rep}	T_{mount}	U_{SAB}	I_{DCI}	λ_0	P_{λ_p}
unit	mm	GHz	°C	V	mA	nm	dBm
	25	6.0	20.0	−2.7	200.0	787.76	−32.19
	100	1.5	20.0	−5.0	160.0	787.94	−22.52
	150	1.0	20.0	−5.0	180.0	790.15	−26.22

In the optical spectrum, the effects of increasing the length of the optical resonator are manifold. It can be seen that increasing the resonator length leads to a strong broadening of the optical spectrum, from about 4.2 nm to 7.5 nm at 20 dBc. In conjunction, the longer wavelength wing of the spectrum steepens and the shorter wavelength part of the spectrum develops a sharply rising wing with a slowly rising shoulder. Additionally, the peak wavelength shifts to longer wavelengths, relatively and absolutely, see Fig. 4.2(a) and Tab. 4.2. As the average optical power and the pulse width remain nearly constant, the reason for this behavior can be found with the increasing pulse peak power (energy), see Sec. 3.4.5. Increasing optical peak power results in an increasingly strong SPM effect [154]. Hereby, the occurring gain saturation leads to non-linearities of the refractive index which shift the optical spectrum to longer wavelengths and increase the spectral bandwidth. Moreover, strong gain saturation also results in an increasing up-chirp of the pulse where the leading part of the pulse (in time) sharpens and subsequent parts of the pulse experience less gain at the wavelength of the leading part. SPM, hence, causes a wavelength shift of the later part of the pulse resulting in an increasing gain for that part of the pulse. The red-shift, which is typical for semiconductor lasers [154], can be inferred from the λ_0 as given in Tab. 4.2 and the red-shift of the peak wavelength of the optical spectra, see Fig. 4.2(a). Thus, SPM may not only cause the shift of the peak wavelength but also a stronger spectral broadening with increasing optical power of the pulses. Please note that this effect can (at least partially) also be caused by the modified values of operating parameters (Tab. 4.2) required to achieve the broadest spectral bandwidth. High optical peak powers, however, can also lead to instable mode-locking which can be counteracted by adjusting the reverse voltage at the saturable absorber section and gain section current, as was done here, see Tab. 4.2.

The effect of increasing the resonator length on the RF stability can be determined by investigating the FN-PSD of the frequency fluctuations of the pulse repetition rate, see Fig. 4.2(b). The FN-PSD spectra are determined from a 100 s long time trace recorded with a sampling rate of 160 kHz and an IQ bandwidth of 128 kHz. The RBW of the FN-PSD is set to 1 Hz. The FN-PSD of the short resonator, $L_{res} = 25$ mm, exhibits a Lorentzian-based FN-PSD across the frequency range displayed resulting in a FWHM RF linewidth of about 2.3 kHz. The power line hum and its even harmonic are present as dominant noise peaks on this spectrum. The medium size resonator, $L_{res} = 100$ mm, shows a white noise floor corresponding to a FWHM RF linewidth of around 4 Hz for Fourier frequencies above 60 Hz. The increase in FN-PSD level

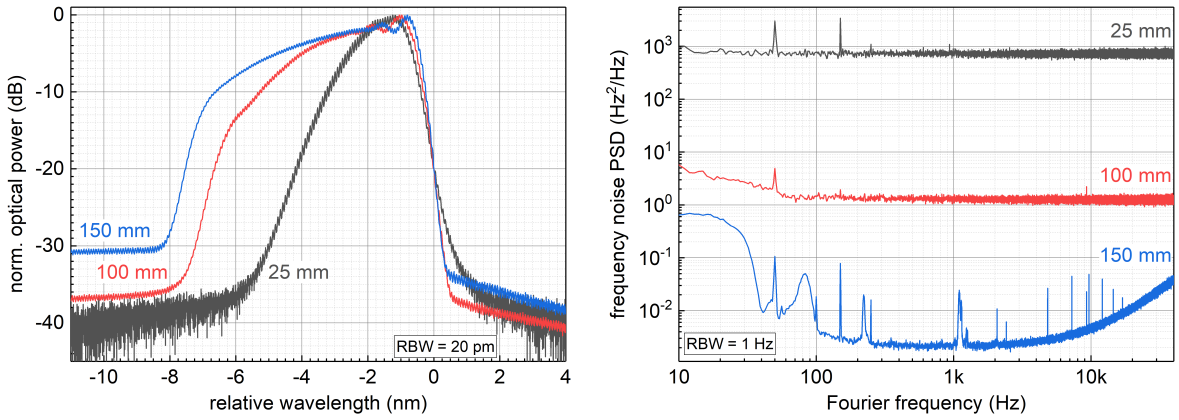

(a) optical spectrum (b) FN-PSD

Figure 4.2.: (a) Optical spectra and (b) FN-PSDs of ML-ECDLs with different resonator lengths. The optical spectra are normalized to their respective peak power levels P_{λ_p}. The spectra are shifted in wavelength with respect to the 20 dBc level at the longer wavelength wing (λ_0) for better comparison of the spectral bandwidths and wing steepness. The spectra were recorded for those values of operating parameters that allow for the largest spectral bandwidth at 20 dBc. The values of the operation and the normalization parameters are listed in Tab. 4.2.

at low Fourier frequencies is due to frequency jitter of the carrier. In contrast, the FN-PSD of the long resonator, $L_{res} = 150$ mm, not only features an increase at low Fourier frequencies but is also limited at high Fourier frequencies (above approx. 3 kHz) by the instrument noise floor. Additionally numerous noise peaks become visible on this spectrum due to the overall reduced FN-PSD level. For this long resonator, the FWHM RF linewidth of the pulse repetition rate measures about 7 mHz (detection limited). The reduction of FN-PSD with increasing resonator length is a result of the FN-PSD being, amongst other factors, inversely proportional to the squared resonator length [160]. Thus, a four-times increased resonator length, e.g. from 25 mm to 100 mm, should reduce the FN-PSD by factor of 16. However, a reduction by a factor of about 570 can be observed. This discrepancy can, on the one hand, be explained by a modification of the timing structure of the pulses with increasing resonator length as a result of higher pulse peak power and thus increasing SPM which may result in a higher stability of the pulse repetition rate. On the other hand, the effect of strongly reduced RF linewidth can be explained by a modified amount of feedback from the extended cavity into the diode laser chip as follows. The emission from the diode laser chip is collimated by minimizing the beam diameter in a distance larger than three Rayleigh ranges. Then, the laser resonator of the ML-ECDL is aligned. In mode-locked operation, the collimation is optimized for a resonator length of about 40 mm that corresponds to a pulse repetition rate of around 3.4 GHz. The resulting position of the lens is kept constant for all resonator lengths investigated in this work. This constant lens position modifies the coupling efficiency of the beam in the extended cavity into the diode laser chip for the different resonator lengths. This modified coupling efficiency leads to a decreasing amount of feedback level with increasing resonator length. However, a detailed investigation of

the physical effects underlying these results was not within the scope of this thesis, but is of interest for future investigations.

A consequence of the results presented here is to realize mode-locked lasers with a maximum possible resonator length. Observing the limits set by the future MIOBs and adhering to the required pulse repetition rates, the final resonator length is chosen to be about 44 mm. This corresponds to a pulse repetition rate of 3.4 GHz.

4.2.4. Epitaxial layer design of the diode laser chip

Within this thesis work, the results presented in this section were already partially published in Ref. [100].

The main task of this thesis work is to develop a diode laser-based OFCG which fulfills the requirements given in Sec. 1.2.4. Hence, a design of the active region that supports the fulfillment of those requirements needs to be employed. As pointed out in the evaluation criteria (Sec. 4.1), a large spectral bandwidth and a high RF stability are of utmost importance.

QD lasers that typically generate a large spectral bandwidth mode-locked emission with highly stable RF characteristics are not readily available in the wavelength range around 780 nm [114, 172–174]. Diode lasers with an active region comprising a single quantum well (SQW) structure can feature a gain bandwidth broad enough [32] to cover the wavelength range of the K and Rb D2 transitions when tailored appropriately. These lasers, however, provide only a relatively small net modal gain which is detrimental to the stability of mode-locked operation [175]. However, the modal gain bandwidth of diode lasers featuring a higher number of QWs decreases with the QW number [135]. Thus, increasing the QW number, typically, is detrimental to the mode-locked spectral bandwidth. Increasing the modal gain bandwidth of multi quantum well (MQW) devices can be achieved by means of tailoring the wavelength of the modal gain peak separately for each QW. This tailoring can be done via optimization of the thickness and the composition of the epitaxial layer structure of the active region [176–179]. By this means, a tuning range of CW emission lasers of more than 88 nm has been demonstrated [178]. Similar devices implemented in an extended cavity have been shown to operate in a mode-locked regime with a narrow spectral bandwidth of about 2 nm [180]. These devices were optimized for wavelength tunability of the mode-locked spectrum, not for the spectral bandwidth. The mode-locked optical spectrum could be tuned by about 60 nm by means of an external frequency selective diffraction grating acting as back reflector of the extended cavity [180]. In this work, the increased modal gain bandwidth offered by such MQW structures that feature separately optimized QWs is exploited for realizing an OFCG with large spectral bandwidth.

As only a spectral range of about 13 nm is to be bridged, an asymmetric double quantum well (aDQW) structure with individually optimized QWs is realized and investigated in the following. The emission of that device is compared to symmetric double quantum well (sDQW) structures with identical QWs.

The vertical layer structure of all the diode laser chips employed in this thesis was grown by MOVPE on 3" (100) GaAs substrates. The epitaxial layer structure can be divided into two constituents: the active layers consisting of QWs and barrier layers, and a vertical optical waveguide. The influence of the optical waveguide was discussed above in Sec. 4.2.1. The influence of the active epitaxial layers is discussed in the following.

Influence of As content of the QWs

The stochiometric composition of the QWs of a DQW structure is varied to explore their influence on the spectral characteristics of the mode-locked ECDL, such as center wavelength and spectral bandwidth. For emission in the 770 nm spectral range, an Al-free, tensile-strained $GaAs_yP_{1-y}$ DQW structure embedded in $Al_{0.4}Ga_{0.6}As$ barrier layers is employed. Here, y denotes the As content in the respective layer. Employment of a tensile-strained active region is preferred in that wavelength range due to emission efficiency properties [95, 114]. The optical gain can be optimized by means of the stochiometric composition and the thickness of the QWs. To that end, the As concentration was varied from 0.75 to 0.81 to allow for realization of sDQW structures emitting at 760 nm, 770 nm, and 780 nm, respectively. Additionally, an aDQW structure featuring a different stoichiometric composition in each QW, $y_1 = 0.81$ and $y_2 = 0.75$, was grown to investigate the possibility of broadening the mode-locked optical spectrum by slightly shifting the gain peak of one QW with respect to the other. The QW and barrier layer thickness was optimized for a maximum modal gain. Table 4.3 summarizes the fabricated vertical layer

Table 4.3.: Design properties of active epitaxial layer structures.

QW design	As content y_{QW1} | y_{QW2}	thickness of QW | barrier	design center wavelength	denotation
symmetric	0.75	10 nm | 9 nm	760 nm	sDQW(760)
symmetric	0.78	11 nm | 10 nm	770 nm	sDQW(770)
symmetric	0.81	14 nm | 10 nm	780 nm	sDQW(780)
asymmetric	0.81 | 0.75	10 nm | 9 nm	775 nm	aDQW

structures. The specific designs and simulations of these epitaxial layer structures were done by Dr. Hans Wenzel (FBH). Thermal effects were not included in the simulation. The lasers employing the epitaxial layer structures described above will be called sDQW laser and aDQW laser, respectively, henceforth.

First, the calculated modal gain spectra (simulation) and the amplified spontaneous emission spectra (experiment) of the realized diode laser chips are compared. Second, the mode-locked optical spectra of the corresponding, fully assembled 44 mm long ML-ECDLs were recorded with those values of the operating parameters that allow for the largest spectral bandwidths at 20 dBc. The values of the operating parameters of the realized devices are collected in Tab. 4.4.

The modal gain spectra of the active epitaxial layer structures listed in Tab. 4.3 are depicted in Fig. 4.3(a). With Eq. 2.11, the modal gain was calculated for a carrier density of $4 \cdot 10^{18}/\mathrm{cm}^3$ and a temperature of 300 K. For the simulation, a confinement factor and effective refractive index of $\Gamma = 0.012$ and $n_{eff} = 3.39$, respectively, were used [181].

From the simulated modal gain spectra of the sDQW structures, see Fig. 4.3(a) and Tab. 4.5, it can be seen that an increase of the As content of only 0.03 results in a shift of the peak wavelength of the spectrum of about 10 nm to longer wavelengths, as expected from Ref. [114].

The modal gain spectrum of the aDQW features a double peak structure, see Fig. 4.3(a).

Table 4.4.: Values of operation (op.) parameters for data shown in Figs. 4.3 and 4.4. The mount temperature T_{mount} is set to 20.0 °C. These values of the operating parameters allow for the largest spectral bandwidth of each device.

operation mode	ASE	mode-locking	
op. parameter / QW design	I_{DCI}/mA	U_{SAB}/V	I_{DCI}/mA
sDQW(760)	245.0	-1.40	250.0
sDQW(770)	245.0	-2.14	250.0
sDQW(780)	100.0	-4.16	250.0
aDQW	245.0	-1.55	245.0

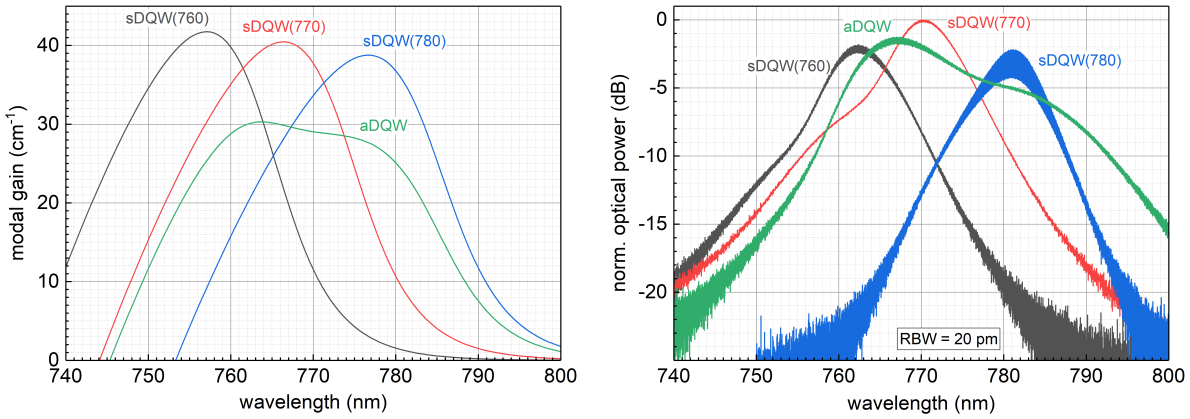

(a) calculated modal gain spectrum

(b) measured ASE spectrum

Figure 4.3.: (a) Calculated modal gain spectra and (b) measured ASE spectra of diode laser chips with different As content of the QWs. The DQWs of the 2 mm long diode laser chips are optimized for emission at 760 nm (grey), 770 nm (red), 780 nm (blue), and 760 - 780 nm (green). The values of the operating parameters and key spectral characteristics are listed in Tabs. 4.4 and 4.5, respectively.

Table 4.5.: Peak wavelengths λ_p and spectral bandwidths $\Delta\lambda_3$ and $\Delta\lambda_{20}$ at 3 dBc and 20 dBc, respectively, for the calculated modal gain spectra (SIM) and measured ASE (ASE) of different diode laser chips, and for optical spectra (ML) of corresponding ML-ECDLs.

QW design		λ_p/nm			$\Delta\lambda_3$/nm		$\Delta\lambda_{20}$/nm
		SIM	ASE	ML	ASE	ML	ML
sDQW(760)		757	762	766.49	9	1.18	2.67
sDQW(770)		767	770	775.52	9	1.89	4.07
sDQW(780)		777	781	788.87	9	2.30	5.17
aDQW	peak 1	764	767	771.22	17	1.67	16.12
	peak 2	773	782	782.22			

This double peak spectral feature is determined by the QWs with an As content of 0.75 and 0.81, respectively, which corresponds to the As content of the sDQW(760) and sDQW(780) devices, see Tab. 4.3. The individual wavelength peaks of both QWs of the aDQW device cannot be clearly identified. However, rough estimations of the respective peaks by means of determination of the local minima of the absolute value of the first derivative of the modal gain allow for investigation of general tendencies. The shorter and longer wavelength peak are at about 764 nm and 773 nm, respectively. The simulation results (Fig. 4.3(a)) also show that the spectral coverage of the aDQW laser is smaller than the joint spectral coverage of the sDQW(760) and sDQW(780) lasers.

For comparison, the ASE spectra of 2 mm long diode laser chips were recorded. For this measurement, all sections of the diode laser chips were contacted in parallel. The heatsink was stabilized to a temperature T_{mount} of 20.0 °C. To prevent optical feedback, the components of the laser resonator were removed and the divergent emission was captured by a beam dump. The resulting ASE spectra are depicted in Fig. 4.3(b). The optical spectra for the ASE operation are normalized to the common peak.

The wavelength shift observed in the modal gain spectra of the sDQW devices (Fig. 4.3(a)) can also be found in the corresponding ASE spectra, see Fig. 4.3(b). However, the peak wavelength shift observed experimentally exceeds the shift derived from the simulation. This can be due to a slightly modified As content in the realized devices. Using the nominal wavelength shift of 10 nm per change As content of 0.03, a deviation of the As content from the intended values (see Tab. 4.3) to 0.765, 0.789, and 0.822 for the sDQW(760), sDQW(770), and the sDQW(780) devices, respectively, can be estimated.

As expected, the double peak structure observed in the modal gain spectrum of the aDQW device is also present on the corresponding ASE spectrum. Similar to the modal gain spectrum, the spectral peak on the longer wavelength side of the ASE spectrum cannot be clearly identified. The wavelength of the shorter and longer wavelength peak can roughly be estimated to about 767 nm and 782 nm, respectively, see Tab. 4.5. As observed with the sDQW devices, the ASE spectrum of the aDQW device is shifted to longer wavelengths compared to the modal gain spectrum. For the aDQW device, the shorter wavelength peak is shifted by about 3 nm to longer wavelengths, the longer wavelength peak is shifted by about 9 nm to about 782 nm. Thus, it can be assumed that a deviation of As content from the nominal values, see Tab. 4.3, occurred during wafer growth. A deviation of 0.009 to 0.759 and 0.027 to 0.837 for the shorter and longer wavelength peaks, respectively, can be estimated. In contrast to the modal gain spectrum of the aDQW device, the spectral coverage of the corresponding ASE spectrum is similar to that of the joint spectral coverage of the sDQW(760) and sDQW(780) devices.

The mode-locked optical spectra of the fully assembled ML-ECDL, corresponding to the diode laser chips investigated above for their (calculated) modal gain, and ASE spectra, are depicted in Fig. 4.4. The mode-locked optical spectra are normalized to their common peak. Compared to the corresponding ASE spectra, the mode-locked spectra are shifted to longer wavelengths. This is due to the influence of the saturable absorber reverse voltage which red-shifts the optical spectra [97, 182]. Nevertheless, the mode-locked optical spectrum follows the general behavior observed for the modal gain and ASE spectra.

The spectral bandwidth at 20 dBc of the mode-locked sDQW lasers increases with increasing

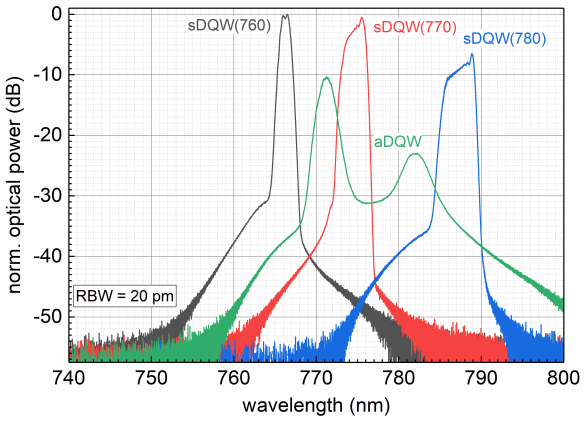

Figure 4.4.: Mode-locked optical spectra of ML-ECDLs with different As content in the QWs corresponding to the data shown in Fig. 4.3. The ML-ECDLs were operated at those values of operating parameters that allow for the largest spectral bandwidths at 20 dBc. The values of the operating parameters and key spectral characteristics are listed in Tabs. 4.4 and 4.5, respectively.

As content by roughly 1.2 nm per increase of As content of nominal 0.03 from about 2.7 nm to 5.2 nm, see Tab. 4.5. The increase of spectral bandwidth at 3 dBc for this range of As content is comparably low with 0.7 nm at maximum, see Tab. 4.5. A conclusion that can be drawn from these results is that a higher As content, at which the tensile strain is reduced [114], leads to larger spectral bandwidths and shifts the emission to longer wavelengths.

Similar to the modal gain spectrum and the corresponding ASE spectrum, the mode-locked optical spectrum of the aDQW laser features a double peak structure, see Fig. 4.4. While the individual peaks cannot be clearly identified in the corresponding modal gain and ASE spectra, the mode-locked optical spectrum shows two clearly separable spectral bands. The peak wavelengths of the shorter and longer spectral band are about 771.2 nm and 782.2 nm (Tab. 4.5), respectively. In mode-locked operation, in comparison to ASE operation, the longer wavelength peak is observed at the same wavelength. In contrast, the shorter wavelength peak is shifted to longer wavelengths by about 4 nm. This finding indicates that the saturable absorber reverse voltage has a stronger influence on the shorter wavelength part of the spectrum. The spectral bandwidth at 3 dBc of the aDQW device lies between the respective values for the sDQW(760) and sDQW(770) devices. This is expected as the spectral bandwidth of the sDQW devices increases with increasing As content and the wavelength peak of the shorter wavelength QW of the aDQW device lies between the values of the sDQW(760) and sDQW(770) devices. The strongly increased bandwidth of the modal gain results in a spectral bandwidth at 20 dBc of the mode-locked optical spectrum of the aDQW laser that is about a factor of more than 5 and still about a factor of 3 larger than that of the sDQW(760) and sDQW(780) laser, respectively, see Tab. 4.5.

The mode-locked optical spectrum of the aDQW device features, in contrast to the corresponding ASE spectrum, a reduced spectral coverage that was also observed in the corresponding modal gain spectrum.

Another effect resulting from increasing the As content in the sDQW devices is a reduction

of the modal gain maximum, see Fig. 4.3(a), resulting in a reduction of optical power. Further, the modal gain peaks of the aDQW structure are reduced compared to that of the corresponding sDQW structures. Thus, while a mode-locked optical spectrum can be expected of the aDQW diode laser chips to be much broader than that of the sDQW lasers, the average optical output power of the aDQW laser is also expected to be much lower. However, the optical power is not the focus of this section and will not be discussed here. Please note that the average optical power exceeds the requirement (Tab. 1.1) for all devices.

In conclusion, the good qualitative agreement between simulation and experiment is observed. The investigations show that implementation of an ML-ECDL featuring an aDQW device allows for a spectral bandwidth exceeding the requirement, see Tab. 1.1.

Influence of carrier density

To investigate the influence of the gain section current on the spectral properties of the sDQW and aDQW structures, simulations of the modal gain spectra, and measurements of the ASE and mode-locked optical spectra were performed for the sDQW(760) device and for the aDQW device, see Figs. 4.5 and 4.6. For the simulation of the modal gain, only the carrier density in the quantum wells is taken into account. The relationship between carrier density in the active region and injection current into the diode laser chip is described by Eqs. 2.3 and 2.4. It can be seen that the carrier density in the active region is roughly proportional to the injected current. In the simulation, the loss of carriers due to non-stimulated emission and the collection efficiency of carriers into the active region are neglected. Thus, the behavior of the modal gain with increasing carrier density can be considered proportional to the expected behavior of the ASE spectrum with increasing injection current.

For the investigation presented here, the same values of operating parameters as in the previous paragraph were employed, see Tab. 4.4. Here, however, the gain section injection current I_{DCI} was varied to investigate the influence of the carrier density/current on the modal gain, ASE operation, and the mode-locked operation.

The effect of increasing carrier density on the modal gain of the sDQW and aDQW devices is shown in Fig. 4.5(a). It can be seen that with increasing carrier density, the modal gain of both, the sDQW and the aDQW device, increases. The modal gain of the sDQW device shows one dominant peak at the shorter-wavelength part of the spectrum. For the aDQW device, two peaks are visible. The longer-wavelength peak dominates the modal gain spectrum for carrier densities below $4 \cdot 10^{18}$ /cm^3. Further increase of the carrier density reverses this relationship. Even further increase of the carrier density starts to saturate the modal gain of both, the sDQW and the aDQW device.

For the sDQW device, the behavior of the wavelength peak is as follows. For all investigated carrier densities, the peak wavelength of the modal gain shifts towards shorter wavelengths by about -0.5 nm/(10^{18} cm^3) and -8 pm/mA, respectively. The rate of the wavelength shift slightly reduces for increasing carrier densities.

For the aDQW laser, the spectral bands provided by each QW show a different behavior. While the shorter-wavelength peak of the modal gain of the aDQW structure shifts to shorter wavelength by roughly -0.6 nm/(10^{18} cm^3), the longer-wavelength peak shifts towards longer

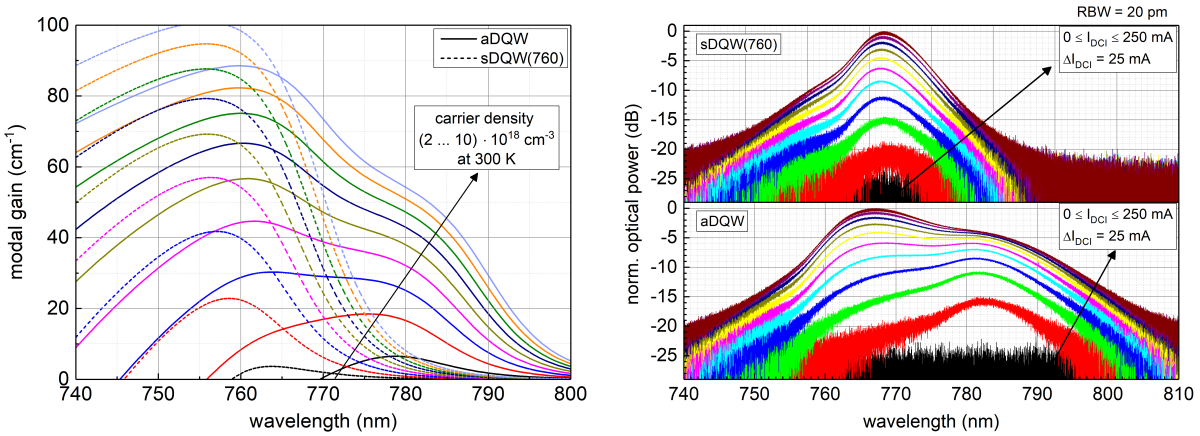

(a) calculated modal gain spectrum

(b) measured ASE spectrum

Figure 4.5.: (a) Calculated modal gain spectra of diode laser chips for different carrier densities, and (b) measured ASE spectra of diode laser chips for different gain section injection current settings for a sDQW(760) and a aDQW device. For the modal gain spectra, the carrier density is increased from $2 \cdot 10^{18}/\mathrm{cm}^3$ to $10 \cdot 10^{18}/\mathrm{cm}^3$ in $1 \cdot 10^{18}/\mathrm{cm}^3$ steps. For the ASE spectra, the gain section injection current I_{DCI} is increased from 0 mA to 250 mA in 25 mA steps and a mount temperature 20.0 °C is set. The measured spectra are normalized to the common peak.

wavelengths by approx. 1 nm/(10^{18} cm^3) over the investigated carrier density range.

The spectral bandwidth of both, the sDQW and the aDQW device, increases for increasing carrier density in the displayed range of carrier densities.

The simulated behavior of the modal gain is qualitatively reflected by the experimental ASE spectra for both devices, see Fig. 4.5(b). The ASE spectrum of the sDQW diode laser shows one dominant peak while that of the aDQW laser shows two peaks. Below a current of about 175 mA, the longer-wavelength peak dominates the ASE spectrum of the aDQW device. Above that current, the shorter-wavelength peak dominates the ASE spectrum of the aDQW device. Further, the increase of peak ASE power starts to saturate with increasing gain section injection current for both, the sDQW and aDQW lasers.

The behavior of the spectral bandwidth at 3 dBc of the ASE spectrum with increasing gain section injection current also shows a good agreement with the simulation. However, the spectral bandwidth at 3 dBc of the ASE spectrum of the aDQW device reaches a maximum at a gain section injection current of about 175 mA. A further increase of the carrier density and injection current, respectively, leads to a decrease of spectral bandwidth at 3 dBc.

For the sDQW laser, the wavelength shift of the peak wavelength of the ASE spectrum shows a good agreement with the simulation below a gain section injection current of about 175 mA. Above 175 mA, the wavelength shift changes direction for the ASE spectrum. The ASE spectrum experiences a shift in the opposite direction at about the inverse rate of before, i.e. about 8 pm/mA.

For the aDQW laser, the general behavior observed in the simulation is partially reproduced in the experiment. The ASE spectrum features a spectral shift towards shorter wavelengths with

a rate of about -30 pm/mA and -8 pm/mA for the shorter-wavelength and longer-wavelength peak, respectively. The rate of the wavelength shift reduces with increasing gain section injection current until, above 175 mA, almost no spectral shift is detectable, similar to the behavior of the modal gain spectra with increasing carrier density. The good agreement of the ASE operation with the simulation suggests that carrier related wavelength shifts dominate.

Similar optical characteristics as observed in the modal gain and the ASE spectra can be seen in the experimentally determined mode-locked optical spectrum, see Fig. 4.6.

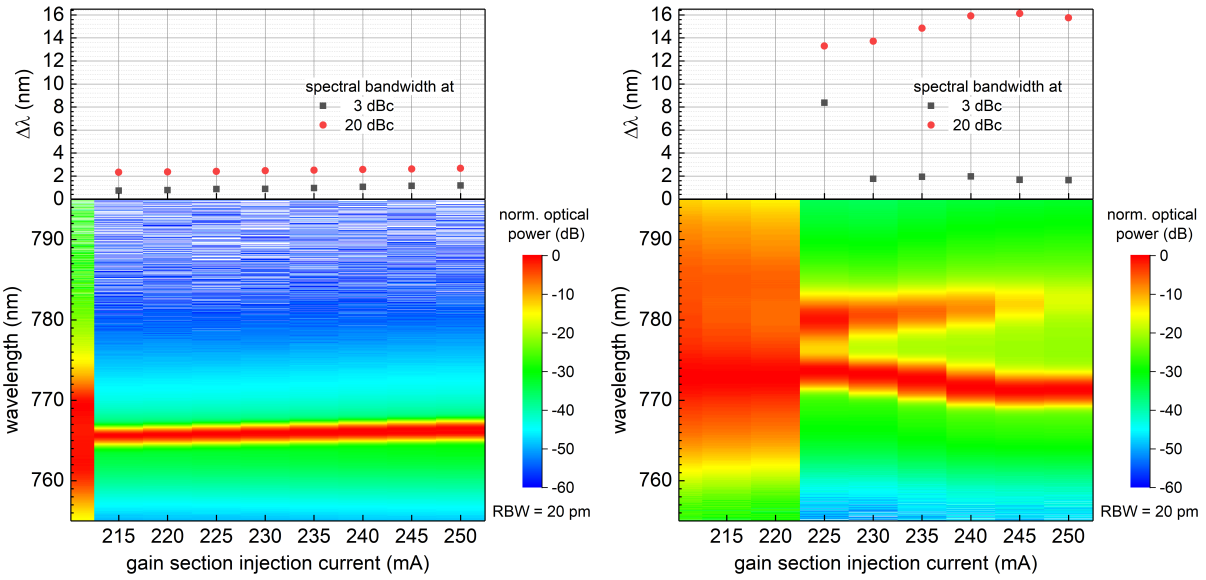

(a) sDQW laser

(b) aDQW laser

Figure 4.6.: Mode-locked optical spectra and spectral bandwidths of (a) a sDQW(760) and (b) an aDQW laser. The values of the operating parameters are given in Tab. 4.4.

Mode-locking occurs for both the sDQW and the aDQW laser from just above the threshold current until maximum current. Both laser types show a threshold current of more than 200 mA. The sDQW laser provides a threshold current smaller than that of the aDQW laser by 20 mA.

It can clearly be seen that the sDQW laser features a single spectral band while the aDQW laser shows two overlapping spectral bands, see Figs. 4.6(a) and 4.6(b), respectively. With increasing gain section injection current, spectral power of the longer-wavelength peak of the aDQW laser decreases.

The peak wavelength of the mode-locked optical spectrum of the sDQW shows a behavior different from the simulation and the ASE spectrum. The peak wavelength always shifts to longer wavelengths by about 25 pm/mA. This indicates thermal heating of the diode laser chip. However, the diode laser chip is mounted on a temperature stabilized mount (Sec. 3.3.1). This suggests that the increase of temperature in the diode laser chip is due to the thermal resistance of the laser test mount.

In contrast, the mode-locked optical spectrum of the aDQW device shows a wavelength shift

of -95 pm/mA and 100 pm/mA for the shorter-wavelength and longer-wavelength peaks, respectively. This qualitative agreement with the simulation, which does not account for thermal effects, emphasizes that the experimentally observed behavior of the optical spectrum of the aDQW laser in ASE as well as in mode-locked operation is dominated by carrier effects.

The spectral bandwidth of the sDQW laser is nearly constant at about 1 nm at 3 dBc and 2.5 nm at 20 dBc for the displayed current range, see Fig. 4.6(a). The spectral bandwidth at 3 dBc of the aDQW laser is at maximum about 8 nm just above the threshold current, see Fig. 4.6(b). At this current, the spectral power in the shorter-wavelength and longer-wavelength peak is similar. Above about 230 mA, the spectral bandwidth at 3 dBc of the aDQW laser remains almost constant at about 2 nm. The spectral bandwidth at 20 dBc of the aDQW laser increases with increasing gain section injection current up to more than 16 nm at 245 mA. Above 245 mA, the spectral bandwidth of the aDQW device decreases with further increasing gain section injection current as the spectral power of the longer-wavelength peak decreases to about 20 dBc.

In conclusion to this section, the aDQW device is found to provide a spectral bandwidth exceeding the requirement in a broad range of gain section injection current.

4.2.5. Longitudinal design of the diode laser chip

In this section the influence of the length of the diode laser chip and its sections, see Fig. 4.7, is investigated. The lengths of the diode laser chip, and of the gain and saturable absorber section are denoted L_{chip}, L_{gain} and L_{SA}, respectively. The sections are separated from each other by a 30 µm long passive, unpumped region which provides sufficient electrical isolation of the p-contacts of both sections. A 15 µm long passive region is located between the facet and the adjacent section to avoid excessive thermal and carrier load close to the facets. In the following, the influence of the section lengths L_{gain} and L_{SA} is investigated. To that end, those mode-locking performance characteristics that show the strongest influence of the section lengths will be discussed in detail.

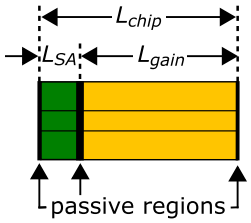

Figure 4.7.: Schematic of physical dimensions of diode laser chips.

Influence of the gain section length

To investigate the influence of the length of the gain section on the mode-locking performance, 1 mm (DLC1000) and 2 mm (DLC2000) long diode laser chips with a saturable absorber section of 100 µm were employed. Thus, the gain sections are 900 µm and 1900 µm long, respectively. The diode laser chips feature an sDQW(780) region as, at the time of these experiments, aDQW devices were not available. Although the facets could not be coated in the same process run due to the length difference, nominally identical facet coatings (R_f = 5 %, $R_r = 10^{-4}$) were employed. The values of operating parameters applied to the diode lasers, see Tab. 4.6, were chosen in order to provide the maximum spectral bandwidth at 20 dBc possible with each device.

Table 4.6.: Operating parameters of ML-ECDLs with different gain section lengths.

	chip denotation	DLC1000	DLC2000
chip parameter	L_{chip}/µm	1000	2000
	L_{SA}/µm	100	100
	L_{gain}/µm	900	1900
	L_{SA}/L_{gain}/%	≈ 11	≈ 53
ML-ECDL (operating) parameter	T_{mount}/°C	20.0	20.0
	U_{SAB}/V	-1.0	-4.0
	I_{DCI}/mA	210.0	270.0
	L_{res}/mm	≈ 42	≈ 38

The optical spectra of the DLC1000 and DLC2000 devices are shown in Fig. 4.8. The mode-locking characteristics of the investigated devices extracted from Fig. 4.8 are summarized in Tab. 4.7. It can be seen that the spectral bandwidth at 3 dBc of the DLC1000 device is slightly larger than that of the DLC2000 device (Tab. 4.7). This relationship is reversed for the spectral bandwidth at 20 dBc (Tab. 4.7) which is the decisive parameter in this work. However, the difference is not significant.

Table 4.7.: Mode-locking performance of ML-ECDLs with different gain section lengths L_{gain}. DLC1000 - L_{gain} = 900 µm, DLC2000 - L_{gain} = 1900 µm.

parameter	λ_p	$\Delta\lambda_3$	$\Delta\lambda_{20}$	L_{res}	f_{rep}	Δf_{rep}^L	t_p	P_{avg}	P_p
unit	nm	nm	nm	mm	GHz	Hz	ps	mW	W
DLC1000	787.58	2.56	5.24	42	3.59	1092	4.7	60.8	3.2
DLC2000	789.45	2.05	5.61	38	3.97	86	5.0	105.8	4.7

The main difference between both lasers can, however, be determined by means of time-based investigations of the RF characteristics. The RF linewidth is determined via a Lorentzian fit of the RF spectrum (Fig. 4.9) reconstructed from time domain IQ measurements of the pulse repetition rate. The IQ data were recorded for 500 ms with a sampling rate of 160 kHz which provided an IQ bandwidth of 128 kHz. Please note that the pulse repetition rate of the

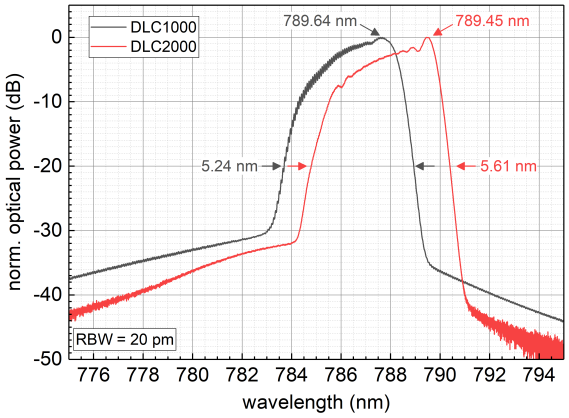

Figure 4.8.: Optical spectra of ML-ECDLs with different gain section lengths L_{gain}. DLC1000 - L_{gain} = 900 µm, DLC2000 - L_{gain} = 1900 µm.

DLC1000 laser is less than 10 % smaller than that of the DLC2000 laser. This slight difference is not significant enough to strongly influence the RF linewidth. With an RF linewidth of only about 86 Hz, the DLC2000 device provides an RF linewidth Δf_{rep}^{L} smaller than an order of magnitude in comparison to the DLC1000 (Δf_{rep}^{L} = 1092 Hz), see Tab. 4.7.

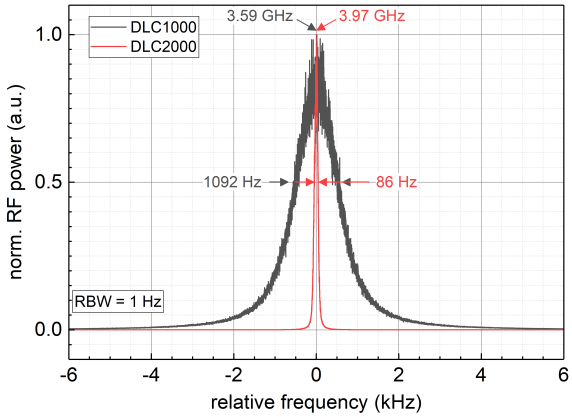

Figure 4.9.: RF spectra of ML-ECDLs with different gain section lengths L_{gain}. The RF spectra are reconstructed from IQ data (see text for details). The carrier frequency is the respective pulse repetition rate. DLC1000 - L_{gain} = 900 µm, DLC2000 - L_{gain} = 1900 µm.

Further, it can be seen that the DLC2000 device provides a higher average optical power by a factor of about 2 compared to the DLC1000 device. This increases the optical power for comb lines at 20 dBc. With a similar pulse width and almost twice the average power of the DLC1000 device, the DLC2000 device features a peak power larger than that of the DLC1000 device by about 50 %, providing a better compliance with the requirements on the optical power of the mode-locked laser, see Sec. 1.2.4. The higher output power can be attributed to the longer gain section of the DLC2000 device due to relatively reduced losses (non-linear and linear) compared

to the DLC1000 [183]. Consequently, the higher RF stability of the DLC2000 device may also be a result of a smaller carrier density and, thus, reduced ASE in the diode laser chip.

In conclusion, the investigation of the influence of the gain section length shows that longer gain sections, here 1900 µm as compared to 900 µm, are preferable for the purpose of this thesis work.

Influence of the saturable absorber length

For onset and stability of the mode-locked operation, the length of the saturable absorber section L_{SA} is an important parameter [183]. The absorber section does not only provide the nonlinear losses necessary to establish and maintain mode-locked operation. It also features linear losses that, if too high, increase the threshold current and limit the maximum optical power, see Sec. 2.4. Typical ratios of the saturable absorber and the gain section lengths are between 1:50 and 1:5, see, e.g., [160, 183–185]. A short saturable absorber is preferable as this minimizes the amount of linear losses in the laser and maximizes the optical output power. Thus, investigation of the influence of the saturable absorber length with diode laser chips providing a large spectral bandwidth is required.

The investigation of the influence of the saturable absorber length could not be performed using the sDQW lasers used in the investigation of the gain section length. The reason for that is that the length of the saturable absorber (100 µm) was kept constant for those lasers. However, the aDQW lasers, that were available later in this work than the sDQW laser, were realized with different absorber lengths. The 2 mm long aDQW diode laser chips were provided by FBH with 50 µm (SA50) and 100 µm (SA100) long saturable absorber sections, respectively. The ratios of the saturable absorber and gain section lengths are about 1:38 and 1:19, respectively. The diode laser chips were implemented in ML-ECDLs with an optical resonator length L_{res} of approximately 44 mm corresponding to a pulse repetition rate of about 3.4 GHz. The mode-locking performance is compared for those values of operating parameters that allow for the largest spectral bandwidth at 20 dBc. The laser and operating parameter are summarized in Tab. 4.8.

Table 4.8.: Operating parameters of ML-ECDLs with different saturable absorber lengths.

	chip denotation:	SA50	SA100
chip parameter	L_{chip}/µm	2000	2000
	L_{gain}/µm	1950	1900
	L_{SA}/µm	50	100
	L_{SA}/L_{gain}/%	≈ 2.6	≈ 5.3
ML-ECDL (operating) parameters	T_{mount}/°C	20.0	20.0
	U_{SAB}/V	-1.70	-1.55
	L_{res}/mm	44	44

The optical frequency domain characteristics are shown in Fig. 4.10. The optical spectra as a function of the gain section injection current are shown in Fig. 4.10(a). The peak wavelengths

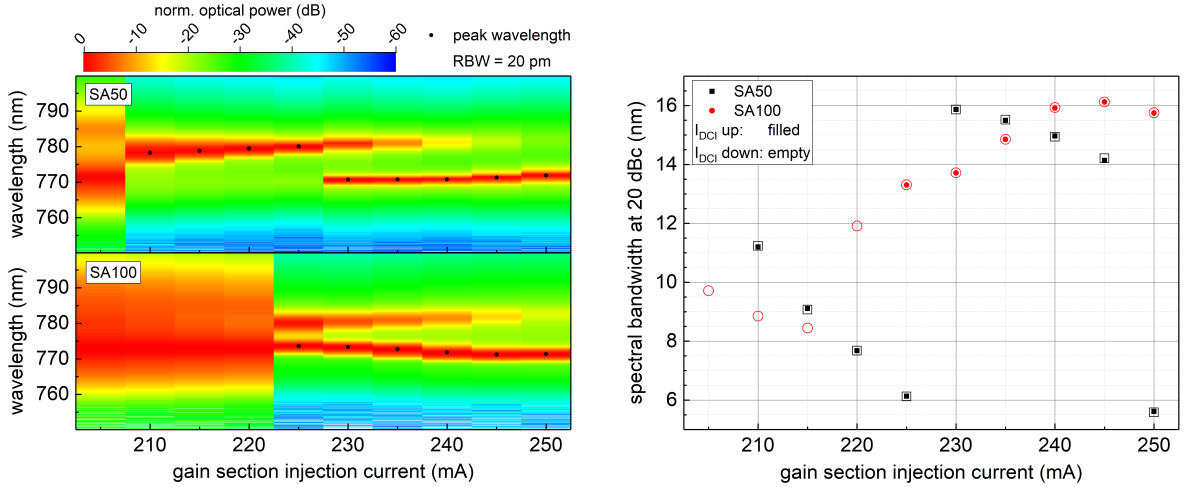

(a) optical spectra

(b) spectral bandwidths at 20 dBc

Figure 4.10.: (a) Optical spectra and (b) spectral bandwidths at 20 dBc of ML-ECDLs with different saturable absorber section lengths L_{SA}. SA50 - $L_{SA} = 50$ µm, SA100 - $L_{SA} = 100$ µm.

are indicated. The optical spectra are individually normalized to the maximum optical power provided at each gain section injection current. The spectral bandwidths at 20 dBc as extracted from the optical spectra are depicted in Fig. 4.10(b).

It can be seen (Fig. 4.10(a)) that the SA50 and SA100 devices feature similiar threshold currents, about 210 mA and 225 mA, respectively. Below 230 mA, the SA50 device provides a peak wavelength of about 780 nm corresponding to the longer-wavelength QW, see Fig. 4.3. With increasing gain section injection current, the relative optical power of the longer-wavelength QW decreases. At about 230 mA, the shorter wavelength QW dominates and the peak wavelength jumps to about 770 nm.

In contrast, the SA100 device provides similar optical power in both spectral bands at about 770 nm and 780 nm just above the threshold current. It can be clearly seen that the relative optical power of the longer-wavelength QW reduces with increasing gain section injection current similar to the SA50 device. This tendency will eventually result in a drastic reduction of spectral bandwidth of the SA100 at gain section injection currents above 250 mA, similar to the SA50 device.

Nevertheless, both devices allow for spectral bandwidths of about 16 nm at the 20 dBc level for similar values of operating parameters, 230 mA and 245 mA, respectively, see Fig. 4.10(b). In contrast to the SA50 device, the SA100 device provides a smoother behavior of the optical spectrum with increasing gain section injection current, showing no jumps in peak wavelength and spectral bandwidth. Thus, for the implementation of the ML-ECDL in future QUANTUS experiments, the SA100 device would be preferable in terms of the spectral characteristics.

To further evaluate the ML-ECDL (see Sec. 4.1), the RF stability of both mode-locked lasers was investigated with regard to the RF linewidth (Fig. 4.11(a)) and RMS integrated timing jitter (Fig. 4.11(b)) determined from recorded IQ data. In the low frequency range (1 Hz - 80 kHz), a

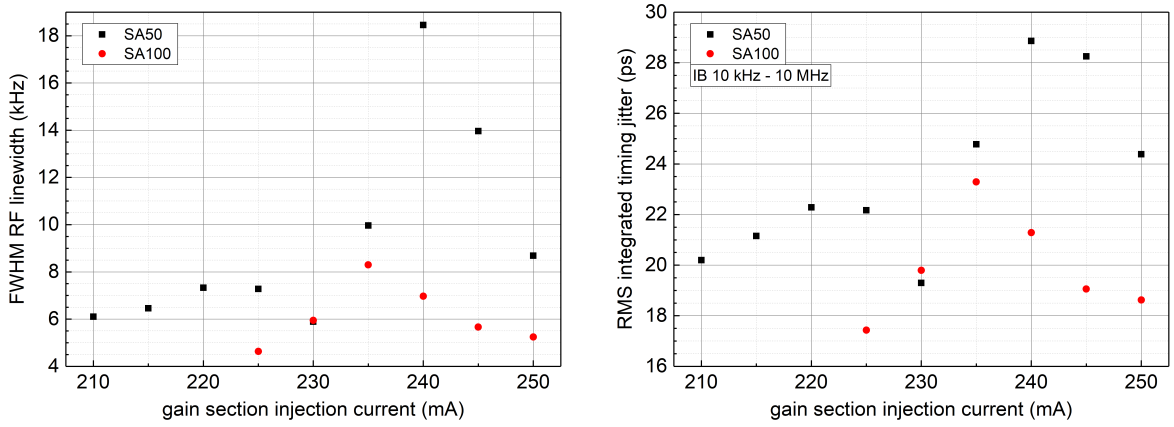

(a) RF linewidth

(b) RMS integrated timing jitter

Figure 4.11.: (a) RF linewidths and (b) RMS integrated timing jitters of ML-ECDLs with different saturable absorber section lengths L_{SA}. SA50 - L_{SA} = 50 µm, SA100 - L_{SA} = 100 µm.

sampling rate of 160 kHz providing an IQ bandwidth of 128 kHz, and time record length of 100 s were employed, while in the higher frequency (100 Hz - 12.8 MHz) range, 32 MHz, 25.6 MHz, and 500 ms were used, respectively. The RF linewidths were determined via Lorentzian fit of the RF spectra reconstructed from low frequency range IQ data. The RMS integrated timing jitter is calculated in an integration band(width) (IB) from 10 kHz to 10 MHz. The same values of operating parameters were applied that were used for the investigation of the spectral characteristics of the SA50 and SA100 laser.

The SA50 device shows a sharp increase in RF linewidth from about 6 kHz to more than 18 kHz with increasing gain current in the large spectral bandwidth operation regime, see Figs. 4.10(a) and 4.11(a). In contrast, in the single spectral band operation regime for gain currents below 230 mA and above 245 mA, RF linewidths of at maximum 8.7 kHz are achieved. The increase of RF linewidth in the intermediate range of gain current occurs when optical power of the longer-wavelength QW is more than 10 dB above that of the the shorter-wavelength QW, see Fig. 4.10(a). The reason for this behavior can be found in a competition of the dominating spectral bands centered at around 770 nm and around 780 nm. This can be assumed as below 230 mA and well above the jump of the dominating spectral band similar RF linewidths can be achieved.

The SA100 device shows an RF linewidth of at most 8.4 kHz. Although those RF linewidths are about an order of magnitude larger than the RF linewidths typical for sDQW devices (about 500 Hz for sDQW(760) [100]) both devices still meet the requirements on the lasers that are to be developed within this thesis, see Tab. 1.1.

The behavior of the RF linewidth is reflected in the behavior of the RMS integrated timing jitter that was determined from the high frequency range IQ data, see Fig. 4.11(b). For both devices RMS integrated timing jitter values in the range of 17 to 29 ps are determined. The SA100 device again displays a higher RF timing stability, i.e. lower timing jitter values. The timing jitter of an sDQW device, e.g. sDQW(760), is about a factor 4 reduced compared to

those determined here [100].

The results shown above already indicate comparable spectral bandwidths and higher RF stability as well as a broader accessible gain section injection current range for the SA100 device. Investigation of the swept RF spectrum allows for further evaluation of the SA50 and SA100 lasers. This measurement technique allows for investigations at Fourier frequencies too large to be accessible with the IQ measurement tool.

Fig. 4.12 shows the RF spectrum in a bandwidth of 500 MHz around the fundamental frequency of the RF signal of the pulse train (i.e. the pulse repetition rate) for the values of operating parameters given in Tab. 4.8. The applied gain currents are 230 mA and 245 mA for the SA50 and SA100 laser, respectively. These values of operating parameters allow for the broadest optical spectra at 20 dBc for each device. To facilitate comparison, both spectra are shown for Fourier frequencies relative to the pulse repetition rate and are normalized to their common peak level.

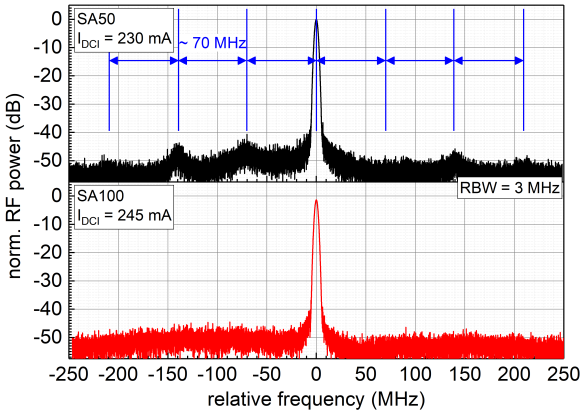

Figure 4.12.: RF spectra of the SA50 and the SA100 device in a broad frequency range. The RF spectra are depicted versus carrier frequency corresponding to the pulse repetition rate ($f_{rep} \approx 3.4$ GHz). The applied gain currents are 230 mA and 245 mA for the SA50 and SA100 laser, respectively. The values of the other operating parameters are given in Tab. 4.8.

It can be seen that the SA100 device (red, bottom plot of Fig. 4.12) shows a higher SNR than the SA50 device (black, top plot of Fig. 4.12). The main difference, though, can be identified in the noise floor of the RF spectra. The RF spectrum of the SA50 device features a periodic peak structure with a frequency period of about 70 MHz. Further, the RF power of the peaks is asymmetric with respect the central RF frequency. In contrast to the RF spectrum provided by the SA50 laser, the RF spectrum of the SA100 device features an asymmetric noise floor (instrument[1] noise floor approx. -50 dB) but no periodic peak structure.

The periodic peak structure observed for the SA50 device indicates a periodic amplitude modulation of the pulse train. If its underlying cause was optical feedback from an external source, this source would be found in a distance of about 2 m. Blocking the rear-output of

[1]This means the instrument chain comprising the fast photodetector, the broadband amplifier, and the electrical spectrum analyzer used for RF analysis.

the SA50 laser shows no change in the structure of the RF spectrum. Thus, the feedback does not originate from that direction. Further, the optical isolator which is implemented in the experimental setup, see Fig. 3.3, does eliminate optical feedback to the front facet of the laser. The input facet of the optical isolator is only about 60 cm away from the ML-ECDL and is, hence, not the source of possible optical feedback. A possible internal source for the amplitude modulation is insufficient saturable absorption leading to Q-switched (amplitude modulated pulse train) mode-locked operation [126, 175, 183, 186]. The asymmetry of the RF power of the periodic peak structure indicates a noisy amplitude structure of the pulse train [187]. While the physical origin of the periodic noise peaks of the RF spectrum of the SA50 device is not yet identified, their appearance clearly shows that the SA100 device is to be preferred for the purpose of this thesis.

In addition to the noisy RF spectrum, the mode-locked operation of the SA50 device can be disturbed by optical feedback to the front facet of the laser. This has been observed when coupling into the autocorrelator which leads to a feedback of about 25 % of the in-coupled optical power. For this path of the experimental setup, the optical isolator has been omitted as its dispersion may deform the temporal shape pulses. Thus, for measuring the autocorrelation function, the alignment to the autocorrelator was required to be slightly misaligned from optimum. As optical feedback was not noticed during operation of the SA100 laser, insufficient absorption due to shorter absorber length may be a reason [183]. Detailed investigation of the influence of external optical feedback on the mode-locking behavior is not within the scope of this thesis and, hence, had to be postponed to future investigations.

The results discussed above clearly show that an absorber section length of 100 µm provides better RF stability than a length of 50 µm. As a consequence of the investigations presented in this chapter section, the SA100 device featuring a 2 mm long diode laser chip with a 100 µm long saturable absorber is found to be the most suitable for the purpose of this thesis.

4.2.6. Facet reflectivity of the diode laser chip

For the operation of the ML-ECDL, the reflectivities of the diode laser chips' facets (Fig. 2.9) are important parameters influencing, e.g., the RF stability of the OFC and the output power. In the following, the influence of the diode laser chips' facets' reflectivities will be investigated in detail.

Resonator-side facet reflectivity

For the investigations presented here, a 2 mm long sDQW(780) laser is employed. The diode laser chip features a 100 µm long saturable absorber and a 1900 µm long gain section. The front facet of the diode laser chip acting as laser output is coated to 5 % reflection. The resonator-side facet of the diode laser chip is anti-reflection coated to a reflectivity[2] of about 10^{-4}. It is known that insufficient AR coating leads to formation of parasitic cavities. This can reduce the mode-locking stability, lead to an output consisting of multiple instead of single pulses, or even

[2]The reflectivity was measured by FBH using dummy substrates that were included in the coating process.

inhibit a pulse build-up [91, 113, 188–190]. Experimental work, see, e.g. Ref. [190], has shown that it is necessary to reduce the residual reflectivity at the resonator-side facet to 10^{-4} or less in order to allow for stable mode-locking.

Multiple pulses have not been detected with any of the diode laser chips investigated in this thesis work. However, another effect is detected, so-called self-lasing of the diode laser chip without optical feedback from the external mirror, see Fig. 4.13. To ascertain that the effect is due to an insufficient AR coating of the rear facet (reflectivity of 10^{-4}), the intra-cavity micro-lens of the ML-ECDL (Fig. 2.9) has been omitted from the test mount. Additionally, the highly divergent beam has been blocked by means of a beam dump. All sections of the 2 mm long diode laser chip were electrically contacted in parallel. To investigate self-lasing, the optical power emitted through the front facet of the diode laser chip as a function of the gain section injection current is depicted in Fig. 4.13(a). The laser threshold is reached at about 115 mA without any feedback from the external mirror. At an injection current of 250 mA, an optical output power of around 20 mW is achieved. Due to the lack of spectral selection in the laser cavity which consists of only the diode laser chip, an unstable (longitudinal) multi-mode operation regime is observed, see Fig. 4.13(b). With increasing injection current an effective red shift of the peak wavelength occurs with a rate of around 12.9 pm/mA due to thermal heating of the active region [191].

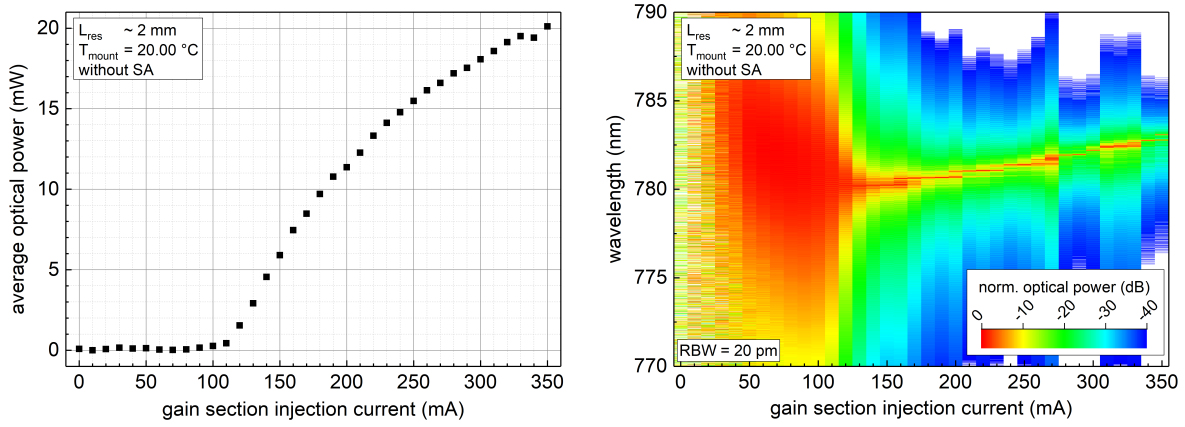

(a) average optical power

(b) optical spectrum

Figure 4.13.: Self-lasing of the diode laser chip as a result of insufficient AR coating of the intra-cavity facet of the diode laser chip. The (a) average optical power and the (b) optical spectrum were recorded without feedback from the extended cavity. To that end, the intra-cavity facet lens was omitted and the divergent beam was captured by a beam dump. Additionally, all sections of the laser were connected in parallel, i.e. the laser was operated without a saturable absorber (SA). The optical spectra are normalized to the individual peak optical power of each step of the gain section injection current.

Next, the ML-ECDL is assembled with the diode laser chip used in the investigation described above. In mode-locked operation, a modulation of the optical spectrum of the ML-ECDL is found, see Fig. 4.14. For the shoulder of this spectrum, see inset of Fig. 4.14, an average

wavelength period of the modulation of $\langle \Delta\lambda \rangle_{39\ \text{peaks}} = 38.05\ \text{pm} \pm 0.98\ \text{pm}$ with a modulation depth up to about 0.5 dB can be estimated. This wavelength period corresponds well to the physical length of the diode laser chip, assuming an effective refractive index of about 3.8. This suggests parasitic feedback from the resonator-side facet of the diode laser chip due to an insufficient AR coating. However, the RF linewidth and the RMS integrated timing jitter of the pulse repetition rate (about 3.97 GHz) measure only about 320 Hz (RBW = 1 Hz, Lorentzian fit) and about 1 ps (IB 10 kHz - 10 MHz), respectively. This points to a stable mode-locked regime despite the parasitic feedback.

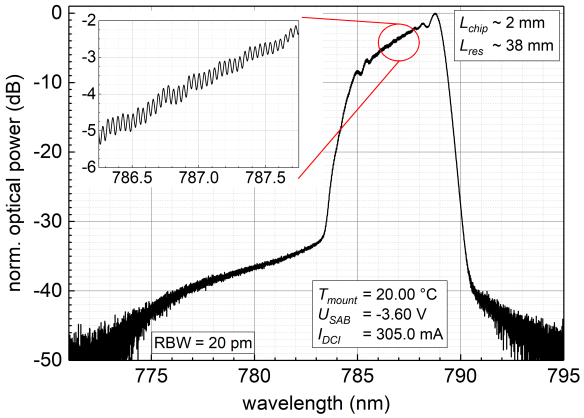

Figure 4.14.: Modulation of the mode-locked optical spectrum due to parasitic feedback from the resonator-side facet. The mode-locked optical spectrum was recorded for the same diode laser chip which was employed for the measurements shown in Fig. 4.13. The inset shows a narrow spectral range of the shoulder of the optical spectrum to highlight the influence of the power modulation.

Reduction of residual reflectivity of the resonator-side facet of the diode laser chip can be realized by, e.g., tilting the waveguide w.r.t the resonator-side facet [91, 113, 190, 192]. Implementation of such tilts, however, requires a new wafer whose production is not feasible within this work but needs to be considered for future developments.

The findings show that an AR coating in the order of 10^{-4}, which has been reported as maximum acceptable resonator-side facet reflectivity for stable mode-locking [190], is insufficient to suppress formation of parasitic cavities but is sufficient to provide a mode-locking performance with high RF stability, i.e. an RF linewidth better than 10 kHz, see Sec. 1.2.4.

Front facet reflectivity

It is known that the reflectivity of the front facet of an ML-ECDL affects, e.g., the optical power within the optical resonator, the spectral bandwidth, and the RF stability [154, 193–195]. To investigate the influence of the front facet reflectivity of the ML-ECDL, two nominally identical 2 mm long diode laser chips (sDQW(780)) featuring front facet reflectivities of 5 % (sDQW-5) and 10 % (sDQW-10) were employed. This study was conducted very early in this work when only diode laser chips featuring an sDQW epitaxial layer structure designed for emission around 780 nm were available. The values of operating parameters for the ML-ECDLs are summarized

in Tab. 4.9. Key parameters of the mode-locking performance of the investigated ML-ECDLs are summarized in Tab. 4.10.

Table 4.9.: Operating parameters of the ML-ECDLs featuring sDQW diode laser chips with different front facet reflectivities R_f. I_{DCI} - gain section injection current, L_{res} - laser resonator length, T_{mount} - mount temperature, U_{SAB} - saturable absorber reverse voltage.

reflectivity	chip	operating parameter			
R_f/%	denotation	T_{mount}/°C	U_{SAB}/V	I_{DCI}/mA	L_{res}/mm
5	sDQW-5	20.0	-3.60	305.0	37
10	sDQW-10	20.0	-3.70	280.0	38

Table 4.10.: Key parameters of the mode-locking performance of the ML-ECDLs featuring sDQW diode laser chips with different front facet reflectivities R_f. λ_p - peak wavelength, $\Delta\lambda_3$ and $\Delta\lambda_{20}$ - spectral bandwidth at 3 dBc and 20 dBc, f_{rep} - pulse repetition rate, Δf_{rep}^{L} - RF linewidth, t_p - pulse width at FWHM, P_{avg} and P_p - average and peak optical power.

parameter	R_f	λ_p	$\Delta\lambda_3$	$\Delta\lambda_{20}$	f_{rep}	Δf_{rep}^{L}	t_p	P_{avg}	P_p
unit	%	nm	nm	nm	GHz	Hz	ps	mW	W
sDQW-5	5	788.76	1.78	5.81	4.00	321	8.4	91.5	2.40
sDQW-10	10	789.64	2.19	5.83	3.97	535	5.4	117.4	4.82

The sDQW devices with front facet reflectivities of 5 % and 10 % show very similar spectral characteristics (peak wavelength λ_p, spectral bandwidths $\Delta\lambda_3$ at 3 dBc and $\Delta\lambda_{20}$ at 20 dBc). Differences between these lasers can be found in the RF linewidth, the pulse width, and the optical power.

The sDQW-5 laser provides an RF linewidth Δf_{rep}^{L} of about 321 Hz which amounts to only about two thirds of the RF linewidth of the sDQW-10 device. This result indicates a higher RF stability for the sDQW-5 device.

The pulse width t_p (sech^2 shape) of the sDQW-5 device is by about a factor of 1.6 larger than that of the sDQW-10 device. However, in contrast to the expectation, the average optical power P_{avg} of the sDQW-5 device about 20 % lower than that of the sDQW-10 laser. Typically, at a lower facet reflectivity and similar values of operating parameters a higher output power would be expected. The result suggests that the sDQW-5 device is operated in a regime with strong gain saturation [154].

The results of the investigation presented above show no distinct advantage for using a low (5 %) or high (10 %) front facet reflectivity. Thus, further investigations were performed with a larger difference in front facet reflectivity. To this end, the mode-locking performance of nominally identical ML-ECDLs using 2 mm long aDQW diode laser chips with a front facet reflectivity of 5 % (aDQW-5) and 30 % (aDQW-30), respectively, was compared. The values of operating parameter of those devices that allow for the largest spectral bandwidths at 20 dBc are given in Tab. 4.11. Key parameters of the mode-locking performance are compared in Tab. 4.12 and discussed in the following.

Table 4.11.: Operating parameters of the ML-ECDLs featuring aDQW diode laser chips with different front facet reflectivities R_f. I_{DCI} - gain section injection current, L_{res} - laser resonator length, T_{mount} - mount temperature, U_{SAB} - saturable absorber reverse voltage.

reflectivity	chip	operating parameters			
R_f/%	denotation	T_{mount}/°C	U_{SAB}/V	I_{DCI}/mA	L_{res}/mm
5	aDQW-5	20.0	-1.55	245.0	44
30	aDQW-30	21.8	-4.16	240.0	44

Table 4.12.: Key parameters of the mode-locking performance of the ML-ECDLs featuring aDQW diode laser chips with different front facet reflectivities R_f. λ_p - peak wavelength, $\Delta\lambda_3$ and $\Delta\lambda_{20}$ - spectral bandwidth at 3 dBc and 20 dBc, f_{rep} - pulse repetition rate, Δf_{rep}^L - RF linewidth, t_p - pulse width at FWHM, P_{avg} and P_p - average and peak optical power.

parameter	R_f	λ_p	$\Delta\lambda_3$	$\Delta\lambda_{20}$	f_{rep}	Δf_{rep}^L	t_p	P_{avg}	P_p
unit	%	nm	nm	nm	GHz	kHz	ps	mW	W
aDQW-5	5	771.22	1.67	16.12	3.40	5.3	4.9	25.34	1.34
aDQW-30	30	774.66	5.60	15.01	3.40	1.5	4.4	14.46	0.85

The peak wavelength λ_p of the aDQW-5 device is slightly reduced compared to the aDQW-30 device.

The spectral bandwidth at 3 dBc of the aDQW-5 device is only about a third of that of the aDQW-30 device. However, both devices feature a similar spectral bandwidth at 20 dBc, see Tab. 4.12. Thus, both devices exceed the requirement on the spectral bandwidth of more than 13 nm, see Sec. 1.2.4.

The RF linewidth Δf_{rep}^L of the aDQW-5 device measures about 5.3 kHz. Compared to the RF linewidth of the aDQW-30 device, this value is about a factor of 3.5 larger. Thus, both devices show RF linewidths that are about an order of magnitude larger than those of the sDQW-5 and sDQW-10 devices investigated above (see Tab. 4.10). Nevertheless, both, the aDQW-5 and the aDQW-30 device are still well within the requirements defined in Sec. 1.2.4.

The pulse widths of both lasers are about 5 ps pulses (sech^2 shape).

The average and peak optical power of the aDQW-5 laser are about a factor of 1.8 and 1.6, respectively, larger than those of the aDQW-30 laser. This is qualitatively expected due to the lower front facet reflectivity of the aDQW-5 device compared to the aDQW-30 device.

The investigation presented in this section shows that the front facet reflectivity has only a minor influence on the spectral bandwidth at 20 dBc. However, a tendency towards a slightly larger spectral bandwidth with a front facet reflectivity of only 5 % can be seen for the aDQW devices. As these devices provide a spectral bandwidth at 20 dBc exceeding the requirement of about 13 nm, a front facet reflectivity of 5 % is preferred in this work. Nevertheless, the results discussed here show that if future applications lay a focus on other criteria, like the RF linewidth, such performance characteristics could be optimized by means of the front facet reflectivity with only minor loss of spectral bandwidth at 20 dBc.

4.2.7. Conclusion for optimization of the laser design

At the beginning of this work, no diode laser-based OFC in the wavelength range around 773.5 nm providing a spectral bandwidth of at least 13 nm and featuring a pulse repetition rate in the gigahertz range was available. In close cooperation with the FBH, such a diode laser was to be developed. The development was limited to those lasers that could be micro-integrated on a micro-integration platform FBH was developing for CW-ECDLs. The investigations presented in this chapter have shown the following laser design to be best suited to fulfill the requirements defined in Sec. 1.2.4:

Optical design: An optical design of the mode-locked ECDL is selected that is based on the design of CW-ECDLs developed at FBH. The laser comprises a diode laser chip, two single aspheric micro-lenses with an effective focal length of 2 mm for (resonator internal and external) collimation, and an external mirror.

External mirror: A plane dielectric mirror featuring a coating with a reflectivity of 97 % and approximately zero GVD at the resonator-side facet, and an AR coating at the other facet is selected. Within this work the commercially available Layertec GmbH 10108 mirror is used. This mirror can also be grinded to dimensions so that it can be implemented in the micro-integrated laser module.

Laser resonator length: The length of the laser resonator was investigated with regard to the spectral bandwidth and the RF stability. It was found that the ML-ECDL with a longer the laser resonator provided the larger the spectral bandwidth and the higher the RF stability. Thus, while originally a resonator length of about 22 mm (f_{rep} = 6.8 GHz) was planned, a laser resonator of about 44 mm length (f_{rep} = 3.4 GHz) that can be implemented in a micro-integrated laser module, is selected.

Epitaxial layer structure of diode laser chip: In the wavelength range of interest, tensile-strained GaAsP QW layers will be employed. The arsenic content of the QWs strongly influences the peak wavelength of the laser emission. It was found that by increasing the As content by an amount of only 0.06 from 0.75 to 0.81 the peak wavelength of the modal gain of an sDQW structure can be shifted from 760 nm to 780 nm. The corresponding mode-locked optical spectra feature slightly longer peak wavelengths of around 766.5 nm and 789.4 nm, respectively. This wavelength shift with arsenic content was employed in an aDQW structure where the As contents of one and the other QW correspond to that of the sDQW structures emitting at 760 nm and at 780 nm, respectively. The modal gain of that aDQW shows a strongly increased bandwidth with peaks at the wavelengths corresponding to each of the two QWs. A diode laser chip featuring such an aDQW was implemented in a mode-locked ECDL. The mode-locked optical spectrum clearly shows the double subband structure. It provides a spectral bandwidth of more than 16 nm at 20 dBc which fulfills the requirements on the spectral bandwidth. The RF linewidth measured about 6 kHz which is within the requirements. Therefore, diode laser chips featuring the aDQW epitaxial layer structure is selected.

Longitudinal design of the diode laser chip: The influence of the length of the saturable absorber

section as well as the influence of the length of the gain section were investigated. It was found that 2 mm long diode laser chips with a 100 µm long saturable absorber section provide the largest spectral bandwidth at 20 dBc and also the highest RF stability.

Facet reflectivity of the diode laser chip: In a last step, the facet reflectivities of the diode laser chips were investigated. It was shown, that an optimized AR coating is required for the resonator-side facet, as an insufficiently low AR coating leads to build-up of a parasitic sub-cavity. A low-reflectivity (5 %) coating of the front facet of the diode laser chip provides the largest spectral bandwidth while still meeting the RF stability requirement. Thus, an optimal front facet reflectivity was determined to correspond to 5 %.

A ML-ECDL featuring this optimal laser design was realized in the (macroscopic) laser test mount. In the following, this ML-ECDL and its performance will be described in detail.

4.3. Influence of the laser operating parameters on the performance of the best suited device

In this section, the influence of the operating parameters, particularly of the gain section injection current, will be investigated. To that end, an ML-ECDL featuring the optimal laser design that was determined in the preceding section was implemented in the laser test mount (Sec. 3.3.1).

The investigations above have shown that the ML-ECDL providing the required spectral bandwidth consists of a diode laser chip with an aDQW epitaxial layer structure integrated into an approx. 44 mm long extended cavity, aspheric micro-lenses, and an external mirror with nearly zero-GVD. The diode laser chip is 2 mm long and features a 100 µm long saturable absorber and a 1900 µm long gain section. The front facet of the diode laser chip situated at the absorber section and acting as laser output facet is coated to 5 % reflection, while the rear facet is AR coated. The optical mode is shaped in the diode laser chip by a 4.8 µm thick vertical ASLOC structure and a 4 µm wide ridge waveguide. The diode laser chip's emission is collimated internally and externally of the laser resonator by means of aspheric micro-lenses with an effective focal length of 2.0 mm. In the following, this laser will be referred to as aDQW laser.

In this section, the mode-locking characteristics of the aDQW laser will be discussed. To provide the largest spectral bandwidth, the test setup was temperature stabilized to 20.0 °C and a reverse voltage of -1.55 V was applied to the saturable absorber section of the aDQW laser. To investigate the mode-locking, the injection current of the gain section was varied from slightly below threshold current to the value at which the spectral bandwidth starts to decrease. In the course of this investigation, the influence of the mount temperature was also studied.

4.3.1. Optical frequency domain characteristics

The optical frequency domain, i.e. spectral, characteristics of the aDQW laser are shown in Fig. 4.15. The optical spectra of the aDQW laser for increasing and decreasing gain section injection current are depicted in false-color plots in Figs. 4.15(a) and 4.15(b), respectively. In Figs. 4.15(a) and 4.15(b), the K D2 transition wavelength ($\approx$ 776.70 nm) and the Rb D2

transition wavelength ($\approx$ 780.24 nm) are marked for reference. Additionally, the wavelengths at 20 dBc are highlighted by black dots. The peak wavelength λ_p, and the spectral bandwidth $\Delta\lambda_3$ at 3 dBc and $\Delta\lambda_{20}$ at 20 dBc extracted from the optical spectra are shown in Figs. 4.15(c) and 4.15(d), respectively.

Increasing the gain section injection current shows a lasing threshold of about 225 mA. Mode-locking is achieved from this lasing threshold up the maximum investigated gain section injection current setting of 250 mA, see Fig. 4.15. It can be seen that with increasing gain section injection current, the peak wavelength λ_p decreases, as expected from the results shown in Fig. 4.6 (Sec. 4.2.4). This relationship is reversed for the maximum gain section injection current settings. The peak wavelength reaches its minimum value at the gain section injection current that provides the maximum spectral bandwidth. The results suggest that above a gain section injection current of about 245 mA, thermal heating dominates over carrier related effects.

At the lasing threshold, a maximum spectral bandwidth $\Delta\lambda_3$ at 3 dBc of about 8.4 nm is achieved. For higher gain section injection current, $\Delta\lambda_3$ is almost constant at about 1.8 nm. It can also be seen from the 3 dBc spectral bandwidth, that the spectral band generated by one of the QWs dominates the optical spectrum. By means of the peak wavelength, this spectral band is identified as the shorter-wavelength band that is generated by the QW with the lower As content.

The spectral bandwidth $\Delta\lambda_{20}$, in contrast, features a minimum at the lasing threshold of about 13.3 nm. With increasing gain section injection current, $\Delta\lambda_{20}$ increases until a maximum of about 16.1 nm is achieved at 245 mA. At the maximum gain section injection current, $\Delta\lambda_{20}$ decreases due to the strongly decreasing optical power in the longer-wavelength spectral band. Further, the optical power contained in the longer-wavelength spectral band decreases with increasing gain section injection current.

When decreasing the gain section injection current, the same spectral characteristics (λ_p, $\Delta\lambda_3$, $\Delta\lambda_{20}$) are achieved when increasing the gain section injection current above a gain section injection current of about 220 mA (lasing threshold for increasing gain section injection current). Below a gain section injection current of 220 mA, the peak wavelength jumps to longer wavelengths by about 6 nm. In this gain section injection current range, the spectral band of the longer-wavelength QW dominates. With further decreasing gain section injection current, the peak wavelength decreases by about 0.5 nm. Aside from the value at 225 mA, the spectral bandwidth $\Delta\lambda_3$ remains nearly constant for the investigated current range. The spectral bandwidth $\Delta\lambda_{20}$ decreases below 225 mA. Between 220 and 215 mA, this decrease corresponds to a jump of about 3.5 nm. For further decreasing gain section injection current, $\Delta\lambda_{20}$ increases by about 0.1 nm/mA.

From the results described above, the ML-ECDL shows a strong hysteresis effect with increasing and decreasing gain section injection current. Where mode-locked operation exists for both increasing and decreasing gain section injection current, no change in the spectral characteristics can be determined for increasing and decreasing gain section injection current. Mode-locked operation is maintained down to a gain section injection current of 205 mA.

While the spectral bandwidth requirement is clearly met, it can be seen (Figs. 4.15(a) and 4.15(b)) that the K D2 transition wavelength is outside the 20 dBc limit by at least 2.05 nm. However, further tuning of the spectrum towards shorter wavelengths by means of the gain

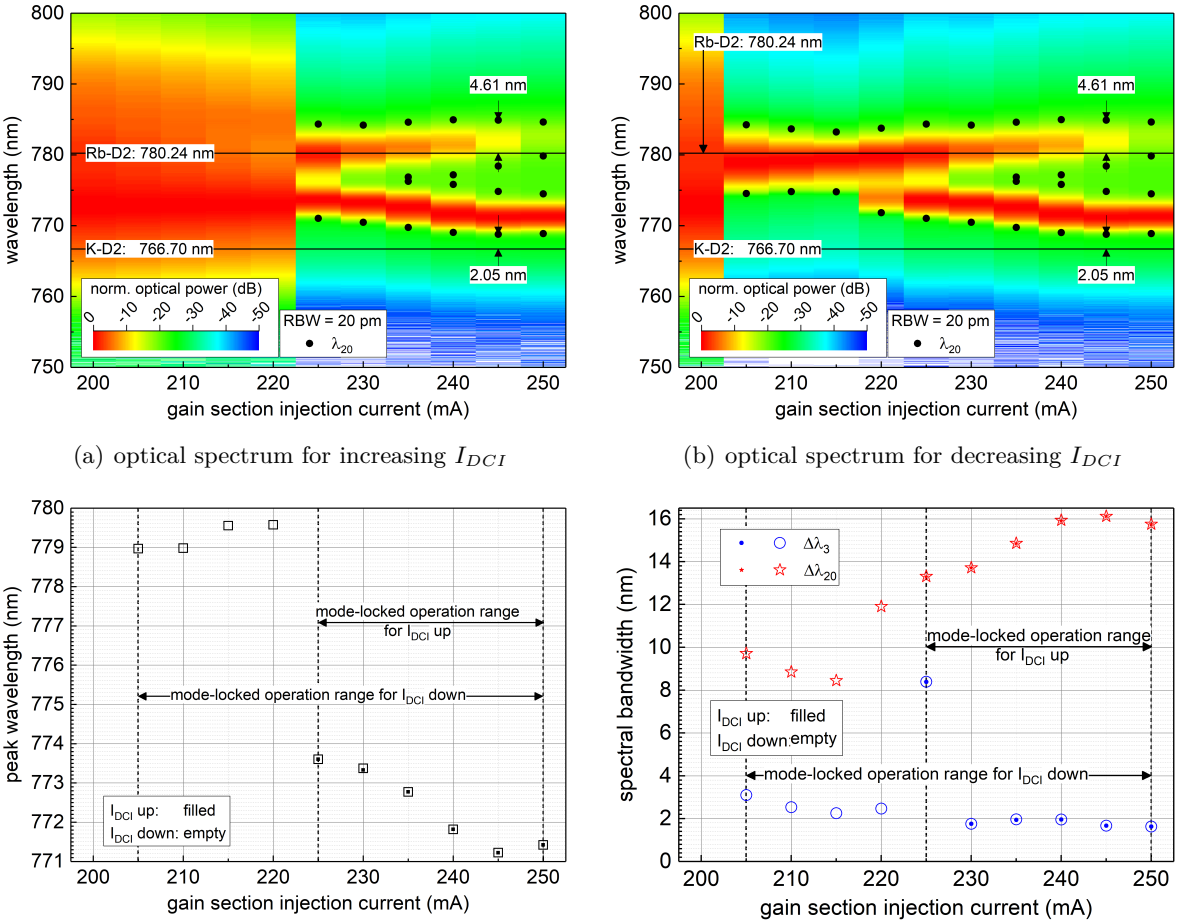

(a) optical spectrum for increasing I_{DCI}

(b) optical spectrum for decreasing I_{DCI}

(c) peak wavelengths extracted from (a) and (b)

(d) spectral bandwidths extracted from (a) and (b)

Figure 4.15.: Optical spectra for (a) increasing and (b) decreasing gain section injection current (I_{DCI}). Extracted from the optical spectra are (c) the peak wavelengths and (d) the spectral bandwidths $\Delta\lambda_3$ at 3 dBc and $\Delta\lambda_{20}$ at 20 dBc of the large spectral bandwidth ML-ECDL. In the optical spectra (a) and (b), the wavelengths at 20 dBc are highlighted in black dots. The extracted spectral characteristics (λ_p, $\Delta\lambda_3$, $\Delta\lambda_{20}$) are depicted for increasing (filled symbols) and decreasing (empty symbols) gain section injection current. The values of operating parameters (mount temperature T_{mount} = 20.0 °C and saturable absorber reverse voltage U_{SAB} = -1.55 V) were optimized at a gain section injection current (DCI) of 245 mA to provide the broadest mode-locked optical spectrum.

section injection current would be detrimental to the spectral bandwidth. Therefore, a different tuning actuator is required for further tuning of the optical spectrum.

Another wavelength tuning actuator is the laser temperature which can be tuned via the mount temperature T_{mount} [135]. To investigate the temperature dependency of the optical spectrum of the ML-ECDL, the mount temperature is varied from 16 °C to 24 °C, see Fig. 4.16. The corresponding optical spectra are shown in Fig. 4.16(a). For better insight into the spectral characteristics, the peak wavelengths of the spectral band provided by each QW (QW1 and QW2, shorter- and longer-wavelength QW, respectively) and the wavelengths (L1, L2, L3, L4) at which the relative optical power of 20 dBc is achieved are depicted in Fig. 4.16(b). The spectral bandwidth $\Delta\lambda_3$ of each spectral band (for QW1 and QW2) and the spectral bandwidth $\Delta\lambda_{20}$ are shown in Fig. 4.16(c). For each temperature, the values of the operating parameters, i.e. the reverse voltage of the saturable absorber and the gain section injection current, are optimized to allow for the largest spectral bandwidth, see Tab. 4.13.

First, the dependence of the peak wavelengths on the mount temperature (Fig. 4.16(b)) is discussed. Almost no change of the peak wavelength λ_{pQW1} of the shorter-wavelength QW of the aDQW structure is found for temperatures between 16 °C and 22 °C. For the last two temperature settings, to 24 °C and 26 °C, however, λ_{pQW1} increases by roughly 0.75 nm/K. In contrast, the peak wavelength λ_{pQW2} of the longer-wavelength QW of the aDQW structure increases monotonically with temperature. Except for the temperature increase from 16 °C to 18 °C (about 1.3 nm/K), a wavelength shift of at least 0.4 nm/K can be estimated. This results suggests that the longer-wavelength QW of the aDQW structure features a stronger sensitivity to temperature variations. This sensitivity may be due to the larger arsenic content of the longer-wavelength QW compared to the shorter-wavelength QW. A detailed analysis of this is, however, not within the scope of this thesis.

Second, the overlap of the optical spectrum presented above and the required wavelength range (from the K D2 transition wavelength, approx. 766.7 nm, to the Rb D2 transition wavelength, approx. 780.24 nm) is investigated. To that end, the dependence of the wavelengths λ_{20} at 20 dBc on the mount temperature is analyzed, see Fig. 4.16(a). For the shortest (L1) and longest (L4) wavelengths λ_{20}, the dependence of the wavelength on the mount temperature is determined by means of a line fit. This yields a wavelength shift of approximately 0.27 nm/K and 0.34 nm/K for L1 and L4, respectively. Thus, to allow for L1 to be at 766.7 nm (K D2), the mount temperature would need to be decreased to 11 °C. At this mount temperature, L4 would measure about 780.9 nm. Thus, at a mount temperature of about 11 °C, the optical spectrum would cover the required wavelength range. To verify this, the mount temperature

Table 4.13.: Values of operating parameter of the ML-ECDL for the investigation of the temperature dependency of the optical spectrum.

parameter	parameter value					
T_{mount}/°C	16.0	18.0	20.0	22.0	24.0	26.0
U_{SAB}/V	−1.75	−0.95	−1.55	−1.08	−0.67	−0.61
I_{DCI}/mA	226.71	244.86	245.00	250.29	250.80	250.79

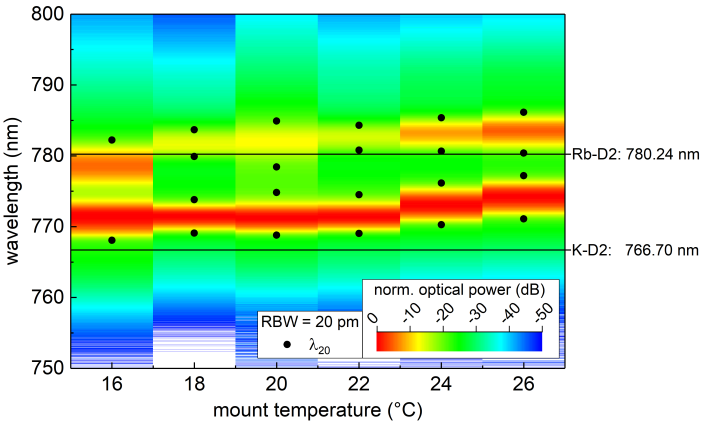

(a) map of optical spectra

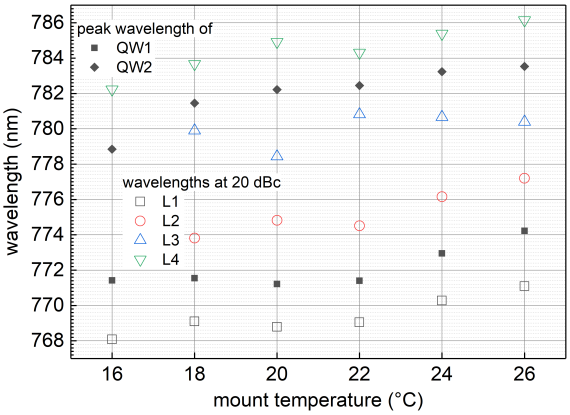

(b) peak wavelengths and wavelengths at 20 dBc

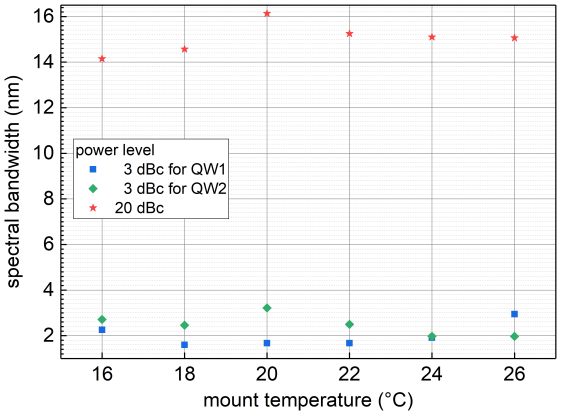

(c) spectral bandwidths

Figure 4.16.: Dependence of the optical spectrum on the mount temperature. The values of the operating parameters are listed in Tab. 4.13. These values provide the broadest spectral bandwidth at 20 dBc for the respective mount temperatures.

needs to be set to 11 °C. However, this decrease of the mount temperature is not feasible with an unpackaged laser due to the risk of condensation. Appropriate packaging is possible, see, e.g. Ref. [78], but not feasible in this work. To relax the requirements on the packaging, the As content of the QWs could be adjusted. In particular, reducing the As content of the shorter wavelength QW should allow for operation at room temperature. This solution would, however, require growing another wafer with appropriate composition parameters which is not feasible in this thesis. Therefore, the ML-ECDL that best meets the requirements (see Sec. 1.2.4) is presented here.

Third, the dependence of the spectral bandwidth on the mount temperature (Fig. 4.16(c)) is discussed. It can be seen that a maximum spectral bandwidth at 3 dBc of about 2.3 nm and 3.0 nm, respectively, is achieved for the lowest and highest mount temperatures, see Fig. 4.16(b).

For the intermediate mount temperatures, spectral bandwidths at 3 dBc of less than 2 nm are reached.

For the spectral bandwidths $\Delta\lambda_{20}$ at 20 dBc, it can be seen (Fig. 4.16(c)) that a maximum is achieved at 20 °C. For further increasing and further decreasing mount temperatures, $\Delta\lambda_{20}$ decreases. Nevertheless, a spectral bandwidth $\Delta\lambda_{20}$ at 20 dBc exceeding 14 nm is achieved across the whole investigated range of mount temperatures. This is well within the requirements of more than 13.5 nm, see Sec. 1.2.4.

4.3.2. RF frequency domain characteristics

The RF spectra corresponding to the optical spectra achieved with a mount temperature of 20.0 °C and a reverse voltage applied to the saturable absorber of -1.55 V are shown in Fig. 4.17.

To give details on the RF spectrum in a broad frequency range, Fig. 4.17(a) depicts the RF spectrum corresponding to the broadest optical spectrum. It can be seen that the pulse repetition rate is about 3.4 GHz and features a SNR of more than 50 dB (limited by the noise floor of the measurement instrument (combination of fast photodetector, broadband amplifier, and electrical spectrum analyzer)). Its 8$^{\text{th}}$ harmonic (n_H) still shows a SNR of about 50 dB indicating a well modulated pulse train.

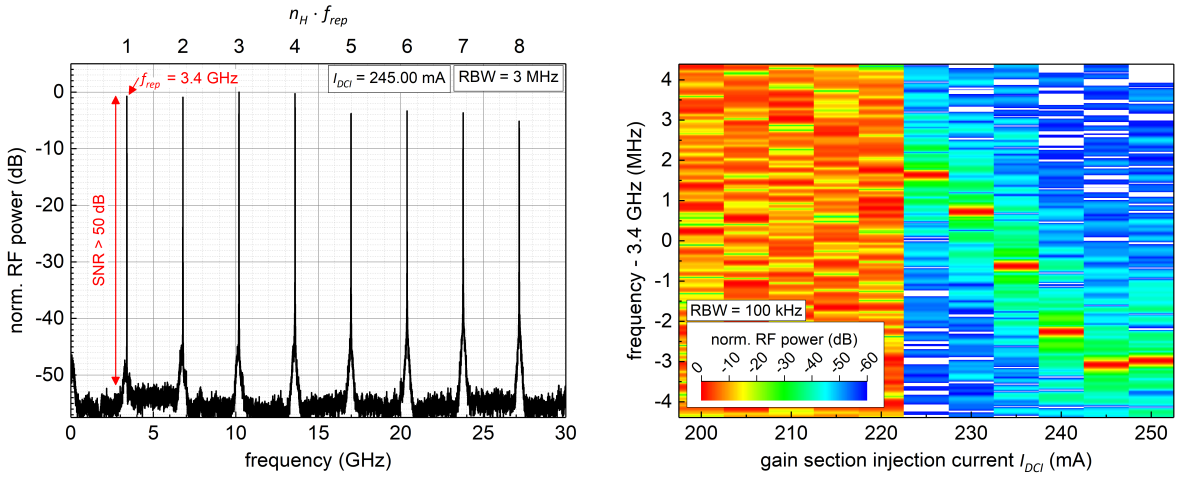

(a) RF spectrum for single I_{DCI}

(b) map of RF spectra for increasing I_{DCI}

Figure 4.17.: RF spectra recorded simultaneously to the optical spectrum shown Fig. 4.15. (a) The RF spectrum is depicted for those values of operating parameters that allow for the largest spectral bandwidth at 20 dBc. (b) The dependence of the RF spectrum on the increasing gain section injection current I_{DCI} is shown in a false-color plot of the corresponding RF spectra in a narrow frequency range around the pulse repetition rate ($f_{rep} \approx 3.4$ GHz). A mount temperature of 20.0 °C and a saturable absorber reverse voltage of -1.55 V were set.

To investigate the dependence of the RF spectrum on increasing gain section injection current, the RF spectra are depicted in Fig. 4.17(b) in a narrow frequency range around $f_{rep} = 3.4$ GHz.

The (peak) level indicating the pulse repetition rate is shown in red. It can be seen that the pulse repetition rate first decreases by roughly 250 kHz/mA with increasing gain section injection current until a minimum is reached at $I_{DCI} = 245$ mA. This minimum pulse repetition rate is reached for the same gain section injection current that allows for the maximum spectral bandwidth at 20 dBc, see Fig. 4.15. This decrease of the pulse repetition rate could be explained by the increase of pulse energy which would lead to a decrease of the pulse repetition rate [196]. However, the average optical power is almost constant for increasing the gain section injection current, as will be shown later in Fig. 4.20. Thus, it is unlikely that the pulse energy is the source for that behavior. Another approach for an explanation is the fact that increasing gain section injection current also modifies the gain saturation level [189]. This modification can in turn lead to changes in the pulse repetition rate. Above 245 mA, the pulse repetition rate starts to increase again. The overall behavior of the pulse repetition rate with increasing DCI suggests that it is a combined result of changes of the level of the modal gain [196] as well as changes of the refractive index due to changed values of the DCI [197]. Further, the change of the gain section injection current also affects the laser temperature and the peak wavelength which, both, also change the refractive index [197]. Please note, that the behavior of the pulse repetition rate with increasing gain section injection current corresponds to that of the peak wavelength of the optical spectrum, see Sec. 4.3.1. This suggest a dominant influence of the peak wavelength on the refractive index and, thus, on the pulse repetition rate.

For future optimization of the ML-ECDL, a detailed investigation of the dependency of the RF spectrum on all values of operating parameters of the ML-ECDL is recommended.

4.3.3. Time domain-based RF characteristics

The dependence of the FN-PSD of the frequency fluctuations of the pulse repetition rate of the ML-ECDL on increasing gain section injection current is shown in Fig. 4.18.

The FN-PSD is composed of two consecutively recorded measurements to allow for investigations in broad range of Fourier frequencies. For investigation of the low Fourier frequency range (10 Hz - 64 kHz, RBW 1 Hz), a 100 s long time trace was recorded with a sampling rate of 160 kHz and an IQ-RBW of 128 kHz . The high Fourier frequency range (100 Hz - 10 MHz, RBW 100 Hz) was investigated by means of a 500 ms long time that was recorded with a sampling rate of 32 MHz and an IQ-RBW of 25.6 MHz. For the graphical presentation, the RBW of the FN-PSD was adjusted for each Fourier frequency decade to 10 % of the first frequency of each Fourier frequency decade, see top axis labeling in Fig. 4.18(a).

At small Fourier frequencies, the FN-PSD features a peak at the power line frequency of 50 Hz and a vibration noise peak around 13 Hz. It can be seen that with increasing gain section injection current the level of the FN-PSD first slightly increases and later decreases again to a slightly higher level than the level just above threshold. Nevertheless, the dependence of FN-PSD on the gain section injection current is not significant.

At Fourier frequencies above approx. 4 MHz, the FN-PSD slightly increases for all investigated gain section injection current settings. This increase could be a result of the instruments' white phase noise floor. This would lead to a quadratic increase in the FN-PSD with increasing Fourier frequency. However, due the limited single-sided bandwidth (12.8 MHz) available for the IQ measurements, the instruments' white phase noise floor could not unambiguously be

identified as the source of the described behavior of the FN-PSD.

The RF linewidth determined from integrating the FN-PSD (β-separation line method, lower frequency limit 100 Hz, resulting in a measurement time scale of 10 ms) also follows the behavior of the FN-PSD at low Fourier frequencies. Below a gain section injection current of 235 mA, the RF linewidth increases from about 4.6 kHz to around 5.95 kHz. After a jump to around 8.3 kHz at a gain current of 235 mA, the RF linewidth decreases with further increasing gain section injection current to around 5.2 kHz. This corresponds to a variation by less than a factor of 2. The values and behavior of RF linewidth with the gain section injection current could also be determined from the reconstructed RF spectrum.

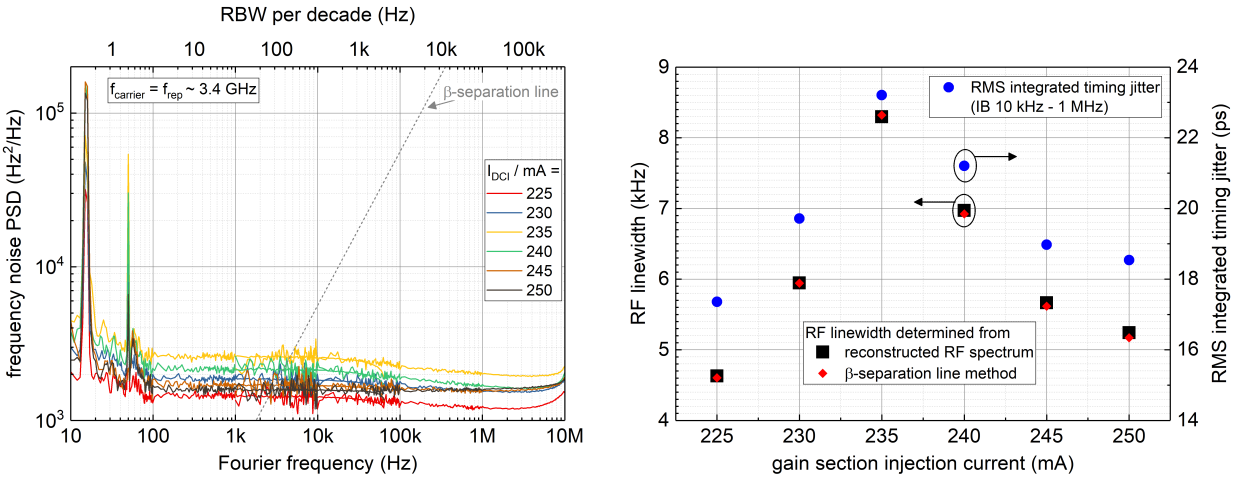

(a) FN-PSD

(b) RF linewidth and RMS integrated timing jitter

Figure 4.18.: (a) FN-PSDs and (b) RF linewidths and RMS integrated timing jitters of RF spectrum with pulse repetition rate as carrier, corresponding to RF spectra shown in Fig. 4.17(b) and the optical spectra depicted in Fig. 4.15. The mount temperature is set to 20.0 °C and a reverse voltage of -1.55 V is applied to the saturable absorber.

As with the RF linewidth, the RMS integrated timing jitter shows little dependence on the gain section injection current, see Fig. 4.18(b). The RMS integrated timing jitter was determined by integration of the FN-PSD shown in Fig. 4.18(a). An integration band (IB) of 10 kHz to 10 MHz was chosen. The upper integrating limit is given by the noise floor of the measurement instruments which can be inferred from the beginning increase of the FN-PSD at around 10 MHz. From threshold on, the RMS integrated timing jitter increases from about 17 ps to around 23 ps at a gain section injection current of 235 mA. A further increase of gain section injection current results in a reduction of timing jitter down to about 18.5 ps.

The behavior of the noise characteristics can be explained by analyzing the optical spectrum, see Fig. 4.15. Below a gain section injection current of 235 mA, the spectral subbands generated by each QW overlap. However, the overlap reduces with increasing gain section injection current. This reduction in overlap can cause a reduction of phase coherence (mode-locking) between the spectra emitted by each QW. When both subbands split at a gain section injection current of around 235 mA, the timing jitter increases (negligibly) by a factor of less than 2. For further

increasing DCI, the RF linewidth and the timing jitter decrease again to about the values determined just above threshold.

The results presented here indicate that in the range of the gain section injection current where a strong relative wavelength shift of the spectral subbands occurs, the mode-locking stability is reduced in terms of lower RF linewidths and RMS integrated timing jitter values. However, the results also suggest that operation in a regime of strong overlap of the spectral bands is to be preferred. In this case, a strong phase coherence between all components of the generated frequency comb is expected. Thus, for future implementation of the ML-ECDL, further advancement of the employed diode laser chip to feature QW that provide strongly overlapping spectral bands is suggested. Using the results presented in Sec. 4.2.4, such a diode laser chip can be realized by, e.g., implementation of an active region with multiple QWs (N_{QW}>2) that feature a smaller step in As content.

4.3.4. Time domain characteristics

In this section, the pulse width and shape corresponding to the optical spectra (see Fig. 4.15) achieved with a mount temperature of 20.0 °C and a reverse voltage applied to the saturable absorber of -1.55 V is investigated.

An indication of reduced spectral coherence which led to the reduction of the RF linewidth can be found by analyzing the temporal shape and width of the mode-locked pulses, see Fig. 4.19. The typical pulse shape is depicted in Fig. 4.19(a) for those values of the operating parameters that provide the largest spectral bandwidth, see Fig. 4.15.

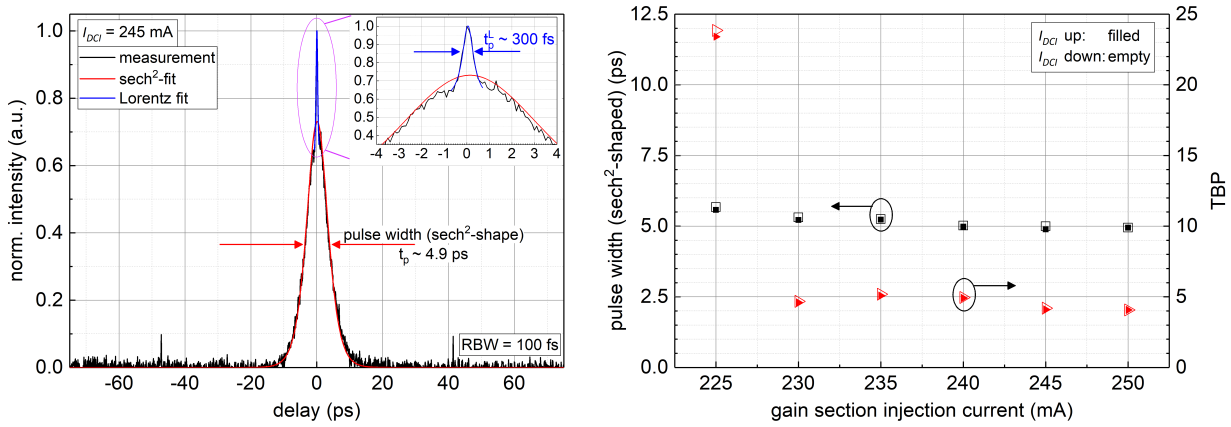

(a) pulse shape

(b) pulse width and shape

Figure 4.19.: (a) Typical autocorrelation function for those values of operating parameters that allow for the largest spectral bandwidth at 20 dBc, and (b) pulse widths and TBPs corresponding to the optical spectra shown in Fig. 4.15.

The autocorrelation function can be described by a sech^2 function overlapped with a Lorentzian-shaped peak. This peak at zero delay suggests spectral incoherence [198]. This coherence spike

is present for the complete range of gain section injection current that is investigated for this laser. In contrast, the sDQW lasers, also investigated in this thesis for their spectral bandwidth, do not show this feature. This finding suggests that the spectral separation of the QWs of the aDQW chip is too wide. However, diode laser chips with an asymmetric QW design with a smaller difference of As content were not available. For future work, a multi-QW (N_{QW}>2) epitaxial layer structure as discussed in the previous section (Sec. 4.3.3) needs to be considered.

The pulse width was deduced from the full width at half maximum (FWHM) of the sech^2-shaped part of the autocorrelation function. It is found that the pulse width of about 5 ps is nearly independent of the gain section injection current, see Fig. 4.19(b).

Calculated from the pulse width and the spectral bandwidth at 3 dBc, the TBP of around 5 (except for just above threshold) is well above the Fourier-limit for sech^2-shaped pulses (about 0.315). This indicates strongly chirped pulses. Due to the near independence of the pulse width (Fig. 4.19(b)) and the spectral bandwidth at 3 dBc (Fig. 4.15(d)) of the gain section injection current, the TBP is also found to be nearly independent of the gain section injection current.

4.3.5. Optical power characteristics

The optical power of the large spectral bandwidth ML-ECDL corresponding to the results shown above is depicted in Fig. 4.20. For this measurement, a mount temperature of 20.0 °C was set and a reverse voltage of -1.55 V was applied to the saturable absorber. The sudden onset of lasing and mode-locking at a gain section injection current of about 225 mA is also evident here. An average optical power of around 28 mW is reached just above threshold. It can be seen that the average optical power slightly decreases with increasing gain section injection current which is accompanied by an increase of spectral bandwidth, see Fig. 4.15.

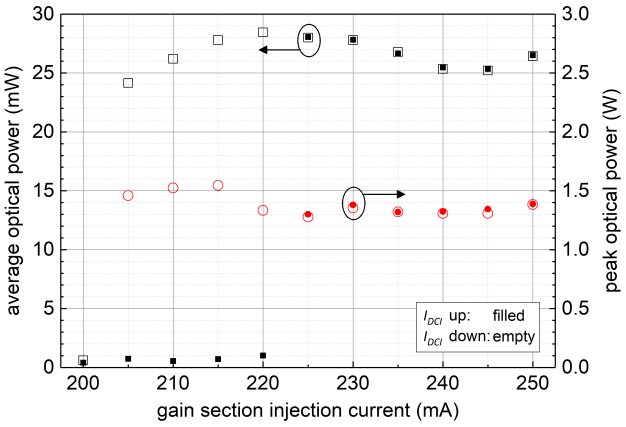

Figure 4.20.: Average and peak optical powers of large spectral bandwidth ML-ECDL, corresponding to the optical spectra shown in Fig. 4.15. A mount temperature of 20.0 °C and a saturable absorber reverse voltage of -1.55 V were set.

A peak optical power of more than 1.3 W (calculated assuming sech^2-shaped pulses, see Fig. 4.19(a)) is achieved. It is found to be almost independent of the gain section injection current. At that gain section injection current (I_{DCI} = 245 mA) that provides the largest

spectral bandwidth, $\Delta\lambda_{20} = 16.12$ nm, see Fig. 4.15, an average and a peak optical power of about 25.4 mW and 1.34 W is reached, respectively. Using the mode-locking characteristics provided by this ML-ECDL, an optical power of about 660 nW can be estimated for those frequency comb lines at 20 dBc at the shorter-wavelength and longer-wavelength part of the optical spectrum, respectively, well exceeding the requirement of at least 100 nW, see Sec. 1.2.4.

4.4. Conclusion of the development of the diode laser-based optical frequency comb

In this chapter, the development of a diode laser-based OFC for the wavelength range centered at around 773.5 nm was presented. To that end, the dependence of the mode-locking performance on relevant parameters was analyzed. The optimization focused on determining the optimal chip design and optimal values for the operating parameters.

First, the dependence of the mode-locking performance on the laser design parameters was investigated. Here, the optimization focused on the determination of the optimal optical design of the ML-ECDL including the optimal choice of an external mirror, and the optimal laser resonator length, as well as the optimal epitaxial layer structure, longitudinal design, and reflectivities of the facet coatings of the diode laser chip. Mechanical limitations of the ML-ECDL setup were given by the size of the micro-optial bench into which the developed laser is to be micro-integrated.

The optical design of the ML-ECDL was developed, showing that single-aspheric micro-lenses with an effective focal length of 2 mm can be employed for shaping the beam emitted by the diode laser chip at both the output and the resonator-side facet. A plane external mirror providing nearly-zero group velocity dispersion can be used as back reflector to minimize temporal pulse distortion. The investigation of the dependence of the mode-locking performance on the laser resonator length has shown that a longer resonator provides a larger spectral bandwidth and a reduced RF noise. Accounting for the aforementioned mechanical limitations, a resonator length of about 44 mm corresponding to a pulse repetition rate of 3.4 GHz was found to be preferable for use of the ML-ECDL in the target experiment.

The investigations of the dependence of the mode-locking performance on the epitaxial layer structure of the diode laser chip were performed. It was verified that the center wavelength of the mode-locked optical spectrum can be red-shifted by increasing the As content of the quantum wells. To that end, the modal gain spectrum, the ASE spectrum, and the mode-locked optical spectrum of diode laser chips featuring an active region with a symmetric double quantum well with different As content ($y_{QW1} = y_{QW2} = 0.75$, 0.78, 0.81, respectively) were compared. To optimize the spectral bandwidth diode laser chips with an asymmetric double quantum well structure ($y_{QW1} = 0.75$, $y_{QW2} = 0.81$) were realized. This enabled the modal gain spectrum, the ASE spectrum, and the mode-locked optical spectrum of this device to be significantly broader than those of the symmetric double quantum well devices. The resulting mode-locked spectral bandwidth of about 16 nm well exceeds the requirement of the target application of more than 13 nm. However, the wavelength range of the OFC generated with the aDQW device was found to be slightly red-shifted compared to the wavelength range required for the target application.

Suggestions for future improvements of the wavelength range were given.

The dependence of the mode-locking performance on the longitudinal structure of the diode laser chip was investigated. First, 1 mm and 2 mm long diode laser chips featuring a 100 µm long saturable absorber section were compared. Second, 2 mm long diode laser with a saturable absorber section length of 50 µm and 100 µm were compared. It was found that the 2 mm long diode laser chips with a 100 µm long saturable absorber section provided enhanced mode-locking performance.

Further, the dependence of the mode-locking performance on the facet reflectivities of the diode laser chip was investigated. It was shown that the best RF stability could be achieved with diode laser chips featuring an optimized AR coating of the resonator-side facet. Moreover, a reflectivity of 5 % of the front facet provides a maximum spectral bandwidth.

Second, the dependence of the mode-locking performance of the device best suited for the target application on the laser operating parameters, particularly the gain section injection current, was investigated.

The best suited device provided a spectral bandwidth of more than 16 nm at 20 dBc in the wavelength range around 773.5 nm. It was shown that the optical spectrum of this device consists of two spectral bands that strongly overlap just above the threshold gain section injection current of about 225 mA. Increasing the gain section injection current to a maximum of 250 mA increases the spectral bandwidth at 20 dBc. The spectral bandwidth at 3 dBc has shown to be nearly independent of the gain section injection current. Investigation of the dependence of the optical spectrum on the temperature has shown the 3 dBc and the 20 dBc spectral bandwidth to be nearly independent of the temperature. A maximum of about 3.2 nm and more than 16 nm at 3 dBc and 20 dBc, respectively, was achieved at 20.0 °C.

The investigation of dependence of the RF spectrum, particularly the pulse repetition rate, of the best suited device on the gain section injection current was performed. For this analysis, the resonator length was set to correspond to a pulse repetition rate of about 3.4 GHz. The pulse repetition rate decreased with increasing gain section injection current up to the gain section injection current value that provided the maximum spectral bandwidth at 20 dBc.

The investigation of the time domain-based RF characteristics showed the best suited device provides an FN-PSD that is nearly independent of the gain section injection current. Further, the FN-PSD features a white noise floor across almost the complete investigated range of Fourier frequencies. The RF linewidth (full width, β-separation line method) measures less than 6 kHz. The RMS integrated timing jitter shows values around 20 ps (integration range 10 kHz - 1 MHz).

Further, the best suited device provides sech^2-shaped pulses with a width of about 5 ps. The pulse shape and width were found to be nearly independent of the gain section injection current. Consequently, the time-bandwidth-product was also found to be nearly independent of the gain section injection current. This result showed that the pulses generated by the best suited devices were strongly chirped.

The investigation of the optical power of the best suited device showed that its average and peak optical power is nearly independent of the gain section injection current. An average power of more than 25 mW and a peak optical power of more than 1.3 W were achieved. Analysis revealed that the OFC generated with the best suited device features an optical power in excess

of 600 nW at 20 dBc. This result exceeded the requirement on the optical power of the comb lines at 20 dBc.

The results presented here show that only the wavelength range achieved with the ML-ECDL needs further optimization for future implementation in the application, see Sec. 1.2. Improvement strategies, e.g. adjustment of the As content of the QWs of the aDQW epitaxial layer structure, were derived. The other requirements on the ML-ECDL (see Sec. 1.2.4) could be reached or even surpassed. Therefore, the hybrid micro-integration of the developed ML-ECDL is the next logical step in the development of a space-suitable diode laser-based OFCG.

5. Micro-integration of the diode laser-based optical frequency comb generator

The results presented in this chapter were already partially published in Refs. [199, 200].

5.1. Introduction to the micro-integration concept

One important goal of this thesis is the demonstration that the diode laser-based optical frequency comb generator (OFCG) can be hybrid integrated into the micro-integration technology platform that was being developed within the LASUS project series, see Sec. 1.2. The technology platform comprises the MIOB into which the laser is hybrid integrated and the heatsink onto which the MIOB is mounted. For cost reasons, re-design of the CW-ECDL-MIOB and realization of a dedicated ML-ECDL-MIOB was not an option. Therefore, critical aspects for hybrid integration of an ML-ECDL and operation of that module were identified and tackled for the already existing ECDL-type MIOB. In order to prepare for hybrid integration into the intended MIOB, the predecessor version of the MIOB was employed to develop a suitable integration concept. In this work, an ML-ECDL is micro-integrated for the first time [199].

In the following, the design of the micro-integration technology platform at the beginning of this work will be described. The critical issues will be highlighted and approaches to resolve these issues introduced. First, the development of a hybrid integrated ML-ECDL based on the most simple approach will be introduced. Then, the next generation, advanced ML-ECDL module will be presented where lessons learned from that first generation ML-ECDL module have been accounted for. The developed and advanced integration concepts utilized for each MIOB will be presented. Furthermore, the mode-locking performance of each module will be discussed in the course of this chapter.

5.2. First generation ML-ECDL module

In this section, the first generation ML-ECDL module will be introduced. It was realized to provide a proof-of-concept with the most simple approach. The hybrid integration of this module was employed to identify critical aspects for hybrid integration of an ML-ECDL. In the following, the micro-integration technology platform, the integration strategy for the ML-ECDL, and the mode-locking performance of the ML-ECDL module will be detailed.

5.2.1. The micro-integration technology platform

The micro-integration technology platform employed for hybrid integration of the ML-ECDL has been developed to cope with the harsh environmental condition of an operation in the ZARM

drop tower experiments [18, 19]. The wide variety of laser modules realized with this multi-purpose platform type include narrow linewidth ECDL-type lasers [18, 76], high power MOPA-type diode lasers [18, 19, 201], and second harmonic generation (SHG)-type laser modules to access wavelengths not directly accessible by GaAs-based diode lasers [18].

The ECDL-type module for hybrid integration of CW-ECDLs

The micro-integration technology platform was already introduced in Sec. 1.2.3. Here, aspects essential for the realization of a micro-integrated CW-ECDL laser module will be presented. A photo of a micro-integrated CW-ECDL module, which is the basis for the development of the ML-ECDL module, is shown in Fig. 5.1(a). The laser comprises a diode laser chip, aspheric micro-lenses for collimation, and a VHBG.

The MIOB consists of a 1 mm thick Au-plated AlN substrate with a footprint of 10×50 mm^2 onto which a second, slightly narrower Au-plated AlN substrate of half the length is adhesively bonded. The second AlN substrate, which carries the diode laser chip (on a submount) and the lenses, allows for height compensation in relation to the VHBG which, for separate thermal control, is placed onto a micro-TEC element. On each side of the MIOB parallel rails made of AlN with a structured Au plating are mounted. They function as optics rails for mounting micro-lenses and as bond pads for electrical interconnection. The abovementioned laser components are directly micro-integrated into the MIOB via adhesive bonding. The lower MIOB is mounted onto a heat-spreader, the conduction-cooled package (CCP). Along each longitudinal side of the MIOB, the CCP features seven electrically isolated contact pads onto which electrical pin jacks are soldered.

Modification of the CW-ECDL module for hybrid integration of an ML-ECDL

The first generation, micro-integrated ML-ECDL module is depicted in Fig. 5.1(b). As a test-bed, the most simple approach for the MIOB is employed compared to the MIOBs used for the CW-ECDL (Fig. 5.1(a)).

A single 1 mm thick AlN ceramic with a footprint of 10×50 mm^2 is used as no height compensation is required for the external mirror compared to the VHBG of the CW-ECDL. Short optics rails, only measuring half the length of the MIOB, are integrated. These rails provide a sufficient number of electrical contact pads.

The electrical interconnection of the diode laser chip is realized in a way similar to how it is realized for the CW-ECDL. Thus, the requirement for two p-side contacts (saturable absorber and gain section) is accounted for. The p-side contact of the gain section and the common n-side contacts are wire-bonded to one side of the MIOB (top in Fig. 5.1(b)) and the p-side contact of the absorber section to the other side (bottom left in Fig. 5.1(b)). For thermal control of the whole MIOB, a temperature sensor (Betatherm GA10K3CG679) is integrated. Its electrical contacts both are wire-bonded to one side of the MIOB (bottom right contact pads in Fig. 5.1(b)).

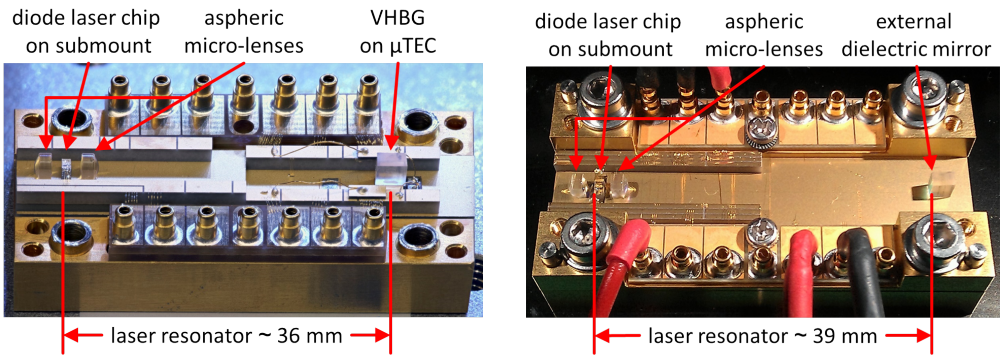

(a) CW-ECDL (b) ML-ECDL

Figure 5.1.: Photo of (a) a CW-ECDL (© FBH/schurian.) and (b) the first ML-ECDL module micro-integrated into the multi-purpose technology platform.

5.2.2. Integration strategy

The integration strategy employed for the ML-ECDL module is based on the one that was employed for the CW-ECDL module. Thus, the integration strategy for the CW-ECDL is briefly introduced first. Then, the integration strategy derived for the ML-ECDL is presented.

Integration strategy for the CW-ECDL

The diode laser chip is soldered p-side up on an AlN submount. This assembly as well as a temperature sensor (Betatherm GA10K3CG679) are adhesively bonded onto the MIOB. Electrical interconnection is realized via wire bonding between the structured Au-plating on the top of the optics rails to the p-side contact of the diode laser chip and to the contact panel on the submount which is connected to the n-side contact of the diode laser chip. The integration of the diode laser chip is performed by the Mounting & Assembly Department of the FBH. Integration of the micro-optics (lenses and VHBG) is realized by means of a nano-positioner (Physik Instrumente (PI) GmbH & Co. KG F-206.S HexAlign™ 6-axis hexapod) featuring a translational resolution of 0.1 µm and an angular resolution of 2 µrad. The micro-optics are held by vacuum tweezers during the alignment process. All optics are adhesively bonded to the surface of the MIOB or of the µTEC by means of a UV-curing glue (Norland NOA88). To that end, the round aspheric micro-lenses were grinded appropriately. The integration of the ECDL is carried out as a two step process. In the first step, the ECDL is aligned for minimum threshold current, and the resonator lens and the VHBG are adhesively bonded directly to the MIOB or to the µTEC, respectively. In a second step, the output lens is used to collimate the ECDL output and adhesively bonded in the same way as the resonator lens.

Integration strategy for the ML-ECDL

The integration strategy for the ML-ECDL includes the integration of the diode laser chip, the preparation of the external mirror, and the assembly process for the micro-optics (lenses and external mirror).

Micro-integration of the diode laser chip

The diode laser chip (details to the integrated diode laser chip in Sec. 5.2.3) and a temperature sensor (Betatherm GA10K3CG679) are integrated into the MIOB using the same strategy that is used for the CW-ECDL. For establishing the electrical interconnection, the need to provide a separate electrical contact for the saturable absorber and the gain section is taken into account. As with the CW-ECDL module, this part of the integration of the ML-ECDL is performed by the Mounting & Assembly Department of the FBH.

Preparation of the external mirror

The external mirror is adhesively bonded to the MIOB. To avoid large angles between the bottom of the external mirror and the MIOB, which can lead to strong beam displacement during curing of the adhesive, the mirror facet is required to be perpendicular to the bottom of the mirror. To allow for that, a round 1/2" commercial mirror (Layertec 101085[1]) is grinded to provide a mirror facet area of 2×4 mm^2. The thickness of the original mirror is grinded from 6.35 mm to 2 mm providing the micro-mirror with a footprint of about 4 mm^2. Consequently, the AR coating of the mirror's rear facet is lost. To avoid parasitic reflections from the rear facet, the micro-mirror's substrate is cut at an angle of around 1° (front facet surface to rear surface).

Assembly process for the micro-optics

The development of the ML-ECDL has shown that the mode-locking performance of the ML-ECDL depends strongly on the feedback angle of the external mirror. To take this sensitivity into account, the optical and RF spectra are monitored during the alignment of the ML-ECDL. To evaluate the diode laser chip for possible defects before completing the integration of the ML-ECDL, the laser resonator is fully aligned before integration of the micro-optics. As the integration robot only allows for integration of a single micro-optic at a time, a temporary micro-lens (at the laser output) and a temporary micro-mirror are employed. The temporary micro-lens is adhesively bonded to an AlN ceramic for rough height alignment to the diode laser chip. To allow for adjustment of the feedback angle, the temporary micro-mirror is mounted into a mirror mount by means of an adapter. To position the temporary mirror into the optical axis of the laser and to optimize the resonator length of the ML-ECDL, the mirror mount is mounted on linear translation stages that are placed next to the integration robot. Further, the development of the ML-ECDL has shown that the diode laser chip requires a burn-in in mode-locked operation for reliable large spectral bandwidth operation. To meet these requirements,

[1] This is a mirror with the same features as the one used in the laser test mount.

the micro-integration is conducted in the following steps:

1. The CCP carrying the MIOB is mounted onto the integration setup with screws that are tightened with a torque of 30 cNm. This step is identical to that of the CW-ECDL modules.

2. To monitor the mode-locking performance during the assembly, the laser output is temporarily collimated by means of the temporary micro-lens. This lens is mounted onto the integration robot, aligned to collimate the laser output, and placed onto the MIOB.

3. The intra-cavity micro-lens is mounted onto the integration robot and positioned to collimate the resonator-side output of the diode laser chip by minimizing the beam diameter in a distance of more than three times the Rayleigh range (Rayleigh range $\approx$ 20 cm). In this step, the intra-cavity micro-lens is not yet adhesively bonded to the MIOB.

4. Then, the temporary micro-mirror is employed to fully align the ML-ECDL.

5. After alignment of the ML-ECDL, the burn-in is performed. Afterwards, the laser is realigned.

6. After burn-in, the intra-cavity lens is adhesively bonded to the MIOB. Beam displacement as a result of glue shrinkage during UV-curing can be compensated for by re-alignment of the temporary micro-mirror.

7. To finish the micro-lenses' micro-integration, the temporary micro-lens at the laser output is removed. The micro-lens that is intended for micro-integration is mounted onto the integration robot and the laser output collimated. Then, this micro-lens is adhesively bonded to the MIOB.

8. In the last step, the temporary external mirror is removed. The micro-mirror that is intended for micro-integration is mounted onto the integration robot. After alignment of the ML-ECDL, the adhesive is applied to the mirror's bottom surface. In a first test run for curing of the adhesive, asymmetric glue shrinkage occurred that led to beam displacement which even stopped laser oscillation. Thus, integration of the micro-mirror in an approach similar to that applied for the VHBG is not possible. Best results are achieved by stepwise curing of the adhesive and realignment of the laser resonator. Here, the adhesive is cured for a very short (less than 1 s) time, the UV illumination stopped, and the mirror realigned. Further, the values of the operating parameters are adjusted to those values that provide the largest spectral bandwidth. These steps are repeated until no further beam displacement can be (indirectly) observed in either the optical or the RF spectrum during UV illumination. About ten iterations amounting to less than 10 s are required. Following this, the adhesive is UV illuminated twice for 10 min for complete curing.

With the micro-integration of the external mirror, the assembly process for the mode-locked ECDL is completed. In the subsequent section, the mode-locking performance of this very first micro-integrated mode-locked ECDL module is investigated.

5.2.3. Mode-locking performance

The micro-integration strategy for the ML-ECDL was developed in parallel to the ML-ECDL itself. Thus, for the first realization of an ML-ECDL module, the at the time best suited device was micro-integrated. For this first micro-integrated ML-ECDL module, a 1000 µm long diode laser chip with a 100 µm long saturable absorber section was employed. The diode laser chip featured an sDQW(780) epitaxial layer structure designed for emission around 780 nm (see, e.g., Sec. 4.2.4). In the vertical direction, a 4.8 µm thick AlGaAs-based waveguide provided a vertical beam divergence angle of about 19° (full width at $1/e^2$ intensity). In the lateral direction, a 4 µm wide ridge waveguide provided a lateral beam divergence angle of about 12° (full width at $1/e^2$ intensity). The front facet of the diode laser chip was coated to 10 % reflection, while the resonator-side facet was AR coated.

The mode-locking performance of the micro-integrated ML-ECDL was analyzed (i) before micro-integration of the external mirror (pre-mirror integration) but with the external mirror mounted on the integration robot, (ii) with the fully micro-integrated module mounted on the integration setup, and (iii) after micro-integration with the module mounted in the measurement setup (see Fig. 3.3). For measurement situations (i) and (ii) the optical power, and the optical and RF spectrum could be investigated. For measurement situation (iii), the pulse width and shape could also be analyzed as the laser module was mounted in the measurement setup of which the autocorrelator is a part. The values of the operating parameters that allow for the largest spectral bandwidth for each analysis step (i, ii, iii) are summarized in Tab. 5.1.

Table 5.1.: Values of the operating parameters of the first ML-ECDL module that provide the largest spectral bandwidth before integration of the external mirror (pre-mirror integration), on the integration setup, and on the measurement setup, respectively.

measurement situation	operating parameters		
	T_{MIOB}/°C	U_{SAB}/V	I_{DCI}/mA
(i) pre-mirror integration	20.00	-0.60	180.00
(ii) integration setup	20.00	-3.60	237.59
(iii) measurement setup	18.05	-0.50	300.00

Comparing the values of the operating parameters for the ML-ECDL before (measurement situation (i)) and after the micro-integration (measurement situation (ii)) of the external mirror shows that different values of the operating parameters provide the largest spectral bandwidth. The reason for that is the alignment of the ML-ECDL that was partially lost during curing of the adhesive for the external mirror. However, mode-locking could partially be re-established by adjusting the values of the operating parameters. Please note that the module was not removed from the integration setup between completion of the integration and these measurements.

The optical spectra before (grey, measurement situation (i)) and after (red, measurement situation (ii)) micro-integration of the external mirror are shown in Fig. 5.2 and the extracted spectral parameters are summarized in Tab. 5.2. Before micro-integration of the external mirror, a peak wavelength about 789.9 nm, and a spectral bandwidths of about 3.1 nm and 5.2 nm at 3 dBc and 20 dBc level, respectively, were observed. Thus, this micro-integrated ML-ECDL

module can reproduce the spectral characteristics observed for a similar ML-ECDL mounted in the laser test mount, see, e.g., Tabs. 4.7 and 4.10. Comparing the spectral bandwidths in measurement situations (i) and (ii), it can be seen that the peak wavelength remained at about 789 nm during curing of the adhesive for the external mirror. However, the spectral bandwidth after completing the hybrid integration was reduced by about 27 % at 3 dBc and about 16 % at 20 dBc to 2.2 nm and 4.4 nm, respectively, compared to before the mirror integration. Further, the average optical power of the laser was reduced by about 16 % from about 95.2 mW to 80.2 mW. This is attributed to the mis-alignment of the laser resonator. Please note that the RF linewidth was not recorded directly before micro-integration of the mirror as the module could not be sufficiently housed because of the need for the integration robot to hold the external mirror. This lack of housing resulted in a strong RMS integrated timing jitter due to air flow in the laboratory. An evaluation of such a measurement does not give an insight on the actual module performance and was hence omitted.

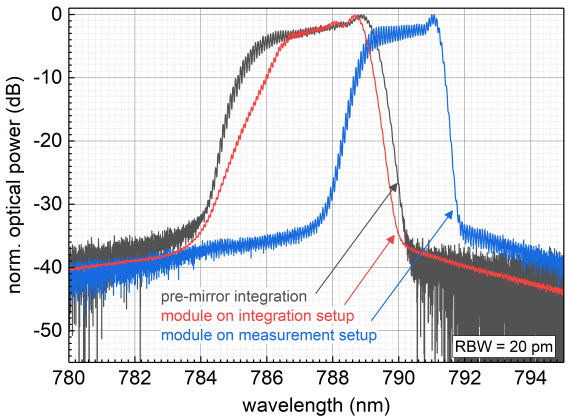

Figure 5.2.: Optical spectra of the first ML-ECDL module (grey) before micro-integration of the external mirror (pre-mirror integration, measurement situation (i)), (red) with the fully micro-integrated module still mounted on the integration setup (measurement situation (ii)), and (blue) after micro-integration and moving of the module to the measurement setup (measurement situation (iii)).

Table 5.2.: Peak wavelengths λ_p, and spectral bandwidths $\Delta\lambda_3$ at 3 dBc and $\Delta\lambda_{20}$ at 20 dBc, respectively, extracted from optical spectra of the first ML-ECDL module shown in Fig. 5.2.

measurement situation	spectral characteristics		
	λ_p/nm	$\Delta\lambda_3$/nm	$\Delta\lambda_{20}$/nm
(i) pre-mirror integration	788.86	3.07	5.23
(ii) integration setup	788.66	2.24	4.40
(iii) measurement setup	791.07	2.09	3.33

These results show that the curing process employed for the external mirror (step 8 of the assembly process) allowed only partial recovery of the mode-locked operation with large spectral

bandwidth. Thus, further improvement of the micro-integration concept of the external mirror was required.

After investigation of the influence of the adhesive bonding process for the external mirror on the mode-locking performance, the laser module's mode-locking performance was further analyzed. To that end, the fully completed ML-ECDL module was moved from the integration robot (measurement situation (ii)) to the measurement setup (measurement situation (iii)). However, mounting the MIOB in nominally the same way onto the measurement setup as on the integration setup (step 1 of assembly process, Sec. 5.2.2) resulted in such an angular beam displacement that no laser operation could be detected at all. Mode-locked operation could partially be recovered as follows.

The angular beam displacement can be attributed to the mechanical stability of the micro-integrated laser resonator that is insufficient for an ML-ECDL. This insufficient mechanical stability results in a deformation of the MIOB when mounted on the measurement setup as described above. This was then used to partially re-align the ML-ECDL by applying appropriate torques to the screws that deform the MIOB accordingly. In conjunction, the values of the operating parameters that provide the largest spectral bandwidth needed to be adjusted, see Tab. 5.1. However, the mode-locked performance recorded on the integration setup could not be fully re-established.

Next, the optical spectrum of the ML-ECDL module is compared for measurement situations (ii) and (iii). Both optical spectra are shown in Fig. 5.2. It can be seen that the peak wavelength achieved for measurement situation (iii) is shifted by about 2 nm to longer wavelengths relative to the optical spectrum recorded for measurement situation (ii). Further, the spectral bandwidths at 3 dBc and at 20 dBc are reduced by about 7 % to about 2.0 nm and by about 24 % to about 3.3 nm, respectively, for measurement situation (iii) compared to measurement situation (ii). These differences in the optical spectra can be attributed, on the one hand, to an only partially compensated beam displacement and, on the other hand, to different optimal values of the operating parameters for measurement situations (ii) and (iii).

After hybrid integration of the ML-ECDL was completed, the RF characteristics could be investigated as the laser module could be sufficiently covered to shield it from air flow in the laboratory. The pulse repetition rate of about 3.4 GHz is increased by about 1 MHz (approximately 0.03 %) for measurement situation (iii) compared to measurement situation (ii), see Fig. 5.3. The RF noise characteristics of the pulse repetition rate recored for measurement situations (ii) and (iii) are similar. This is shown with the RF spectra depicted in Fig. 5.3. The spectra were reconstructed from IQ data that were recorded with a sampling rate of 32 MHz, a bandwidth of 25.6 MHz, and a time record length of 500 ms. For the RF spectra, the IQ data records were split into overlapping time slices of 10 ms length, the RF spectra reconstructed, and averaged (see Sec. 3.4.3). The RF linewidths were determined by means of Lorentzian fits from the RF spectra reconstructed from IQ records. Similar RF linewidths were achieved for measurement situations (ii) and (iii), about 170 Hz and about 380 Hz, respectively. These RF linewidths are similar to the RF linewidths observed for similar ML-ECDLs mounted in the laser test mount, see, e.g., Tabs. 4.7 and 4.10. This finding shows that the RF stability is not compromised by the modification of the operating parameters introduced by mechanical stress.

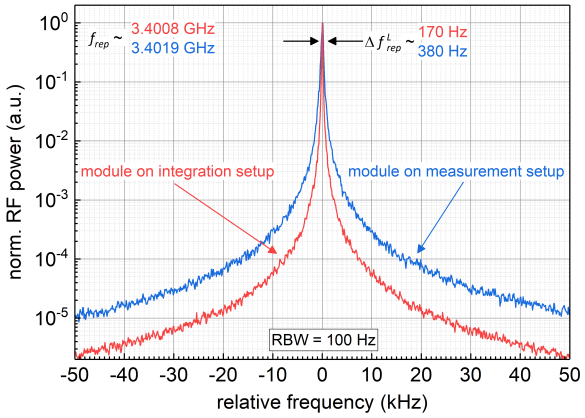

Figure 5.3.: RF spectra of the first ML-ECDL module around the pulse repetition frequency. The spectra are reconstructed from IQ data for measurement situations (ii) (red, module on integration setup) and (iii) (blue, module on measurement setup), respectively. The spectra were reconstructed from IQ data that were recorded with a sampling rate of 32 MHz, a bandwidth of 25.6 MHz, and a time record length of 500 ms. For the RF spectra, the IQ data records were split into overlapping time slices of 10 ms length, the RF spectra reconstructed, and averaged.

The reported differences observed between measurements carried out on the integration work place and on the measurement setup also include a strong reduction of the average optical power. Additional to the 16 % reduction of optical power determined between measurement situations (i) and (ii), further reduction of optical power occurs for measurement situation (iii) compared to measurement situation (ii). This reduction amounts to 20 %, from 80.2 mW to 64.3 mW. This reduction can be attributed to insufficient re-alignment of the laser resonator.

As the pulse shape and width could not be investigated on the integration setup, they will be described in the following for the measurement setup. Sech^2-shaped pulses with a width of about 6.6 ps could be determined resulting in an optical peak power of approximately 2.5 W. With a slightly longer pulse width and a resulting lower optical peak power, the results determined from the micro-integrated ML-ECDL module differ slightly from those determined from a similar ML-ECDL on the test mount, see, e.g., Tab. 4.7.

5.2.4. Conclusions from the first generation micro-integrated ML-ECDL

The results achieved with the very first micro-integrated ML-ECDL module have shown that such a laser can be micro-integrated successfully. The ML-ECDL module shows a similar mode-locking performance as a similar ML-ECDL investigated in the laser test mount (see Tab. 4.7). Nevertheless, several critical points of the micro-integration concept and the module itself have been identified.

For successful deployment of a micro-integrated ML-ECDL module, however, these challenges need to be overcome. In the subsequent section, an ML-ECDL integrated on an advanced MIOB will be presented.

5.3. Advanced ML-ECDL module

The advancement of the micro-integrated ML-ECDL presented in this section is based on the advancement of the MIOB for micro-integration of CW-ECDLs [77], see photo in Fig. 1.6. In the following the advanced MIOB which will be employed for integration of the ML-ECDL will be described. The advanced micro-integration concept will be discussed and the mode-locking performance of the resulting ML-ECDL module will be presented.

5.3.1. The micro-integration technology platform

The advanced micro-integration technology platform is specifically designed for ECDL- or MOPA-type lasers, see Sec. 1.2.3. This advanced platform comprises the MIOB and a heatsink. In this work, the ECDL-type module is used for hybrid integration of the ML-ECDL. Details of the advanced platform with the MIOB employed for the CW-ECDL and the modification of that MIOB for implementation of the ML-ECDL will be discussed in the following.

The advanced ECDL-type MIOB for hybrid integration of CW-ECDLs

In contrast to the MIOB introduced in the previous section (Sec. 5.2), the advanced MIOB consists of multi-layer stacked lithographically structured AlN ceramics, see Fig. 5.4. This MIOB has a footprint of 25×80 mm^2. The multi-layer structure of the MIOB allows for highly compact integration and wire-bonding. Its ceramic base plate is 4 mm thick to provide high mechanical stiffness. The MIOB features an electric interface (DC port 1) for the diode laser chip's gain section injection current, an electrical interface for RF modulation of the injection current, temperature sensors (T sensors), and temperature control of a VHBG by means of a micro-TEC (µTEC) onto which the VHBG is adhesively bonded. The multi-layer stacked AlN ceramics provide parallel rails that offer the means for compact electrical interfacing as well as hybrid integration of micro-lenses. In the following, the channel formed by these rails will be called optics channel. Typically, rotational symmetric micro-lenses are employed for beam-shaping of the diode laser chip's output.

The electric interface allows for use of RF capable connectors and cables. The electrical interface for RF modulation of the injection current features an RF and a DC port (DC port 2). The DC port 2 is implemented with a conic inductor (red cone above the µisolator in Fig. 5.4) providing a low pass filter with a cut-off frequency of 1 MHz. Electrical interfacing between the diode laser chip and the electrical interface of the MIOB is realized by wire-bonding. The distance between the conducting paths on the rails of the optics channel and the submount onto which the diode laser chip is mounted measures just a few hundred micrometers to minimize the length of the wire-bonds.

An optical micro-isolator (grey cylinder in cut-out to the left of ECDL mark in Fig. 5.4, µisolator) is hybrid integrated into the module to protect the diode laser from external optical feedback. Further, a fiber-coupler for the laser output (towards the left-hand side, in Fig. 5.4) can be micro-integrated onto the large Au surface of the MIOB on the left of the µisolator.

To enhance the mechanical stiffness of the MIOB, the MIOB is attached to a phosphorus bronze (CuSn8) heatsink. The 6 mm thick heatsink has a footprint of 42×98 mm^2. The

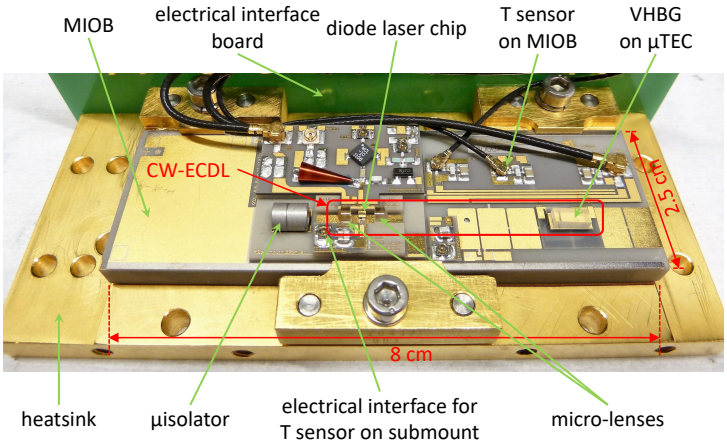

Figure 5.4.: Photo of an advanced CW-ECDL module (© FBH/schurian). The module's laser output is to the left-hand side. T - temperature, µTEC - micro-TEC, µisolator - optical micro-isolator.

heatsink consists of the mounting area for the MIOB (center, MIOB area) and areas (mounting area) along the short sides of the MIOB that feature boreholes for screws to mount the heatsink to a setup, e.g. the integration setup. The MIOB is attached to the heatsink at three points (line contacts) to reduce mechanical strain, at two points on one long side of the MIOB and at one on the other with a torque of 10 cNm and 20 cNm, respectively. A torque of 30 cNm is applied to the screws that fix the heatsink to a setup.

The laser module can be housed to protect the laser from the environment. The housing walls along the long sides of the module are RF capable electrical interface boards (one is shown in Fig. 5.4 at the top of the photo). The housing walls on the short sides of the MIOB and the lid are Al boards (not shown in Fig. 5.4). The Al housing walls feature boreholes to allow free-space output of the laser emission. All housing walls are directly attached to the heatsink.

Modification of the advanced ECDL-type MIOB for hybrid integration of the ML-ECDL

For hybrid integration of the advanced ML-ECDL, the advanced ECDL-type module (Fig. 5.4) is used. A fully micro-integrated ML-ECDL is shown in Fig. 5.5. Here, the general modifications of the advanced ECDL-type MIOB for hybrid integration of the ML-ECDL will be discussed. Details will be given in the subsequent section of this chapter.

For current injection into the gain section and for application of a reverse bias voltage to the saturable absorber, the DC and RF capable electrical interfaces of the ECDL-type MIOB are used, respectively. To allow for use of very short wire-bonds, an AlN bondpad was employed. Details will be discussed in Sec. 5.3.2.

The µTEC, that was implemented into the CW-ECDL module for temperature control of the VHBG (see Fig. 5.4), was omitted during production of the MIOB. This provides the means for implementation of an advanced assembly process for the external mirror, see Sec. 5.3.2. The MIOB thus allows for optical resonator lengths from 23 mm to 45 mm including a safety margin

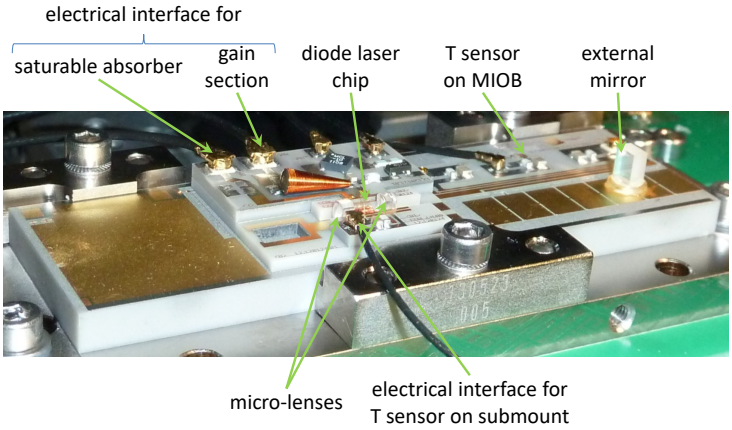

Figure 5.5.: Photo of the advanced ML-ECDL module. The ML-ECDL is micro-integrated into an advanced ECDL-type MIOB. The MIOB is mounted on its heatsink.

of a few millimeters between the edge of the MIOB and the external mirror.

For this proof-of-concept module, the hybrid integration of the optical µisolator (see Fig. 5.4) was omitted.

5.3.2. Integration strategy

The integration strategy of the CW-ECDL is in parts adopted and in parts modified to suit the requirements of an ML-ECDL. In the following, the integration strategy of a CW-ECDL is discussed and the implemented modifications of the integration strategy of an ML-ECDL are introduced.

Integration strategy of the CW-ECDL

The integration strategy of the CW-ECDL is similar to the aforementioned integration strategy of the CW-ECDL discussed as preparation for the first micro-integrated ML-ECDL module. The diode laser chip and a temperature sensor are soldered onto a structured submount with a footprint of 2×2 mm^2. The submount is then adhesively bonded onto the MIOB between parallel rails formed by the multi-layer stacked AlN ceramics.

Electrical interfacing between the diode laser chip and the electrical interface of the MIOB is realized by wire-bonding. The p-side contact is realized by wire-bonding from the p-side of the diode laser chip to the conducting path of the DC port 1 or the RF modulation interface. The n-side contact is realized by wire-bonding from the structured submount to a lower layer of the multi-layer AlN ceramic that is electrically interfaced to both, the DC port 1 and the RF modulation interface.

The narrow optics channel enables adhesive bonding of the rotational symmetric micro-lenses employed for beam shaping of the diode laser chip's output to the optics rails on both sides of the lenses. Thus, beam displacement through glue shrinkage during curing can be minimized.

The integration strategy of the VHBG for the advanced MIOB is the same as for the simple MIOB introduced in Sec. 5.2.2 - the VHBG is adhesively bonded directly to the surface of the µTEC.

Integration strategy of the ML-ECDL

Integration of the diode laser chip

The diode laser chip of the ML-ECDL module (details on the integrated diode laser chip in Sec. 5.3.3) is integrated in the same way as the diode laser chip of the CW-ECDL module. However, an electrical interface is required for the ML-ECDL that supports access to both, the gain section and the saturable absorber section of the diode laser chip. A schematic of the bonding scheme is depicted in Fig. 5.6(b) and a photo of the area containing the micro-integrated diode laser chip is shown in Fig. 5.6(a). A common n-side contact is realized by wire-bonding (pink lines in Fig. 5.6(b)) to the AlN ceramic which provides a common outer contact for the electrical interface ports for the diode laser chip. The p-side contact of the saturable absorber section is realized via DC port 1 of the MIOB. The p-side contact of the gain section is realized by the DC port (DC port 2) of the RF modulation interface of the MIOB which features a conic inductor. To allow for very short wire-bonds, a bondpad is implemented for this electrical interface. The bondpad is made of an AlN ceramic with a Au-plated top layer. It is adhesively bonded on top of the electrical interface of DC port 1 and DC port 2. Thus, the p-side contact of the gain section is first wire-bonded to the bondpad. Then, wire-bonds from the bondpad to the conducting path of DC port 2 connect the p-side contact of the gain section to DC port 2.

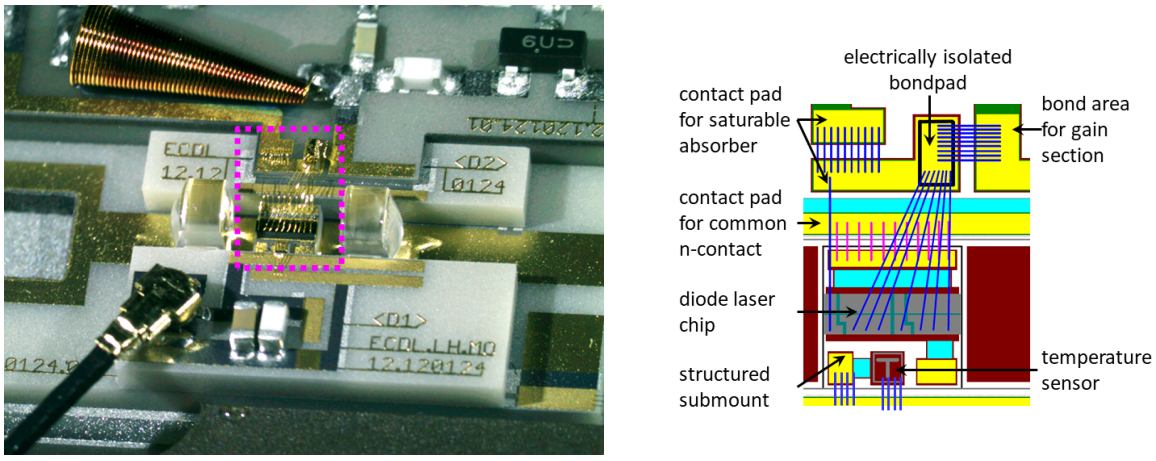

(a) (b)

Figure 5.6.: (a) Detail photo and (b) schematic of the area of the advanced ML-ECDL module that contains the diode laser chip. The pink box in (a) highlights the section of the integrated diode laser chip and associated wire-bonds. For better visualization, the schematic in (b) shows the wire-bonds of the diode laser chip to the MIOB.

Integration of the micro-lenses

The micro-lenses' micro-integration concept has been advanced for this generation of ECDL-type MIOBs to minimize beam misalignment. To this end, the round aspheric lenses are appropriately grinded so that they can be adhesively bonded between the rails on either side, see Fig. 5.6(a). To that end, the round aspheric micro-lenses have been precision grinded on three sides to allow them to fit into the optics channel and provide minimal gaps for adhesive bonding. The procedure has been adopted from the CW-ECDL modules. The alignment procedure described for assembly of the first ML-ECDL module has also been employed here.

Integration of the external mirror

The external mirror's micro-integration concept has completely been revised as adhesive bonding directly to the MIOB has shown to cause strong beam misalignment due to glue shrinkage during curing, see Sec. 5.2. To allow for adhesive bonding of the external mirror to the advanced MIOB without beam misalignement during curing, a gap-free integration strategy has been implemented as follows.

Figs. 5.7(a) and 5.7(b) show the technical implementation and a photo of the fully integrated mirror assembly, respectively. The plane mirror used for the first ML-ECDL module (see Fig. 5.2) is replaced by a mirror assembly consisting of a micro-mirror, a spherical cap and a ring with flat sides. The external mirror is provided by grinding a mirror of the same type used throughout this work (Layertec 101085) to feature a mirror surface of 4×3.3 mm^2 on a 2 mm thick substrate. This external mirror is adhesively bonded to a 1 mm thick spherical cap that is grinded from a precision sphere with 5 mm diameter. This assembly is placed into an 800 µm thick sapphire ring that provides the base layer of the mirror assembly. The ring features a conical cut-out with an outer diameter of 3.6 mm and a cylindrical center cut-out with a diameter of 2.6 mm. Thus, the spherical cap carrying the external mirror is held by the conical surface without touching the MIOB surface beneath the sapphire ring. The gap only measures approx. 40 µm. The integration strategy of a micro-mirror has been developed within another project for MIOBs that feature conic cut-outs [78] and advanced within this work to be used for the integration of an arbitrary micro-mirror on a flat MIOB as the one that was employed here.

The assembly procedure

The assembly procedure for the second generation MIOB can be divided into three steps.

1. The first step covers the preparation of the MIOB. Here, the diode laser chip which is mounted on a structured submount is micro-integrated into the MIOB. An additional temperature sensor is micro-integrated into the MIOB. Finally, electrical interfacing is realized via wire-bonding. This step is facilitated by the Mounting & Assembly Department of the FBH.

2. The second step consists of the preparation of the mirror assembly. Here, the mirror is

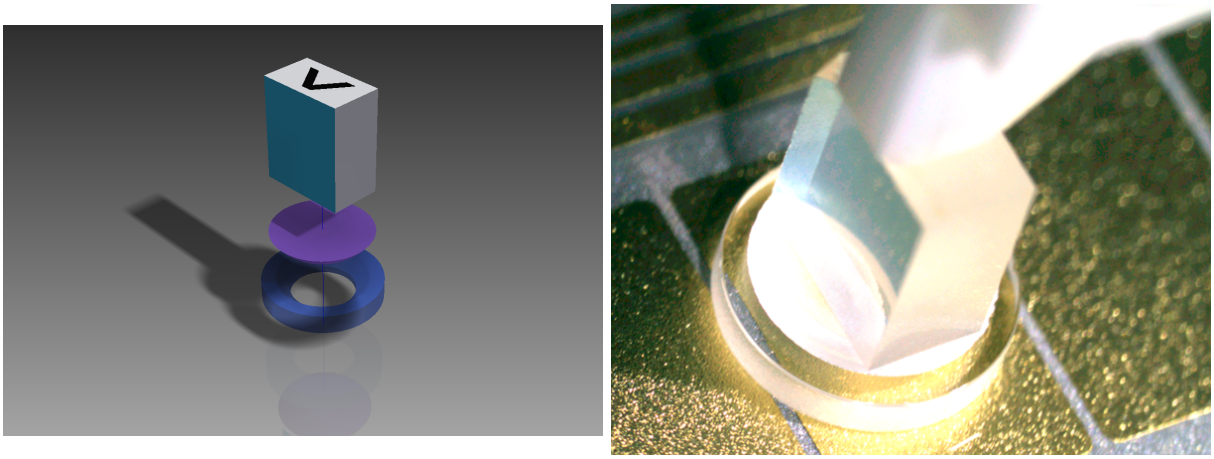

(a) schematic (b) photo

Figure 5.7.: (a) Schematic and (b) photo of the mirror assembly consisting of a sapphire ring, a spherical cap, and a dielectric mirror. In the photo, the mirror, that is attached to the spherical cap, is held by a vacuum tweezer and placed into the sapphire ring for alignment of the laser resonator of the ML-ECDL.

adhesively bonded to the spherical cap.

3. The third step includes the integration of the micro-optics into the MIOB. The following steps correspond to the micro-integration concept that was successfully developed for the first ML-ECDL module and include the integration of the mirror assembly into the MIOB.
   a) First, the MIOB is mounted onto its heatsink which in turn is then mounted onto the integration setup. Pre-defined torques (see Sec. 5.3.1) are applied to the screws.
   b) Second, the laser output is collimated by means of the temporary micro-lens (see micro-lens on the left-hand side of the diode laser chip in Fig. 5.6(a)).
   c) Third, the laser resonator is aligned. To that end, the resonator-side micro-lens is mounted on the integration robot and the temporary external mirror is held in place by the external adapter mount. During alignment, the optical and the RF spectra are monitored.
   d) Then, the laser is burned in in mode-locked operation. Afterwards, the laser alignment is reviewed via measurement of the optical and the RF spectra.
   e) Afterwards, the intra-cavity lens is adhesively bonded to the optics rails.
   f) In the next step, the temporary output collimation micro-lens is replaced by the lens intended for micro-integration. The laser output is re-collimated and the lens adhesively bonded to the optics rails.
   g) The final step is the micro-integration of the external mirror. To that end, the mirror assembly is picked up by a vacuum tweezer that is held by the integration robot.

Then, the laser is re-aligned to emit the largest optical spectrum, with the position of the mirror along the resonator axis selected so that a repetition rate of 3.4 GHz is achieved. Then, the sapphire ring is placed onto the MIOB, the mirror assembly is placed into it, and the laser is re-aligned. The sapphire ring is first adhesively bonded to the MIOB. Without need for re-alignment, the mirror assembly is gap-free adhesively bonded to the sapphire ring.

A photo of the advanced fully micro-integrated ML-ECDL is shown in Fig. 5.5.

5.3.3. Mode-locking performance

For this advanced micro-integrated ML-ECDL module, the diode laser chip design investigated in this work that is best suited to provide a large spectral bandwidth diode laser based OFC is employed. This design was investigated in detail in Sec. 4.3. Here, a diode laser chip from the same bar as the one implemented in the laser test mount introduced in Sec. 4.3 is used. The diode laser chip is 2.0 mm long and features a 100 µm long saturable absorber section. The epitaxial layer structure is realized as an asymmetric double quantum well (aDQW) structure that is optimized for large spectral bandwidth emission in the wavelength range around 773 nm. A combination of a 4 µm wide ridge waveguide and a 4.8 µm wide vertical waveguide provides an almost round fundamental optical mode that can be collimated by a single rotational symmetric micro-lens. The front facet of the diode laser chip is coated to 5 % reflectivity while the rear facet (intra-cavity) is anti-reflection coated to avoid formation of parasitic sub-cavities.

Validation of the integration concept for the external mirror

The optical spectrum of the micro-integrated ML-ECDL module was observed during curing of the adhesive for the external mirror to validate the mirror assembly concept. The values of the operating parameters that provide the largest spectral bandwidth at 20 dBc before and after curing are listed in Tab. 5.3. The corresponding optical spectra are depicted in Fig. 5.8 and the spectral characteristics (peak wavelengths λ_p, and spectral bandwidths $\Delta\lambda_3$ at 3 dBc and $\Delta\lambda_{20}$ at 20 dBc) extracted from those spectra are summarized in Tab. 5.4. The optical spectra were measured before and after integration of the external mirror as well as after optimization of the values of the operating parameters with respect to the spectral bandwidth at 20 dBc. The details are discussed in the following.

Table 5.3.: Values of operating parameters of advanced ML-ECDL module during the process of curing the adhesive for the external mirror.

mount	values of operating parameters		
	T_{MIOB}/°C	U_{SAB}/V	I_{DCI}/mA
before completing of hybrid integration	20.0	-0.99	244.0
after completing of hybrid integration	20.0	-0.99	244.0
after optimization of values of operating parameters	20.0	-1.22	250.0

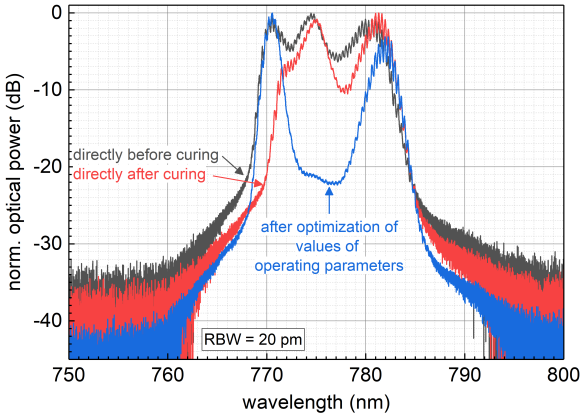

Figure 5.8.: Optical spectra of the advanced ML-ECDL module (grey) before and (red) after hybrid integration of the external mirror, and (blue) after optimization of the values of operating parameters of the completed advanced ML-ECDL module.

Table 5.4.: Peak wavelengths λ_p, and spectral bandwidths $\Delta\lambda_3$ at 3 dBc and $\Delta\lambda_{20}$ at 20 dBc, respectively, extracted from optical spectra of the advanced ML-ECDL module shown in Fig. 5.8.

measurement situation	spectral characteristics		
	λ_p/nm	$\Delta\lambda_3$/nm	$\Delta\lambda_{20}$/nm
before completion of hybrid integration of external mirror	774.46	11.86	16.07
after completion of hybrid integration of external mirror	781.30	8.33	14.32
after optimization of operating parameter values	770.56	1.34	15.85

It can be seen that the shapes of the optical spectra before and directly after completing the hybrid integration of the laser module, and after optimization of the values of the operating parameters differ strongly from each other. Nevertheless, the optical spectra cover nearly the same spectral range within the 20 dBc level. Before micro-integration, the optical spectrum shows three strongly overlapping spectral bands centered around 770 nm, 774 nm and 781 nm, respectively. As nominally identical diode laser chips (from same laser bar) are used in the module and in the laser test mount, a spectral shape featuring only two spectral bands centered around 770 nm and 781 nm, respectively, (see, e.g., Fig. 4.15) is expected. An optical spectrum featuring three spectral bands has not been observed before. Thus, the different shape of the optical spectrum reported here suggests differences between the modal gain spectrum of the diode laser chip that was integrated into the module and the one that was investigated in the laser test mount (Fig. 4.15). These differences in the modal gain spectra may be a result of accidental local variation in epitaxial growth of the diode laser chip, see, e.g. the variations of the spectral shape achieved by variation of the As content in the QWs (Fig. 4.4). Another possible explanation may be that different strain was introduced into the active region of the diode laser chip during assembly of the diode laser chip into the laser module. Evaluation of the mode-locked performance achievable with the diode laser chip before integration into a laser

module would allow for selection of the best suited diode laser chip. It would also allow for investigation of possible changes of the properties of the diode laser chip, e.g. introduction of addition strain, that could occur during integration. Thus, for future ML-ECDL modules, the mode-locking performance of the diode laser chip intended for integration should be analyzed before integration.

Completion of the hybrid integration of the laser module results in further changes of the optical spectrum. Comparing the spectral shape before and after completing the hybrid integration shows that the shortest wavelength spectral band of the optical spectrum recorded before completion has disappeared. The optical spectrum recorded after completion is slightly shifted to longer wavelengths by about 1 nm compared to that recorded before completion. After optimization of the values of the operating parameters, the shape of the optical spectrum changed again. At this point, the optical spectrum consists of two spectral bands centered around 770 nm and 781 nm, respectively. This spectral shape is similar to those recorded for similar lasers mounted in the laser test mount, see Sec. 4.3. Such a similar spectral shape is expected for nominal identical diode laser chips when the largest spectral bandwidth was achieved by optimizing the values of the operating parameters. The investigations concerning optical spectrum achieved with the first generation laser module (Sec. 5.2.3) suggest that misalignment of the laser resonator of the ML-ECDL during UV-curing of the external mirror is the cause of the different optical spectra recorded before and after completing the hybrid integration. Optimization of the values of the operating parameters for a maximum spectral bandwidth at 20 dBc allows for only partial recovery of the shape of the optical spectrum achieved before completion of hybrid integration. A detailed investigation of the cause for the difference in spectral shape, however, was beyond the scope of this work. Future investigations should include a more detailed theoretical analysis of the mode-locked regime for further development.

In the following, the variation of the peak wavelength along the integration process is discussed. It can be seen (Fig. 5.8 and Tab. 5.4) that the peak wavelengths of the optical spectra before ($\approx$ 774.46 nm) and after ($\approx$ 781.30 nm) completion of the hybrid integration, and after optimization of the values of the operating parameters ($\approx$ 770.56 nm) are strongly shifted in wavelength. These shifts are a consequence of strong modifications of the shape of the optical spectra. As mentioned before, the wavelength range covered at the 20 dBc level remains nearly unchanged.

Due to the strong modifications of the shape of the optical spectra, the spectral bandwidth $\Delta\lambda_3$ at 3 dBc differs strongly between the three characterizations. Before completion of the hybrid integration, the spectral bandwidth at 3 dBc measures about 11.9 nm, see Fig. 5.8 and Tab. 5.4. This is a record value for the lasers investigated in this thesis. This value is a result of the shape of the optical spectrum before completion of the hybrid integration where all three spectral bands feature similar peak powers. After completion of the hybrid integration, the shorter wavelength spectral band observed before completion disappeared. This leads to a reduction of spectral bandwidth at 3 dBc by about 30 %. This reduction is similar to what was observed for the first generation module, see Sec. 5.2.3. The modification of the optical spectrum during optimization of the values of the operating parameters leads to a further loss of spectral bandwidth at 3 dBc by about 84 %. This is due to the strongly reduced optical power of the longer-wavelength spectral band and the complete loss of the center spectral band.

In contrast to the spectral bandwidth at 3 dBc, the spectral bandwidth at 20 dBc remains almost constant, see Fig. 5.8 and Tab. 5.4. Comparing the spectral bandwidth at 20 dBc before and after completing the hybrid integration, a reduction of spectral bandwidth of less than 11 % from around 16.1 nm to about 14.3 nm is observed. This is similar to the reduction observed for the first generation module (about 16 %). In contrast to the first generation module, the spectral bandwidth at 20 dBc could be increased again by about 10 % by optimizing the values of the operating parameters. Thus, an overall reduction of the spectral bandwidth at 20 dBc of only about 1.4 % was found. The reason for these slight modifications are the slight modifications of the optical spectra at 20 dBc.

Thus, the overall spectral characteristic of the ML-ECDL mounted in the laser test mount (Sec. 4.3) could be reproduced with the advanced ML-ECDL module. While modifications occurred in the optical spectrum of the ML-ECDL module during integration of the external mirror, the most important spectral characteristic, the spectral bandwidth at 20 dBc, remained well above the requirement of this work, see Sec. 1.2.4. Although further analysis of the micro-integration concept of the external mirror is required, the results discussed highlight the success of the advancement of the micro-integration concept, in particular that of the external mirror.

Mode-locking performance of the advanced ML-ECDL module after completing the hybrid integration

In the following, the mode-locking performance of the advanced ML-ECDL module is investigated after completing the hybrid integration, i.e. (i) before and (ii) after the module was moved from the integration setup to the measurement setup, and (iii) after optimization of the torque applied to the screws that hold the module on the measurement setup. For measurement situations (i) and (ii), the module is mounted to the respective setup with the same mounting procedure - a torque of 30 cNm is applied to all four screws fixing the module to the setup. For each of these situations, the values of the operating parameters were optimized for maximum spectral bandwidth, see Tab. 5.5. The focus of the investigations presented here is on the optical spectrum.

Table 5.5.: Values of operating parameters of advanced ML-ECDL module before and after moving the module from the integration setup to the measurement setup, and after optimization of the torque applied to the screws that fasten the module to the measurement setup. MS - measurement setup.

measurement situation	values of operating parameters		
	T_{MIOB}/°C	U_{SAB}/V	I_{DCI}/mA
(i) integration setup	20.0	-0.99	218 - 250
(ii) measurement setup (MS)	20.0	-1.22	170 - 250
(iii) MS after torque optimization	22.4	-2.40	230 - 280 - 235

First, the mode-locking performance of the advanced ML-ECDL module is investigated in measurement situation (i). Here, the ML-ECDL is still mounted on the integration setup after

completing the hybrid integration. The optical spectrum and the extracted spectral bandwidths at 3 dBc and 20 dBc, respectively, are shown in Fig. 5.9 for increasing and decreasing gain section injection current (I_{DCI}). It can be seen that the ML-ECDL module has a lasing threshold of about 221 mA. For lower gain section injection current of about 221 mA - 237 mA, the laser emits dominantly from the longer-wavelength QW at around 780 nm. The spectral bandwidths at 3 dBc and 20 dBc measure about 1.5 nm and 5.5 nm, respectively. For gain section injection currents of 238 mA - 250 mA (maximum I_{DCI}), the optical spectrum shows emission from both QW. In this current range, maximum spectral bandwidths of up to about 12 nm at 3 dBc and about 16 nm at 20 dBc were achieved. The peak wavelength of around 771 nm in this current range is dominated by the shorter-wavelength QW. A strong hysteresis is found as (a) similar spectral characteristics can be determined for increasing and decreasing gain section injection current above approx. 205 mA and (b) mode-locked operation extends below that current for further decreasing DCI. This indicates strong mode-locking. Similar spectral characteristics could be achieved for a nominally identical ML-ECDL mounted on the test setup (Sec. 4.3, Fig. 4.15). These results highlight the successful implementation of the advanced integration strategy.

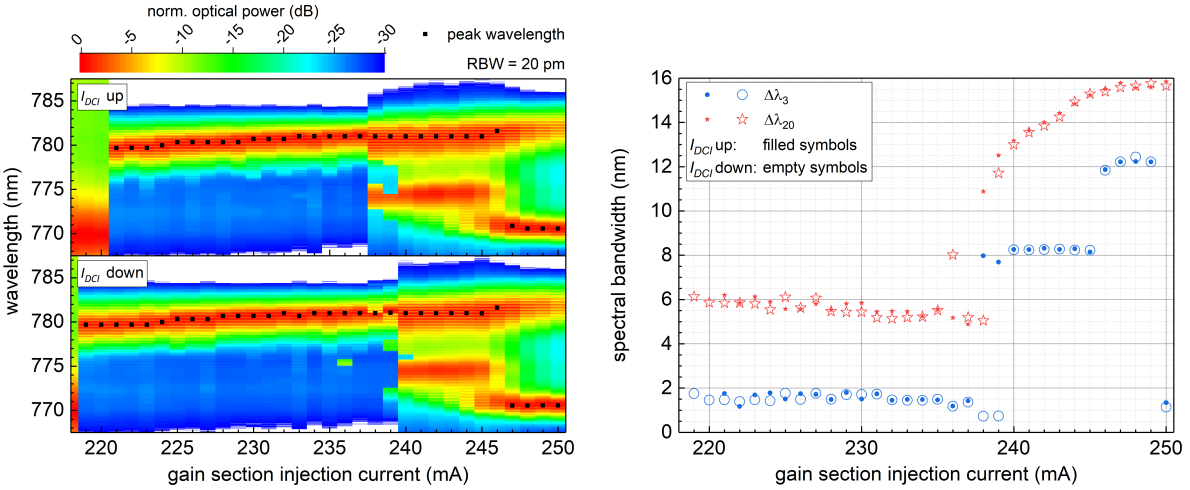

(a) optical spectra

(b) spectral bandwidths

Figure 5.9.: (a) Optical spectra and (b) extracted spectral bandwidths at 3 dBc (blue circles) and 20 dBc (red stars) of the advanced ML-ECDL module mounted on the integration setup (measurement situation (i)) for increasing (filled symbols) and decreasing (empty symbols) gain section injection current (I_{DCI}). The peak wavelengths of the optical spectra are highlighted in (a).

Second, the mode-locking performance of the advanced ML-ECDL module is investigated in measurement situation (ii). Here, the ML-ECDL is moved from the integration setup to the measurement setup (see Fig. 3.3). The screws fixing the module to the setup are tightened by applying the same torque (30 cNm) as with measurement situation (i). The optical spectrum and extracted spectral bandwidths at 3 dBc and 20 dBc, respectively, are shown in Fig. 5.10 for increasing and decreasing gain section injection current (I_{DCI}).

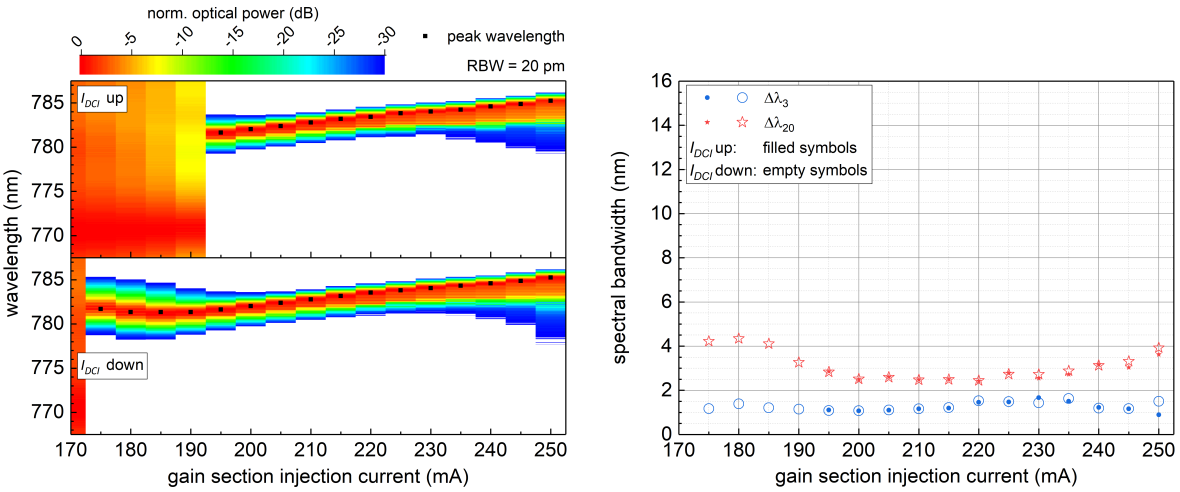

(a) optical spectra

(b) spectral bandwidths

Figure 5.10.: (a) Optical spectra and (b) extracted spectral bandwidths at 3 dBc (blue circles) and 20 dBc (red stars) of the advanced ML-ECDL module mounted on the measurement setup (measurement situation (ii)) for increasing (filled symbols) and decreasing (empty symbols) gain section injection current (I_{DCI}). The peak wavelengths of the optical spectra are highlighted in (a). For better comparison with measurement situation (i), the y-axes of both Figs. are kept constant.

It can be seen that the laser emits only from the longer-wavelength QW. The lasing threshold is at about 195 mA, about 25 mA less than recorded in measurement situation (i). The peak wavelength increases from about 780 nm to about 785 nm with increasing gain section injection current due to thermal heating of the diode laser chip. The spectral bandwidths at 3 dBc and 20 dBc measure about 1.5 nm and 3 nm, respectively. Similar to measurement situation (i), a strong hysteresis is found. Comparing these results with those determined for the measurement situation (i) shows that either the laser is defect, the values of the operating parameters were modified or the laser resonator of the ML-ECDL was misaligned by changing the setup onto which the module is mounted. Adjustment of the values of the operating parameters did not restore large spectral bandwidth, mode-locked operation. However, similar effects due to misalignment of the laser resonator have been observed with the first ML-ECDL module (Sec. 5.2). That misalignment was attributed to insufficient mechanical stiffness of the first module. The fact that, in contrast to the first ML-ECDL module, the laser still starts laser operation after being moved to the measurement setup, is an indication of an improved mechanical stiffness of the module. Nevertheless, similar to the first ML-ECDL module, the mode-locking performance of the laser in measurement situation (i) should be at least partially restorable.

To test the hypothesis of insufficient mechanical stiffness, the torque applied to the screws that fix the module to the setup (at the front and back of the heatsink along the short side of the module, see Fig. 5.4) was modified. The best results have been achieved by combined torque adjustment (40 cNm and 5 cNm for front and back screws, respectively) and adjustment of the values of the operating parameters.

Thus, third, the mode-locking performance of the advanced ML-ECDL module is investigated in measurement situation (iii). Here, the ML-ECDL was mounted on the measurement setup and the torque applied to the screws that fix the module to the setup was adjusted. The optical spectrum and the extracted spectral bandwidths at 3 dBc and 20 dBc, respectively, are shown in Fig. 5.11 for increasing and decreasing gain section injection current (I_{DCI}). It can be seen in Fig. 5.10(a)), that the peak wavelength of the optical spectrum is determined by the shorter-wavelength part of the optical spectrum. Further, just above the lasing threshold at about 259 mA, a large spectral bandwidth at 20 dBc of more than 10 nm could achieved. For increasing gain section injection current, the relative optical power of the longer-wavelength part of the optical spectrum strongly decreases. For gain section injection currents exceeding 268 mA, the optical spectrum is dominated by the shorter-wavelength QW. In that current range, the spectral bandwidth at 20 dBc measures less than 6 nm. The spectral bandwidth at 3 dBc, in contrast, remains nearly constant at about 1.5 nm for increasing gain section injection current. For decreasing gain section injection current, similar spectral characteristics can be determined and a hysteresis similar to measurement situations (i) and (ii) can be observed. For decreasing gain section injection current, the current range with a large spectral bandwidth at 20 dBc of more than 10 nm spans nearly 20 mA ($\approx$ 250 mA - 268 mA). A maximum spectral bandwidth of about 11 nm can be determined. Due to a strong spectral overlap of the longer-wavelength and the shorter-wavelength spectral band of the optical spectrum at a gain section injection current of around 250 mA, the spectral bandwidth at 3 dBc exceeds 6 nm. For gain section injection currents below 250 mA, the optical spectrum is dominated by a single spectral band and the spectral bandwidths at 3 dBc and 20 dBc decrease. These results show that by means of combined adjustment of the torque applied to the screws that fix the module to the measurement setup and of the values of the operating parameters, the spectral characteristics of measurement situation (i) could partially be restored.

After analysis of the influence of the mounting parameters on the optical spectrum of the ML-ECDL, the RF linewidth, the optical power, and the pulse width and shape will be discussed in the following to complete the information about the ML-ECDL module.

First, the RF linewidth is discussed. The RF linewidth was determined by a Lorentzian fit of the RF spectrum centered around the pulse repetition rate. The RF spectrum was reconstructed from 500 ms long IQ time traces that were recorded with a sampling rate of 32 MHz and an IQ bandwidth of 25.6 MHz. Fig. 5.12 depicts the RF linewidths determined in measurement situations (i), (ii) and (iii).

It can be seen that in measurement situation (i), the ML-ECDL module provides an RF linewidth of about 10 kHz when the laser operates with a large spectral bandwidth (gain section injection current range of 238 mA - 250 mA), see Fig. 5.9. The fluctuations in RF linewidth might be attributed to temperature fluctuations of the diode laser chip due to air flow on the integration setup which could not be housed sufficiently. Due to these fluctuations, the dependence of the RF linewidth on decreasing gain section injection current was not investigated. Nevertheless, the results of measurement situation (i) show that the ML-ECDL module fulfills the RF linewidth requirements stated in Sec. 1.2.4.

For measurement situation (ii), RF linewidths below 10 kHz can be determined. This measurement situation, however, features only a small spectral bandwidth, see Fig. 5.10, which is

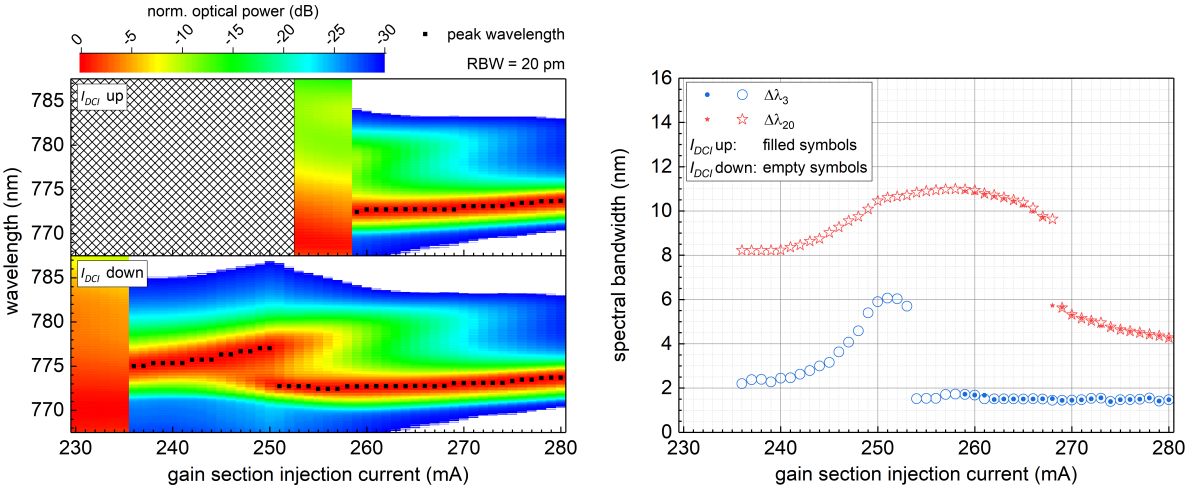

(a) optical spectra

(b) spectral bandwidths

Figure 5.11.: (a) Optical spectra and (b) extracted spectral bandwidths at 3 dBc (blue circles) and 20 dBc (red stars) of the advanced ML-ECDL module mounted on the measurement setup with adjusted torque (measurement situation (iii)) for increasing (filled symbols) and decreasing (empty symbols) gain section injection current (I_{DCI}). The peak wavelength of the optical spectrum is highlighted in (a). For better comparison with measurement situations (i) and (ii), the y-axes of both Figs. are kept constant.

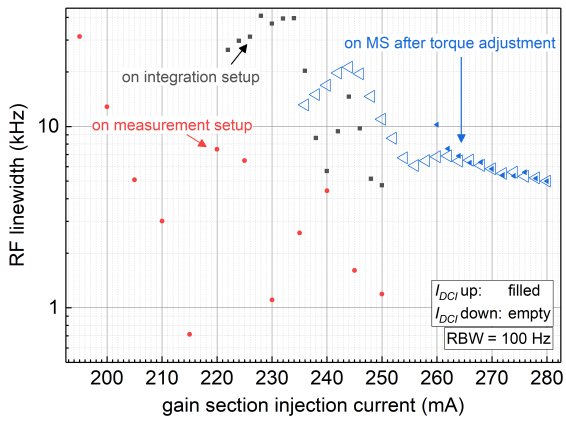

Figure 5.12.: RF linewidths determined by a Lorentzian fit of the RF spectra reconstructed from IQ data recorded for the advanced ML-ECDL module when still mounted on the integration setup (black boxes), mounted on the measurement setup (MS) with same mounting procedure (red circles), and with the torque used to fixed the MIOB's heatsink on the measurement setup adjusted (blue triangles). The RF spectra were reconstructed from IQ data that have been recorded with a sampling rate of 32 MHz, a bandwidth of 25.6 MHz, and a time record length of 500 ms. For the RF spectra, the IQ data records were split into overlapping time slices of 10 ms length, the RF spectra reconstructed, and averaged.

a result of misalignment of the laser resonator of the ML-ECDL module. Thus, this is not a desirable measurement situation. Therefore, the dependence of the RF linewidth on decreasing gain section injection current was not investigated here.

In measurement situation (iii), the large spectral bandwidth mode-locking determined for measurement situation (i) could be partially restored, see Fig. 5.11. The corresponding RF linewidth is less than 10 kHz, see Fig. 5.12. In this measurement situation, in contrast to measurement situation (i), the ML-ECDL module was completely housed and shielded from air flow. Thus, only small fluctuations of the RF linewidth compared to measurement situation (i) were detected with increasing or decreasing gain section injection current.

Second, the optical power determined in measurement situation (i), (ii), and (iii) is discussed. The average optical power is depicted in Fig. 5.13 for all three measurement situations. The pink boxes highlight the respective range of DCI that provides a large spectral bandwidth (> 10 nm at 20 dBc). In measurement situation (i), an optical power of up to 40 mW is achieved for large spectral bandwidth, mode-locked operation. In measurement situation (ii), an average optical power exceeding 60 mW could be achieved. However, this measurement situation was determined to be undesirable due to misalignment of the laser resonator of the ML-ECDL module. In measurement situation (iii), in which the mode-locked operation of measurement situation (i) could be partially restored, an average optical power of more than 25 mW could be achieved in that gain section injection current range that provided a large spectral bandwidth. The reduced optical power of this measurement situation compared to measurement situation (i) can be attributed to only partial restoring of the alignment of the laser resonator in measurement situation (i). Please also note that measurement situation (i) and (iii) feature different values of operating parameters.

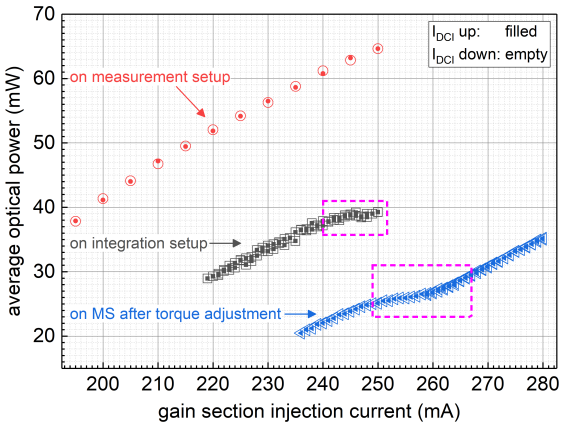

Figure 5.13.: Average optical power of the advanced ML-ECDL module in measurement situations (i) on integration setup, (ii) on measurement setup (MS), and (iii) on MS after torque adjustment. The pink boxes highlight the respective range of gain section injection currents that provides a large spectral bandwidth (> 10 nm at 20 dBc).

To complete the information about the mode-locking performance on the ML-ECDL module

in measurement situation (iii), the pulse shape and width is discussed[2]. For those gain section injection currents that provide large spectral bandwidths, mode-locked operation, the ML-ECDL module emits sech^2-shaped pulses with a width of around 5 ps. Those pulses feature a TBP of around 4. Thus, the pulse width and the TBP of a nominally identical ML-ECDL mounted on the laser test mount, see Sec. 4.3, could be reproduced in the micro-integrated ML-ECDL module. Further, a similar average optical power of about 25 mW could be achieved for those values of the operating parameters, that provide the largest spectral bandwidth. Consequently, a similar pulse peak power of around 1.4 W can be determined for the ML-ECDL on the test mount and its micro-integrated version.

5.3.4. Conclusion from the advanced ML-ECDL module

In this section, successful hybrid integration of an advanced ML-ECDL module was presented. For its realization, the advanced micro-integration technology platform that was originally developed at FBH for CW-ECDL-type lasers was used. Advancements of the module such as RF suitable cables and an integrated electrical interface, as well as a housing to shield the module from airflow were successfully employed. The electrical interface was modified to allow for implementation of separate electrical contacts for both, the saturable absorber and the gain section, with minimal bond-wire length.

Further, an advanced integration strategy that was developed based on the results of the first ML-ECDL module presented in the previous section (Sec. 5.2) was successfully implemented. Problems of the micro-integration concept identified with the first ML-ECDL module were solved:

- Misalignment of optical components caused by shrinkage of the adhesive during UV-curing was avoided by bonding the micro-lenses symmetrically on the two grinded sides.

- Misalignment-free micro-integration of the external mirror is realized by gap-free adhesive bonding the external miror to the MIOB by means of a sapphire ring and a spherical cap.

It was shown that the ML-ECDL module provided mode-locking performance characteristics on the integration setup similar to those determined with a nominally identical ML-ECDL on the test setup (Sec. 4.3). However, insufficient mechanical stiffness of the module when moving it from the integration setup to the measurement setup resulted in a partial loss of mode-locking performance, particularly in spectral bandwidth at 20 dBc, due to beam misalignment. The large spectral bandwidth, mode-locked operation could partially be restored by combined adjustment of the torque applied to the screws that fix the module to the measurement setup and of the values of the operating parameters.

[2]The pulse shape and width could only be determined for the ML-ECDL module mounted on the measurement setup.

5.4. Conclusion from micro-integration of a diode laser-based optical frequency comb generator

In this chapter, the successful hybrid integration of an ML-ECDL was demonstrated for the first time. Within the limits pre-set for the development of the micro-integrated module, a designated module for an ML-ECDL could, for cost-reasons, not be developed. Thus, the most simple approach based on a multi-purpose micro-integration technology platform developed at FBH was employed to identify critical aspects of the hybrid integration. An integration strategy was developed to solve those problems. Successful implementation of that advanced integration strategy was demonstrated with an advanced micro-integration technology platform that was developed at FBH for CW-ECDLs. The advanced module body was modified to allow for separate electrical contacts of both, the saturable absorber and gain section, and for misalignment-free hybrid integration of the external mirror of the ML-ECDL.

The mode-locking performance of both, the first and the advanced, module was investigated and compared to that determined for nominally identical ML-ECDLs mounted in the test setup (Chap. 4). The advanced integration strategy allowed for similar mode-locking performance characteristics in the respective comparison. This result highlights the success of the hybrid integration of the ML-ECDL developed in this work.

Further, the mechanical stiffness of the laser module was identified as a critical aspect in the advanced ML-ECDL module. In a future development step, this issue needs to be addressed by mechanically decoupling the MIOB from its heatsink by means of, e.g., adhesively bonding the MIOB to the heatsink with a frame made of sufficiently elastic material in-between that allows for compensation of mechanical stress.

6. Pulse repetition rate stabilization

6.1. Introduction to stabilization of the pulse repetition rate

For the implementation of the ML-ECDL in a system that compares two optical frequencies, that are within the spectral bandwidth of the ML-ECDL's optical spectrum, control of the pulse repetition rate is necessary. Fluctuations of the repetition frequency (timing noise) can readily be reduced by electrical modulation of the saturable absorber bias voltage with a frequency corresponding to the pulse repetition rate, see Sec. 2.3. Further, avoiding this indirect control by means of an RF oscillator and directly employing one of the ML-ECDL's (operating) parameters as an actuator for frequency control of the pulse repetition rate would be advantageous. Stabilization of the pulse repetition rate of linear extended cavity lasers is typically realized by employing the physical resonator length as an actuator [202, 203]. However, as the mode-locked ECDL is to be micro-integrated with no moving parts, that option is excluded. The remaining operating parameters are (i) the gain section injection current, (ii) the reverse voltage applied to the saturable absorber, and (iii) the module's temperature. Taking into account the utilized micro-integration platforms, the laser temperature (here the mount/MIOB temperature) can only be used as slow (<1 Hz) actuator to compensate for slow frequency drifts. In contrast, the saturable absorber reverse voltage and the gain section injection current can, in principle, be used to implement fast (up to GHz) and large bandwidth actuators, as demonstrated by hybrid mode-locking [204].

In the course of this work, the influence of the gain section injection current on the pulse repetition rate was investigated in detail, see Sec. 4.3.2. The gain section injection current was identified as possible actuator with a tuning rate of approximately 250 kHz/mA for the pulse repetition rate. Here, a feedback stabilization scheme using the gain section injection current as actuator will be exploited to investigate the stabilization of the pulse repetition rate. To that end, the experimental setup will be described and the mode-locking performance of a free-running and a stabilized ML-ECDL comparatively discussed. For a consistent presentation of the mode-locking performance of the ML-ECDL in this work, the comparison of the RF stability of the free-running and the stabilized ML-ECDL will be done by discussing the respective FN-PSDs.

6.2. Experimental setup

In the following, the principle of the control setup is discussed first. Then, the implementation of the experimental setup is described. Finally, the experimental setup is characterized.

Principle setup

The goal of the work discussed here is the demonstration of stabilization of the pulse repetition rate using the gain section injection current. Complex loop filters and modulation circuits will be avoided. Here, the phase of the pulse repetition rate will be compared and stabilized to the phase of an RF reference signal. The detection of the phase and the subsequent control of the pulse repetition rate effectively implements an integrator. To that end, the output of a phase detector [205] is used to generate an error signal which is then directly employed as control signal in an active stabilization scheme. To simplify the superimposition of this control signal with the gain section injection current in this demonstrator setup, the current controller (ILX LDC-3724C, DCIctrl) is used. This controller features a modulation input (MODin) that readily provides a means for superimposing a control signal onto the gain section injection current with a bandwidth of 1 MHz. In parallel to this control loop, simultaneous monitoring of the mode-locking performance during stabilization of the pulse repetition rate is carried out.

Implementation of the stabilization setup

The stabilization setup is depicted in Fig. 6.1. For implementation of the stabilization setup the part of the measurement setup (meas. setup, Fig. 3.3) employed for the analysis of the RF mode-locking characteristics (box in Fig. 6.1) was modified to include the feedback loop. To allow for simultaneous monitoring of the autocorrelation function, the first mirror after the ML-ECDL in the measurement setup (Fig. 3.3) was exchanged for a beam splitter (BS, Newport 20RQ00UB.2). The optical spectrum and the average optical power path were left unchanged. The resulting setup allows for stabilization of the pulse repetition rate and simultaneous monitoring of the mode-locking performance. Please note that the stabilization scheme was implemented with an ML-ECDL mounted in the laser test mount (Fig. 3.2) which is not optimized for this purpose. The use of the ML-ECDL module presented in Sec. 5.3 was not possible as the integrated electronic circuit for the gain section injection current comprises an RF choke.

In this setup, the phase of the pulse repetition rate is compared and stabilized relative to the phase of an RF reference signal. For detection of this phase difference, the phase detector of a phase-/frequency-detector (PFD) module (PFD, see Ref. [205]) is utilized.

First, the input signal to the reference port (ref) of the PFD is discussed. That port requires a signal with a frequency of 320 MHz and an RF power of of (-3 ± 1) dBm. This signal is provided by an ultra-low noise microwave signal generator (SG2, Agilent E8257D, BW 250 kHz - 50 GHz, f = 320 MHz, A = -3 dBm). All employed signal generators and analyzers were referenced to a common 10 MHz reference, in this case provided by GPS.

Second, the part of the demonstrator setup concerning the pulse repetition rate (signal under test) is discussed. The signal port (sig) of the PFD is the input port for the signal under test. The port requires an input signal with a frequency between 5 MHz and 800 MHz at a level of (7.6 ± 6) dBm. In this work, the phase detector's output signal will be directly employed as

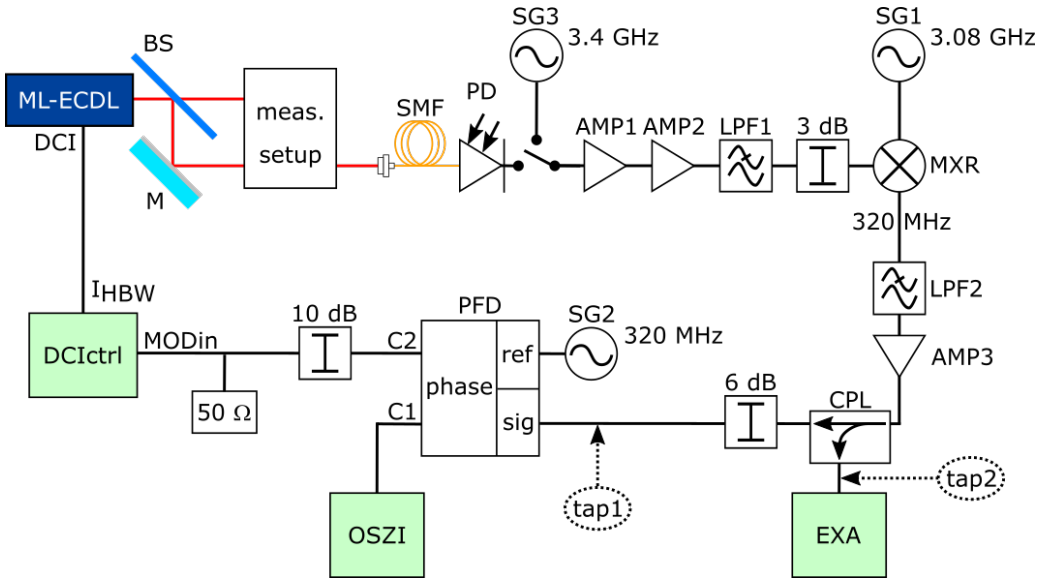

Figure 6.1.: Experimental setup for stabilization of the pulse repetition rate. The components and their corresponding abbreviations are explained in the text.

control signal. Thus, an (initial) input frequency at the signal port (sig) of the PFD similar to the input frequency at the reference port (ref) of the PFD, i.e. 320 MHz, is required. To down-convert the pulse repetition rate of about 3.4 GHz to 320 MHz, the following setup is used.

The optical pulse train generated by the ML-ECDL is converted into a corresponding pulsed electrical signal using a fast photodetector (PD, Newport 1004), see Sec. 3.3.2. Before inserting that electrical signal into a frequency mixer (MXR, MiniCircuits ZX05-30W-S+, BW 300 MHz - 4 GHz, $A_{RF} = 0$ dBm, $A_{LO} = 7$ dBm) for down-conversion, the electrical signal is amplified by a chain of amplifiers (AMP1, Centellax TA0L50VA; AMP2, each twice: MiniCircuits ZJL-7G+ and ZX60-14012L-S+). Then, a low pass filter (LPF1, MiniCircuits VLP-54, BW DC - 4 GHz) eliminates high frequency (noise) components of the pulsed electrical signal. Henceforth, that electrical signal will be called pulse repetition rate signal. A 3 dB attenuator is then used to adjust the RF power of the pulse repetition rate signal to the required input power of the MXR. By means of the MXR and an ultra-low noise microwave signal generator (SG1, Agilent E8257D, BW 250 kHz - 20 GHz, $f = 3.08$ GHz, $A = 7$ dBm) the pulse repetition rate signal is down-converted to the input frequency required for the sig input of the PFD ($f_{sig} = 320$ MHz). A low pass filter (LPF2, MiniCircuits SLP-600+, BW DC - 580 MHz) eliminates higher harmonics and residual high frequency components. To allow for simultaneous stabilization and monitoring of the pulse repetition rate signal, the down-converted pulse repetition rate signal is amplified (AMP3, MiniCircuits ZFL-500HLN+) and directed through a directional coupler (CPL, MiniCircuits ZFDC-10-1). The coupled path is directed to the electrical spectrum analyzer (EXA, Rohde & Schwarz FSV-30, 10 kHz - 30 GHz) for monitoring of the RF spectrum of the ML-ECDL. The transmitted path is then used as input signal for the sig input port of

the phase detector of the PFD which provides the error signal that is also used as the control signal. The electrical power of the transmitted path is adjusted to the required electrical input power of the sig port of 7.6 dBm.

The error signal is observed on an oscilloscope (OSZI, Agilent DSO-X 3024A) using one of the three identical outputs of the phase detector of the PFD (C1). From a second output (C2) of the PFD, the error signal is used as control signal and directly fed back to the gain section injection current by superimposing the error signal onto the DC current through the modulation input (MODin) of the current controller (DCIctrl, ILX LDC-3724C). Impedance matching is realized with a 50 Ω resistor that is also attached to the MODin of the current controller by means of a BNC T-adapter. To allow for large bandwidth modulation, the output mode of the current controller is changed to high bandwidth mode (option I_{HBW}, BW DC - 1 MHz) and the low noise filter (ILX LNF-320, see Sec. 3.3.2) in between the current source and the laser is removed. For optimization of the stabilization of the pulse repetition rate, the swept RF spectrum of the ML-ECDL is monitored with the electrical spectrum analyzer (EXA, Rohde & Schwarz FSV-30, 10 kHz - 30 GHz, see Sec. 3.4.2) that is employed throughout this work. The achieved servo bandwidth detected in the monitored stabilized RF spectrum is optimized by adjusting the amplitude of the control signal fed into MODin. The best result is achieved with 10 dB attenuator inserted between the PFD phase detector output and MODin. For detailed analysis of the stabilized pulse repetition rate, the frequency noise PSD (FN-PSD) of the frequency fluctuations of the pulse repetition rate of the ML-ECDL is analyzed. The results will be discussed in Sec. 6.3.

Characterization of the experimental setup

In order to evaluate the results of the stabilization of the pulse repetition rate, the stabilization setup and the corresponding measurement setup need to be characterized.

As part of the characterization of the stabilization setup, the transfer factor F_{trans} that translates the measured phase difference into a change of the pulse repetition rate is estimated. To that end, the transfer factors of the three components (PFD incl. 10 dB attenuator, current controller, and ML-ECDL) are determined.

The transfer factor of the phase detector of the PFD is measured as follows. SG3 is directly connected to the signal input of the PFD. Then, the frequency of SG3 is increased by 1 kHz relative to the frequency of SG2. By this means, the corresponding voltage shift per phase shift is determined by means of an oscilloscope (OSZI). The resulting transfer factor F_{PFD} at the output of the 10 dB attenuator corresponds to approximately 0.16 V/rad. Please note that the transfer function of the phase detector of the PFD is constant up to about 1 MHz [205].

The transfer factor F_t of the current controller from voltage to current is specified to 50 mA/V. The bandwidth of the modulation input of the current controller is specified to 1 MHz.

The transfer factor F_{las} of the ML-ECDL from current to pulse repetition rate was measured to be about 250 kHz/mA, see Sec. 4.3.2.

Thus, the resulting transfer factor F_{trans} is determined to be about $2 \cdot 10^6$ Hz/rad.

The electronic circuit that is employed to prepare the RF signal provided by the ML-ECDL for the signal input (sig) of the PFD is investigated at tap1. The corresponding RF signal which allows for monitoring of the RF spectrum of the ML-ECDL is investigated at tap2. For those measurements, the optical components of the stabilization setup, ML-ECDL to PD in the stabilization setup (Fig. 6.1), are omitted. That part of the setup is replaced by an ultra-low noise signal generator (SG3, Agilent E8257D, BW 250 kHz - 20 GHz) to synthesize an RF signal with a frequency of 3.4 GHz and an RF power of -40 dBm. That RF power is chosen as it provides an RF power of 0 dBm at the frequency mixer MXR and, thus, corresponds to the RF power provided by the corresponding RF signal of the ML-ECDL at the frequency mixer MXR. The FN-PSDs at tap1 and tap2 are characterized to investigate the influence of the electronic circuit on the FN-PSD of the RF signal of the ML-ECDL. The measurements are performed with the IQ measurement tool provided by the EXA.

The results of the characterization of the experimental setup will be shown and discussed together with the results of the stabilization of the pulse repetition rate in the subsequent section.

6.3. Results

The ML-ECDL chosen to investigate the pulse repetition rate stabilization capabilities is the ML-ECDL that is best suited to fulfill the requirements of the application, see Sec. 4.3. The ML-ECDL is mounted on the test setup. The values of the operating parameters are set as follows. The mount temperature is set to 20.0 °C. A reverse voltage of -1.55V is applied to the saturable absorber. The gain section injection current is set to 226 mA. A detailed analysis of the mode-locking performance of the free-running ML-ECDL can be found in Sec. 4.3.

6.3.1. RF characteristics

The RF spectra and the PSDs of the frequency fluctuations of the pulse repetition rate that are derived from IQ records are depicted in Fig. 6.2. In the low frequency range (10 Hz - 64 kHz, RBW 1 Hz), the FN-PSDs are determined from 10 s long time records that were acquired with a sampling rate of 160 kHz and an IQ bandwidth of 128 kHz. With those datasets, the RF spectra are also reconstructed. In the high frequency range (1 kHz - 10 MHz, RBW 100 Hz), the FN-PSDs are determined from 500 ms long time records with a sampling rate of 32 MHz and an IQ bandwidth of 25.6 MHz. In the representation of the FN-PSDs, the RBW of each frequency decade is set to 1/100 of the upper cut-off frequency of each decade which allows for reduction of statistical uncertainty.

First, the RF spectra of the free-running and the stabilized ML-ECDL are investigated. It can be seen in Fig. 6.2(a) that the stabilization of the pulse repetition rate reduces its linewidth by a factor of at least 3400 from around 4.76 kHz for the 3 dBc free-running pulse repetition rate to at most 1.4 Hz (resolution limited, RBW 1 Hz) for the stabilized one. Further details can be derived from the FN-PSD of both, the free-running and the stabilized ML-ECDL.

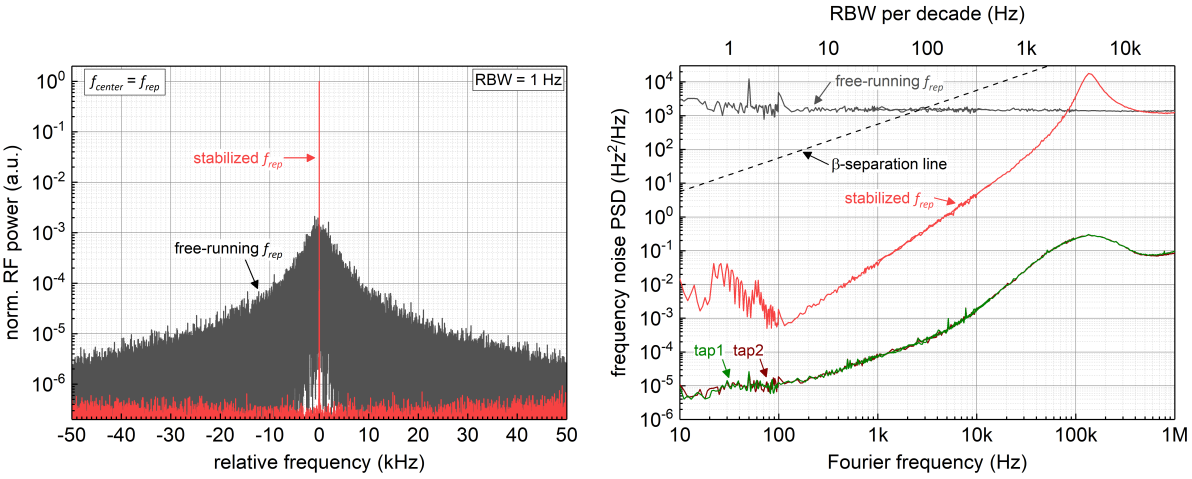

(a) RF spectrum (b) FN-PSD

Figure 6.2.: (a) RF spectra with a center frequency corresponding to the pulse repetition rate f_{rep} and (b) FN-PSDs of the frequency fluctuations of the pulse repetition rate f_{rep} for a stabilized and free-running ML-ECDL. Fig. (b) also depicts the FN-PSD derived for the signal generators SG1, SG2, and SG3 employed in the stabilization setup as well as reference measurements at tap1 and tap2. The signal generators were operated at those settings used in the stabilization setup - SG1: 7 dBm at 3.08 GHz, SG2: -3 dBm at 320 MHz, SG3: -40 dBm at 3.4 GHz.

Second, the FN-PSDs of the free-running and the stabilized ML-ECDL are investigated, see Fig. 6.2(b). The FN-PSD representing the free-running ML-ECDL features a white noise floor of about $1.5 \cdot 10^3$ Hz^2/Hz across almost the complete depicted frequency range. For Fourier frequencies above 1 MHz, the measurement is limited by the noise floor of the measurement setup. The characterization of the experimental setup for the stabilization, discussed below, indicates that the noise of the photodetector (PD) dominates in this frequency range. Thus, the FN-PSD for Fourier frequencies above 1 MHz is omitted from the graph.

In the following, the behavior of the FN-PSD corresponding to the stabilized pulse repetition rate is discussed in detail. It can be seen that for Fourier frequencies below about 80 kHz, the suppression of the FN-PSD of the stabilized ML-ECDL increases by two orders of magnitude per frequency decade towards smaller Fourier frequencies. This is the expected behavior of a control loop with a single integrator. The servo bandwidth of the stabilization loop is determined at that Fourier frequency at which the FN-PSD of the stabilized ML-ECDL is suppressed by 3 dB compared to the FN-PSD of the free-running ML-ECDL. Thus, a servo bandwidth of about 72 kHz can be estimated. For Fourier frequencies between 80 kHz and 400 kHz, the frequency noise of the stabilized ML-ECDL is amplified compared to the frequency noise of the free-running ML-ECDL. This so-called servo bump features a maximum FN-PSD at a Fourier frequencies of around 130 kHz. Comparison of the FN-PSD and the β-separation line [164] suggests that the RF spectrum is essentially Lorentzian shaped and features a δ-like peak at the

pulse repetition rate. Thus, on the investigated time scales, the RF spectrum is coherent. Hence, the RF linewidth of about 1.4 Hz that was determined from the reconstructed RF spectrum of the stabilized ML-ECDL provides an upper limit.

For Fourier frequencies below 100 Hz, the FN-PSD of the stabilized ML-ECDL shows an increase of noise. To investigate the source of this noise, the experimental setup is investigated.

To that end, the noise of the electronic circuit that is employed to down-convert the RF signal provided by the photodetector (PD) is analyzed at tap1 and tap2. The employed signal generators are set to provide the values of frequency (f_{SG1} = 3.08 GHz, f_{SG2} = 320 MHz, f_{SG3} = 3.4 GHz) and RF power (A_{SG1} = 7 dBm, A_{SG2} = -3 dBm, A_{SG3} = -40 dBm) described in Sec. 6.2. The FN-PSDs derived for the RF signals at tap1 and tap2 are depicted in Fig. 6.2(b). Comparing the determined FN-PSDs with the specifications of the electrical spectrum analyzer [206] shows that all these measurements are detection limited. However, the level of the determined FN-PSDs is below that of the FN-PSD of the stabilized ML-ECDL. Thus, no conclusion concerning the source of the increased noise of the stabilized ML-ECDL for Fourier frequencies below 100 Hz can be drawn from these measurements.

However, the stabilization loop should provide a control signal that also suppresses the FN-PSD of the free-running ML-ECDL for Fourier frequencies below 100 Hz. This suggests that noise is added during the phase comparison by, e.g., SG2 or the PFD. This noise is then translated into noise of the pulse repetition rate due to the large transfer factor F_{trans} of about $2 \cdot 10^6$ Hz/rad (see Sec. 6.2) provided by the stabilization loop. For the corresponding PSDs, $F_{trans}^2 \approx 4 \cdot 10^{12}$ Hz^2/rad^2 needs to be taken into account. The order of magnitude of the excessive noise that might be added by SG2 or the PFD can be estimated as follows. Taking into account the noise level of about 10^{-3} Hz^2/Hz that was determined for the stabilized ML-ECDL at a Fourier frequency of 100 Hz, see Fig. 6.2(b), the excessive added noise has to be in the order of 10^{-15} rad^2/Hz at Fourier frequencies of 100 Hz. To investigate a noise source of this order, a spectrum analyzer featuring a noise floor below 10^{-15} rad^2/Hz at Fourier frequencies of 100 Hz is required. However, such a device was not available at the time of this investigation. Thus, the source of the increase of the FN-PSD of the stabilized ML-ECDL at Fourier frequencies below 100 Hz could not unambiguously be determined in this work.

6.3.2. Optical characteristics

Considering the influence of the stabilization on other mode-locking characteristics, it can be shown that the optical spectrum of the stabilized ML-ECDL remains similar to that of the ML-ECDL with the free-running pulse repetition rate, see Fig. 6.3. The peak wavelength and the spectral width remain constant within the margin given by the resolution bandwidth, 774.10 nm, 1.7 nm at 3 dBc, 10.3 nm at 15 dBc, and 11.5 nm at 20 dBc for the free-running and the stabilized ML-ECDL, respectively. For comparison of the spectral shape, both spectra were normalized relative to their peak power. Additionally, the quotient between the free-running (P_{free}) and the stabilized (P_{stab}) spectrum was calculated, see Fig. 6.3. It is found that the spectra differ by less than 1 dB in the central part. Please note that the measurement of the optical spectrum is limited by the noise floor for wavelengths shorter and longer than approx. 771 nm and 785 nm, respectively.

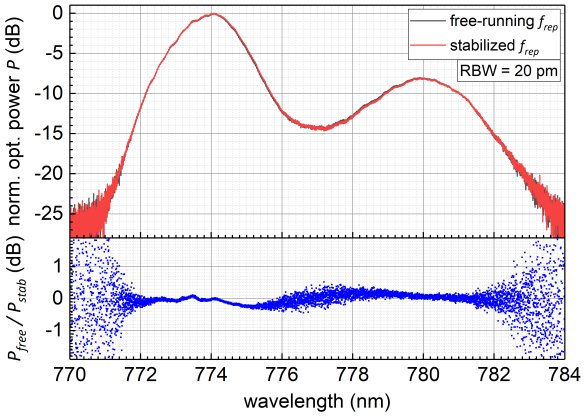

Figure 6.3.: Comparison of optical spectra recorded for the free-running (P_{free}, black) and the stabilized (P_{stab}, red) ML-ECDL. For better visualization, the quotient P_{free}/P_{stab} is also shown.

6.3.3. Temporal and optical power characteristics

The pulse shape (sech^2) and width (about 5.5 ps) remain nearly constant within the measurement accuracy (RBW = 100 fs) with stabilization of the pulse repetition rate, see Fig. 6.4. The noise peaks in the lower and upper delay range are measurement artifacts resulting from the low optical power available for this measurement.

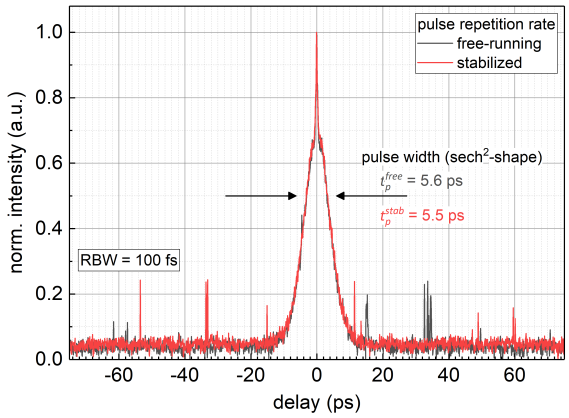

Figure 6.4.: Autocorrelation functions of the free-running and of the stabilized ML-ECDL.

Further, as the average optical power also remains constant with stabilization of the pulse repetition rate, the peak optical power remains constant at about 1.5 W.

6.4. Conclusion from the stabilization of the pulse repetition rate

The successful stabilization experiment shows that using an active stabilization scheme, a control signal for the gain section injection current can be generated to stabilize the pulse repetition

rate. Comparison of the frequency noise of the free-running and the stabilized pulse repetition rate reveals a servo bandwidth (3 dB suppression) of about 72 kHz with a servo bump at around 130 kHz. The transfer function of the open loop corresponds to a single integrator so that the suppression of the free-running FN-PSD increases by two orders of magnitude per decade towards smaller Fourier frequencies in closed loop operation. An upper limit of the RF linewidth of the stabilized pulse repetition rate of about 1.4 Hz (resolution limited, for an integration time of 1 s) was determined. No significant influence of the stabilization of the pulse repetition rate on the mode-locking performance characteristics other than the RF characteristics of pulse repetition rate was found.

The demonstrated frequency stabilization scheme of the pulse repetition rate allows for implementation of the advanced stabilization scheme for future QUANTUS experiments, see electrical circuits sketched in pink in Fig. 1.4(b). This concept only requires a stabilized pulse repetition rate but does not require stabilization of the absolute optical frequency, see Eq. 1.9. Employing both actuators, the gain section injection current and the saturable absorber reverse voltage, could allow for stabilization of the pulse repetition rate and the offset frequency of the frequency comb in the advanced stabilization scheme, see dark blue lines in Fig. 1.4(b). This would enable more versatile absolute frequency measurements. Thus, future investigation should also include the control of both, the gain section injection current and the saturable absorber reverse voltage.

7. Conclusion and outlook

7.1. Conclusion

The main goal of this dissertation was to develop a passively mode-locked diode laser for future experiments within the QUANTUS project series (Sec. 1.2). The laser should provide a spectral bandwidth exceeding 13.5 nm (20 dBc) in the wavelength range around 780 nm. A pulse repetition rate of 6.8 GHz or subharmonics with a free-running RF linewidth better than 10 kHz (3 dBc) was required. The laser had to provide an optical power of more than 100 nW for comb lines at 20 dBc. Micro-integration of the laser into a technology platform with no moving parts was required to provide the required compactness and robustness for future space-borne experiments. The pulse repetition rate needed to be stabilized for future implementation of the laser within the QUANTUS experiments. Further details on the requirements on the laser can be found in Sec. 1.2.4.

In the first part of this work, the design and components of the diode laser were investigated to optimize the mode-locking performance. To enable this development, an experimental setup comprising a laser test mount and a measurement setup were designed and implemented. Further details on the experimental setup and techniques can be found in Chap. 3.

First, the optical design of the laser including the external mirror was optimized. By comparing typical performance characteristics of various laser resonator concepts, an ECDL-type optical design comprising the diode laser chip, collimation micro-optics, and an external mirror was selected. A linear laser resonator was set as required by the micro-integration technology platform. Further details can be found in Secs. 2.5, 4.2.1, and 4.2.2.

Then, the influence of the resonator length on the mode-locking performance was analyzed. It was found that with increasing resonator length L_{res}, the pulse repetition rate decreases as $1/L_{res}$, as expected, the RF linewidth decreases, and the spectral bandwidth and the optical power increase. The optimization showed that long laser resonators are better suited to fulfill the requirements. Hence, with a length of 44 mm the longest laser resonator that can technologically be implemented in the intended micro-integration platform was set. This corresponds to a pulse repetition rate of about 3.4 GHz (first subharmonic of 6.8 GHz). Further details can be found in Sec. 4.2.3.

In a subsequent step, the epitaxial layer design of the diode laser chips was investigated. It was found that the epitaxial layer design is the most important design parameter for optimizing the spectral bandwidth. The stochiometric composition of the quantum wells was employed to optimize the spectral bandwidth. Different symmetric DQW structures featuring an As content of the QWs of 0.75 to 0.81, respectively, were compared. The corresponding mode-locked optical spectra feature single spectral bands with peak wavelengths of 760 nm to 780 nm, respectively,

and spectral bandwidths at 20 dBc of at most 7 nm. To increase the spectral bandwidth, an asymmetric DQW structure featuring an As content of 0.75 in one QW and 0.81 in the other QW was realized. The corresponding optical spectrum of the ML-ECDL comprised two spectral bands with a peak wavelength around 770 nm and 780 nm, respectively. Spectral bandwidths of more than 16 nm at 20 dBc were achieved fulfilling the requirement set out in Sec. 1.2.4. The required center wavelength of about 773.5 nm could not be achieved by optimizing the operation temperature in the experimentally accessible range of 15 °C and 40 °C. However, it was estimated that the ML-ECDL would cover the required wavelength range at about 11 °C. Hence, diode laser chips featuring aDQW structures were found to be the best suited devices. Further details can be found in Sec. 4.2.4.

The longitudinal design of the diode laser chip was explored with the goal to optimize the mode-locking performance characteristics. A strong influence of the longitudinal design on the RF stability was observed. First, diode laser chips with sDQW structure and chip lengths of 1 mm and 2 mm were investigated. Both devices provide similar spectral bandwidth of about 5 nm at 20 dBc. However, the increase of chip length leads to a strong decrease of RF linewidth from about 1 kHz to 0.1 kHz. Second, 2 mm long diode laser chips with aDQW structures and 50 µm and 100 µm long saturable absorbers were compared. Similar spectral bandwidths and RF linewidths were observed for both devices. However, the RF spectrum of the device with 50 µm long saturable absorber, in contrast to that of the device with a 100 µm long saturable absorber, features a periodic peak structure with a frequency period of about 70 MHz. Thus, a 2 mm long diode laser chip with a 100 µm long saturable absorber was found to be the best suited device. Further details can be found in Sec. 4.2.5.

Next, the influence of the reflectivity of the output (front) and the resonator-side facet of the diode laser chip on the mode-locking performance was studied. Asymmetric DQW devices with different front facet reflectivities R_f were compared. It was found that decreasing R_f from 30 % to 5 % resulted in an increase of the RF linewidth from 1.5 kHz to 5.3 kHz (3 dBc). Both values are well within the requirement. The spectral bandwidth at 20 dBc and the optical power increased from 15 nm to 16 nm and 15 mW to 25 mW, respectively, for the diode laser with $R_f = 5$ % compared to that with $R_f = 30$ %. Thus, the diode laser chip with $R_f = 5$ % was found to be the best suited device. Further, the influence of the AR coating of the resonator-side facet was investigated. It was found that an insufficient AR coating leads to a power modulation which can be observed as a modulation of the mode-locked optical spectrum with a period corresponding to the diode laser chip length. Thus, an optimized AR coating of the resonator-side facet was implemented. Further details can be found in Sec. 4.2.6.

The influence of the values of the operating parameters on the mode-locking performance of the ML-ECDL best suited to fulfill the aforementioned requirements was investigated. Optimization of the values of the operating parameters showed that the best suited device provides a spectral bandwidth at 20 dBc exceeding 16 nm with a peak wavelength around 773 nm and a center wavelength around 777 nm. A pulse repetition rate of 3.4 GHz with an RF linewidth of 6.5 kHz (3 dBc) is achieved. The ML-ECDL emits 5 ps (FWHM) long, sech^2-shaped pulses. The average optical power exceeds 25 mW providing a pulse peak power of about 1.3 W and a comb line power at 20 dBc of more than 650 nW.

The second part of this thesis work focuses on the hybrid micro-integration of an OFC based on the design optimized in the first part of this work to further demonstrate the suitability of the developed ML-ECDL for implementation in future experiments within the QUANTUS project series. In a first step, a small spectral bandwidth ML-ECDL was successfully integrated to identify technology gaps, e.g., displacement-free integration of the external mirror. In a second step, an advanced integration strategy was developed. This strategy was then successfully applied to integrate the large spectral bandwidth ML-ECDL that is best suited for future implementation in the application (Sec. 1.2). It was demonstrated that the mode-locking performance of a nominally identical ML-ECDL mounted on the laser test mount could successfully be reproduced with the advanced ML-ECDL module.

To demonstrate the suitability of the developed OFCG for implementation in future precision frequency comparison experiments, investigations on the stabilization of the pulse repetition rate to an external RF reference were conducted in the third part of this thesis work. For these, an experimental test bed was developed. This setup allows for stabilization of the phase of the pulse repetition rate relative to an external RF reference signal. Here, the gain section injection current was used as actuator. With a servo bandwidth of around 72 kHz, a reduction of the RF linewidth from 4.8 kHz to 1.4 Hz (resolution limited) was demonstrated. No significant changes of the mode-locking performance characteristics were observed. This RF linewidth surpasses the requirement by more than one order of magnitude.

In conclusion, the ML-ECDL developed within this thesis is best suited to fulfill the requirements derived from the application. Hence, it holds a promising potential for the envisioned implementation in future space-borne precision frequency comparison experiments and beyond.

7.2. Outlook on future advancements

The investigations presented in this thesis have shown that diode laser-based optical frequency combs have the potential to provide an alternative to already established solid-state or fiber-based frequency combs in frequency comparison experiments. In the course of the investigations, however, several possible improvements have been identified which promise to further enhance the performance of diode laser-based OFCs in the future.

Improvements of the diode laser chip

In order for the frequency comb to span the intended wavelength range at room temperature, the center wavelength of the mode-locked optical spectrum needs to be blue-shifted. Taking into account the shift of the center wavelength of the mode-locked optical spectrum with the As content of the QWs, this blue-shift can be realized by reducing the As content by an amount of less than 0.02 in each QW of the aDQW structure.

While the requirement for spectral bandwidth has successfully been met, using two QWs separated in wavelength by about 9 nm resulted in a reduced spectral overlap of the spectral bands emitted by each QW and a reduced RF stability. Reducing the spectral distance of the

modal gain peaks of each QW by reducing the steps of the As content between the QWs would avoid this problem. At the same time, however, the spectral bandwidth would be reduced. This can be accounted for by designing an active region featuring multi-QWs with spectrally closely shifted gain spectra. Further improvement can be brought about by not only modifying the As content and the number of QWs but also the layer thickness of the active region [176–179].

Insufficient AR coating of the resonator-side facet of the diode laser chip has shown to be detrimental to the stability of the mode-locking process, see, e.g., Fig. 4.14. Reduction of reflectivity of the resonator-side facet by several orders of magnitude can be realized by employing bent ridge waveguides providing an angle between the ridge waveguide and said facet [91].

Improvements regarding the laser concept

A disadvantage arising from spectral broadening is a reduction of optical power as observed for the aDQW lasers compared to the sDQW ones. A way to increase the optical power is to configure the laser in a MOPA configuration where the ML-ECDL is the master oscillator.

For further improvements, the properties of the external mirror need to be reconsidered. Employing chirped mirrors would allow for pulse shaping in the laser resonator to optimize the spectral gain in the master diode laser chip via gain recovery during the pulse duration. These mirrors can, e.g., be grown from semiconductor material [156, 158].

Future investigations should extent the stabilization process to include the saturable absorber reverse voltage as an actuator. Thus, two actuators, the reverse voltage applied to the absorber and the gain section injection current, would be available to simultaneously stabilize the pulse repetition rate and the offset frequency of the optical frequency comb. In this case, more versatile absolute frequency measurements would be possible.

For implementation in a harsh environment for, e.g., space-borne experiments, the micro-integrated ML-ECDL module requires a hermetic housing to shield it from environmental influence, RF suitable electrical feedthroughs, and a fiber coupled output. The next generation technology platform developed at the FBH does provide such capabilities and also allows for micro-integration of a MOPA type laser configuration [78]. Further, environmental stress tests, such as thermal cycling, and vibration and shock tests need to be conducted to demonstrate the ML-ECDL module's mechanical robustness. For actual space deployment, radiation tests, depending on the chosen orbit, are required. Successful space deployment of GaAs-based diode lasers developed by FBH has already been demonstrated, see, e.g., Ref. [6, 207], putting the future space deployment of the diode laser-based OFC developed within this work within reach.

Implementation of other technologies

In parallel to implementing improvements of the components or concept of the mode-locked laser, considering other technological approaches is of importance.

One aspect is the choice of gain medium. For broadening the optical gain of the diode laser chip, e.g., exploiting quantum dots (QD) instead of QWs should be considered. QDs are known to provide broad gain spectra resulting in, typically, large spectral bandwidth mode-locked optical spectra, and higher levels of RF stability [91, 92]. CW operating QD lasers in the

wavelength range of 775 nm have already been demonstrated [173, 174, 208].

Hybridization of the diode laser chip provides an option for separate optimization of the gain section and the saturable absorber, in form of using the full length of the diode laser chip as gain section and, e.g., a semiconductor saturable absorber mirror (SESAM) as saturable absorber and external mirror. A similar approach has been implemented in the early years of mode-locked diode laser development but has been disregarded in favor of integrating the saturable absorber with the gain section into a single diode laser chip, see, e.g., Ref. [108]. This approach can also be realized in a linear laser geometry and micro-integrated into the existing platforms by adhesively bonding the SESAM to an adapter substrate.

While also leading to a higher system complexity, employing the ML-ECDL as seed source is a follow-up step of hybridization on system level. One example is to use the ML-ECDL in a MOPA configuration to boost the system's optical output power. Another example is the use of a nonlinear waveguide or micro-resonator seeded by the ML-ECDL to broaden the system's optical spectrum [87, 209, 210]. The next-generation micro-integration technology platform discussed above, would, with minor modifications, also allow for micro-integration of those components. With regard to these concepts, the results presented in this thesis provide a promising basis for the development of systems tailored for the needs of various applications.

A. Derivation of equations

A.1. Influence of the spectroscopy stabilization in the advanced stabilization scheme

Here, the contribution of the uncertainty of the spectroscopy stabilization $\delta\nu_2$ to the uncertainty of the Eötvös ratio $\delta\eta$ is estimated.

As stated in Eq. 1.23, Δa is given as

$$\Delta a = a_1 - a_2 \approx \frac{c}{4\pi} \cdot \left[\frac{\Phi_1}{T_1^2} \cdot \frac{1}{\nu_2 + \Delta\nu} - \frac{\Phi_2}{T_2^2} \cdot \frac{1}{\nu_2} \right], \tag{A.1}$$

with

$$\frac{\partial(\Delta a)}{\partial(\nu_2)} \approx \frac{c}{4\pi} \cdot \left[\frac{-\Phi_1}{T_1^2 \cdot (\nu_2 + \Delta\nu)^2} + \frac{\Phi_2}{T_2^2 \cdot \nu_2^2} \right] = -\frac{a_1}{\nu_1} + \frac{a_2}{\nu_2}. \tag{A.2}$$

For $\delta\eta$, it follows analogously to Sec. 1.2.2 that

$$\delta\eta > \left| \frac{\partial\eta}{\partial\nu_2} \right| \cdot \delta\nu_2 = \left| \frac{\partial\eta}{\partial(\Delta a)} \cdot \frac{\partial(\Delta a)}{\partial\nu_2} \right| \cdot \delta\nu_2 \approx \left| \frac{1}{\bar{a}} \cdot \left(\frac{a_2}{\nu_2} - \frac{a_1}{\nu_1} \right) \right| \cdot \delta\nu_2. \tag{A.3}$$

Approximating $a_1 \approx a_2 \approx \bar{a}$, see Sec. 1.2.2, yields

$$\delta\nu_2 < \delta\eta \cdot \frac{1}{\left| \frac{1}{\nu_2} - \frac{1}{\nu_1} \right|} = \delta\eta \cdot \nu_1 \cdot \frac{\nu_2}{\Delta\nu} \approx \delta\eta \cdot \nu_1 \cdot 60. \tag{A.4}$$

Thus, compared to an individual spectroscopy stabilization at the K and Rb frequency, the requirement for the uncertainty $\delta\nu_2$ of the remaining spectroscopy stabilization is relaxed by a factor of 60.

A.2. Optical gain and absorption

This section describes the derivation of the fast optical gain in Eq. 2.10.

The derivation of the fast optical gain starts with Eq. 2.6. Fast optical gain means that the optical gain reacts instantaneously to incident optical power, $\mathrm{d}g/\mathrm{d}t = 0$. Neglecting carrier injection, the temporal behavior of the optical gain can be described by

$$\frac{\mathrm{d}g(N)}{\mathrm{d}t} = 0 = -\frac{g(N) + g' N_{tr}}{\tau_g} - g' v_g g(N) S(t). \tag{A.5}$$

Reorganizing Eq. A.5 for $g(N)$ results in

$$g(N) = \frac{-g' N_{tr}}{1 + \tau_g g' v_g S(t)}. \tag{A.6}$$

Using the relationship of photon density and optical power $S(t) = P(t)/(v_g \hbar \omega A_g)$, the relationship of saturation energy (Eq. 2.2) and saturation optical power $P_s^g = E_s^g/\tau_g$ gives

$$g(N) = \frac{g(N=0)}{1 + \frac{P(t)}{P_s^g}}. \tag{A.7}$$

List of Figures

1.1. Schematic of an optical frequency comb . . . 3
1.2. Schematic of the temporal distribution of multiple emitted longitudinal modes at a fixed point outside the laser resonator . . . 5
1.3. Measurement of optical frequencies and frequency differences . . . 6
1.4. Schematic of an advanced frequency comparison and frequency control for future QUANTUS experiments. . . . 10
1.5. Photos of a micro-integrated CW-ECDL and a micro-integrated CW-MOPA laser module . . . 14
1.6. Photo of an advanced ECDL-type laser module. . . . 15

2.1. Schematic of a sectioned diode laser chip . . . 26
2.2. Schematic of the epitaxial layer structure of a diode laser chip. . . . 27
2.3. Active mode-locking of a diode laser . . . 29
2.4. Schematic of a logarithmic model for optical gain and absorption . . . 31
2.5. Passive mode-locking of a diode laser . . . 31
2.6. Schematic of an electrical interface for hybrid mode-locking. . . . 33
2.7. Schematic of the energy-band diagram of a DQW double heterostructure . . . 33
2.8. Schematic of a mode-locked diode laser in a monolithic cavity . . . 37
2.9. Schematic of an ML-ECDL . . . 38

3.1. Schematic of test bed for development of passively mode-locked ECDL . . . 41
3.2. Photo of the fully assembled laser test mount. . . . 44
3.3. Functional schematic of measurement setup. . . . 46
3.4. Schematic of an optical spectrum . . . 48
3.5. Schematic of an RF spectrum . . . 49
3.6. Schematic of IQ data acquisition and analysis. . . . 52
3.7. Schematic of an FN-PSD and a reconstructed RF spectrum . . . 53
3.8. Schematic of an experimental setup for measurement of the intensity autocorrelation function. . . . 54

4.1. Schematic of the optical design of the ML-ECDL . . . 63
4.2. Optical spectra and FN-PSDs of ML-ECDLs with different resonator lengths . . . 66
4.3. Calculated modal gain spectra and measured ASE spectra of diode laser chips with different As content in the QWs. . . . 69
4.4. Mode-locked optical spectra of ML-ECDLs with different As content in the QWs corresponding to the data shown in Fig. 4.3 . . . 71

4.5. Calculated modal gain spectra and measured ASE spectra of diode laser chips with different carrier densities and gain section injection currents, respectively. . 73
4.6. Mode-locked optical spectra and spectral bandwidths of a sDQW(760) and an aDQW laser. 74
4.7. Schematic of physical dimensions of diode laser chips. 75
4.8. Optical spectra of ML-ECDLs with different gain section lengths. 77
4.9. RF spectra of ML-ECDLs with different gain section lengths. 77
4.10. Optical spectra and spectral bandwidths of ML-ECDLs with different saturable absorber section lengths 79
4.11. RF linewidths and RMS integrated timing jitters of ML-ECDLs with different saturable absorber section lengths 80
4.12. RF spectra of the SA50 and the SA100 device in a broad frequency range. 81
4.13. Self-lasing of the diode laser chip. 83
4.14. Modulation of the mode-locked optical spectrum due to parasitic feedback from the resonator-side facet. 84
4.15. Optical spectra, and peak wavelengths and spectral bandwidths at 3 dBc and 20 dBc of the large spectral bandwidth ML-ECDL. 90
4.16. Dependence of the optical spectrum on the mount temperature 92
4.17. RF spectra recorded simultaneously to the optical spectrum shown Fig. 4.15. . . 93
4.18. (a) FN-PSDs and (b) RF linewidths and RMS integrated timing jitters 95
4.19. (a) Autocorrelation function and (b) pulse widths and TBPs 96
4.20. Average and peak optical powers of large spectral bandwidth ML-ECDL, corresponding to the optical spectra shown in Fig. 4.15 97

5.1. Photo of a CW-ECDL and the first ML-ECDL module micro-integrated into the multi-purpose technology platform 103
5.2. Optical spectra of the first ML-ECDL module 107
5.3. RF spectra of the first ML-ECDL module 109
5.4. Photo of an advanced CW-ECDL module. 111
5.5. Photo of the advanced ML-ECDL module. 112
5.6. Detail photo of the advanced ML-ECDL module and schematic of the wire-bonds of the diode laser chip 113
5.7. Schematic and photo of the mirror assembly 115
5.8. Optical spectra of the advanced ML-ECDL module before and after hybrid integration of the external mirror, and after optimization of the values of operating parameters of the completed advanced ML-ECDL module. 117
5.9. Optical spectra and extracted spectral bandwidths at 3 dBc and 20 dBc of the advanced ML-ECDL module mounted on the integration setup 120
5.10. Optical spectra and extracted spectral bandwidths at 3 dBc and 20 dBc of the advanced ML-ECDL module mounted on the measurement setup 121
5.11. Optical spectra and extracted spectral bandwidths at 3 dBc and 20 dBc of the advanced ML-ECDL module mounted on the measurement setup with adjusted torque 123

5.12. RF linewidths of the advanced ML-ECDL. 123
5.13. Average optical power of the advanced ML-ECDL module 124

6.1. Experimental setup for stabilization of the pulse repetition rate 129
6.2. RF spectra and FN-PSDs of free-running and stabilized ML-ECDL 132
6.3. Comparison of optical spectra of free-running and stabilized ML-ECDL. 134
6.4. Autocorrelation functions of the free-running and of the stabilized ML-ECDL. . . 134

List of Tables

1.1. Spectral requirements for diode laser-based OFC. 18
1.2. Platform-related requirements for diode laser-based OFCG. 20
1.3. State of the art OFC generation in the wavelength range around 780 nm. 21

3.1. Constant k for typical pulse shape. 55
3.2. Pulse shape dependent form factor p_s for typical pulse shapes 57
3.3. Fourier-limited TBP for typical pulse shapes 60

4.1. Surface and coating characteristics of external mirror (Layertec 101085). 64
4.2. Operating parameters and normalization parameter for data shown in Fig. 4.2 . 65
4.3. Design properties of active epitaxial layer structures. 68
4.4. Values of the operating parameters for data shown in Figs. 4.3 and 4.4 69
4.5. Peak wavelengths and spectral bandwidths for the calculated modal gain spectra and measured ASE of different diode laser chips, and optical spectra of corresponding ML-ECDLs 69
4.6. Operating parameters of ML-ECDLs with different gain section lengths. 76
4.7. Mode-locking performance of ML-ECDLs with different gain section lengths . . . 76
4.8. Operating parameters of ML-ECDLs with different saturable absorber lengths. . 78
4.9. Operating parameters of the ML-ECDLs featuring sDQW diode laser chips with different front facet reflectivities 85
4.10. Key parameters of the mode-locking performance of the ML-ECDLs featuring sDQW diode laser chips with different front facet reflectivities 85
4.11. Operating parameters of the ML-ECDLs featuring aDQW diode laser chips with different front facet reflectivities 86
4.12. Key parameters of the mode-locking performance of the ML-ECDLs featuring aDQW diode laser chips with different front facet reflectivities 86
4.13. Values of operating parameter of the ML-ECDL for the investigation of the temperature dependency of the optical spectrum. 91

5.1. Values of the operating parameters of the first ML-ECDL module 106
5.2. Peak wavelengths and spectral bandwidths of the first ML-ECDL module 107
5.3. Values of operating parameters of advanced ML-ECDL module during the process of curing the adhesive for the external mirror. 116
5.4. Peak wavelengths and spectral bandwidths of the advanced ML-ECDL module . 117
5.5. Values of operating parameters of advanced ML-ECDL module 119

List of abbreviations

aDQW	asymmetric double quantum well
ACF	autocorrelation function
ACPM	anti-colliding pulse mode-locking
Ag	silver
Al	aluminum
AlGaAs	aluminum gallium arsenide
AlN	aluminum nitride
AR	anti-reflection
As	arsenic
ASE	amplified spontaneous emission
ASLOC	asymmetric super-large optical cavity
Au	gold
BBO	beta barium borate
BW	bandwidth
C	carbon
CAD	computer-aided design
CCP	conduction-cooled package
CEO	carrier-envelope-offset
CM	concave mirror
COMD	catastrophic optical mirror damage
Cu	copper
CW	continuous wave
CW-ECDL	continuous wave extended-cavity diode laser
DBW	demodulation bandwidth
DC	direct current
DCI	gain section injection current
DQW	double quantum well
ECDL	extended-cavity diode laser
EDM	electric discharge machining
EFL	effective focal length
FBH	Ferdinand-Braun-Institut, Leibniz-Institut für Höchstfrequenztechnik
FN-PSD	power spectral density of the frequency fluctuations of the pulse repetition rate
FWHM	full width at half maximum
GaAs	gallium arsenide
GaAsP	gallium arsenide phosphide
GVD	group velocity dispersion
HUB	Humboldt-Universität zu Berlin

HR	high-reflection
HWP	half-wave plate
I	in-phase
IB	integration band(width)
IF	intermediate frequency
IR	infra-red
IQ	in-phase and quadrature
K	potassium
LR	low-reflection
ML-ECDL	mode-locked extended-cavity diode laser
MIOB	micro-optial bench
MOPA	master oscillator power amplifier
MOVPE	metal-organic vapor-phase epitaxy
MQW	multi quantum well
NA	numerical aperture
Ni	nickel
OFC	optical frequency comb
OFCG	optical frequency comb generator
OSA	optical spectrum analyzer
P	phosphorus
PCB	printed circuit board
PFD	phase-/frequency-detector
PMT	photomultiplier tube
PN-PSD	phase noise power spectral density
PR	partial reflection
PSD	power spectral density
Q	quadrature
QD	quantum dot
QW	quantum well
Rb	rubidium
RBW	resolution bandwidth
RF	radio frequency
RMS	root-mean-square
RW	ridge waveguide
SA	saturable absorber section
SAB	saturable absorber reverse voltage
SCH	separate confinement heterostructure
SCPM	self-colliding pulse mode-locking
sDQW	symmetric double quantum well
sech^2	squared hyperbolic secant
SESAM	semiconductor saturable absorber mirror
SFG	sum frequency generation
SHG	second harmonic generation

Si	silicon
SiN$_x$	silicon nitride
SMA	SubMiniature version A
SNR	(coherent) signal-to-noise-ratio
SPM	self-phase modulation
SQW	single quantum well
TBP	time-bandwidth-product
TEC	thermo-electric cooler
TM	transverse magnetic
UFF	universality of free fall
UV	ultraviolet
VHBG	volume holographic Bragg grating
WEP	weak equivalence principle
WGM	whispering gallery mode

List of symbols

symbol	unit	description
$A(t)$	1	amplitude fluctuations of a mode-locked pulse train
A_r	1/s	non-radiative recombination processes
A_a	m^2	effective cross-section area of optical mode in the saturable absorber section
A_{az}	m^2	area of active region
A_g	m^2	effective cross-section area of optical mode in the gain section
a	m/s^2	local acceleration
$\bar{a}$	m/s^2	average of local accelerations
a_i	m/s^2	local acceleration of test mass i
$\alpha\prime$	m^2	differential absorption
α_0	1/m	absorption before arrival of pulse
$\alpha_{slow,fast}$	1/m	time-dependent slow, fast saturable absorption
$\alpha(N)$	1/m	carrier dependent absorption
B_r	m^3/s	spontaneous recombination processes
β	1/m	propagation constant
C_r	m^6/s	Auger recombination processes
c_0	m/s	speed of light in vacuum
d_{az}	m	thickness of active region
Δa	m/s^2	difference in local accelerations
ΔE_F	J	difference in quasi-Fermi levels of conduction and valence band
Δf_{rep}^L	Hz	RF linewidth of the pulse repetition rate determined with a Lorentzian fit of the RF spectrum
Δf_{rep}^β	Hz	RF linewidth of the pulse repetition rate determined with the β-separation line method
$\Delta\phi_{ceo}$	rad	phase slip from pulse to pulse
$\Delta\lambda_x$	m	spectral bandwidth of an optical spectrum at x dBc
$\Delta\nu$	Hz	frequency difference between the K and Rb lasers
$\Delta\nu_x$	Hz	spectral bandwidth x dBc
$\Delta\nu_{res}$	Hz	optical frequency resolution
$\Delta\bar{\omega}$	Hz	difference frequency between angular frequency of selected baseband signal and set center frequency
Δt	s	inverse sampling rate
$\delta\eta$	m/s^2	measurement uncertainty of the Eötvös ratio
$\delta(\Delta a)$	m/s^2	uncertainty of determination of Δa

symbol	unit	description
$\delta(\Delta\nu)$	Hz	uncertainty of frequency transfer $\Delta\nu$
$\delta I(t)$	W/m^2	noisy part of the temporary intensity profile of a mode-locked pulse train
$\delta\nu_K$	Hz	frequency uncertainty of the K laser
$\delta\nu_{Rb}$	Hz	frequency uncertainty of the Rb laser
$\delta\nu_{trans}$	Hz	frequency uncertainty introduced by the frequency stability transfer with the OFC
$E(\omega)$	Vs/m	Fourier-transform of electrical field of a pulse train $E(t)$
$E(t)$	V/m	electrical field of a pulse train
E_{CB}	J	energy level of the conduction band
E_{VB}	J	energy level of the valence band
E_{FC}	J	quasi-Fermi level of the conduction band
E_{FV}	J	quasi-Fermi level of the valence band
E_g	J	bandgap energy
E_p	J	pulse energy
$E_p(t)$	V/m	time-dependent electrical field of a single pulse
ϵ^{QW}	1	local dielectric function of QW
ϵ	cm^3	phenomenological coefficient
E_s^i	J	saturation energy of i (saturable absorption, optical gain)
η	1	Eötvös ratio
η_i	1	efficiency of current transfer into active region
F_t	mA/V	transfer factor from voltage to current of current controller
F_{las}	Hz/mA	transfer factor from current to pulse repetition rate of the ML-ECDL
F_{PFD}		transfer factor for voltage shift per phase shift of phase detector of PFD
$\bar{f}$	Hz	frequency set to record the IQ data
f_{bi}	Hz	beat note frequency with counter bi
f_{b-i}	Hz	beat note frequency of comb line closest to ν_i with ν_i
f_{ceo}	Hz	carrier-envelope-offset frequency
f_{cut}	Hz	cut-off frequency
f_{rep}	Hz	pulse repetition rate
$\bar{f}_{rep}$	Hz	time averaged pulse repetition rate
f_1, f_2, f_{ref}	Hz	reference frequencies in advanced stabilization scheme
$G_x(t)$	a.u.	autocorrelation function of function x
$g(N)$	1/m	carrier dependent optical gain
g'	m^2	differential gain
g_0	1/m	optical gain before arrival of pulse
g_m	1/m	modal gain
$g_{slow,fast}$	1/m	time-dependent slow, fast optical gain
Γ	1	confinement factor
Γ_a	1	confinement factor in saturable absorber section
Γ_g	1	confinement factor in gain section
$\hbar$	Js	reduced Planck constant
$I_{AF}(\tau)$	1	normalized (optical) intensity autocorrelation function

symbol	unit	description
I_{DCI}	A	gain section injection current
$I_0(t)$	W/m^2	intensity profile of a perfectly mode-locked pulse train
$I_p(t)$	W/m^2	time dependent intensity of a single pulse
$I(t)$	W/m^2	intensity
$I(t)$	[V(t)]	in-phase component of $V(t)$
$J(x)$	W/m	vertical distribution of the optical power
$J(t)$	1/(sm^2)	carrier injection into active region
$J_t(t)$	1	timing fluctuations of a mode-locked pulse train
j_t	s	RMS integrated timing jitter
k	1/m	absolute value of the difference of the wave vectors of the counter-propagating light pulses of the atom interferometer
k_{eff}	1/m	effective wave vector of the counter-propagating light pulses of the atom interferometer
k_i	1/m	wave vector of a light pulse i in the atom interferometer
k_p	1	pulse shape-dependent constant
$\mathfrak{L}(f)$	Hz^2/Hz	*one half of the one-sided* power *spectral density of* the *phase fluctuations* [161]
L_{az}	m	length of active region
L_β	Hz	β-separation line
L_{chip}	m	diode laser chip length
L_{gain}	m	gain section length
L_{res}	m	resonator length
L_{SA}	m	saturable absorber section length
λ	m	wavelength
λ_c	m	center wavelength
λ_p	m	peak wavelength
λ_{pQWi}	m	peak wavelength of spectral band corresponding to QW i
m	1	counter
m_{ci}	1	counter for comb line ci
N	1/m^3	carrier concentration
N_{tr}	1/m^3	transparency carrier density
N_{QW}	1	number of QWs
n	1	counter
n_{eff}	1	effective refractive index
n_g	1	group refractive index
ν_c	Hz	center optical frequency
νci	Hz	optical frequency of comb line ci
ν_i	Hz	optical frequency with counter i
n_H	1	harmonic number
n_p	1	number of measurement points
ν_K	Hz	frequency of the D2 transition of potassium
ν_{Rb}	Hz	frequency of the D2 transition of rubidium

symbol	unit	description
ν_{trans}	Hz	part of frequency difference between K and Rb lasers that is directly bridged by the OFC
ω	Hz	angular frequency
ω_{ca}	Hz	angular carrier frequency
ω_{n_H}	Hz	angular frequency of harmonic n_H of pulse repetition rate
$P(t)$	W	time dependent optical power
P_s^{α}	W	saturation optical power in saturable absorber
P_s^{g}	W	saturation optical power in gain section
P_{avg}	W	average optical output power
P_i	W	optical power of comb line i
P_K	W	optical power of the comb line closest to the K D2 transition frequency
P_{lambda_p}	W	maximum optical power of the optical spectrum
P_p	W	peak optical power
P_{pulse}	W	optical power of a single pulse
P_{Rb}	W	optical power of the comb line closest to the Rb D2 transition frequency
$P(t)$	W	time-dependent optical power of a pulse train
$p(t)$	1	temporal pulse shape
p_{max}	1	maximum of $p(t)$
p_s	1	pulse shape dependent form factor
$\varphi(t)$	rad	instantaneous phase
$\partial(x)$	a.u.	partial derivative of function x
φ_{n_H}	rad	time dependent phase of a harmonic n_H of the pulse repetition rate
Φ	rad	accumulated interferometer phase shift
ϕ_{ceo}	rad	carrier-envelope-offset phase
ϕ_0	rad	carrier-envelope-offset phase at time zero
$Q(t)$	[V(t)]	in-quadrature component of $V(t)$
$R(N)$	$1/(\mathrm{m}^3\mathrm{s})$	carrier recombination
$S(t)$	$1/\mathrm{m}^3$	time dependent photon density
$S_x(f)$	$[\mathrm{x}]^2/\mathrm{Hz}$	one-sided power spectral density that corresponds to function x
τ	s	time delay
τ_g	s	carrier lifetime in gain section
τ_p	s	width of $I_{AF}(\tau)$ determined as FWHM intensity
τ_α	s	carrier life time in saturable absorber
t_p	s	pulse width determined as FWHM intensity
T	s	interrogation time
T_m	s	measurement time
T_{mount}	°C	mount temperature
T_{rep}	s	periodicity of the pulses, round trip time of pulses in laser resonator
U_{SAB}	V	saturable absorber reverse voltage
V_{az}	m^3	volume of active region
v_g	m/s	group velocity

symbol	unit	description
$V(t)$	V	RF signal corresponding to the intensity profile of the mode-locked pulse train
V_{n_H}	V	voltage amplitude at a frequency corresponding to a harmonic n_H of the pulse repetition rate
w_0	m	beam diameter ($1/e^2$, intensity)
y_i	1	arsenic content of QW i
z_R	m	Rayleigh range
$< x >$	[x]	average of function x
$\mathfrak{F}(x)$	a.u.	Fourier-transform of function x
$\Im(x)$	[x]	imaginary part of complex function x
$\Re(x)$	[x]	real part of complex function x
$\dot{x}$	[x]	time-derivative of function x
$\hat{x}$	[x]	envelope of function x

Bibliography

[1] T. E. Mehlstäubler, G. Grosche, C. Lisdat, P. O. Schmidt, and H. Denker, "Atomic clocks for geodesy," *Reports Prog. Phys.*, vol. 81, p. 064401, 2018.

[2] P. Trocha, M. Karpov, D. Ganin, M. H. Pfeiffer, A. Kordts, S. Wolf, J. Krockenberger, P. Marin-Palomo, C. Weimann, S. Randel, W. Freude, T. J. Kippenberg, and C. Koos, "Ultrafast optical ranging using microresonator soliton frequency combs," *Science*, vol. 359, pp. 887–891, 2018.

[3] A. V. Muraviev, V. O. Smolski, Z. E. Loparo, and K. L. Vodopyanov, "Massively parallel sensing of trace molecules and their isotopologues with broadband subharmonic mid-infrared frequency combs," *Nat. Photonics*, vol. 12, pp. 209–214, 2018.

[4] M. Lezius, T. Wilken, C. Deutsch, M. Giunta, O. Mandel, A. Thaller, V. Schkolnik, M. Schiemangk, A. Dinkelaker, A. Kohfeldt, A. Wicht, M. Krutzik, A. Peters, O. Hellmig, H. Duncker, K. Sengstock, P. Windpassinger, K. Lampmann, T. Hülsing, T. W. Hänsch, and R. Holzwarth, "Space-borne frequency comb metrology," *Optica*, vol. 3, pp. 1381–1387, 2016.

[5] B. Barrett, L. Antoni-Micollier, L. Chichet, B. Battelier, T. Lévèque, A. Landragin, and P. Bouyer, "Dual matter-wave inertial sensors in weightlessness," *Nat. Commun.*, vol. 7, p. 13786, 2016.

[6] D. Becker, M. D. Lachmann, S. T. Seidel, H. Ahlers, A. N. Dinkelaker, J. Grosse, O. Hellmig, H. Müntinga, V. Schkolnik, T. Wendrich, A. Wenzlawski, B. Weps, R. Corgier, T. Franz, N. Gaaloul, W. Herr, D. Lüdtke, M. Popp, S. Amri, H. Duncker, M. Erbe, A. Kohfeldt, A. Kubelka-Lange, C. Braxmaier, E. Charron, W. Ertmer, M. Krutzik, C. Lämmerzahl, A. Peters, W. P. Schleich, K. Sengstock, R. Walser, A. Wicht, P. Windpassinger, and E. M. Rasel, "Space-borne Bose–Einstein condensation for precision interferometry," *Nature*, vol. 562, pp. 391–395, oct 2018.

[7] E. R. Elliott, M. C. Krutzik, J. R. Williams, R. J. Thompson, and D. C. Aveline, "NASA's cold atom lab (CAL): system development and ground test status," *npj Microgravity*, vol. 4, p. 16, dec 2018.

[8] J. L. Hall, "Defining and measuring optical frequencies (Nobel lecture)," *Rev. Mod. Phys.*, vol. 78, no. 4, pp. 1279–1295, 2006.

[9] T. W. Hänsch, "Passion for precision (Nobel lecture)," *Rev. Mod. Phys.*, vol. 78, no. 4, 2006.

[10] S. A. Diddams, J. Ye, L. Hollberg, Y. E. Ye, and S. E. Cundiff, *Femtosecond optical frequency comb: principle, operation, and applications*. Boston: Kluwer Academic Publishers, 2005.

[11] H. R. Telle, G. Steinmeyer, A. E. Dunlop, J. Stenger, D. H. Sutter, and U. Keller, "Carrier-envelope offset phase control: a novel concept for absolute optical frequency measurement and ultrashort pulse generation," *Appl. Phys. B*, vol. 69, pp. 327–332, 1999.

[12] T. Udem, J. Reichert, R. Holzwarth, and T. W. Hänsch, "Absolute optical frequency measurement of the cesium D_1 line with a mode-locked laser," *Phys. Rev. Lett.*, vol. 82, pp. 3568–3571, 1999.

[13] K. Iwakuni, S. Okubo, O. Tadanaga, H. Inaba, A. Onae, F.-L. Hong, and H. Sasada, "Generation of a frequency comb spanning more than 3.6 octaves from ultraviolet to mid infrared," *Opt. Lett.*, vol. 41, pp. 3980–3983, 2016.

[14] S. T. Cundiff and J. Ye, "Colloquium : Femtosecond optical frequency combs," *Rev. Mod. Phys.*, vol. 75, pp. 325–342, mar 2003.

[15] M. Anderson, N. G. Pavlov, J. D. Jost, G. Lihachev, J. Liu, T. Morais, M. Zervas, M. L. Gorodetsky, and T. J. Kippenberg, "Highly efficient coupling of crystalline microresonators to integrated photonic waveguides," *Opt. Lett.*, vol. 43, p. 2106, 2018.

[16] P. Manurkar, E. F. Perez, D. D. Hickstein, D. R. Carlson, J. Chiles, D. A. Westly, E. Baumann, S. A. Diddams, N. R. Newbury, K. Srinivasan, S. B. Papp, and I. Coddington, "Fully self-referenced frequency comb consuming 5 watts of electrical power," *OSA Contin.*, vol. 1, pp. 274–282, 2018.

[17] J. N. Eckstein, A. I. Ferguson, and T. W. Hänsch, "High-resolution two-photon spectroscopy with picosecond light pulses," *Phys. Rev. Lett.*, vol. 40, pp. 847–850, 1978.

[18] A. Sahm, C. Fiebig, S. Spießberger, M. Schiemangk, E. Luvsandamdin, K. Paschke, G. Erbert, and G. Tränkle, "Modular assembly of diode lasers in a compact and reliable setup for a wide range of applications," in *IEEE 62nd Electron. Components Technol. Conf.*, (San Diego, CA, USA), pp. 1852–1857, IEEE, 2012.

[19] M. Schiemangk, K. Lampmann, A. Dinkelaker, A. Kohfeldt, M. Krutzik, C. Kürbis, A. Sahm, S. Spießberger, A. Wicht, G. Erbert, G. Tränkle, and A. Peters, "High-power, micro-integrated diode laser modules at 767 and 780 nm for portable quantum gas experiments," *Appl. Opt.*, vol. 54, pp. 5332–5338, 2015.

[20] A. N. Dinkelaker, M. Schiemangk, V. Schkolnik, A. Kenyon, K. Lampmann, A. Wenzlawski, P. Windpassinger, O. Hellmig, T. Wendrich, E. M. Rasel, M. Giunta, C. Deutsch, C. Kürbis, R. Smol, A. Wicht, M. Krutzik, and A. Peters, "Autonomous frequency stabilization of two extended-cavity diode lasers at the potassium wavelength on a sounding rocket," *Appl. Opt.*, vol. 56, pp. 1388–1396, 2017.

[21] M. C. Amann, F. Capasso, A. Larsson, and M. Pessa, "Focus on advanced semiconductor heterostructures for optoelectronics," *New J. Phys.*, vol. 11, p. 125012, 2009.

[22] P. T. Ho, L. A. Glasser, E. P. Ippen, and H. A. Haus, "Picosecond pulse generation with a CW GaAlAs laser diode," *Appl. Phys. Lett.*, vol. 33, pp. 241–242, 1978.

[23] S. Gee and J. E. Bowers, "Ultraviolet picosecond optical pulse generation from a mode-locked InGaN laser diode," *Appl. Phys. Lett.*, vol. 79, pp. 1951–1952, 2001.

[24] D. Derickson, R. Helkey, A. Mar, J. Karin, J. Wasserbauer, and J. Bowers, "Short pulse generation using multisegment mode-locked semiconductor lasers," *IEEE J. Quantum Electron.*, vol. 28, pp. 2186–2202, 1992.

[25] A. Hugi, G. Villares, S. Blaser, H. C. Liu, and J. Faist, "Mid-infrared frequency comb based on a quantum cascade laser," *Nature*, vol. 492, pp. 229–233, 2012.

[26] T. van Zoest, N. Gaaloul, Y. Singh, H. Ahlers, W. Herr, S. T. Seidel, W. Ertmer, E. Rasel, M. Eckart, E. Kajari, S. Arnold, G. Nandi, W. P. Schleich, R. Walser, A. Vogel, K. Sengstock, K. Bongs, W. Lewoczko-Adamczyk, M. Schiemangk, T. Schuldt, A. Peters, T. Konemann, H. Muntinga, C. Lammerzahl, H. Dittus, T. Steinmetz, T. W. Hänsch, and J. Reichel, "Bose-Einstein condensation in microgravity," *Science*, vol. 328, pp. 1540–1543, 2010.

[27] S. Herrmann, H. Dittus, and C. Lämmerzahl (for the QUANTUS and PRIMUS teams), "Testing the equivalence principle with atomic interferometry," *Class. Quantum Gravity*, vol. 29, p. 184003, 2012.

[28] H. Müntinga, H. Ahlers, M. Krutzik, A. Wenzlawski, S. Arnold, D. Becker, K. Bongs, H. Dittus, H. Duncker, N. Gaaloul, C. Gherasim, E. Giese, C. Grzeschik, T. W. Hänsch, O. Hellmig, W. Herr, S. Herrmann, E. Kajari, S. Kleinert, C. Lämmerzahl, W. Lewoczko-Adamczyk, J. Malcolm, N. Meyer, R. Nolte, A. Peters, M. Popp, J. Reichel, A. Roura, J. Rudolph, M. Schiemangk, M. Schneider, S. T. Seidel, K. Sengstock, V. Tamma, T. Valenzuela, A. Vogel, R. Walser, T. Wendrich, P. Windpassinger, W. Zeller, T. van Zoest, W. Ertmer, W. P. Schleich, and E. M. Rasel, "Interferometry with Bose-Einstein condensates in microgravity," *Phys. Rev. Lett.*, vol. 110, p. 093602, 2013.

[29] D. Schlippert, J. Hartwig, H. Albers, L. L. Richardson, C. Schubert, A. Roura, W. P. Schleich, W. Ertmer, and E. M. Rasel, "Quantum test of the universality of free fall," *Phys. Rev. Lett.*, vol. 112, p. 203002, 2014.

[30] T. Schuldt, C. Schubert, M. Krutzik, L. G. Bote, N. Gaaloul, J. Hartwig, H. Ahlers, W. Herr, K. Posso-Trujillo, J. Rudolph, S. Seidel, T. Wendrich, W. Ertmer, S. Herrmann, A. Kubelka-Lange, A. Milke, B. Rievers, E. Rocco, A. Hinton, K. Bongs, M. Oswald, M. Franz, M. Hauth, A. Peters, A. Bawamia, A. Wicht, B. Battelier, A. Bertoldi, P. Bouyer, A. Landragin, D. Massonnet, T. Lévèque, A. Wenzlawski, O. Hellmig, P. Windpassinger, K. Sengstock, W. von Klitzing, C. Chaloner, D. Summers, P. Ireland, I. Mateos, C. F. Sopuerta, F. Sorrentino, G. M. Tino, M. Williams, C. Trenkel, D. Gerardi,

M. Chwalla, J. Burkhardt, U. Johann, A. Heske, E. Wille, M. Gehler, L. Cacciapuoti, N. Gürlebeck, C. Braxmaier, and E. Rasel, "Design of a dual species atom interferometer for space," *Exp. Astron.*, vol. 39, pp. 167–206, 2015.

[31] S. Kulas, C. Vogt, A. Resch, J. Hartwig, S. Ganske, J. Matthias, D. Schlippert, T. Wendrich, W. Ertmer, E. Maria Rasel, M. Damjanic, P. Weßels, A. Kohfeldt, E. Luvsandamdin, M. Schiemangk, C. Grzeschik, M. Krutzik, A. Wicht, A. Peters, S. Herrmann, and C. Lämmerzahl, "Miniaturized lab system for future cold atom experiments in microgravity," *Microgravity Sci. Technol.*, vol. 29, pp. 37–48, 2017.

[32] A. Azouz, N. Stelmakh, P. Langlois, J.-M. Lourtioz, and P. Gavrilovic, "Nonlinear chirp compensation in high-power broad-spectrum pulses from single-stripe mode-locked laser diodes," *IEEE J. Sel. Top. Quantum Electron.*, vol. 1, pp. 577–582, 1995.

[33] J. R. C. Woods, *A mode-locked diode laser frequency comb for ultracold atomic physics experiments*. Dissertation, University of Southhampton, 2016.

[34] M. Karpov, M. H. Pfeiffer, J. Liu, A. Lukashchuk, and T. J. Kippenberg, "Photonic chip-based soliton frequency combs covering the biological imaging window," *Nat. Commun.*, vol. 9, p. 1146, 2018.

[35] N. G. Pavlov, S. Koptyaev, G. V. Lihachev, A. S. Voloshin, A. A. Gorodnitskii, and M. L. Gorodetsky, "Narrow linewidth lasing and soliton Kerr-microcombs with ordinary laser diodes," *Nat. Photonics*, vol. 12, pp. 694–698, 2018.

[36] A. S. Raja, A. S. Voloshin, H. Guo, S. E. Agafonova, J. Liu, A. S. Gorodnitskiy, M. Karpov, N. G. Pavlov, E. Lucas, R. R. Galiev, A. E. Shitikov, J. D. Jost, M. L. Gorodetsky, and T. J. Kippenberg, "Electrically pumped photonic integrated soliton microcomb," *Nat. Commun.*, vol. 10, p. 680, 2019.

[37] C. Lämmerzahl and S. Herrmann, "Präzisionsinterferometrie mit Materiewellen unter Schwerelosigkeit (PRIMUS): Abschlußbericht," tech. rep., Universität Bremen, Zentrum für angewandte Raumfahrttechnologie und Mikrogravitation (ZARM), Bremen, 2011.

[38] A. L. Schawlow and C. H. Townes, "Infrared and optical masers," *Phys. Rev.*, vol. 112, pp. 1940–1949, 1958.

[39] T. H. Maiman, "Stimulated optical radiation in ruby," *Nature*, vol. 187, pp. 493–494, 1960.

[40] K. Gürs and R. Müller, "Breitband-Modulation durch Steuerung der Emission eines optischen Masers (Auskoppelmodulation)," *Phys. Lett.*, vol. 5, pp. 179–181, 1963.

[41] K. Gürs, "Beats and modulation in optical ruby lasers," in *Quantum Electron. III* (P. Grivet and N. Bloembergen, eds.), pp. 1113–1119, New York: Columbia Univ. Press, 1964.

[42] H. Statz and C. L. Tang, "Zeeman effect and nonlinear interactions between oscillating laser modes," in *Quantum Electron. III* (P. Grivet and N. Bloemberg, eds.), pp. 469–498, New York: Columbia Univ. Press, 1964.

[43] H. W. Mocker and R. J. Collins, "Mode competition and self-locking effects in a Q-switched ruby laser," *Appl. Phys. Lett.*, vol. 7, pp. 270–273, 1965.

[44] D. A. Stetser and A. J. DeMaria, "Optical spectra of ultrashort optical pulses generated by mode-locked Glass:Nd lasers," *Appl. Phys. Lett.*, vol. 9, pp. 118–120, 1966.

[45] A. J. DeMaria, D. A. Stetser, and H. Heynau, "Self mode-locking of lasers with saturable absorbers," *Appl. Phys. Lett.*, vol. 8, pp. 174–176, 1966.

[46] N. Basov, P. Kriukov, V. Letokhov, and Y. Senatskii, "Generation and amplification of ultrashort optical pulses," *IEEE J. Quantum Electron.*, vol. 4, pp. 606–609, 1968.

[47] M. Di Domenico, "Small-signal analysis of internal (coupling-type) modulation of lasers," *J. Appl. Phys.*, vol. 35, pp. 2870–2876, 1964.

[48] L. E. Hargrove, R. L. Fork, and M. A. Pollack, "Locking of He–Ne laser modes induced by synchronous intracavity modulation," *Appl. Phys. Lett.*, vol. 5, pp. 4–5, 1964.

[49] A. Yariv, "Internal modulation in multimode laser oscillators," *J. Appl. Phys.*, vol. 36, pp. 388–391, 1965.

[50] H. Statz and C. L. Tang, "Phase locking of modes in lasers," *J. Appl. Phys.*, vol. 36, pp. 3923–3927, 1965.

[51] H. Statz, G. A. DeMars, and C. L. Tang, "Self-locking of modes in lasers," *J. Appl. Phys.*, vol. 38, pp. 2212–2222, 1967.

[52] J. R. Klauder, "Spectral criterion for mode locked laser signals," *Appl. Phys. Lett.*, vol. 14, pp. 147–148, 1969.

[53] T. Udem, J. Reichert, R. Holzwarth, and T. W. Hänsch, "Accurate measurement of large optical frequency differences with a mode-locked laser," *Opt. Lett.*, vol. 24, pp. 881–883, 1999.

[54] J. Reichert, R. Holzwarth, T. Udem, and T. Hänsch, "Measuring the frequency of light with mode-locked lasers," *Opt. Commun.*, vol. 172, pp. 59–68, 1999.

[55] M. Bellini and T. W. Hänsch, "Phase-locked white-light continuum pulses: toward a universal optical frequency-comb synthesizer," *Opt. Lett.*, vol. 25, pp. 1049–1051, 2000.

[56] T. Udem, R. Holzwarth, and T. W. Hänsch, "Optical frequency metrology," *Nature*, vol. 416, pp. 233–237, mar 2002.

[57] R. Holzwarth, M. Zimmermann, T. Udem, and T. W. Hänsch, "Optical clockworks and the measurement of laser frequencies with a mode-locked frequency comb," *IEEE J. Quantum Electron.*, vol. 37, pp. 1493–1501, 2001.

[58] J. Ye, H. Schnatz, and L. Hollberg, "Optical frequency combs: from frequency metrology to optical phase control," *IEEE J. Sel. Top. Quantum Electron.*, vol. 9, pp. 1041–1058, 2003.

[59] T. Udem and F. Riehle, "Frequency combs applications and optical frequency standards," *Rev. del nuovo Cim.*, vol. 30, pp. 563–606, 2007.

[60] A. Bartels, D. Heinecke, and S. A. Diddams, "10-GHz self-referenced optical frequency comb," *Science*, vol. 326, p. 681, 2009.

[61] T. J. Kippenberg, R. Holzwarth, and S. A. Diddams, "Microresonator-based optical frequency combs," *Science*, vol. 332, pp. 555–559, 2011.

[62] J. Kim and Y. Song, "Ultralow-noise mode-locked fiber lasers and frequency combs: principles, status, and applications," *Adv. Opt. Photonics*, vol. 8, pp. 465–540, 2016.

[63] S. T. Cundiff, "Phase stabilization of ultrashort optical pulses," *J. Phys. D. Appl. Phys.*, vol. 35, pp. R43–R59, 2002.

[64] A. Tager, "Mode competition and mode locking in compound cavity semiconductor lasers," *IEEE Photonics Technol. Lett.*, vol. 6, pp. 164–166, 1994.

[65] C. Rullière, ed., *Femtosecond laser pulses - principles and experiments.* Springer-Verlag, 2005.

[66] S. Singh, R. Smith, and M. Di Domenico, "Axial modes of a ruby laser with external reflectors," *Proc. IEEE*, vol. 53, pp. 507–508, 1965.

[67] T. Shimizu, X. Wang, and H. Yokoyama, "Asymmetric colliding-pulse mode-locking in InGaAsP semiconductor lasers," *Opt. Rev.*, vol. 2, pp. 401–403, 1995.

[68] H. Schnatz, "Measurement of optical frequencies and frequency ratios," *Meas. Sci. Technol.*, vol. 14, pp. 1200–1215, 2003.

[69] L. Shao, N. Wex, and M. Kramer, "Testing the universality of free fall towards dark matter with radio pulsars," *Phys. Rev. Lett.*, vol. 120, p. 241104, 2018.

[70] V. Schkolnik, O. Hellmig, A. Wenzlawski, J. Grosse, A. Kohfeldt, K. Döringshoff, A. Wicht, P. Windpassinger, K. Sengstock, C. Braxmaier, M. Krutzik, and A. Peters, "A compact and robust diode laser system for atom interferometry on a sounding rocket," *Appl. Phys. B Lasers Opt.*, vol. 122, p. 217, 2016.

[71] A. Peters, K. Y. Chung, and S. Chu, "High-precision gravity measurements using atom interferometry," *Metrologia*, vol. 38, pp. 25–61, 2001.

[72] D. Schlippert, *Quantum test of the universality of free fall.* Dissertation, dr. rer. nat., Gottfried Wilhelm Leibniz Universität Hannover zur, 2014.

[73] J. Kitching, "Chip-scale atomic devices," *Appl. Phys. Rev.*, vol. 5, p. 031302, 2018.

[74] D. A. Steck, "Rubidium 87 D Line Data." http://steck.us/alkalidata/, 2015 (accessed: 01.03.2018).

[75] D. N. Aguilera, H. Ahlers, B. Battelier, A. Bawamia, A. Bertoldi, R. Bondarescu, K. Bongs, P. Bouyer, C. Braxmaier, L. Cacciapuoti, C. Chaloner, M. Chwalla, W. Ertmer, M. Franz, N. Gaaloul, M. Gehler, D. Gerardi, L. Gesa, N. Gürlebeck, J. Hartwig, M. Hauth, O. Hellmig, W. Herr, S. Herrmann, A. Heske, A. Hinton, P. Ireland, P. Jetzer, U. Johann, M. Krutzik, A. Kubelka, C. Lämmerzahl, A. Landragin, I. Lloro, D. Massonnet, I. Mateos, A. Milke, M. Nofrarias, M. Oswald, A. Peters, K. Posso-Trujillo, E. Rasel, E. Rocco, A. Roura, J. Rudolph, W. Schleich, C. Schubert, T. Schuldt, S. Seidel, K. Sengstock, C. F. Sopuerta, F. Sorrentino, D. Summers, G. M. Tino, C. Trenkel, N. Uzunoglu, W. von Klitzing, R. Walser, T. Wendrich, A. Wenzlawski, P. Weßels, A. Wicht, E. Wille, M. Williams, P. Windpassinger, and N. Zahzam, "STE-QUEST - test of the universality of free fall using cold atom interferometry," *Class. Quantum Gravity*, vol. 31, p. 115010, 2014.

[76] E. Luvsandamdin, S. Spießberger, M. Schiemangk, A. Sahm, G. Mura, A. Wicht, A. Peters, G. Erbert, and G. Tränkle, "Development of narrow linewidth, micro-integrated extended cavity diode lasers for quantum optics experiments in space," *Appl. Phys. B*, vol. 111, pp. 255–260, 2013.

[77] E. Luvsandamdin, C. Kürbis, M. Schiemangk, A. Sahm, A. Wicht, A. Peters, G. Erbert, and G. Tränkle, "Micro-integrated extended cavity diode lasers for precision potassium spectroscopy in space," *Opt. Express*, vol. 22, pp. 7790–7798, 2014.

[78] A. Wicht, A. Bawamia, M. Krüger, C. Kürbis, M. Schiemangk, R. Smol, A. Peters, and G. Tränkle, "Narrow linewidth diode laser modules for quantum optical sensor applications in the field and in space," in *Proc. SPIE, Components Packag. Laser Syst. III* (A. L. Glebov and P. O. Leisher, eds.), vol. 10085, p. 100850F, 2017.

[79] M. Schiemangk, *Ein Lasersystem für Experimente mit Quantengasen unter Schwerelosigkeit*. Dissertation, Humboldt-Universität zu Berlin, 2019.

[80] J. Pahl, A. N. Dinkelaker, C. Grzeschik, J. Kluge, M. Schiemangk, A. Wicht, A. Peters, and M. Krutzik, "Compact and robust diode laser system technology for dual-species ultracold atom experiments with rubidium and potassium in microgravity," *Appl. Opt.*, vol. 58, pp. 5456–5464, 2019.

[81] Dr. E. Kovalchuk. private communication, 2010.

[82] W. Liang, A. A. Savchenkov, V. S. Ilchenko, D. Eliyahu, D. Seidel, A. B. Matsko, and L. Maleki, "Generation of a coherent near-infrared Kerr frequency comb in a monolithic microresonator with normal GVD," *Opt. Lett.*, vol. 39, pp. 2920–2923, 2014.

[83] S. Vasilyev, I. Moskalev, V. Smolski, J. Peppers, M. Mirov, A. Muraviev, K. Vodopyanov, S. Mirov, and V. Gapontsev, "Multi-octave visible to long-wave IR femtosecond continuum generated in Cr:ZnS-GaSe tandem," *Opt. Express*, vol. 27, p. 16405, 2019.

[84] S. Hakobyan, V. J. Wittwer, P. Brochard, K. Gürel, S. Schilt, A. S. Mayer, U. Keller, and T. Südmeyer, "Full stabilization and characterization of an optical frequency comb from a

diode-pumped solid-state laser with GHz repetition rate," *Opt. Express*, vol. 25, p. 20437, 2017.

[85] K. Gürel, V. J. Wittwer, S. Hakobyan, S. Schilt, and T. Südmeyer, "Carrier envelope offset frequency detection and stabilization of a diode-pumped mode-locked Ti:sapphire laser," *Opt. Lett.*, vol. 42, pp. 1035–1038, 2017.

[86] G. Ycas, S. Osterman, and S. A. Diddams, "Generation of a 660-2100 nm laser frequency comb based on an erbium fiber laser," *Opt. Lett.*, vol. 37, pp. 2199–201, 2012.

[87] D. Yoon Oh, K. Y. Yang, C. Fredrick, G. Ycas, S. A. Diddams, and K. J. Vahala, "Coherent ultra-violet to near-infrared generation in silica ridge waveguides," *Nat. Commun.*, vol. 8, pp. 1–7, 2017.

[88] E. S. Lamb, D. R. Carlson, D. D. Hickstein, J. R. Stone, S. A. Diddams, and S. B. Papp, "Optical-frequency measurements with a Kerr microcomb and photonic-chip supercontinuum," *Phys. Rev. Appl.*, vol. 9, p. 24030, 2018.

[89] S. H. Lee, D. Y. Oh, Q. F. Yang, B. Shen, H. Wang, K. Y. Yang, Y. H. Lai, X. Yi, X. Li, and K. Vahala, "Towards visible soliton microcomb generation," *Nat. Commun.*, vol. 8, p. 1295, 2017.

[90] S. P. Yu, T. C. Briles, G. T. Moille, X. Lu, S. A. Diddams, K. Srinivasan, and S. B. Papp, "Tuning Kerr-soliton frequency combs to atomic resonances," *Phys. Rev. Appl.*, vol. 11, p. 044017, 2019.

[91] Y. Ding, M. A. Cataluna, D. Nikitichev, I. Krestnikov, D. Livshits, and E. Rafailov, "Broad repetition-rate tunable quantum-dot external-cavity passively mode-locked laser with extremely narrow radio frequency linewidth," *Appl. Phys. Express*, vol. 4, p. 062703, 2011.

[92] T. Habruseva, D. Arsenijević, M. Kleinert, D. Bimberg, G. Huyet, and S. P. Hegarty, "Optimum phase noise reduction and repetition rate tuning in quantum-dot mode-locked lasers," *Appl. Phys. Lett.*, vol. 104, p. 021112, 2014.

[93] M.-C. Lo, R. Guzmán, M. Ali, R. Santos, L. Augustin, and G. Carpintero, "1.8-THz-wide optical frequency comb emitted from monolithic passively mode-locked semiconductor quantum-well laser," *Opt. Lett.*, vol. 42, pp. 3872–3875, 2017.

[94] J. C. Balzer, R. H. Pilny, B. Dopke, A. Klehr, G. Erbert, G. Trankle, C. Brenner, and M. R. Hofmann, "Passively mode-locked diode laser with optimized dispersion management," *IEEE J. Sel. Top. Quantum Electron.*, vol. 21, pp. 16–23, 2015.

[95] H. Wang, L. Kong, A. Forrest, D. Bajek, S. E. Haggett, X. Wang, B. Cui, J. Pan, Y. Ding, and M. A. Cataluna, "Ultrashort pulse generation by semiconductor mode-locked lasers at 760 nm," *Opt. Express*, vol. 22, p. 25940, 2014.

[96] M. Kuramoto, N. Kitajima, H. Guo, Y. Furushima, M. Ikeda, and H. Yokoyama, "Two-photon fluorescence bioimaging with an all-semiconductor laser picosecond pulse source," *Opt. Lett.*, vol. 32, pp. 2726–2728, 2007.

[97] G. Tandoi, C. N. Ironside, J. H. Marsh, and A. C. Bryce, "Output power limitations and improvements in passively mode locked GaAs/AlGaAs quantum well lasers," *IEEE J. Quantum Electron.*, vol. 48, pp. 318–327, 2012.

[98] P. P. Vasil'ev, H. Kan, H. Ohta, T. Hiruma, and K. A. Tanaka, "Mode locking of an external cavity asymmetric quantum-well GaAs/AlGaAs semiconductor laser," *Quantum Electron.*, vol. 36, pp. 1065–1071, 2006.

[99] G. Tandoi, K. Seunarine, C. N. Ironside, C. A. Bryce, S. D. McDougall, W. Meredith, and A. N. Luiten, "Passively mode-locked semiconductor laser for coherent population trapping in ^{87}Rb," *2011 Conf. Lasers Electro-Optics Eur. 12th Eur. Quantum Electron. Conf. (CLEO Eur.*, vol. 7198, no. 3, p. 719811, 2011.

[100] H. Christopher, E. V. Kovalchuk, H. Wenzel, F. Bugge, M. Weyers, A. Wicht, A. Peters, and G. Tränkle, "Comparison of symmetric and asymmetric double quantum well extended-cavity diode lasers for broadband passive mode-locking at 780 nm," *Appl. Opt.*, vol. 56, pp. 5566–5572, 2017.

[101] R. N. Hall, G. E. Fenner, J. D. Kingsley, T. J. Soltys, and R. O. Carlson, "Coherent light emission from GaAs junctions," *Phys. Rev. Lett.*, vol. 9, pp. 366–368, nov 1962.

[102] V. N. Morozov, V. V. Nikitin, A. A. Sheronov, and P. N. Lebedev, "Self-synchronization of modes in a GaAs semiconductor injection laser," 1968.

[103] E. P. Harris, "Spiking in current-modulated CW GaAs external cavity lasers," *J. Appl. Phys.*, vol. 42, pp. 892–893, 1971.

[104] L. Glasser, "C.W. modelocking of a GaInAsP diode laser," *Electron. Lett.*, vol. 14, pp. 725–726, 1978.

[105] H. Ito, H. Yokoyama, S. Murata, and H. Inaba, "Picosecond optical pulse generation from an r.f. modulated AlGaAs d.h. diode laser," *Electron. Lett.*, vol. 15, pp. 738–740, 1979.

[106] E. P. Ippen, D. J. Eilenberger, and R. W. Dixon, "Picosecond pulse generation by passive mode locking of diode lasers," *Appl. Phys. Lett.*, vol. 37, pp. 267–269, 1980.

[107] C. Harder, J. S. Smith, K. Y. Lau, and A. Yariv, "Passive mode locking of buried heterostructure lasers with nonuniform current injection," *Appl. Phys. Lett.*, vol. 42, pp. 772–774, 1983.

[108] Y. Silberberg, P. W. Smith, D. J. Eilenberger, D. A. B. Miller, A. C. Gossard, and W. Wiegmann, "Passive mode locking of a semiconductor diode laser," *Opt. Lett.*, vol. 9, pp. 507–509, 1984.

[109] K. Y. Lau, I. Ury, and A. Yariv, "Passive and active mode locking of a semiconductor laser without an external cavity," *Appl. Phys. Lett.*, vol. 46, pp. 1117–1119, 1985.

[110] V. Moskalenko, J. Javaloyes, S. Balle, M. Smit, and E. Bente, "Theoretical study of colliding pulse passively mode-locked semiconductor ring lasers with an intracavity Mach-Zehnder modulator," *IEEE J. Quantum Electron.*, vol. 50, pp. 415–422, 2014.

[111] W. Pallmann, C. Zaugg, M. Mangold, V. Wittwer, H. Moench, S. Gronenborn, M. Miller, B. Tilma, T. Südmeyer, and U. Keller, "Gain characterization and passive modelocking of electrically pumped VECSELs," *Opt. Express*, vol. 20, pp. 24791–24802, 2012.

[112] J. Bowers, P. Morton, A. Mar, and S. Corzine, "Actively mode-locked semiconductor lasers," *IEEE J. Quantum Electron.*, vol. 25, pp. 1426–1439, 1989.

[113] M.-T. Choi, W. Lee, J.-M. Kim, and P. J. Delfyett, "Ultrashort, high-power pulse generation from a master oscillator power amplifier based on external cavity mode locking of a quantum-dot two-section diode laser," *Appl. Phys. Lett.*, vol. 87, p. 221107, 2005.

[114] G. Erbert, F. Bugge, A. Knauer, J. Sebastian, A. Thies, H. Wenzel, M. Weyers, and G. Tränkle, "High-power tensile-strained GaAsP-AlGaAs quantum-well lasers emitting between 715 and 790 nm," *IEEE J. Sel. Top. Quantum Electron.*, vol. 5, pp. 780–784, 1999.

[115] R. Diehl, ed., *High-power diode lasers - fundamentals, technology, applications*. Springer-Verlag Berlin Heidelberg, 78th ed., 2000.

[116] A. Knauer, G. Erbert, R. Staske, B. Sumpf, H. Wenzel, and M. Weyers, "High-power 808 nm lasers with a super-large optical cavity," *Semicond. Sci. Technol.*, vol. 20, pp. 621–624, 2005.

[117] S. L. Chuang, *Physics of photonic devices*. Wiley Series in Pure and Applied Optics, Wiley & Sons, Inc., 2nd ed., 2009.

[118] H. Wenzel, F. Bugge, M. Dallmer, F. Dittmar, J. Fricke, K. H. Hasler, and G. Erbert, "Fundamental-lateral mode stabilized high-power ridge-waveguide lasers with a low beam divergence," *IEEE Photonics Technol. Lett.*, vol. 20, pp. 214–216, 2008.

[119] J. P. van der Ziel, "Active mode locking of double heterostructure laser in an external cavity," *J. Appl. Phys.*, vol. 52, pp. 4435–4446, 1981.

[120] A. C. Bordonalli, B. Cai, A. J. Seeds, and P. J. Williams, "Generation of microwave signals by active mode locking in a gain bandwidth restricted laser structure," *IEEE Photonics Technol. Lett.*, vol. 8, pp. 151–153, jan 1996.

[121] F. Quinlan, S. Ozharar, S. Gee, and P. J. Delfyett, "Harmonically mode-locked semiconductor-based lasers as high repetition rate ultralow noise pulse train and optical frequency comb sources," *J. Opt. A Pure Appl. Opt.*, vol. 11, p. 103001, 2009.

[122] P. Vasil'ev, *Ultrafast Diode Lasers - Fundamentals and Applications*. Artech House, 1995.

[123] E. P. Ippen, "Principles of passive mode locking," *Appl. Phys. B-Lasers Opt.*, vol. 58, pp. 159–170, 1994.

[124] H. A. Haus, "Modelocking of semiconductor laser diodes," *Jpn. J. Appl. Phys.*, vol. 20, pp. 1007 – 1020, 1981.

[125] D. J. Derickson, P. A. Morton, J. E. Bowers, and R. L. Thornton, "Comparison of timing jitter in external and monolithic cavity mode-locked semiconductor-lasers," *Appl. Phys. Lett.*, vol. 59, pp. 3372–3374, 1991.

[126] J. H. Zarrabi, E. L. Portnoi, and A. V. Chelnokov, "Passive mode locking of a multistripe single quantum well GaAs laser diode with an intracavity saturable absorber," *Appl. Phys. Lett.*, vol. 59, pp. 1526–1528, 1991.

[127] P. B. Hansen, G. Raybon, U. Koren, P. P. Iannone, B. I. Miller, G. M. Young, M. A. Newkirk, and C. A. Burrus, "InGaAsP monolithic extended-cavity lasers with integrated saturable absorbers for active, passive, and hybrid mode locking at 8.6 GHz," *Appl. Phys. Lett.*, vol. 62, pp. 1445–1447, 1993.

[128] W. Franz, "Einfluss eines elektrischen Feldes auf eine optische Absorptionskante," *Zeitschrift für Naturforschung. A, Astrophys. Phys. und Phys. Chemie*, vol. 13, pp. 484–489, 1958.

[129] D. A. B. Miller, D. S. Chemla, T. C. Damen, A. C. Gossard, W. Wiegmann, T. H. Wood, and C. A. Burrus, "Band-edge electroabsorption in quantum well structures: the quantum-confined Stark Effect," *Phys. Rev. Lett.*, vol. 53, pp. 2173–2176, 1984.

[130] P. A. Morton, J. E. Bowers, L. A. Koszi, M. Soler, J. Lopata, and D. P. Wilt, "Monolithic hybrid mode-locked 1.3 μm semiconductor lasers," *Appl. Phys. Lett.*, vol. 56, pp. 111–113, 1990.

[131] P. J. Delfyett, A. Dienes, J. P. Heritage, M. Y. Hong, and Y. H. Chang, "Femtosecond hybrid mode-locked semiconductor laser and amplifier dynamics," *Appl. Phys. B Laser Opt.*, vol. 58, pp. 183–195, 1994.

[132] D. Novak, Y. Kim, H. F. Liu, Z. Ahmed, and Y. Ogawa, "Locking range of a hybrid mode-locked monolithic DBR semiconductor laser at millimeter-wave frequencies," *IEEE Microw. Guid. Wave Lett.*, vol. 6, pp. 320–322, 1996.

[133] H. Haus, "Theory of mode locking with a slow saturable absorber," *IEEE J. Quantum Electron.*, vol. 11, pp. 736–746, 1975.

[134] H. A. Haus, "Theory of mode locking with a fast saturable absorber," *J. Appl. Phys.*, vol. 46, pp. 3049–3058, 1975.

[135] G. P. Agrawal and N. K. Dutta, *Semiconductor Lasers*. Kluwer Academic Publishers, 2000.

[136] L. A. Coldren and S. W. Corzine, *Diode Lasers and Photonic Integrated Circuits*. Wiley Series in Mircrowave and Optical Engeneering, Wiley-Interscience, 1995.

[137] M. G. A. Bernard and G. Duraffourg, "Laser conditions in semiconductors," *Phys. status solidi*, vol. 1, pp. 699–703, 1961.

[138] C. Henry, "Theory of the linewidth of semiconductor lasers," *IEEE J. Quantum Electron.*, vol. 18, pp. 259–264, 1982.

[139] Y. Arakawa and A. Yariv, "Theory of gain, modulation response, and spectral linewidth in AlGaAs quantum well lasers," *IEEE J. Quantum Electron.*, vol. 21, pp. 1666–1674, 1985.

[140] C.-Y. Tsai, C. a. Tsai, R. M. Spencer, Y.-H. Lo, and L. F. Eastman, "Nonlinear gain coefficients in semiconductor lasers: effects of carrier heating," *IEEE J. Quantum Electron.*, vol. 32, pp. 201–212, 1996.

[141] J. Wang and H. C. Schweizer, "A quantitative comparison of the classical rate-equation model with the carrier heating model on dynamics of quantum well laser: the role of carrier energy relaxation, electron-hole interaction, and auger effect," *IEEE J. Quantum Electron.*, vol. 33, pp. 1350–1359, 1997.

[142] H. Wenzel, G. Erbert, and P. M. Enders, "Improved theory of the refractive-index change in quantum-well lasers," *IEEE J. Sel. Top. Quantum Electron.*, vol. 5, pp. 637–642, 1999.

[143] A. Fox, D. Miller, G. Livescu, J. Cunningham, and W. Y. Jan, "Quantum well carrier sweep out: relation to electroabsorption and exciton saturation," *IEEE J. Quantum Electron.*, vol. 27, pp. 2281–2295, 1991.

[144] M.-C. Amann and J. Buus, *Tunable Laser Diodes*. Artech House, 1998.

[145] J. R. Karin, R. J. Helkey, D. J. Derickson, R. Nagarajan, D. S. Allin, J. E. Bowers, and R. L. Thornton, "Ultrafast dynamics in field-enhanced saturable absorbers," *Appl. Phys. Lett.*, vol. 64, pp. 676–678, 1994.

[146] A. V. Uskov, J. R. Karin, R. Nagaraja, and J. E. Bowers, "Dynamics of carrier heating and sweepout in waveguide saturable absorbers," *IEEE J. Sel. Top. Quantum Electron.*, vol. 1, pp. 552–561, 1995.

[147] N. Susa and T. Nakahara, "Enhancement of change in the refractive index in an asymmetric quantum well," *Appl. Phys. Lett.*, vol. 60, pp. 2457–2459, 1992.

[148] J. Javaloyes and S. Balle, "Anticolliding design for monolithic passively mode-locked semiconductor lasers," *Opt. Lett.*, vol. 36, pp. 4407–4409, 2011.

[149] C. H. Lee and P. J. Delfyett, "Limits on amplification of picosecond pulses by using semiconductor-laser traveling-wave amplifiers," *IEEE J. Quantum Electron.*, vol. 27, pp. 1110–1114, 1991.

[150] K. Yvind, P. M. W. Skovgaard, J. Mork, J. Hanberg, and M. Kroh, "Performance of External Cavity Mode-Locked Semiconductor Lasers Employing Reverse Biased Saturable Absorbers," *Phys. Scr.*, vol. T101, p. 129, 2002.

[151] G. Erbert, A. Bärwolf, J. Sebastian, and J. Tomm, "High-power broad-area diode lasers and laser bars," in *High-power diode lasers - Fundam. Technol. Appl.* (R. Diehl, ed.), pp. 174–223, Springer-Verlag, 2000.

[152] P. Ressel, G. Erbert, U. Zeimer, K. Hausler, G. Beister, B. Sumpf, A. Klehr, and G. Trankle, "Novel passivation process for the mirror facets of Al-free active-region high-power semiconductor diode lasers," *IEEE Photonics Technol. Lett.*, vol. 17, pp. 962–964, 2005.

[153] G. P. Agrawal and N. A. Olsson, "Amplification and compression of weak picosecond optical pulses by using semiconductor-laser amplifiers," *Opt. Lett.*, vol. 14, pp. 500–502, 1989.

[154] G. Agrawal and N. Olsson, "Self-phase modulation and spectral broadening of optical pulses in semiconductor laser amplifiers," *IEEE J. Quantum Electron.*, vol. 25, pp. 2297–2306, 1989.

[155] K. Kim, S. Lee, and P. J. Delfyett Jr., "Extreme chirped pulse amplification-beyond the fundamental energy storage limit of semiconductor optical amplifiers," *IEEE J. Sel. Top. Quantum Electron.*, vol. 12, pp. 245–254, 2006.

[156] R. Szipöcs, C. Spielmann, F. Krausz, and K. Ferencz, "Chirped multilayer coatings for broadband dispersion control in femtosecond lasers," *Opt. Lett.*, vol. 19, pp. 201–203, 1994.

[157] H. Haus, "Mode-locking of lasers," *IEEE J. Sel. Top. Quantum Electron.*, vol. 6, pp. 1173–1185, 2000.

[158] V. Pervak, C. Teisset, A. Sugita, S. Naumov, F. Krausz, and A. Apolonski, "High-dispersive mirrors for femtosecond lasers," *Opt. Express*, vol. 16, pp. 10220–10233, 2008.

[159] D. von der Linde, "Characterization of the noise in continuously operating mode-locked lasers," *Appl. Phys. B*, vol. 39, pp. 201–217, 1986.

[160] F. Kéfélian, S. O'Donoghue, M. T. Todaro, J. G. McInerney, and G. Huyet, "RF linewidth in monolithic passively mode-locked semiconductor laser," *IEEE Photonics Technol. Lett.*, vol. 20, pp. 1405–1407, 2008.

[161] IEEE Standards Coordinating Commitee 27 on Time and Frequency, "IEEE standard definitions of physical quantities for fundamental frequency and time metrology - random instabilities," 2009.

[162] J. Mulet and J. Mørk, "Analysis of timing jitter in external-cavity mode-locked semiconductor lasers," *IEEE J. Quantum Electron.*, vol. 42, pp. 249–256, 2006.

[163] M. Schiemangk, S. Spießberger, A. Wicht, G. Erbert, G. Tränkle, and A. Peters, "Accurate frequency noise measurement of free-running lasers," *Appl. Opt.*, vol. 53, pp. 7138–7143, 2014.

[164] G. Di Domenico, S. Schilt, and P. Thomann, "Simple approach to the relation between laser frequency noise and laser line shape," *Appl. Opt.*, vol. 49, pp. 4801–4807, 2010.

[165] Newport Corp., *Long scan autocorrelator (application note 27)*. Application Notes, Worldwide Headquarters, 1791 Deere Avenue, Irvine, CA 92606: Technology and Application Center, app.note 2 ed., 2009.

[166] J.-H. Chung and A. Weiner, "Ambiguity of ultrashort pulse shapes retrieved from the intensity autocorrelation and the power spectrum," *IEEE J. Sel. Top. Quantum Electron.*, vol. 7, pp. 656–666, 2001.

[167] K. L. Sala, G. A. Kenney-Wallace, and G. E. Hall, "CW autocorrelation measurements of picosecond laser pulses," *IEEE J. Quantum Electron.*, vol. 16, pp. 990–996, 1980.

[168] H. Christopher, E. V. Kovalchuk, A. Wicht, G. Erbert, G. Tränkle, and A. Peters, "Compact mode-locked diode laser system for high precision frequency comparisons in microgravity," in *SPIE Proc. / Int. Conf. Sp. Opt. — ICSO 2014*, p. 105632U, 2017.

[169] H. Christopher, E. Kovalchuk, A. Wicht, G. Tränkle, and A. Peters, "Compact mode-locked diode laser system for precision frequency comparisons in microgravity experiment," in *Conference on Lasers and Electro-Optics (CLEO:2016)*, p. SM3H.1, 2016.

[170] H. Christopher, E. Kovalchuk, H. Wenzel, F. Bugge, M. Weyers, G. Erbert, A. Wicht, A. Peters, and G. Tränkle, "Development of a compact mode-locked ECDL for precision frequency comparison experiments at 780 nm," in *2017 Conference on Lasers and Electro-Optics & European Quantum Electronics Conference (CLEO/Europe-EQEC:2017)*, pp. CB–P.3, 2017.

[171] E. Luvsandamdin, *Development of micro-integrated diode lasers for precision quantum optics experiments in space*. Dissertation, Technische Universität Berlin, 2017.

[172] E. U. Rafailov, M. A. Cataluna, and W. Sibbett, "Mode-locked quantum-dot lasers," *Nat. Photonics*, vol. 1, pp. 395–401, jul 2007.

[173] T. Schlereth, S. Gerhard, W. Kaiser, S. Hofling, and A. Forchel, "High-performance short-wavelength (∼760 nm) AlGaInAs quantum-dot lasers," *IEEE Photonics Technol. Lett.*, vol. 19, pp. 1380–1382, 2007.

[174] A. B. Krysa, J. S. Roberts, J. Devenson, R. Beanland, I. Karomi, S. Shutts, and P. M. Smowton, "InAsP/AlGaInP/GaAs QD laser operating at ∼770 nm," *J. Phys. Conf. Ser.*, vol. 740, p. 012008, 2016.

[175] B. Hüttl, R. Kaiser, C. Kindel, S. Fidorra, W. Rehbein, H. Stolpe, G. Sahin, U. Bandelow, M. Radziunas, A. Vladimirov, and H. Heidrich, "Experimental investigations on the suppression of Q switching in monolithic 40 GHz mode-locked semiconductor lasers," *Appl. Phys. Lett.*, vol. 88, p. 221104, 2006.

[176] S. Ikeda, A. Shimizu, and T. Hara, "Asymmetric dual quantum well laser - wavelength switching controlled by injection current," *Appl. Phys. Lett.*, vol. 55, pp. 1155–1157, 1989.

[177] V. K. Kononenko, I. S. Manak, and S. V. Nalivko, "Design and characteristics of widely tunable quantum-well laser diodes," *Spectrochim. Acta A*, vol. 55, pp. 2091–2096, 1999.

[178] T. F. Krauss, G. Hondromitros, B. Vögele, and R. M. De La Rue, "Broad spectral bandwidth semiconductor lasers," *Electron. Lett.*, vol. 33, pp. 1142–1143, 1997.

[179] H. S. Gingrich, D. R. Chumney, S.-Z. Sun, S. D. Hersee, L. F. Lester, and S. R. J. Brueck, "Broadly tunable external cavity laser diodes with staggered thickness multiple quantum wells," *IEEE Photonics Technol. Lett.*, vol. 9, pp. 155–157, 1997.

[180] M. J. Brennan, J. N. Milgram, P. Mascher, and H. K. Haugen, "Wavelength tunable ultrashort pulse generation from a passively mode-locked asymmetric-quantum-well semiconductor laser," *Appl. Phys. Lett.*, vol. 81, pp. 2502–2504, 2002.

[181] Dr. H. Wenzel. private communication, 2010.

[182] V. Pusino, M. J. Strain, and M. Sorel, "Passive mode-locking in semiconductor lasers with saturable absorbers bandgap shifted through quantum well intermixing," *Photonics Res.*, vol. 2, pp. 186–189, 2014.

[183] J. Javaloyes and S. Balle, "Mode-locking in semiconductor Fabry-Pérot lasers," *IEEE J. Quantum Electron.*, vol. 46, pp. 1023–1030, 2010.

[184] P. M. Stolarz, J. Javaloyes, G. Mezösi, L. Hou, C. N. Ironside, M. Sorel, A. C. Bryce, and S. Balle, "Spectral dynamical behavior in passively mode-locked semiconductor lasers," *IEEE Photonics J.*, vol. 3, pp. 1067–1082, 2011.

[185] M. S. Buyalo, I. M. Gadzhiev, I. O. Bakshaev, and E. L. Portnoi, "RF linewidth in passively mode locked quantum well lasers," *Tech. Phys. Lett.*, vol. 39, pp. 161–163, 2013.

[186] C. Hönninger, R. Paschotta, F. Morier-Genoud, M. Moser, and U. Keller, "Q-switching stability limits of continuous-wave passive mode locking," *J. Opt. Soc. Am. B*, vol. 16, pp. 46–56, 1999.

[187] E. A. Avrutin and E. L. Portnoi, "Suppression of Q-switching instabilities in broadened-waveguide monolithic mode-locked laser diodes," *Opt. Quantum Electron.*, vol. 40, pp. 655–664, jul 2008.

[188] M. B. Holbrook, W. E. Sleat, and D. J. Bradley, "Bandwidth-limited picosecond pulse generation in an actively mode-locked GaAlAs diode laser," *Appl. Phys. Lett.*, vol. 37, pp. 59–61, 1980.

[189] D. J. Derickson, R. J. Helkey, A. Mar, J. R. Karin, J. E. Bowers, and R. L. Thornton, "Suppression of multiple pulse formation in external-cavity mode-locked semiconductor lasers using intrawaveguide saturable absorbers," *IEEE Photonics Technol. Lett.*, vol. 4, pp. 333–335, 1992.

[190] C. A. Williamson, M. J. Adams, A. D. Ellis, and A. Borghesani, "Mode locking of semiconductor laser with curved waveguide and passive mode expander," *Appl. Phys. Lett.*, vol. 82, pp. 322–324, 2003.

[191] M.-C. Amann, "Thermal resistance of ridge-waveguide lasers mounted upside down," *Appl. Phys. Lett.*, vol. 50, pp. 4–6, 1987.

[192] J. Kuhl, E. O. Göbel, and M. Serenyi, "Bandwidth-limited picosecond pulse generation in an actively mode-locked GaAs laser with intracavity chirp compensation," *Opt. Lett.*, vol. 12, pp. 334–336, 1987.

[193] D. von der Linde, "Mode-locked lasers and ultrashort light pulses," *Appl. Phys.*, vol. 2, pp. 281–296, 1973.

[194] G. Agrawal, "Effect of gain dispersion on ultrashort pulse amplification in semiconductor laser amplifiers," *IEEE J. Quantum Electron.*, vol. 27, pp. 1843–1849, 1991.

[195] R. Koumans and R. Van Roijen, "Theory for passive mode-locking in semiconductor laser structures including the effects of self-phase modulation, dispersion, and pulse collisions," *IEEE J. Quantum Electron.*, vol. 32, pp. 478–492, 1996.

[196] S. Arahira and Y. Ogawa, "Repetition-frequency tuning of monolithic passively mode-locked semiconductor lasers with integrated extended cavities," *IEEE J. Quantum Electron.*, vol. 33, pp. 255–264, 1997.

[197] W. K. Tan, H.-Y. Wong, A. E. Kelly, M. Sorel, J. H. Marsh, and A. C. Bryce, "Temperature behaviour of pulse repetition frequency in passively mode-locked InGaAsP/InP laser diode - experimental results and simple model," *Sel. Top. Quantum Electron. IEEE J.*, vol. 13, pp. 1209–1214, 2007.

[198] P. J. Delfyett, H. Shi, S. Gee, C. P. Barty, G. Alphonse, and J. Connolly, "Intracavity spectral shaping in external cavity mode-locked semiconductor diode lasers," *IEEE J. Sel. Top. Quantum Electron.*, vol. 4, pp. 216–221, 1998.

[199] H. Christopher, A. Wicht, A. Peters, and G. Tränkle, "Development of a micro-integrated mode-locked extended cavity diode laser for frequency comparison experiments at 780 nm," in *2017 European Frequency & Time Forum/IEEE International Frequency Control Symposium (EFTF/IFCS)*, p. 1087, 2017.

[200] H. Christopher, A. Wicht, A. Peters, and G. Trankle, "A Micro-Integrated Mode-Locked Extended-Cavity Diode Laser Emitting in the Wavelength Range Around 780 nm," in *2019 Conference on Lasers and Electro-Optics & European Quantum Electronics Conference (CLEO/Europe-EQEC:2019)*, p. SM3H.1, 2019.

[201] S. Spießberger, M. Schiemangk, A. Sahm, A. Wicht, H. Wenzel, G. Erbert, and G. Tränkle, "1 W narrow linewidth semiconductor based laser module emitting near 1064 nm for the use in coherent optical communication in space," in *Int. Conf. Sp. Opt. Syst. Appl.*, (Santa Monica, USA), pp. 322–324, 2011.

[202] S. Rieger, T. Hellwig, T. Walbaum, and C. Fallnich, "Optical repetition rate stabilization of a mode-locked all-fiber laser," *Opt. Express*, vol. 21, pp. 4889–4895, 2013.

[203] N. Torcheboeuf, G. Buchs, S. Kundermann, E. Portuondo-Campa, J. Bennès, and S. Lecomte, "Repetition rate stabilization of an optical frequency comb based on solid-state laser technology with an intra-cavity electro-optic modulator," *Opt. Express*, vol. 25, p. 2215, 2017.

[204] R. Helkey, D. Derickson, A. Mar, J. Wasserbauer, J. Bowers, and R. Thornton, "Repetition frequency stabilisation of passively mode-locked semiconductor lasers," *Electron. Lett.*, vol. 28, p. 1920, 1992.

[205] N. Strauß, I. Ernsting, S. Schiller, A. Wicht, P. Huke, and R. H. Rinkleff, "A simple scheme for precise relative frequency stabilization of lasers," *Appl. Phys. B Lasers Opt.*, vol. 88, pp. 21–28, 2007.

[206] Rhode & Schwarz GmbH & Co KG, "FSV Signal and Spectrum Analyzer Specifications," 2010.

[207] FBH. https://www.fbh-berlin.de/presse/pressemitteilungen/detail/datenhighway-im-weltall-mit-lasern-aus-dem-fbh, 2016 (accessed 02.02.2016).

[208] S. Kumar, R. Trotta, E. Zallo, J. D. Plumhof, P. Atkinson, A. Rastelli, and O. G. Schmidt, "Strain-induced tuning of the emission wavelength of high quality GaAs/AlGaAs quantum dots in the spectral range of the ^{87}Rb D_2 lines," *Appl. Phys. Lett.*, vol. 99, p. 161118, 2011.

[209] P. Del'Haye, A. Schliesser, O. Arcizet, T. Wilken, R. Holzwarth, and T. J. Kippenberg, "Optical frequency comb generation from a monolithic microresonator.," *Nature*, vol. 450, pp. 1214–1217, 2007.

[210] Z. Wang, K. Van Gasse, V. Moskalenko, S. Latkowski, E. Bente, B. Kuyken, and G. Roelkens, "A III-V-on-Si ultra-dense comb laser," *Light Sci. Appl.*, vol. 6, p. e16260, 2017.

List of publications

The following list comprises all those publications of the author that are connected with this thesis.

Peer-reviewed journal articles and conference proceedings

- H. Christopher, A. Wicht, A. Peters, and G. Tränkle, "A micro-integrated mode-locked extended-cavity diode laser emitting in the wavelength range around 780 nm," in 2019 Conference on Lasers and Electro-Optics Europe & European Quantum Electronics Conference (CLEO/Europe-EQEC), SM3H.1 (2019),
  DOI: 10.1109/CLEOE-EQEC.2019.8872834.

- H. Christopher, E. V. Kovalchuk, H. Wenzel, F. Bugge, M. Weyers, A. Wicht, A. Peters, and G. Tränkle, "Comparison of symmetric and asymmetric double quantum well extended cavity diode lasers for broadband passive mode-locking at 780 nm," Appl. Opt. 56 (24), 5566-5572 (2017), DOI: 10.1364/AO.56.005566.

- H. Christopher, A. Wicht, A. Peters, and G. Tränkle, "Development of a micro-integrated mode-locked extended cavity diode laser for frequency comparison experiments at 780 nm," in 2017 European Frequency & Time Forum/IEEE International Frequency Control Symposium (EFTF/IFCS), 1087 (2017).

- H. Christopher, E. Kovalchuk, H. Wenzel, F. Bugge, M. Weyers, G. Erbert, A. Wicht, A. Peters, and G. Tränkle, "Development of a compact mode-locked ECDL for precision frequency comparison experiments at 780 nm," in 2017 European Conference on Lasers and Electro-Optics & European Quantum Electronics Conference (CLEO/Europe-EQEC 2017), CB-P.3 (2017), DOI: 10.1109/CLEOE-EQEC.2017.8086408.

- H. Christopher, E. Kovalchuk, A. Wicht, G. Tränkle, and A. Peters, "Compact mode-locked diode laser system for precision frequency comparisons in microgravity experiment," in 2016 Conference on Lasers and Electro-Optics (CLEO:2016), SM3H.1 (2016),
  DOI: 10.1364/CLEO_SI.2016.SM3H.1.

- H. Christopher, E. V. Kovalchuk, A. Wicht, G. Erbert, G. Tränkle, and A. Peters, "Compact mode-locked diode laser system for high precision frequency comparisons in microgravity," in SPIE Proc. / International Conference on Space Optics (ICSO), 105632U (2014), DOI: 10.1117/12.2304184.

Oral presentations

- H. Christopher, A. Wicht, A. Peters, and G. Tränkle, "A micro-integrated mode-locked extended-cavity diode laser emitting in the wavelength range around 780 nm," at 2019 Conference on Lasers and Electro-Optics Europe & European Quantum Electronics Conference (CLEO/Europe-EQEC), SM3H.1 (2019),
  DOI: 10.1109/CLEOE-EQEC.2019.8872834.

- H. Christopher, E. Kovalchuk, A. Wicht, G. Tränkle, and A. Peters, "Compact mode-locked diode laser system for precision frequency comparisons in microgravity experiment," at 2016 Conference on Lasers and Electro-Optics (CLEO:2016), SM3H.1 (2016),
  DOI: 10.1364/CLEO_SI.2016.SM3H.1.

- H. Christopher, E. Kovalchuk, A. Wicht, G. Tränkle, and A. Peters, "Compact mode-locked diode laser system for precision frequency comparison in microgravity," at Spring Meeting of the Deutsche Physikalische Gesellschaft (DPG) e.V., Sektion Atome, Moleküle, Quantenoptik und Plasmen (SAMOP), Q35.5 (2016).

- H. Christopher, E. Kovalchuk, A. Wicht, G. Tränkle, and A. Peters, "Compact mode-locked diode laser system for high precision frequency comparison experiments in space," at Spring Meeting of the Deutsche Physikalische Gesellschaft (DPG) e.V., Sektion Atome, Moleküle, Quantenoptik und Plasmen (SAMOP), Q39.1 (2015).

- H. Christopher, "Highly stable mode-locked diode laser system for precision comparisons in microgravity," at Mathematische Modelle der Photonik, Forschungsseminar of the Weierstrass-Institut für Angewandte Analysis und Stochastik (WIAS) (2014).

- H. Christopher, E. V. Kovalchuk, A. Wicht, G. Erbert, G. Tränkle, and A. Peters, "Compact mode-locked diode laser system for high precision frequency comparisons in microgravity," at International Conference on Space Optics (ICSO), 10A.3 (2014) / Proc. SPIE 10563, International Conference on Space Optics - ICSO 2014, 105632U (2017),
  DOI: 10.1117/12.2304184

- H. Christopher, E. Kovalchuk, A. Peters, and The LASUS Team, "Compact mode-locked diode laser system for highly accurate frequency comparisons," at Spring Meeting of the Deutsche Physikalische Gesellschaft (DPG) e.V., Sektion Atome, Moleküle, Quantenoptik und Plasmen (SAMOP), Q10.5 (2013).

- H. Christopher, "Mode-locked diode lasers as compact frequency combs for space applications," at Greenhorn-Meeting (2011).

Poster presentations

- H. Christopher, A. Wicht, A. Peters, and G. Tränkle, "Development of a micro-integrated mode-locked extended cavity diode laser for frequency comparison experiments at 780 nm,"

at European Frequency & Time Forum/IEEE Int'l Frequency Control Symposium (EFTF/IFCS), 1087 (2017).

- H. Christopher, E. Kovalchuk, H. Wenzel, F. Bugge, M. Weyers, G. Erbert, A. Wicht, A. Peters, and G. Tränkle, "Development of a compact mode-locked ECDL for precision frequency comparison experiments at 780 nm," at Conference on Lasers and Electro-Optics - European Quantum Electronics Conference (CLEO/Europe-EQEC), CB-P.3 (2017).

- H. Christopher, E. V. Kovalchuk, A. Wicht, G. Erbert, G. Tränkle, and A. Peters, "Compact mode-locked diode laser system for high precision frequency comparisons in microgravity," at International Conference on Space Optics (ICSO), 105632U (2014), DOI: 10.1117/12.2304184.

- H. Christopher, E. V. Kovalchuk, A. Wicht, G. Erbert, G. Tränkle,and A. Peters, "Highly stable mode-locked diode laser system for precision frequency comparisons in microgravity," at Nonlinear Dynamics in Semiconductor Laser, Workshop of the Weierstrass-Institut für Angewandte Analysis und Stochastik (WIAS) (2014).

- H. Christopher, E. Kovalchuk, A. Wicht, G. Erbert, G. Tränkle, A. Peters, and The LASUS Team, "Compact mode-locked diode laser system for highly accurate frequency comparisons in microgravity," at Spring Meeting of the Deutsche Physikalische Gesellschaft (DPG) e.V., Sektion Atome, Moleküle, Quantenoptik und Plasmen (SAMOP), Q16.75 (2014).

Acknowledgments

My warmest and deepest gratitude goes to the number of people that through their knowledge and support made this work possible. Here, I would like to thank some of them by name.

First of all, I would like to thank my supervisor Prof. Achim Peters for giving me the opportunity to work on this scientifically and technologically interesting and challenging project. His deep knowledge, enthusiasm, and commitment to the highest standards inspired me throughout these years. I am also very grateful for the opportunity to be introduced to project management which has already proven to be beneficial.

I would like to express my sincerest gratitude to Prof. Günther Tränkle for welcoming me at „his“ Ferdinand-Braun-Institut (FBH) as a visiting scientist, and for giving me access to the infrastructure and the well of knowledge that are the people and the technology at the FBH. Greatly appreciated are the many in-depth discussions, his incessant guidance, encouragement, and support throughout the years that he made possible despite his demanding schedule as director of the FBH.

I am indebted to Dr. Andreas Wicht, with whom I have worked since the start of my thesis work at the Joint Lab Laser Metrology (now Joint Lab Quantum Photonic Components) of the FBH. His enthusiasm and knowledge were a major driving force of this research. His perfectionism and his drive to develop the best lasers in the world have guided me in my work. The opportunity to gain insights into project management at a research institute is gratefully appreciated. I also thankfully acknowledge his dedication in commenting this thesis.

Many thanks to Dr. Evgeny Kovalchuk who took me under his wing and taught me the works of an optics lab. I am grateful for the many fruitful discussions and hours spent together in the lab getting stuff to work just as we wanted.

My thanks go to Dr. Max Schiemangk for introducing me to linewidth measurements and hybrid micro-integration of diode lasers. Also, big kudos for proof-reading my thesis.

I also thank Christoph Pyrlik for the CAD drawing of my laser test mount and for being a delightful office buddy.

Many thanks go to the FBH Optoelectronics, Materials Technology, Process Technology, and Mounting & Assembly Departments for designing, growing, processing, and mounting of the diode laser chips. Without them, none of this work would have been possible.

I would also like to thank the active and alumni members of the Joint Lab Laser Metrology (now Joint Lab Quantum Photonic Components) and of the QOM group at the HU for creating a pleasant and creative working atmosphere. You guys and gals were amazing.

A huge thanks is sent to my sister for proof-reading this thesis.

Finally, I would like to acknowledge the essential financial support provided by the Deutsches Zentrum für Luft- und Raumfahrt (DLR) through grant no. 50WM0937, -0940, -1237 and -1240.

And, last but definitely not least, I cannot express how much I thank my family and my partner Max for always supporting and encouraging me throughout this thesis work.

Selbständigkeitserklärung

Ich erkläre, dass ich die vorliegende Arbeit selbständig und nur unter Verwendung der angegebenen Literatur und Hilfsmittel angefertigt habe. Ich habe mich anderweitig nicht um einen Doktorgrad beworben und besitze einen solchen auch nicht. Die dem Verfahren zugrunde liegende Promotionsordnung der Mathematisch-Naturwissenschaftlichen Fakultät der Humboldt-Universität zu Berlin habe ich zur Kenntnis genommen.

Berlin, den 30.06.2020 Heike Christopher